

¹ Observation of the Higgs boson in the WW^*
² channel and search for Higgs boson pair
³ production in the $b\bar{b}b\bar{b}$ channel with the
⁴ ATLAS detector

⁵ A DISSERTATION PRESENTED
⁶ BY
⁷ TOMO LAZOVICH
⁸ TO
⁹ THE DEPARTMENT OF PHYSICS

¹⁰ IN PARTIAL FULFILLMENT OF THE REQUIREMENTS
¹¹ FOR THE DEGREE OF
¹² DOCTOR OF PHILOSOPHY
¹³ IN THE SUBJECT OF
¹⁴ PHYSICS

¹⁵ HARVARD UNIVERSITY
¹⁶ CAMBRIDGE, MASSACHUSETTS
¹⁷ MAY 2016

¹⁸ ©2016 – TOMO LAZOVICH

¹⁹ ALL RIGHTS RESERVED.

²⁰ **Observation of the Higgs boson in the WW^* channel and search
²¹ for Higgs boson pair production in the $b\bar{b}b\bar{b}$ channel with the
²² ATLAS detector**

²³ ABSTRACT

²⁴ This dissertation presents the observation and measurement of the Higgs boson in the $H \rightarrow WW^* \rightarrow$
²⁵ $\ell\nu\ell\nu$ channel at $\sqrt{s} = 7$ TeV and $\sqrt{s} = 8$ TeV and a search for Higgs pair production in the $HH \rightarrow$
²⁶ $b\bar{b}b\bar{b}$ channel at $\sqrt{s} = 13$ TeV with the ATLAS detector in pp collisions at the Large Hadron Collider.

²⁷ First, the discovery of a particle consistent with the Higgs boson in 4.8 fb^{-1} at $\sqrt{s} = 7$ TeV and
²⁸ 5.8 fb^{-1} at $\sqrt{s} = 8$ TeV is discussed. Then, the measurement of the Higgs boson signal strength
²⁹ and cross section in both the gluon fusion and vector boson fusion (VBF) production modes using
³⁰ 20.3 fb^{-1} of $\sqrt{s} = 8$ TeV data combined with 4.8 fb^{-1} of 7 TeV data is shown. The combined signal
³¹ strength is measured to be $\mu = 1.09^{+0.23}_{-0.21}$. The total observed significance of the $H \rightarrow WW^*$ process
³² is observed to be 6.1σ (with 5.8σ expected). Advanced methods for background reduction and estima-
³³ tion, particularly in same-flavor lepton final states, are shown. The VBF signal strength is measured to
³⁴ be $\mu_{\text{VBF}} = 1.27^{+0.53}_{-0.45}$ with an observed significance of 3.2σ (with 2.7σ expected). In the VBF chan-
³⁵ nel, a selection requirement based method, the precursor to the final multivariate technique used for the
³⁶ result, is detailed.

³⁷ Finally, a search for Higgs pair production in the $b\bar{b}b\bar{b}$ final state with 3.2 fb^{-1} at $\sqrt{s} = 13$ TeV is
³⁸ presented. A particular focus is placed on a tailored signal region for resonant production of Higgs pairs
³⁹ at high masses. No significant excesses are observed, and upper limits on cross sections are placed for
⁴⁰ spin-2 Randall Sundrum gravitons (RSG) and narrow spin-0 resonances. The cross section of $\sigma(pp \rightarrow$
⁴¹ $G_{\text{KK}}^* \rightarrow hh \rightarrow b\bar{b}b\bar{b})$ with $k/\bar{M}_{\text{Pl}} = 1$ is constrained to be less than 70 fb for masses in the range
⁴² $600 < m_{G_{\text{KK}}^*} < 3000$ GeV. The cross section upper limits for $\sigma(pp \rightarrow H \rightarrow hh \rightarrow b\bar{b}b\bar{b})$ ranges
⁴³ from 30 to 300 fb in the mass range of $500 < m_H < 3000$ GeV.

Contents

44

45	o INTRODUCTION	I
46	I Theoretical and Experimental Background	5
47	I THE PHYSICS OF THE HIGGS BOSON	6
48	1.1 The Standard Model of Particle Physics	6
49	1.2 Electroweak Symmetry Breaking and the Higgs	8
50	1.3 Higgs Boson Production and Decay	II
51	1.4 Higgs Pair Production in the Standard Model	15
52	1.5 Higgs Pair Production in Theories Beyond the Standard Model	16
53	1.6 Conclusion	21
54	2 THE ATLAS DETECTOR AND THE LARGE HADRON COLLIDER	22
55	2.1 The Large Hadron Collider	23
56	2.2 The ATLAS Detector	25
57	2.3 The ATLAS Muon New Small Wheel Upgrade	36
58	2.4 Object Reconstruction in ATLAS	40
59	II Observation and measurement of Higgs boson decays to WW^* in LHC	
60	Run 1 at $\sqrt{s} = 7$ and 8 TeV	49
61	3 $H \rightarrow WW^* \rightarrow \ell\nu\ell\nu$ ANALYSIS STRATEGY	50
62	3.1 Introduction	50
63	3.2 The $H \rightarrow WW^* \rightarrow \ell\nu\ell\nu$ signal in ATLAS	51
64	3.3 Background processes	52
65	3.4 Shared signal region selection requirements	55
66	3.5 Background reduction in same-flavor final states	58
67	3.6 Parameters of interest and statistical treatment	63
68	4 THE DISCOVERY OF THE HIGGS BOSON AND THE ROLE OF THE $H \rightarrow WW^* \rightarrow \ell\nu\ell\nu$	
69	CHANNEL	69
70	4.1 Introduction	69

71	4.2	Data and simulation samples	70
72	4.3	$H \rightarrow WW \rightarrow e\nu\mu\nu$ search	70
73	4.4	$H \rightarrow \gamma\gamma$ search	75
74	4.5	$H \rightarrow ZZ \rightarrow 4\ell$ search	76
75	4.6	Combined results	77
76	4.7	Conclusion	79
77	5	OBSERVATION OF VECTOR BOSON FUSION PRODUCTION OF $H \rightarrow WW^* \rightarrow \ell\nu\ell\nu$	82
78	5.1	Introduction	82
79	5.2	Data and simulation samples	83
80	5.3	Object selection	87
81	5.4	Analysis selection	90
82	5.5	Background estimation	98
83	5.6	Systematic uncertainties	109
84	5.7	Results	113
85	6	COMBINED RUN I $H \rightarrow WW^* \rightarrow \ell\nu\ell\nu$ RESULTS	118
86	6.1	Introduction	118
87	6.2	Results of gluon fusion $H \rightarrow WW^* \rightarrow \ell\nu\ell\nu$ search	119
88	6.3	Signal strength measurements in ggF and VBF production	121
89	6.4	Measurement of Higgs couplings to vector bosons and fermions	124
90	6.5	Higgs production cross section measurement	125
91	6.6	Conclusion	126
92	III	Search for Higgs pair production in the $HH \rightarrow b\bar{b}b\bar{b}$ channel in LHC	
93		Run 2 at $\sqrt{s} = 13$ TeV	128
94	7	SEARCH FOR HIGGS PAIR PRODUCTION IN BOOSTED $b\bar{b}b\bar{b}$ FINAL STATES	129
95	7.1	Introduction	129
96	7.2	Motivation	130
97	7.3	Data and simulation samples	132
98	7.4	Event reconstruction and object selection	134
99	7.5	Event selection	137
100	7.6	Data-driven background estimation	142
101	7.7	Systematic uncertainties	146
102	7.8	Results	150

103	8 COMBINED LIMITS FROM BOOSTED AND RESOLVED SEARCHES	152
104	8.1 Introduction	152
105	8.2 Resolved results	153
106	8.3 Search technique and results	154
107	8.4 Limit setting	154
108	IV Looking ahead	158
109	9 CONCLUSION	159
110	APPENDIX A <i>b</i>-TAGGING PERFORMANCE AT HIGH p_T	163
111	A.1 Changes in MV2 score at high p_T	163
112	A.2 Tagging efficiency by individual jet	166
113	A.3 Effect of multiple <i>b</i> -quarks inside one jet	167
114	A.4 Changes in track quality at high p_T	168
115	REFERENCES	171

Listing of figures

117	1.1	The particles of the Standard Model and their properties [6].	7
118	1.2	The four most common Higgs boson production modes at the LHC: (a) gluon-gluon fu- sion, (b) vector boson fusion, (c) $W/Z + H$ production, (d) $t\bar{t}H$ production	11
119			
120	1.3	Higgs production cross sections as a function of center of mass energy (\sqrt{s}) at a pp collider [18].	12
121	1.4	Higgs boson branching ratios as a function of m_H [18].	14
122	1.5	The two leading diagrams for Standard Model di-Higgs production at the LHC: (a) box di- agram, (b) Higgs self coupling	16
123	1.6	Diagrams with new vertices for non-resonant Higgs pair production arising in composite Higgs models	17
124	1.7	Generic Feynman diagram for resonant Higgs pair production in BSM theories	18
125	1.8	Branching ratios for a spin-2 Randall-Sundrum graviton as a function of mass computed in MadGraph with the CP3-Origins implementation [24, 30]	18
126	1.9	$\sigma \times BR(HH)$ for RSG as a function of mass computed in MadGraph with the CP3-Origins implementation [24, 30]	19
127	1.10	RSG width as a function of mass computed in MadGraph with the CP3-Origins implemen- tation [24, 30]	20
128	1.11	Branching ratios for heavy Higgs H in Type I (left) and Type II (right) 2HDM models with $\tan \beta = 1.5$ and $\cos(\beta - \alpha) = 0.1(0.01)$ for Type I (Type II). [28]	21
129			
130			
131	2.1	A schematic view of the LHC ring [36]	23
132	2.2	A full diagram of the ATLAS detector [32]	26
133	2.3	The ATLAS coordinate system	27
134	2.4	Layout of the ATLAS Inner Detector system [40]	28
135	2.5	Layout of the ATLAS calorimeter system [32]	30
136	2.6	Layout of the ATLAS muon system [32]	32
137	2.7	Predicted field integral as a function of $ \eta $ for the ATLAS magnet system [32]	34
138	2.8	ATLAS trigger rates for Level-1 triggers as a function of instantaneous luminosity in 2012 and 2015 operation. These are single object triggers for electromagnetic clusters (EM), muons (MU), jets (J), missing energy (XE), and τ leptons (TAU). The threshold of the trigger is given in the name in GeV. [42]	35
139			
140			
141	2.9	Instantaneous luminosity as a function of time for data recorded by ATLAS at different cen- ter of mass energies [43, 44]	36
142			
143			
144			
145			
146			
147			

148	2.10	MDT tube hit (solid) and segment (dashed) efficiency as a function of hit rate per tube [45]	37
149	2.11	Trigger rate as a function of p_T threshold with and without the NSW upgrade [45]	38
150	2.12	Illustrations of the geometry (left) and operating principle (right) of the micromegas detector [45]	39
151	2.13	Geometry of the sTGC detector [45]	40
152	2.14	Illustration of particle interactions in ATLAS [48]	41
153	2.15	Electron performance: (a) reconstruction efficiency as a function of electron E_T [50] (b) energy resolution in simulation as a function of $ \eta $ for different energy electrons [51]	42
154	2.16	Muon performance: (a) reconstruction efficiency as a function of muon p_T (b) dimuon mass resolution as a function of average p_T [52]	44
155	2.17	Jet energy response after calibration as a function of true p_T in simulation [56]	45
156	2.18	Summary of the inputs to the MV2 b -tagging algorithm	46
157	2.19	Light jet rejection (1/efficiency) vs. b -jet efficiency for MV1 and its input algorithms (a) [57] and MV2 (b) [58] in simulated $t\bar{t}$ events. The numbers in the algorithm names in (b) refer to the fraction of charm events used in the MV2 training.	47
158	2.20	Resolution of E_T^{miss} components as a function of $\sum E_T$ before pileup suppression with different pileup techniques [60]	48
161	3.1	Branching ratios for a WW system. q refers to quarks. ℓ can be either an electron or muon, and the leptonic branching ratios of the τ are included. For example, the $\ell\nu qq$ final state includes one W decaying to $e\nu$, $\mu\nu$, or $\tau\nu$. τ_h refer to hadronic decays of the τ .	52
162	3.2	Feynman diagram for Standard Model WW production	53
163	3.3	Feynman diagrams for top pair production (left) and Wt production (right)	53
164	3.4	An example Feynman diagram of W +jets production	54
165	3.5	An example Feynman diagram of Z +jets production	55
166	3.6	An illustration of the unique analysis signal regions [61]. The most sensitive regions for both gluon fusion and vector boson fusion production are underlined.	56
167	3.7	A graphical illustration of the $E_{T,\text{rel}}^{\text{miss}}$ calculation	57
168	3.8	Predicted backgrounds (compared with data) as a function of n_j (a and b) and n_b (c) after pre-selection requirements	59
169	3.9	An event display of a Z/γ^* + jets event illustrating the effect of pileup interactions	60
170	3.10	The RMS of different missing transverse momentum definitions as a function of the average number of interactions per bunch crossing	60
171	3.11	The difference between the true and reconstructed values of the missing transverse momentum (a) and m_T (b) in a gluon fusion signal sample	62
172	3.12	Comparison of f_{recoil} distributions for Z/γ^* +jets, $H \rightarrow WW^*$, and other backgrounds with real neutrinos.	63

184	3.13	Signal significance as a function of required value for f_{recoil} and $p_{\text{T},\text{rel}}^{\text{miss}(\text{trk})}$ in the ggF $H \rightarrow WW^*$ with $n_j = 0$	64
185			
186	4.1	Jet multiplicity distribution in data and MC after applying lepton, jet, and $E_{\text{T},\text{rel}}^{\text{miss}}$ selections. The WW and top backgrounds have been normalized using control samples, and the hashed band indicates the total uncertainty on the prediction. [1]	71
187			
188	4.2	Comparison of m_{T} between data and simulation in the $n_j = 0$ WW (a) and $n_j = 1$ top (b) control samples [1]	73
189			
190	4.3	m_{T} distribution in the $H \rightarrow WW \rightarrow e\nu\mu\nu$ $n_j \leq 1$ channels for 8 TeV data [1].	75
191			
192	4.4	Diphoton mass spectrum in 7 and 8 TeV data. Panel a) shows the unweighted data distri- bution superimposed on the background fit, while panel c) shows the data where each event category is weighted by its signal to background ratio. Panels b) and d) show the respective distributions with background subtracted [1].	76
193			
194	4.5	Four lepton invariant mass spectrum ($m_{4\ell}$) in 7 and 8 TeV data compared to background estimate. A 125 GeV SM Higgs signal is shown in blue [1].	77
195			
196	4.6	Local p_0 distribution as a function of hypothesized Higgs mass for the $H \rightarrow ZZ^* \rightarrow 4\ell$ (a), $H \rightarrow \gamma\gamma$ (b), and $H \rightarrow WW^* \rightarrow \ell\nu\ell\nu$ (c) channels. Dashed curves show expected results, while solid curves show observed. Red curves are from 7 TeV data, blue curves from 8 TeV, and black curved combined [1].	79
197			
198	4.7	Combined 95% CL limits (a), local p_0 values (b), and signal strength measurement (c) as a function of Higgs mass [1].	80
199			
200	4.8	Comparison of measured signal strength μ for a 126 GeV Higgs in the 7 and 8 TeV datasets [1].	81
201			
202	4.9	Two dimensional likelihood as a function of signal strength μ and Higgs mass m_H [1].	81
203			
204	5.1	A comparison of the subleading lepton p_{T} spectrum between VBF $H \rightarrow WW^*$ production and $t\bar{t}$ background	84
205			
206	5.2	Leading jet η in VBF $H \rightarrow WW^*$ (red) and $t\bar{t}$ (black)	92
207			
208	5.3	Distributions of (a) m_{jj} , (b) Δy_{jj} , (c) $C_{\ell 1}$, and (d) $\Sigma m_{\ell j}$, for the VBF analysis. The top panels compare simulation and data, while the bottom panels show normalized distributions for all background processes and signal [61].	94
209			
210	5.4	A cartoon of the WW final state. Momenta are represented with thin arrows, spins with thick arrows. [61]	95
211			
212	5.5	Event display of a VBF candidate event [61].	96
213			
214	5.6	Distributions of $m_{\ell\ell}$ (top left), $\Delta\phi_{\ell\ell}$ (top right), and m_{T} (bottom), Higgs topology vari- ables used in the selection requirements of the cut-based signal region and as inputs to the BDT result. These are plotted after all of the BDT pre-training selection cuts [61].	99
215			
216			
217			

218	5.7 Distributions of m_{jj} (top left), Δy_{jj} (top right), $\sum C_\ell$ (bottom), VBF topology variables used in the selection requirements of the cut-based signal region and as inputs to the BDT result. These are plotted after all of the BDT pre-training selection cuts [61].	100
219		
220		
221	5.8 Distributions of m_{jj} (a) and O_{BDT} (b) in the VBF $n_b = 1$ top CR [61].	102
222		
223	5.9 Comparison of m_{jj} shape in a same flavor $Z \rightarrow \ell\ell$ control region and the VBF cut-based signal region.	104
224		
225	5.10 General illustration of the ABCD region definitions for $Z/\gamma^* \rightarrow \ell\ell$ background estimation.	105
226		
227	5.11 Distribution of $m_{\text{T}2}$ in the WW validation region of the VBF analysis [61].	107
228		
229	5.12 Extrapolation factors for the $W + \text{jets}$ estimate derived for muons (a) and electrons (b) as a function of lepton p_{T} [61].	108
230		
231	5.13 Background composition in final VBF signal region [61].	109
232		
233	5.14 Variations in the top background extrapolation factor in the cut-based analysis due to PDF uncertainties, binned in m_{T}	III
234		
235	5.15 Variations in the top background extrapolation factor in the cut-based analysis due to QCD scale uncertainties, binned in m_{T}	II2
236		
237	5.16 Post-fit distributions in the cut-based VBF analysis. Panel (a) shows the one-dimensional m_{T} distribution, while (b) shows the data candidates split into the bins of m_{T} and m_{jj} used in the final fit [61].	II5
238		
239	5.17 Postfit distributions in the BDT VBF analysis [61].	II6
240		
241	5.18 Overlap between cut-based and BDT VBF signal region candidates in the m_{jj} - m_{T} plane. .	II7
242		
243	6.1 Post-fit m_{T} distribution in the $n_j \leq 1$ regions [61].	120
244		
245	6.2 Best fit signal strength $\hat{\mu}$ as a function of hypothesized m_H [61].	122
246		
247	6.3 Local p_0 as a function of m_H [61].	122
248		
249	6.4 Likelihood as a function of $\mu_{\text{VBF}}/\mu_{\text{ggF}}$ [61].	123
249	6.5 Likelihood scan as a function of μ_{VBF} and μ_{ggF} [61].	124
249	6.6 Likelihood scan as a function of κ_F and κ_V [61].	125
249	6.7 Comparison of signal strength measurements in different Higgs decay channels on ATLAS [90].	127
249		
249	7.1 Parton luminosity ratios as a function of resonance mass M_X for 13/8 TeV and 7/8 TeV [91].	130
249	7.2 Summary of HH branching ratios [92].	131
249	7.3 Minimum ΔR between B decay vertices for different RSG masses in a $G_{\text{KK}}^* \rightarrow HH \rightarrow 4b$ sample with $c = 1$	132

250	7.4 Trigger efficiency for events passing all signal region selections as a function of mass in $G_{\text{KK}}^* \rightarrow HH \rightarrow 4b$ samples with $c = 1$ [101]. In the trigger names, “j” refers to a jet or jets. “ht” refers to H_T , the scalar sum of transverse momenta in the event. “bloose” refers to a loose b -tagging requirement applied to the jet. “aor” refers to anti- k_T jets with $R = 1.0$. The numbers at the end are the thresholds on the given quantity in GeV.	134
251		
252		
253		
254		
255	7.5 Comparison of untrimmed and trimmed jet masses for large radius jets in a RSG sample with $m_{G_{\text{KK}}^*} = 1$ TeV. JES (JMS) refers to the standard jet energy (mass) scale calibration for ATLAS [56].	135
256		
257		
258	7.6 Efficiency of finding two b -jets from each Higgs in an RSG event using calorimeter jets with $R = 0.3$ or different track jet radii [105]	136
259		
260		
261	7.7 Illustration of the boosted selection requirements on Higgs candidates. Each large-radius calorimeter jet (Higgs candidate) must contain two track jets	138
262		
263	7.8 Estimated significance as a function of signal mass for RSG $c = 1$ models in the $3b$ (a) and $4b$ (b) regions for different b -tagging efficiency working points	139
264		
265	7.9 Acceptance \times efficiency as a function of mass for (a) RSG and (b) narrow heavy scalar signal models [108].	140
266		
267	7.10 Efficiency of requiring 3 or 4 b -tagged track jets vs. RSG mass. The efficiency quoted is relative to the previous selection requirements (rather than an absolute efficiency).	141
268		
269	7.11 M_J^{sublead} vs. M_J^{lead} in a $2 b$ -tag data sample. The signal region is defined by the inner black contour ($X_{hh} < 1.6$) and the sideband region is defined by the outer contour ($R_{hh} > 35.8$ GeV). The region between the black contours is the control region. The mass region which is enriched in $t\bar{t}$ background is also shown for illustration. [108]	143
270		
271	7.12 An illustration of the data-driven background estimation technique for the boosted analysis	145
272		
273	7.13 Leading large-R jet mass in the $3b$ (a) and $4b$ (b) sideband regions. The multijet and $t\bar{t}$ backgrounds are estimated using the data-driven methods described above. Because their normalizations are derived in the sideband region, the total background normalization is constrained by default to match the normalization of the data [108].	145
274		
275		
276		
277	7.14 Di-jet invariant mass ($M_{2,J}$) in the $3b$ (a) and $4b$ (b) control regions. The multijet and $t\bar{t}$ backgrounds are estimated using the data-driven methods described above [108].	147
278		
279	7.15 Di-jet invariant mass ($M_{2,J}$) in the $3b$ (a) and $4b$ (b) signal regions. The multijet and $t\bar{t}$ backgrounds are estimated using the data-driven methods described above. In the $3b$ region, a graviton signal with $m_{G_{\text{KK}}^*} = 1.8$ TeV and $c = 1$ is overlaid, with the cross section multiplied by a factor of 50 so that the signal is visible. In the $4b$ region, signals with $m_{G_{\text{KK}}^*} = 1.0$ TeV and $m_{G_{\text{KK}}^*} = 1.5$ TeV are overlaid, both with $c = 1$ and the yields multiplied by factors of 2 and 5 respectively [108].	151
280		
281		
282		
283		
284		
285	8.1 Di-jet invariant mass ($M_{2,J}$) in the resolved signal region. A graviton signal with $m_{G_{\text{KK}}^*} = 800$ GeV and $c = 1$ is overlaid. [108].	154
286		

287	8.2 Expected and observed upper limit as a function of mass for G_{KK}^* in the RSG model with	
288	(a) $c = 1$ and (b) $c = 2$, as well as (c) H with fixed $\Gamma_H = 1$ GeV, at the 95% confidence	
289	level in the CL_s method. [108]	157
290	9.1 Combined ATLAS and CMS measurements in Run 1 for (a) Higgs signal strength in gluon	
291	fusion and VBF and (b) Higgs couplings normalized to their SM predictions	161
292	9.2 Discovery significance for RSG models at the HL-LHC in three different budget scenarios [115].	
293	Systematic uncertainties on the background prediction (σ_B) of 2.5% and 5.0% are both tested.	162
294	A.1 p_T of the leading track jet in the leading calorimeter jet for different signal masses in RSG $c =$	
295	1 models	164
296	A.2 MV2c2o score for the leading track jet (a) and subleading track jet (b) of the leading calorime-	
297	ter jet for different signal masses in RSG $c = 1$ models	164
298	A.3 IP3D log-likelihood ratio ($\log(p_b/p_u)$) of the leading track jet in the leading calorimeter jet	
299	for different signal masses in RSG $c = 1$ models	165
300	A.4 Mass (a) and number of tracks (b) for the secondary vertices computed with the SV1 algo-	
301	rithm. When no secondary vertex is found, the quantities are assigned to default negative val-	
302	ues.	166
303	A.5 Mass (a) and number of tracks (b) for vertices computed with the JetFitter algorithm. When	
304	no vertices are found, the quantities are assigned to default negative values.	166
305	A.6 MV2c2o b -tagging efficiency for each of the four track jets in the boosted $4b$ selection as a func-	
306	tion of RSG mass for $c = 1$ models.	167
307	A.7 MV2c2o score (a) and SV1 mass (b) for leading track jets with two truth b quarks ($n_{tb,lead} =$	
308	2) compared to those with only one truth b ($n_{tb,lead} = 1$).	168
309	A.8 Track fit χ^2/n_{DOF} (a) and number of pixel detector hits (b) for the leading track of the lead-	
310	ing track jet in different mass RSG $c = 1$ samples	169
311	A.9 MV2c2o score (a) and SV1 mass (b) for leading track jets whose leading track jet has at least	
312	four pixel hits ($N_{pix} \geq 4$) compared to those which do not ($N_{pix} < 4$).	169

Listing of tables

313

314	1.1	Production cross sections for a 125 GeV Higgs boson at $\sqrt{s} = 8$ TeV with scale and PDF uncertainties [18].	13
315			
316	1.2	Branching ratios for a 125 GeV Higgs boson [18].	15
317	1.3	Possible channels for Higgs searches. Checkmarks denote the most sensitive production modes [5].	15
318			
319	1.4	Production cross sections for pair production of a 125 GeV Higgs boson at $\sqrt{s} = 14$ TeV with total uncertainty [19]. The uncertainties include QCD scale and PDF variations as well as uncertainties on α_S	16
320			
321			
322	2.1	Evolution of LHC machine conditions [38, 39]	25
323	2.2	Performance requirements for the ATLAS detector [32].	37
324	2.3	Signal efficiencies for WH production with $H \rightarrow b\bar{b}$ and $H \rightarrow WW^* \rightarrow \mu\nu qq$ under different trigger configurations [45].	40
325			
326	3.1	A summary of backgrounds to the $H \rightarrow WW^* \rightarrow \ell\nu\ell\nu$ signal	55
327			
328	4.1	Monte carlo generators used to model signal and background for the Higgs search [1].	70
329	4.2	Normalization factors (ratio of data and MC yields in a control sample) for the Standard Model WW and top backgrounds in the $H \rightarrow WW^* \rightarrow \ell\nu\ell\nu$ analysis [1]. Only statistical uncertainties are shown.	73
330			
331	4.3	Data and expected yields for signal and background in the final $H \rightarrow WW^* \rightarrow \ell\nu\ell\nu$ signal region. Uncertainties shown are both statistical and systematic. [1]	74
332			
333	4.4	Summary of the expected and observed significance and measured signal strengths in the combined 7 and 8 TeV datasets for the Higgs discovery analysis [1].	78
334			
335	5.1	Single lepton triggers used for electrons and muons. A logical “or” of the triggers listed for each lepton type is taken. Units are in GeV, and the i denotes an isolation requirement in the trigger.	84
336			
337			
338	5.2	Di-lepton triggers used for different flavor combinations. The two thresholds listed refer to leading and sub-leading leptons, respectively. The di-muon trigger only requires a single lepton at level-1.	84
339			
340			

341	5.3 Trigger efficiency for signal events and relative gain of adding a dilepton trigger on top of the single lepton trigger selection. The first lepton is the leading, while the second is the sub-leading. Efficiencies shown here are for the ggF signal in the $n_j = 0$ category but are comparable for the VBF signal.	85
345	5.4 Monte Carlo samples used to model the signal and background processes [61].	86
346	5.5 p_T dependent isolation requirements for muons. Muons are required to have the amount of calorimeter or track based cone sums be less than this fraction of their p_T	88
348	5.6 p_T dependent requirements for electrons. Electrons are required to have the amount of calorimeter or track based cone sums be less than this fraction of their E_T	89
350	5.7 Event selection for the $n_j \geq 2$ VBF analysis in the 8 TeV cut-based analysis [61].	97
351	5.8 Top normalization factors computed at each stage of the cut-based selection. Uncertainties are statistical only.	101
353	5.9 Top normalization factors computed for each bin of O_{BDT} . Uncertainties are statistical only.	101
354	5.10 $Z/\gamma^* \rightarrow \tau\tau$ correction factors for the VBF cut-based analysis. Uncertainties are statistical only.	104
355	5.11 $Z/\gamma^* \rightarrow \ell\ell$ normalization factors for cut-based and BDT analyses. Uncertainties are statistical only.	106
358	5.12 Systematic uncertainties for various processes in the cut-based VBF analysis, given in units of % change in yield. Values are given for the low m_{jj} signal region.	111
359	5.13 Composition of the post-fit uncertainties (in %) on the total signal (N_{sig}), total background (N_{bkg}), and individual background yields in the VBF analysis [61].	113
360	5.14 Event selection for the VBF BDT analysis. The event yields in (a) are shown after the pre-selection and the additional requirements applied before the BDT classification (see text). The event yields in (b) are given in bins in O_{BDT} after the classification [61].	114
365	6.1 All signal regions definitions input into final statistical fit [61].	119
366	6.2 Post-fit yields in the different ggF and VBF dedicated signal regions [61].	120
367	7.1 Summary of requirements on objects used in the $X \rightarrow HH \rightarrow b\bar{b}b\bar{b}$ search	137
368	7.2 Effect of boosted selection on data, RSG signal models, $t\bar{t}$, and $Z + \text{jets}$. The numbers from simulation are normalized with the MC generator cross section and do not take into account the data driven estimates described in section 7.6 [109].	142
371	7.3 Mass region definitions used for background estimation	143
372	7.4 Parameters derived for exponential fit to background M_{2J} shape in the 3 b and 4 b signal regions [109]	146
374	7.5 The number of events in data and predicted background events in the boosted 3-tag and 4-tag sideband and control regions. The uncertainties shown are statistical only. [108]	147

376	7.6 Summary of systematic uncertainties in the total background and signal event yields (expressed in %) in the boosted 3-tag and 4-tag signal regions. Systematic uncertainties on the signal normalization are shown for models with $m_{G_{KK}^*} = 1.5$ TeV and both $c = 1$ and $c = 2$ as well as a narrow width heavy scalar.	149
377		
378		
379		
380	7.7 Alternate fit functions used to model the M_{2J} distribution in the QCD multijet background. In the equations, $x = M_{2J}/\sqrt{s}$	150
381		
382		
383		
384	7.8 Observed yields in the 3-tag and 4-tag signal regions for the boosted analysis compared to the predicted number of background events Errors correspond to the total uncertainties in the predicted event yields. The yields for a graviton with $m_{G_{KK}^*} = 1$ TeV and $c = 1$ are also shown. [108]	151
385		
386	8.1 Observed yields in the resolve selection 4-tag signal region compared to the predicted num- ber of background events Errors correspond to the total uncertainties in the predicted event yields. The yields for a graviton with $m_{G_{KK}^*} = 800$ GeV and $c = 1$ are also shown. [108] . .	153
387		
388		

Acknowledgments

391 I have been a member of the Harvard ATLAS group for many years now, first as an undergraduate
 392 and then as a graduate student. As a result, I have had the privilege of interacting with many amazing
 393 people there over the years and have accumulated a large list of folks to thank.

394 First and foremost, I must thank the two people who have effectively been my academic parents since
 395 I started in the Harvard group: João Guimarães da Costa and Melissa Franklin. Melissa Franklin and
 396 João Guimarães da Costa. They have both been so important to both my academic and personal devel-
 397 opment that I can't even put one before the other. João has been an excellent PhD advisor, showing me
 398 how to look at the big picture and helping me navigate the sometimes complicated politics of ATLAS.
 399 He got me started on my first projects with ATLAS as a young college sophomore before there was even
 400 beam in the LHC (go cosmic ray muons!). He has also been a constant source of advice and support,
 401 even when we have been on different continents. Melissa gave me my start in HEP as a summer student
 402 on CDF and has been an unbelievable mentor throughout my time at Harvard. I still remember our
 403 weekly chalkboard particle physics lessons after that first summer. She also graciously took me on as a
 404 co-advisee after João moved on to his new position at IHEP. I am incredibly lucky to have had both of
 405 them as advisors.

406 Another mentor who was essential to my development as a graduate student is Paolo Giromini. His
 407 uncanny knowledge and intuition about detectors is unmatched and I am very grateful to have had the
 408 chance to work with him on the micromegas for the ATLAS New Small Wheel upgrade project. I owe
 409 essentially all my practical knowledge about detectors (and building things in general) to him. I also
 410 appreciated his unique sense of humor which made sometimes difficult tasks much easier to get through.

411 I am grateful to John Huth and Masahiro Morii for their helpful advice as the other professors in the
 412 Harvard ATLAS group as well. I especially thank John for helping me get started on the micromegas
 413 trigger project and being a great professor to TF particle physics for. Additionally I thank Howard

⁴¹⁴ Georgi for serving as my third committee member and offering me feedback throughout my graduate
⁴¹⁵ career.

⁴¹⁶ I also owe enormous thanks to Hugh Skottowe, the postdoc that I worked most closely with in my
⁴¹⁷ early years as a graduate student. He was always able to help me through complicated tasks in everything
⁴¹⁸ from writing code to understanding difficult physics concepts. I particularly enjoyed walking down to
⁴¹⁹ his office in Palfrey at random times and talking through whatever problem I was tackling on that day.

⁴²⁰ Alex Tuna, the second postdoc that I worked closely with at Harvard, deserves great thanks as well.
⁴²¹ He helped me push through to the end of my graduate career and offered great advice along the way.

⁴²² Being at Harvard, I have seen an incredible array of graduate students graduate before me: Ben Smith,
⁴²³ Verena Martinez Outschoorn, Srivas Prasad, Michael Kagan, Giovanni Zevi Della Porta, Laura Jeanty,
⁴²⁴ Kevin Mercurio, William Spearman, and Andy Yen. I want to thank them all for showing me what a
⁴²⁵ good physicist looks like and for patiently answering my questions and offering insightful advice about
⁴²⁶ physics and life.

⁴²⁷ Getting through graduate school would not have been possible without the support and friendship
⁴²⁸ of the other students in our group. Thanks to Emma Tolley for geeking out with me about cool com-
⁴²⁹ puting stuff, going to taste delicious beers with me, and helping start the Palfrey tradition of Taco Tues-
⁴³⁰ days. Thanks to Brian Clark for being a great friend and housing companion both in Kirkland House
⁴³¹ and in our tiny summer apartment in Geneva (and thanks to his partner Allison Goff for the same rea-
⁴³² sons!). Thanks to Siyuan Sun for giving me my first aikido lesson and always being there for great con-
⁴³³ versations, big and small. Tony (Baojia) Tong deserves special recognition for working with me on the
⁴³⁴ 4b analysis and putting up with my sometimes strange requests (and giving me rides to the Val Thoiry
⁴³⁵ Migros so I wouldn't have to pay exorbitant Geneva grocery prices!). Stephen Chan is probably the only
⁴³⁶ student in the group who both understands my references to the Sopranos and makes some of his own.
⁴³⁷ To the younger graduate students - Karri Di Petrillo, Jennifer Roloff, Julia Gonski, and Ann Wang - I
⁴³⁸ want to say thank you for making the group a fun and lively place to be and giving all of us energy that
⁴³⁹ the older graduate students like myself can sometimes lack.

⁴⁴⁰ I'd like to thank Annie Wei and Gray Putnam, the two undergraduates I have worked with as a gradu-

⁴⁴¹ ate student. Their unbelievable intuition and quickness in picking up difficult particle physics concepts
⁴⁴² is inspiring.

⁴⁴³ I would also like to thank all of the postdocs that I have interacted with in my time in the Harvard
⁴⁴⁴ group: Kevin Black, Alberto Belloni (who would always ask me “Do you have it?”...I can now say that
⁴⁴⁵ I do!), Shulamit Moed, Corrinne Mills, Geraldine Conti, David Lopez Mateos, Chris Rogan, Valerio
⁴⁴⁶ Ippolito, and Stefano Zambito.

⁴⁴⁷ There are many people on ATLAS who have helped me get to this point as well. In the *WW* group,
⁴⁴⁸ I have to thank Jonathan Long, Joana Machado Miguens, Ben Cerio, Philip Chang, Bonnie Chow,
⁴⁴⁹ Richard Polifka, Heberth Torres, Tae Min Hong, and Jennifer Hsu for being wonderful colleagues and
⁴⁵⁰ making the entire analysis run smoothly. In the *4b* group, I have to thank Qi Zeng, Tony Tong, Alex
⁴⁵¹ Tuna, Michael Kagan, Max Bellomo, John Alison, and Patrick Bryant.

⁴⁵² Kirkland House was my home for the last three years of graduate school and was an wonderful envi-
⁴⁵³ ronment and support system. I want to thank my fellow tutors, especially Brian Clark and Allison Goff
⁴⁵⁴ (again), Zach Abel, Kelly Bodwin, Alex Lupsasca, John and Pam Park, Luke and Erin Walczewski, and
⁴⁵⁵ Philip Gant for their friendship and support. I also want to thank Kate Drizos Cavell, Bob Butler, and
⁴⁵⁶ the Faculty Deans Tom and Verena Conley.

⁴⁵⁷ There are still a few friends that haven’t been covered yet and deserve great thanks. Jake Connors and
⁴⁵⁸ Meredith MacGregor have been absolutely wonderful friends and I thank them in particular for the
⁴⁵⁹ many home-cooked meals and great conversations we’ve had in their apartment. Nihar Shah has been
⁴⁶⁰ my friend and confidant since we were both wee freshmen in Harvard Yard. Gareth Kafka, though he
⁴⁶¹ sits on the “neutrino” side of Palfrey House, has made days there more fun and has also been an enthusi-
⁴⁶² astic participant in the Palfrey Taco Tuesdays.

⁴⁶³ Being at Harvard necessarily means having to navigate through bureaucracy at some point or another.
⁴⁶⁴ I thank Lisa Cacciabuado, Carol Davis, and Jacob Barandes for always having open doors and being the
⁴⁶⁵ most kind, helpful people in the Physics department.

⁴⁶⁶ I thank Venky Narayananamurti for putting on a great SPU course that I was proud to be a part of and
⁴⁶⁷ TF for. I’d also like to thank Jim Waldo for offering me much advice about working in Computer Science

⁴⁶⁸ and giving me a fun data project to be a part of in my free time.

⁴⁶⁹ I grew up in a very tight knit Serbian community on the south side of Chicago which helped make
⁴⁷⁰ me the person I am today. I would like to thank all of the people at St. Simeon Mirotochivi Serbian
⁴⁷¹ Orthodox Church who have always been sources of enthusiasm and support in my life.

⁴⁷² I would not be here without the unconditional love and constant support and encouragement of my
⁴⁷³ family. To my pokojni Dedas Branko and Miloje, my pokojni Baba Milka, and my Baba Desa, I want to
⁴⁷⁴ say thank you for instilling in me at an early age the love of curiosity and storytelling that I have carried
⁴⁷⁵ throughout my life. To my sister Angelina, I want to say thank you for always loving me and being my
⁴⁷⁶ partner in crime throughout our childhoods. To my parents, Miroljub and Nada, Tata and Mama, I
⁴⁷⁷ really cannot express how grateful I am to you and how much I owe you. As I look back now I see how
⁴⁷⁸ I am a combination of both of your best qualities and every day I am in situations where I understand
⁴⁷⁹ more and more the lessons you made sure to teach me and the sacrifices you made to make sure I got the
⁴⁸⁰ best possible education. I love you all.

⁴⁸¹ Finally, I have to thank my soul mate, the one person in my life who understands me more than any-
⁴⁸² one else, my fiancée Kelly Brock. You are my sounding board, my support system, my cheerleader (fig-
⁴⁸³ uratively and literally!), my best friend, my role model, and my everything. I would not have gotten
⁴⁸⁴ through graduate school without you and my life would not be the same without you. I cannot wait to
⁴⁸⁵ start our new lives together as the married doctors, tackling whatever comes our way with the same zeal
⁴⁸⁶ with which we tackled graduate school. I love you with all my heart and soul.

0

487

488

Introduction

489 The Higgs boson is often described as one of the cornerstones of the Standard Model. Since the con-
490 ception of the Higgs mechanism as the source of electroweak symmetry breaking in the early 1960s,
491 countless collider experiments have searched for this elusive particle. This dissertation presents the story
492 of the Higgs boson from its discovery to its use as a tool in the search for physics beyond the Standard
493 Model with the ATLAS detector at the Large Hadron Collider (LHC).

494 One of the first priorities of the early LHC was the search for the Higgs boson. This search was first
495 tackled in three main channels: $H \rightarrow \gamma\gamma$, $H \rightarrow ZZ^*$, and $H \rightarrow WW^*$. Each channel has its own
496 merits, but the WW^* is particularly suited to searching over a wide range of masses. The $H \rightarrow WW^*$
497 branching ratio is large and it is the primary decay channel above the $2m_W$ mass threshold.

498 While the rate of events produced in $H \rightarrow WW^*$ is large, the channel poses some challenges. First,
499 the most common mode of study for this channel is $H \rightarrow WW^* \rightarrow \ell\nu\ell\nu$. With neutrinos in the
500 final state, it is not possible to fully reconstruct the invariant mass of the parent Higgs like the $\gamma\gamma$ and

501 $ZZ \rightarrow 4\ell$ channels. Second, the final state topology is mimicked by a wide variety of backgrounds that
502 need to be properly estimated. This means tailored selection requirements for background reduction
503 and robust background estimation techniques must both be developed.

504 In 2012, the ATLAS and CMS experiments announced the discovery of a new particle consistent with
505 the Higgs boson [1, 2]. In ATLAS, this discovery was made with 4.8 fb^{-1} collected at $\sqrt{s} = 7 \text{ TeV}$ and
506 5.8 fb^{-1} at $\sqrt{s} = 8 \text{ TeV}$. The $H \rightarrow WW^* \rightarrow \ell\nu\ell\nu$ analysis played an important role in this discovery.
507 After the discovery, measurement of the properties of the newly discovered particle and confirmation
508 of its consistency with the Standard Model Higgs were the main priorities. The WW^* channel is also
509 uniquely suited to these types of measurements. Because of its good rate, it offers some of the best cross
510 section measurements available among the various Higgs decay modes. It is also suited for measurement
511 of multiple Higgs production modes, like the vector boson fusion (VBF) mode, where incoming quarks
512 radiate W/Z bosons which fuse to make a Higgs. In VBF production with the WW^* decay channel,
513 the coupling of the Higgs to the W boson is present in both the production and decay which allows for
514 more precise measurements of this coupling than other channels which rely on gluon fusion production
515 (where gluons couple to the Higgs through a top loop in the production). The measurement of VBF
516 carries the additional challenge that its cross section is an order of magnitude smaller than that of gluon
517 fusion, meaning that the large branching ratio to WW^* offers an additional advantage in isolating this
518 production mode. In the final ATLAS Run 1 results, combining 20.3 fb^{-1} taken at $\sqrt{s} = 8 \text{ TeV}$ with
519 the 4.8 fb^{-1} collected at $\sqrt{s} = 7 \text{ TeV}$, the WW^* channel achieved its first observation of VBF produc-
520 tion of the Higgs.

521 After Run 1 of the LHC, with the existence of the Higgs now firmly established, the focus shifted to
522 searches for physics beyond the Standard Model. In particular, searches for high mass resonances bene-
523 fit from the LHC's increase to $\sqrt{s} = 13 \text{ TeV}$ in Run 2. The cross section for a generic gluon-initiated
524 resonance with a mass of 2 TeV increases tenfold in Run 2, making searches for high mass resonances a
525 high priority. The newly discovered Higgs can be used as a tool in these searches. After the discovery,
526 the Higgs boson provides a large swath of unmeasured phase space where new physics could be discov-
527 ered. Higgs pair production in the Standard Model has a low cross section that requires large datasets

528 (on the order of the LHC’s lifetime) for full measurement. However, new physics can modify this cross
529 section, especially through new resonances which decay to two Higgs bosons. Such high mass resonances
530 also produce difficult to recognize final state topologies due to the merging of decay products from high
531 momentum Higgs bosons. A search for Higgs pair production in the $HH \rightarrow b\bar{b}b\bar{b}$ final state was per-
532 formed with 3.2 fb^{-1} collected with ATLAS at $\sqrt{s} = 13 \text{ TeV}$ in 2015. The results are presented in this
533 dissertation with a focus on a dedicated signal region for boosted final states. This signal region uses new
534 techniques for recognizing jet substructure and b -tagging to the improve signal acceptance of high mass
535 resonances.

536 This dissertation begins by discussing the discovery of the Higgs and the role of the $H \rightarrow WW^* \rightarrow$
537 $\ell\nu\ell\nu$ channel. It then discusses the first observation of the VBF production mode in $H \rightarrow WW^* \rightarrow$
538 $\ell\nu\ell\nu$ with the full ATLAS Run 1 dataset, as well as the final combined Run 1 measurements from this
539 channel. Finally, it presents a search for Higgs pair production in the $HH \rightarrow b\bar{b}b\bar{b}$ channel. It is orga-
540 nized into four parts.

541 Part 1 presents the theoretical and experimental background required for the subsequent parts. Chap-
542 ter 1 gives an overview of Higgs physics, particularly single and double Higgs production in the Standard
543 Model and beyond. Chapter 2 presents details regarding the Large Hadron Collider and the ATLAS
544 experiment. The evolution of machine conditions, descriptions of the ATLAS sub-detectors, and an
545 overview of object reconstruction in ATLAS are all shown. A brief interlude on the ATLAS Muon New
546 Small Wheel upgrade is also given, as this upgrade has been a focus of my graduate work and will have
547 important impact on ATLAS’ ability to study the Higgs at the High Luminosity LHC.

548 Part 2 discusses the observation and measurement of the Higgs in the $H \rightarrow WW^* \rightarrow \ell\nu\ell\nu$
549 channel in the ATLAS Run 1 dataset at $\sqrt{s} = 7$ and 8 TeV . Because I worked in this channel from
550 before the discovery through to the final analysis of the Run 1 dataset, Part 2 is organized in such a way
551 to allow easy presentation of multiple analyses on different subsets of the full Run 1 dataset. Chapter 3
552 presents a general overview of the $H \rightarrow WW^*$ analysis strategy and defines many of the variables and
553 common elements used in the rest of Part 2. Chapter 4 presents the discovery of the Higgs boson, fo-
554 cusing on the role of the WW^* channel in this discovery. Chapter 5 presents the first observation of the

555 VBF production mode of the Higgs in the WW^* channel, a study which was done on the full Run 1
556 ATLAS dataset. In this chapter, the focus is mainly on the selection cut-based VBF analysis. The cut-
557 based analysis was an important first step to the final VBF result which used a Boosted Decision Tree
558 (BDT). Where appropriate, connections between the cut-based and BDT analyses are shown and their
559 compatibility is discussed. Finally, the VBF analysis was an important input into the combined Run 1
560 $H \rightarrow WW^* \rightarrow \ell\nu\ell\nu$ result, which used both the gluon fusion and VBF channels in a combined
561 fit to infer properties of the Higgs, including its couplings to the gauge bosons and its production cross
562 section. This is the topic of Chapter 6.

563 Part 3 presents a search for Higgs pair production in the $HH \rightarrow b\bar{b}b\bar{b}$ channel. Chapter 7 presents
564 an overview of this search in the boosted regime, where the Higgs pairs are the result of the decay of a
565 heavy resonance. Chapter 8 shows the combined results between the boosted regime and the resolved
566 regime, which is sensitive to lower mass resonances and non-resonant Higgs pair production. Finally,
567 Part 4 presents a conclusion and brief outlook of future Higgs physics with ATLAS.

Part I

Theoretical and Experimental Background

In modern physics, there is no such thing as “nothing.”

Richard Morris

1

570

571

The Physics of the Higgs Boson

572 This chapter presents an overview of the Standard Model of Particle Physics and in particular the
573 physics of the Higgs boson. First, a brief overview of the Standard Model and its history are presented.
574 Then, a description of the Higgs mechanism of electroweak symmetry breaking is given. Next, the
575 physics of single Higgs boson production and decay is described. The Standard Model also allows for
576 production of two Higgs bosons and this is detailed as well. Finally, di-Higgs production in two beyond
577 the Standard Model (BSM) theories - Randall-Sundrum gravitons (RSG) and Two Higgs Doublet Mod-
578 els (2HDM) - is shown.

579 **I.I THE STANDARD MODEL OF PARTICLE PHYSICS**

580 The Standard Model (SM) of Particle Physics is a quantum field theory describing the fundamental
581 particles of nature and the forces that govern their interactions. Several comprehensive treatments of
582 the SM already exist in the literature [3–8] and this section will not rehash those. Rather, this section

583 presents a brief overview of the SM particles and forces in order to define them for subsequent discussions.
 584

585 The Standard Model consists of two primary categories of fundamental particles: fermions (spin 1/2
 586 particles) and bosons (integer spin particles). The SM also describes three forces: electromagnetism, the
 587 weak nuclear force, and the strong nuclear force. Gravity is not included in the theory and is largely irrele-
 588 vant at the scales currently probed by collider experiments. Within the fermions, there are both quarks
 589 (which interact via all three forces) and the leptons. The charged leptons interact via electromagnetic and
 590 weak interactions, while neutrinos (neutral leptons) interact only via the weak force. Within the bosons,
 591 there are the W^\pm and Z bosons (the mediators of the weak force), the gluon (g , the mediator of the
 592 strong force), and the photon (γ), the mediator of the electromagnetic force. Finally, there is the Higgs
 593 boson, a fundamental spin-0 particle resulting from the Higgs mechanism of electroweak symmetry
 594 breaking. Figure 1.1 summarizes the fermions and bosons of the SM.

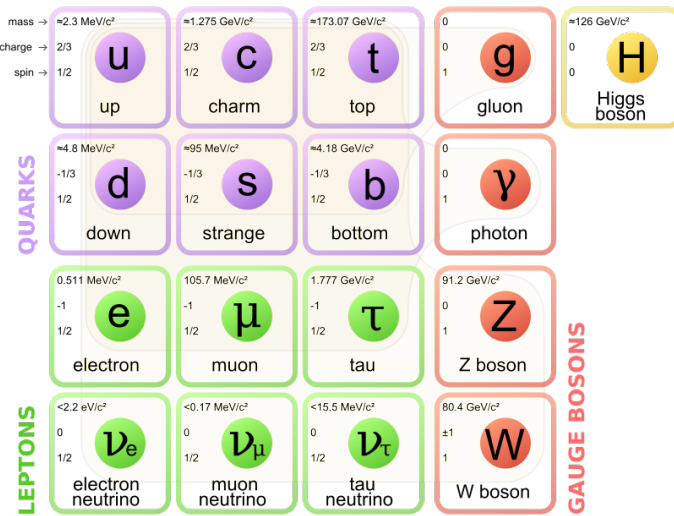


Figure 1.1: The particles of the Standard Model and their properties [6].

595 The Standard Model coalesced into a unified theoretical framework in the 1960s through the work
 596 of Glashow, Weinberg, Salam, and others on the theory of electroweak interactions [9–12]. This theory
 597 characterized both the electromagnetic and weak interactions as unified under a single gauge symmetry
 598 group, namely $SU(2) \times U(1)$. At low enough energy scales (on the order of the W and Z masses,
 599 the electroweak symmetry is broken, as evidenced by the fact that the weak bosons have mass while the

600 photon does not. The discovery of the Higgs boson in 2012 confirmed the Higgs mechanism as the most
 601 likely candidate for this electroweak symmetry breaking [1, 2]. The electroweak theory is then combined
 602 with the theory of quantum chromodynamics (which models the strong sector as a non-Abelian $SU(3)$
 603 gauge group) to form the complete SM [13].

604 1.2 ELECTROWEAK SYMMETRY BREAKING AND THE HIGGS

605 In the Standard Model Lagrangian, it is difficult to include mass terms for the W and Z bosons without
 606 breaking the fundamental gauge symmetry of the Lagrangian. A traditional mass term does not
 607 preserve the $SU(2) \times U(1)$ symmetry. Additionally, scattering of massive W and Z bosons violate
 608 unitarity and these diagrams diverge at high energy scales. In the 1960s, Higgs, Brout, Englert, Guralnik,
 609 Kibble, and Hagen developed a mechanism for spontaneous symmetry breaking via the addition of a
 610 complex scalar doublet to the SM. Three of the four real degrees of freedom of this complex field would
 611 go to the longitudinal modes of the W^\pm and Z , thus allowing them to have mass [14–17]. The remain-
 612 ing degree of freedom would manifest as an additional scalar, known now as the Higgs boson.

613 The mechanism works by introducing a Lagrangian for the newly introduced field that still respects
 614 the symmetry of the Standard Model inherently, but with a minimum at a non-zero vacuum expectation
 615 value for the field. In this minimum of the potential, the electroweak symmetry is broken. Specifically,
 616 consider a complex scalar doublet Φ with four degrees of freedom, as shown in equation 1.1.

$$\Phi = \begin{pmatrix} \phi^+ \\ \phi^0 \end{pmatrix} = \frac{1}{\sqrt{2}} \begin{pmatrix} \phi_1^+ + i\phi_2^+ \\ \phi_1^0 + i\phi_2^0 \end{pmatrix} \quad (1.1)$$

617 The minimal potential of a self-interacting Higgs that still respects the SM symmetry is given in equa-
 618 tion 1.2.

$$V(\Phi) = \mu^2 \Phi^\dagger \Phi + \lambda (\Phi^\dagger \Phi)^2 \quad (1.2)$$

619 If the μ^2 term of this potential is positive, then the potential has a minimum at $\Phi = 0$ and the SM

620 symmetry is preserved. However, if instead $\mu^2 < 0$, then the minimum is at a finite value of Φ , namely

$$\Phi_{\min} = \frac{1}{\sqrt{2}} \begin{pmatrix} 0 \\ v \end{pmatrix} \quad (1.3)$$

621 where $v = \sqrt{\mu^2/\lambda}$. Because this is the location of the minimum, it corresponds to the vacuum expecta-
622 tion value for the field ($\langle \Phi \rangle = \Phi_{\min}$). The excitations of the Higgs can then be parameterized as

$$\Phi = \frac{1}{\sqrt{2}} \begin{pmatrix} 0 \\ v + H \end{pmatrix} \quad (1.4)$$

623 The full scalar Lagrangian, including the kinetic term, is then given as

$$\mathcal{L}_s = (D^\mu \Phi)^\dagger (D_\mu \Phi) - V(\Phi) \quad (1.5)$$

624 where the covariant derivative is defined as

$$D_\mu = \partial_\mu + \frac{ig}{2} \tau^a W_\mu^a + ig' Y B_\mu \quad (1.6)$$

625 and W^1, W^2, W^3 and B are the $SU(2)$ and $U(1)$ gauge fields of the electroweak theory, respectively. g
626 and g' are the corresponding coupling constants. With the scalar Lagrangian in place, the physical gauge
627 fields can then be written as

$$W_\mu^\pm = \frac{1}{\sqrt{2}} (W_\mu^1 \mp i W_\mu^2) \quad (1.7)$$

628

$$Z_\mu = \frac{-g' B_\mu + g W_\mu^3}{\sqrt{g^2 + g'^2}} \quad (1.8)$$

629

$$A_\mu = \frac{g B_\mu + g' W_\mu^3}{\sqrt{g^2 + g'^2}} \quad (1.9)$$

630 Equation 1.7 corresponds to the charged W^+ and W^- bosons, equation 1.8 corresponds to the neutral

631 Z boson, and equation 1.9 corresponds to the neutral photon. The masses of the particles also arise from
 632 the Lagrangian. The photon has zero mass, while the masses of the W and Z bosons are given in equa-
 633 tion 1.10.

$$\begin{aligned} M_W^2 &= \frac{1}{4}g^2v^2 \\ M_Z^2 &= \frac{1}{4}(g^2 + g'^2)v^2 \end{aligned} \tag{1.10}$$

634 The fermion masses also arise through a coupling with the Higgs via the Yukawa interaction (for a de-
 635 tailed description, see [8]). In this case the coupling between the Higgs and the fermions goes as

$$g_{Hf\bar{f}} = \frac{m_f}{v} \tag{1.11}$$

636 The full Lagrangian of Higgs interactions can be written as

$$\mathcal{L}_{\text{Higgs}} = -g_{Hf\bar{f}}\bar{f}fH + \frac{g_{HHH}}{6}H^3 + \frac{g_{HHHH}}{24}H^4 + \delta_V V_\mu V^\mu \left(g_{HV}VH + \frac{g_{HVV}}{2}H^2 \right) \tag{1.12}$$

637 with

$$\begin{aligned} g_{HV} &= \frac{2m_V^2}{v} & g_{HVV} &= \frac{2m_V^2}{v^2} \\ g_{HHH} &= \frac{3m_H^2}{v} & g_{HHHH} &= \frac{3m_H^2}{v^2} \end{aligned} \tag{1.13}$$

638 Here, V refers to the W^\pm and Z , and $\delta_W = 1$ while $\delta_Z = 1/2$. Phenomenologically, there are a few
 639 features of this Lagrangian that are useful to note. First, note that the Higgs mass is a free parameter
 640 of the theory that must be determined experimentally. Second, note that the coupling of the Higgs to
 641 the vector bosons and fermions scales with the masses of these particles, a fact that is important when
 642 considering both the production and decays of the particle. Also note that the branching ratio of the
 643 Higgs to W bosons will be twice that of the branching ratio to Z if the Higgs mass is large enough to
 644 produce the particles on shell because of the extra symmetry factor associated with the W coupling.
 645 Finally, note the presence of the cubic and quartic Higgs self interaction terms, which can lead to final
 646 states with multiple Higgs bosons produced.

647 1.3 HIGGS BOSON PRODUCTION AND DECAY

648 This section discusses the properties of Higgs production and decay mechanisms. The details pre-
649 sented here will focus on the properties of a 125 GeV Higgs boson, as this is the mass closest to that of
650 the newly discovered Higgs.

651 1.3.1 HIGGS PRODUCTION

652 The Higgs is produced by four main production modes at the Large Hadron Collider - gluon-gluon
653 fusion (ggF), vector boson fusion (VBF), associated production with a W or Z boson, or associated
654 production with top quarks ($t\bar{t}H$). Figure 1.2 shows the Feynman diagrams for these four modes.

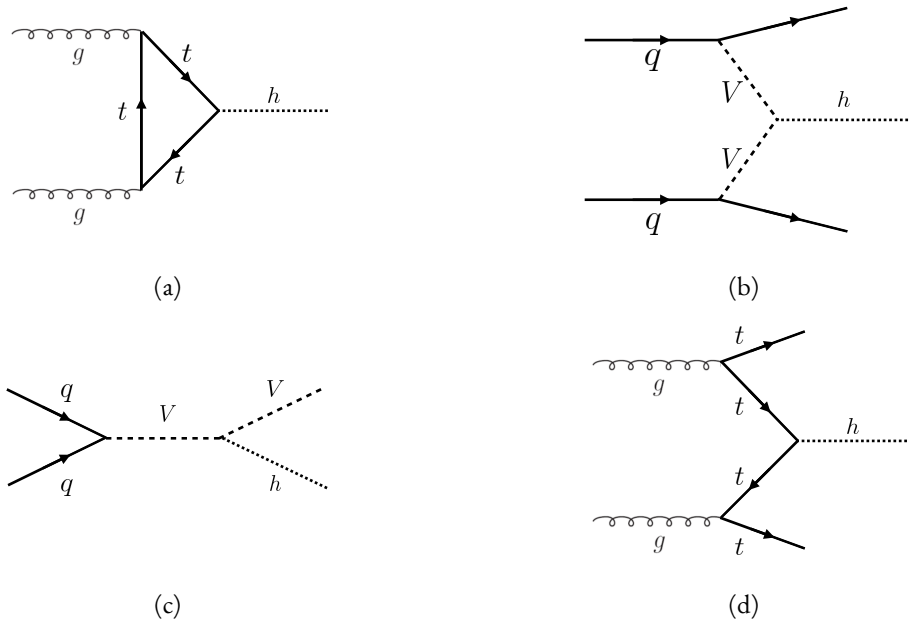


Figure 1.2: The four most common Higgs boson production modes at the LHC: (a) gluon-gluon fusion, (b) vector boson fusion, (c) $W/Z + H$ production, (d) $t\bar{t}H$ production

655 In gluon-gluon fusion, gluons from the incoming protons fuse via a top-quark loop to produce a
656 Higgs. The top quark is the dominant contribution in the loop due to its heavy mass and the fact that
657 the Higgs-fermion coupling constant scales with fermion mass. In vector boson fusion, the incoming
658 quarks each radiate a W or Z boson which fuse to produce the Higgs. This production mode results in
659 a final state with a Higgs boson and two additional jets which tend to be forward because they carry the

660 longitudinal momentum of the incoming partons. The Higgs can also be produced in association with a
 661 W or Z boson. The W/Z is produced normally and then radiates a Higgs (this mode is also sometimes
 662 known as “Higgs-strahlung”). Finally, the Higgs can be produced in association with two top quarks.
 663 Each incoming gluon splits into a $t\bar{t}$ pair, and one of the top pairs combines to create a Higgs. Figure 1.3
 664 shows the production cross section for a 125 GeV Higgs boson in each of these modes at a pp collider as
 665 a function of center of mass energy.

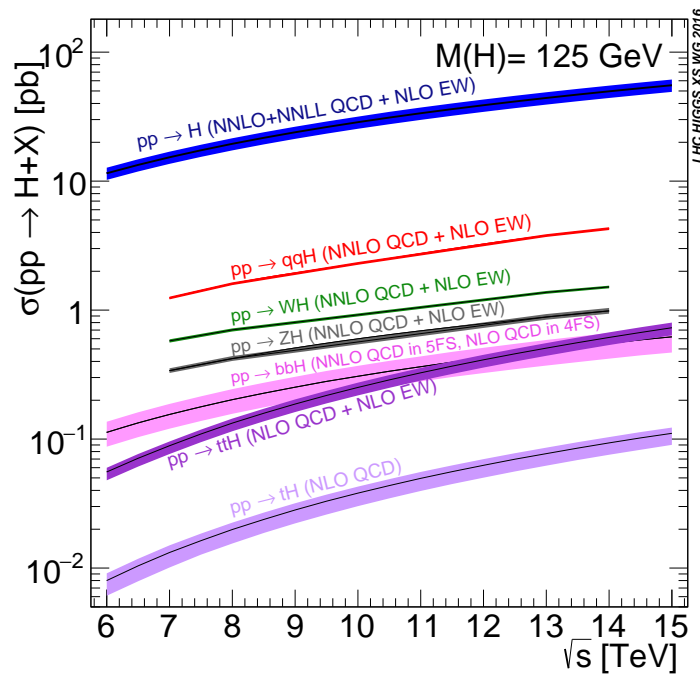


Figure 1.3: Higgs production cross sections as a function of center of mass energy (\sqrt{s}) at a pp collider [18].

666 In figure 1.3, note that gluon fusion has the largest cross section, while VBF is the second largest at
 667 approximately a factor of 10 smaller. The figure also includes the less commonly studied $b\bar{b}H$ and tH
 668 modes. The $b\bar{b}H$ and tH modes are not studied as commonly as $t\bar{t}H$ due to the larger background con-
 669 tributions and lower cross sections, respectively. At $\sqrt{s} = 8$ TeV, ggF production of a 125 GeV Higgs
 670 has a cross section of 19.47 pb, while VBF has a cross section of 1.601 pb [18]. The cross sections of all
 671 of the main Higgs production modes at this center of mass energy, as well as their uncertainties from
 672 varying the renormalization and factorization scales and PDFs, are summarized in table 1.1 for a 125 GeV
 673 Higgs.

Production mode	σ (pb)	QCD scale uncert. (%)	PDF + α_s uncert. (%)
Gluon fusion	19.47	+7.3 / - 8.0	3.1
Vector boson fusion	1.601	+0.3 / - 0.2	2.2
WH	0.7026	+0.6 / - 0.9	2.0
ZH	0.4208	+2.9 / - 2.4	1.7
$t\bar{t}H$	0.1330	+4.1 / - 9.2	4.3
bbH	0.2021	+20.7 / - 22.3	
$t\bar{H}$ (t -channel)	0.01869	+7.3 / - 16.5	4.6
$t\bar{H}$ (s -channel)	1.214×10^{-3}	+2.8 / - 2.4	2.8

Table 1.1: Production cross sections for a 125 GeV Higgs boson at $\sqrt{s} = 8$ TeV with scale and PDF uncertainties [18].

674 1.3.2 HIGGS BRANCHING RATIOS

675 The fact that the Higgs couples more strongly to more massive particles is crucial for understanding
 676 its branching ratios. The width for Higgs decays to fermions is given in equation 1.14 [5].

$$\Gamma(H \rightarrow f\bar{f}) = \frac{N_c \sqrt{2} G_F m_f^2 m_H}{8\pi} \quad (1.14)$$

677 In this case, N_c is the number of colors, G_F is the Fermi constant, m_f is the mass of the fermion, and
 678 m_H is the mass of the Higgs. Note that the width scales with the square of the fermion mass. (This also
 679 assumes that the Higgs mass is large enough to decay with both the fermions on shell.)

680 The decay width to WW is given in equation 1.15 [5].

$$\Gamma(H \rightarrow W^+W^-) = \frac{\sqrt{2} G_F M_W^2 m_H}{16\pi} \frac{\sqrt{1-x_W}}{x_W} (3x_W^2 - 4x_W + 4) \quad (1.15)$$

681 where m_W is the mass of the W and $x_W = 4M_W^2/m_H^2$. To get the branching ratio to ZZ , the equa-
 682 tion is divided by 2 to account for identical particles in the final state, and x_W is replaced with $x_Z =$
 683 $4M_Z^2/m_H^2$. This is shown in equation 1.16 [5].

$$\Gamma(H \rightarrow ZZ) = \frac{\sqrt{2} G_F M_Z^2 m_H}{32\pi} \frac{\sqrt{1-x_Z}}{x_Z} (3x_Z^2 - 4x_Z + 4) \quad (1.16)$$

684 These formulas can also be visualized as a function of Higgs mass. Figure 1.4 shows the branching ratios
as a function of the Higgs mass. There are a few interesting features to note in this figure. First, note that

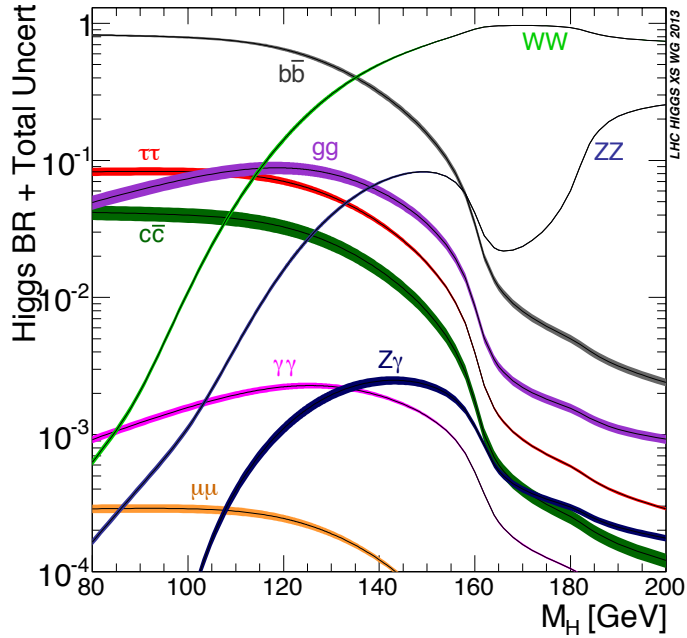


Figure 1.4: Higgs boson branching ratios as a function of m_H [18].

685
686 at high Higgs masses, once on-shell production of both W and Z bosons is possible, these two decays
687 are the dominant ones due to the large masses of the W/Z . Also note that the branching ratio to W s
688 is twice that of Z s at these large masses due to the δ_V symmetry factor noted previously. At 125 GeV,
689 the Higgs is accessible through many different decay modes. The largest branching ratio is the decay
690 $H \rightarrow b\bar{b}$ at 58.24% [18]. This branching is larger than the WW/ZZ decays because one of the two
691 bosons must be produced off-shell for $m_H = 125$ GeV. The second largest branching ratio is to WW^*
692 at 21.37 % (before taking into account the branching ratios of the W). Table 1.2 summarizes the branch-
693 ing ratios for a 125 GeV Higgs. Note that there is in fact a Higgs branching ratio to $\gamma\gamma$ even though
694 photons are massless. This decay happens through a loop (the largest contributions to the loop are top
695 and W) which suppresses the branching ratio.

696 Note that the branching ratios alone do not tell the full story of which Higgs channels are the most
697 sensitive. For example, a $H \rightarrow b\bar{b}$ search in gluon fusion production is incredibly difficult due to the

Decay	Branching ratio (%)
$b\bar{b}$	58.24
WW^*	21.37
gg	8.187
$\tau\tau$	6.272
$c\bar{c}$	2.891
ZZ^*	2.619
$\gamma\gamma$	0.2270
$Z\gamma$	0.1533
$\mu\mu$	0.02176

Table 1.2: Branching ratios for a 125 GeV Higgs boson [18].

698 large QCD dijet background at the LHC. However, in associated production of the Higgs, where a W
 699 or Z gives additional final state particles that can be used to reduce background, a search for $H \rightarrow b\bar{b}$
 700 can be sensitive. The combinations of production and decay modes that are most commonly studied are
 701 summarized in table 1.3 [5].

Decay	Inclusive (incl. ggF)	VBF	WH/ZH	$t\bar{t}H$
$H \rightarrow \gamma\gamma$	✓	✓	✓	✓
$H \rightarrow b\bar{b}$			✓	✓
$H \rightarrow \tau^+\tau^-$		✓		
$H \rightarrow WW^* \rightarrow \ell\nu\ell\nu$	✓	✓	✓	
$H \rightarrow ZZ \rightarrow 4\ell$	✓			
$H \rightarrow Z\gamma \rightarrow \ell\ell\gamma$	very low			

Table 1.3: Possible channels for Higgs searches. Checkmarks denote the most sensitive production modes [5].

702 1.4 HIGGS PAIR PRODUCTION IN THE STANDARD MODEL

703 The Standard Model also allows for processes that produce two Higgs bosons in the final state, known
 704 as Higgs pair production or di-Higgs production. The two main production mechanisms are shown
 705 in figure 1.5. The two diagrams in figure 1.5 interfere destructively with one another, resulting in a low
 706 overall cross section for di-Higgs production at the LHC. Nevertheless, Higgs pair production is quite
 707 interesting to study because it gives direct access to the λ parameter of the Higgs potential, also known as
 708 the Higgs self coupling. The diagram in figure 1.5(b) is sensitive to this coupling through the triple Higgs

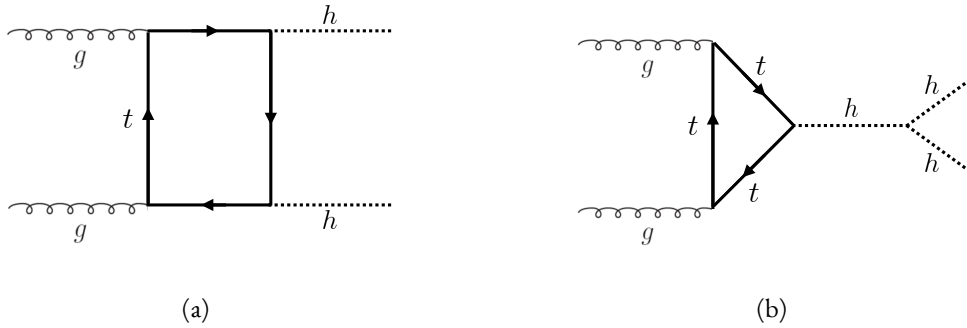


Figure 1.5: The two leading diagrams for Standard Model di-Higgs production at the LHC: (a) box diagram, (b) Higgs self coupling

709 vertex.

710 One can substitute the gluon fusion production of diagram 1.5(b) with any of the other production
 711 modes previously discussed. These other modes do not suffer from interference with the box diagram
 712 in figure 1.5(a) due to the presence of additional particles in the final state. They still have a lower cross
 713 section than the gluon fusion mode, however. The cross sections for di-Higgs production in the differ-
 714 ent modes, as well as their uncertainties, are shown in table 1.4 [19]. These are shown for $\sqrt{s} = 14$ TeV
 715 as the higher center of mass energy is more sensitive to this process. Note that the scale of cross section
 quoted is now in fb rather than pb.

Production mode	σ (fb)	Total uncert. (%)
Gluon fusion	33.89	+37.2 / - 27.8
Vector boson fusion	2.01	+7.6 / - 5.1
$W H H$	0.57	+3.7 / - 3.3
$Z H H$	0.42	+7.0 / - 5.5
$t \bar{t} H$	1.02	-

Table 1.4: Production cross sections for pair production of a 125 GeV Higgs boson at $\sqrt{s} = 14$ TeV with total uncertainty [19]. The uncertainties include QCD scale and PDF variations as well as uncertainties on α_S .

716

717 1.5 HIGGS PAIR PRODUCTION IN THEORIES BEYOND THE STANDARD MODEL

718 The Standard Model Higgs pair production cross section is rather small, and datasets on the scale
 719 of the full lifetime of the LHC will be required to obtain sensitive measurements of the Higgs self-

coupling. However, the discovery of the Higgs also gives particle physicists a new tool that can be exploited in the search for new physics beyond the Standard Model. In particular, Higgs pair production is a promising channel in the search for new physics. The cross section for di-Higgs production can be altered through both resonant and non-resonant production of Higgs pairs. In non-resonant production, di-Higgs production vertices can arise from the presence of a new strong sector and additional colored particles [20–22]. Figure 1.6 shows examples of the types of vertices that can arise. In the resonant case, new heavy particle can decay to Higgs pairs. Such new particles can include heavy Higgs bosons arising in two Higgs doublet models (2HDM) or Higgs portal models as well as heavy gravitons in Randall-Sundrum theories [20, 23–29]. Figure 1.7 shows a generic diagram for a heavy resonance decaying to two Higgs bosons. In the 2HDM, X corresponds to the heavy CP-even scalar H . In the Randall-Sundrum model, X corresponds to a heavy spin-2 graviton G . The next sections provide more detail on the phe-

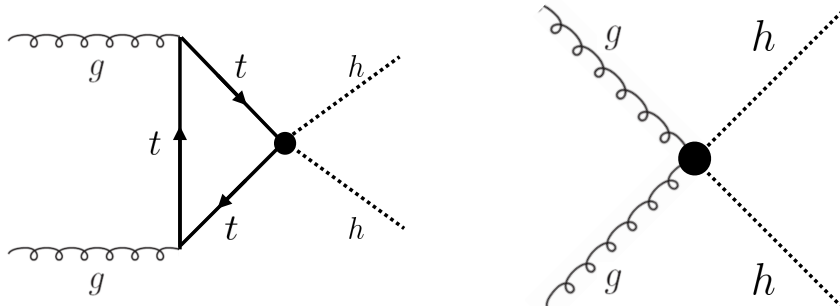


Figure 1.6: Diagrams with new vertices for non-resonant Higgs pair production arising in composite Higgs models

nomenclature of resonant Higgs production in Randall-Sundrum and 2HDM models, as these models will later be tested in a dedicated search for resonant production of boosted Higgs pairs.

1.5.1 RANDALL-SUNDRUM GRAVITONS

The Randall-Sundrum model is a proposed solution to the hierarchy problem that posits a five-dimensional warped spacetime that contains two branes: one where the force of gravity is very strong and a second brane at the TeV scale corresponding to the known Standard Model sector [23]. In the theory, the branes are weakly coupled and the graviton probability function drops exponentially going from the gravity brane to the SM brane, rendering gravity weak on the SM brane. The experimental

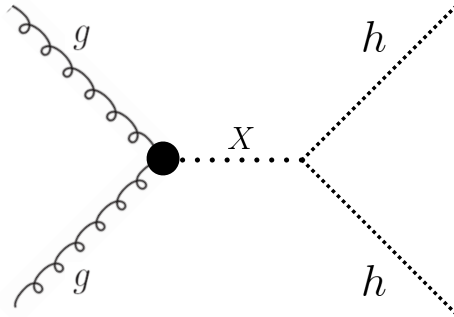


Figure 1.7: Generic Feynman diagram for resonant Higgs pair production in BSM theories

consequence of this theory is a tower of widely spaced (in mass) Kaluza-Klein graviton resonances. In theories where the fermions are localized to the SM brane, production of gravitons from fermion pairs is suppressed and the primary mode of production is gluon fusion [24]. These gravitons have a substantial branching fraction to Higgs pairs, ranging from 6.43% for gravitons with a mass of 500 GeV to 7.66% at 3 TeV. Figure 1.8 shows the branching ratios of the spin-2 Randall Sundrum graviton (RSG) as a function of its mass. The predominant decays are to $t\bar{t}$ above the mass threshold for that channel.

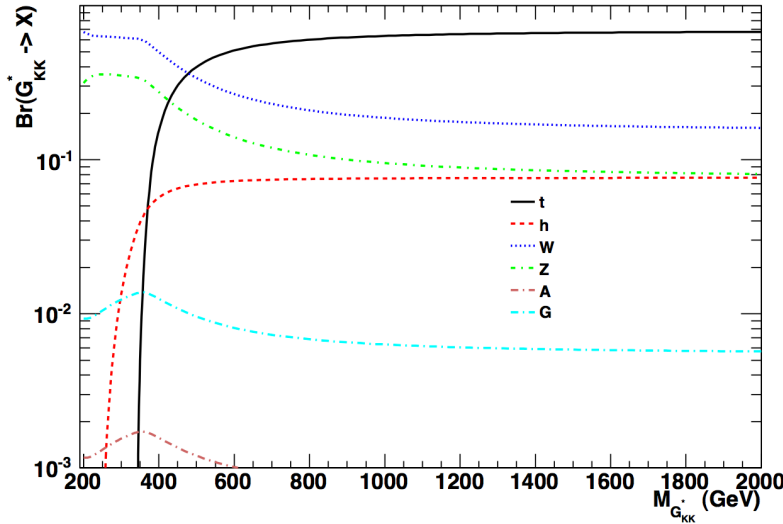


Figure 1.8: Branching ratios for a spin-2 Randall-Sundrum graviton as a function of mass computed in MadGraph with the CP3-Origins implementation [24, 30]

These models have two free parameters - the mass of the graviton and a curvature parameter k . Typically, rather than k , the theory is parameterized using $c \equiv k/\bar{M}_{\text{pl}}$, where \bar{M}_{pl} is the reduced Planck

mass. The cross section for production of the RSG decreases as a function of mass and is strongly dependent on the gluon PDF. The increase in center of mass energy from 8 to 13 TeV in LHC Run 2 greatly increases the cross section at higher mass. Figure 1.9 shows the cross section as a function of graviton mass at $\sqrt{s} = 13$ TeV for RSG models with $c = 1.0$ and $c = 2.0$.

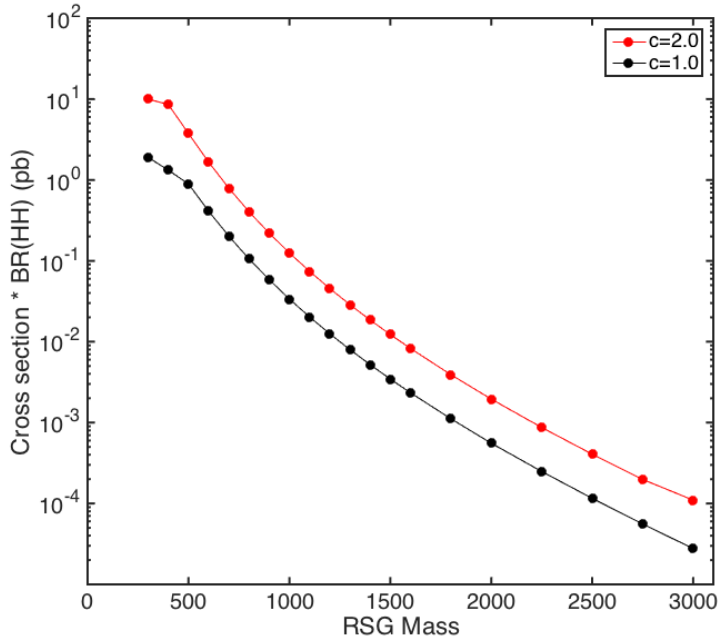


Figure 1.9: $\sigma \times \text{BR}(HH)$ for RSG as a function of mass computed in MadGraph with the CP3-Origins implementation [24, 30]

Another interesting feature of the theory is that the width of the graviton increases with both c and m_G . Figure 1.10 shows the graviton width for both $c = 1.0$ and $c = 2.0$ as a function of mass. In $c = 1.0$, the width starts at 8.365 GeV for a mass of 300 GeV and increases to 187.2 GeV at a mass of 3 TeV. Similarly, with $c = 2.0$, the width starts at 33.46 GeV for $m_G = 300$ GeV and increases to 748.8 GeV at a mass of 3 TeV.

1.5.2 TWO HIGGS DOUBLET MODELS

In Two Higgs Doublet Models (2HDM), a second complex scalar doublet is added to SM [26–28]. In this case, all four degrees of freedom in the second doublet correspond to new particles, meaning that

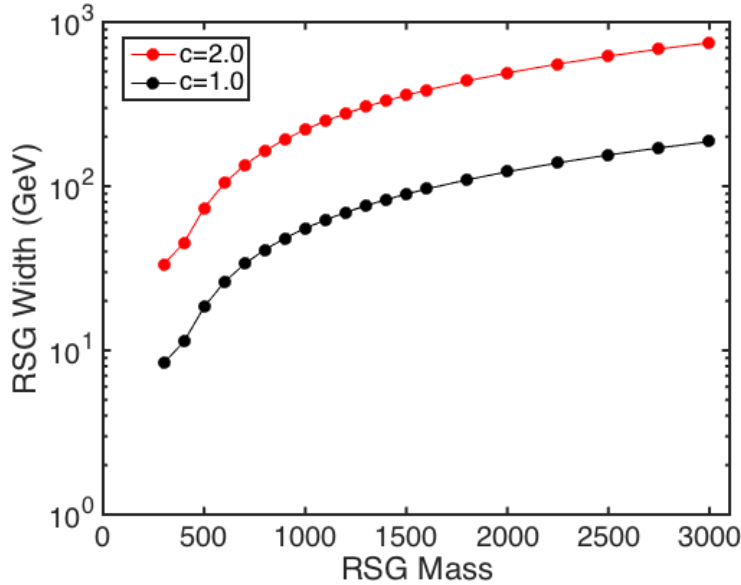


Figure 1.10: RSG width as a function of mass computed in MadGraph with the CP3-Origins implementation [24, 30]

759 there are five total scalars from the two Higgs doublets - h (light CP-even Higgs), H (heavy CP-even
 760 Higgs), A (heavy CP-odd Higgs), and H^\pm (charged Higgs). The model is parameterized by two main
 761 parameters. The first, $\tan \beta \equiv \frac{v_2}{v_1}$, is the ratio of the vacuum expectation values of the two Higgs dou-
 762 blets (where v_1 corresponds to the v in the SM Higgs model described above). The second parameter
 763 is α , a mixing angle between the heavy and light Higgs fields. Models are also often parameterized with
 764 $\cos(\beta - \alpha)$ rather than α directly. The limit where $\cos(\beta - \alpha) = 0$ is called the alignment limit, and it
 765 is in this limit that the light Higgs h has the same couplings as a Standard Model Higgs.

766 2HDM models are usually separated into two main types - Type I and Type II. In Type I models, the
 767 charged fermions only couple to the second Higgs doublet, leading to a fermiophobic light Higgs. In
 768 Type II models, up-type quarks couple to the first doublet while down-type quarks couple to the second
 769 doublet. One specific realization of a Type II 2HDM is the Minimal Supersymmetric Standard Model
 770 (MSSM).

771 Resonant di-Higgs production in this model can proceed through decays of the heavy CP-even Higgs
 772 $H \rightarrow hh$. The branching ratio for $H \rightarrow hh$ depends on the model type as well as the values of $\tan \beta$
 773 and $\cos \beta - \alpha$. Figure 1.11 shows the branching ratios as a function of the mass of the heavy scalar H for

774 both Type I and Type II models. Depending on the type of model hh can be a substantial fraction of the
 775 decays of H .

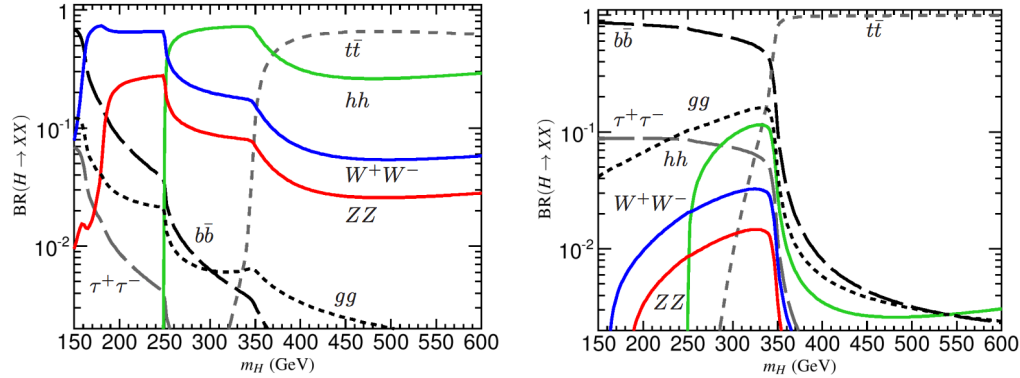


Figure 1.II: Branching ratios for heavy Higgs H in Type I (left) and Type II (right) 2HDM models with $\tan \beta = 1.5$ and $\cos(\beta - \alpha) = 0.1(0.01)$ for Type I (Type II). [28]

776 1.6 CONCLUSION

777 Studying the Higgs sector is essential for understanding the details of how mass arises in the Standard
 778 Model and how the electroweak symmetry is broken. The discovery of the Higgs boson also opens the
 779 door for its use as a tool to search for new physics, and Higgs pair production is an ideal candidate for
 780 this study. Even if no BSM physics is found in Higgs pair production, searches for Higgs pairs will put
 781 constraints on the Higgs self coupling and thus further knowledge of the Standard Model and the details
 782 of the Higgs potential.

The enthusiasm and motivation to explore particle physics at the high-energy frontier knows no borders between the nations and regions of the planet.

Peter Jenni

2

783

784

785

The ATLAS detector and the Large Hadron Collider

786 This chapter presents an overview of the experimental systems used to conduct the measurements
787 presented in this thesis. First, a brief overview of the accelerator, the Large Hadron Collider, will be
788 given. In this section, the accelerator conditions relevant to data-taking are presented as well. Next, an
789 overview of the ATLAS experiment is given. The basics of each sub-detector's role are summarized,
790 as well as the details of the datasets accumulated. Then, a brief interlude on the ATLAS Muon New
791 Small Wheel upgrade is presented. While this new detector does not have a direct impact on any of the
792 datasets taken so far, it will have an impact on future analyses and the work done on it is briefly summa-
793 rized here. Finally, an overview of object reconstruction in ATLAS is given. While the details of all of
794 the algorithms will not be presented in detail, aspects of the reconstruction performance such as object
795 resolutions are shown as these are relevant to the two studies presented later in this thesis.

796 2.1 THE LARGE HADRON COLLIDER

797 The Large Hadron Collider (LHC) is a proton-proton collider at the CERN laboratory in Geneva,
798 Switzerland [31]. It is designed for a maximum collision center of mass energy of $\sqrt{s} = 14$ TeV and
799 has a circumference of 26.7 kilometers. Four main experiments are located at the interaction points (IP)
800 of the accelerator: ATLAS (A Toroidal LHC ApparatuS), CMS (the Compact Muon Solenoid), AL-
801 ICE (A Large Ion Collider Experiment), and LHCb [32–35]. The studies performed in this thesis were
802 all completed with the ATLAS detector. Figure 2.1 shows a schematic of the LHC ring and the various
803 experiments.

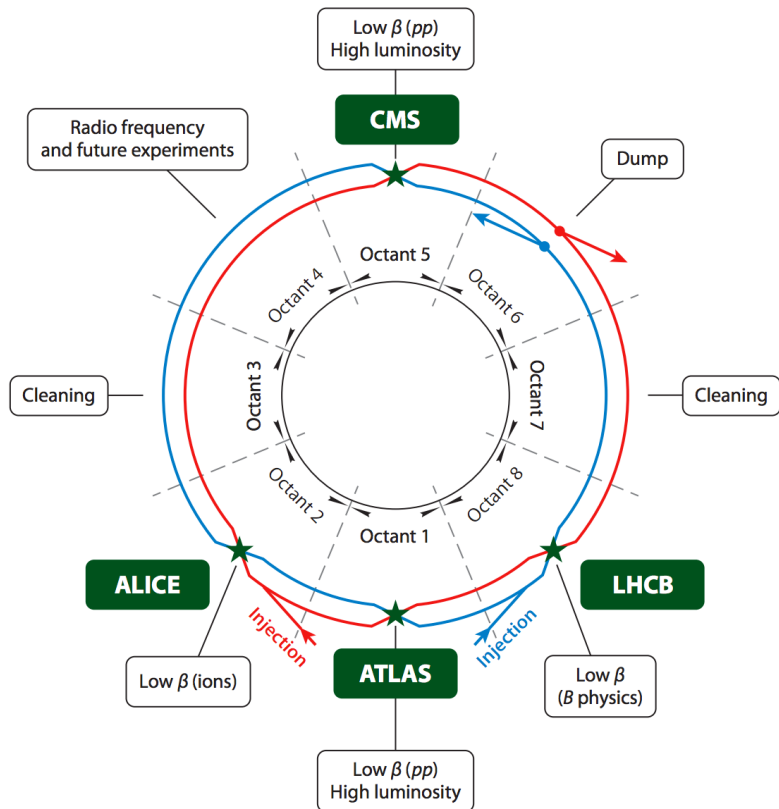


Figure 2.1: A schematic view of the LHC ring [36]

804 One of the most interesting features of the LHC is in its magnet design. Because the tunnel does not
805 have room for separate superconducting magnets for each of the beam pipes, the LHC employs a twin-
806 bore magnet design. Each magnet must hold an 8.3 Tesla magnetic field in order to bend the proton

807 beams at $\sqrt{s} = 14$ TeV. The superconducting magnets are cooled to a temperature of 1.9 Kelvin with
 808 superfluid helium.

809 **2.1.1 INSTANTANEOUS LUMINOSITY**

810 The rate of physics events expected from the accelerator is dependent on the instantaneous luminos-
 811 ity of the machine and the cross section of the physics process, $R_{\text{events}} = L\sigma$. Here, R_{events} is the
 812 number of events per second, L is the instantaneous luminosity of the machine, and σ is the cross sec-
 813 tion for the physics process being measured. The instantaneous luminosity of the LHC is determined
 814 by numerous factors related to machine conditions. Equation 2.1 gives the equation for instantaneous
 815 luminosity of Gaussian beam profile [36].

$$L = \frac{N_b^2 n_b f_{\text{rev}} \gamma_r}{4\pi \epsilon_n \beta^*} F \quad (2.1)$$

816 The LHC collides protons in bunches, and in the above equation N_b is the number of protons per
 817 bunch while n_b is the number of bunches per beam. Nominally, the LHC can hold up to 2808 pro-
 818 ton bunches. f_{rev} is the revolution frequency. ϵ_n is the normalized transverse beam emittance, a mea-
 819 surement of the average spread of the particles position-momentum space which has the dimension of
 820 length. β^* is the value of the *beta* function for the beam at the interaction point. It relates the emittance
 821 to the Gaussian width of the beam with $\sigma_{\text{beam}} = \sqrt{\epsilon \cdot \beta}$. F is a reduction factor that corrects for the
 822 fact that the beams are colliding at an angle at the IP.

823 Another way of writing the instantaneous luminosity is shown in equation 2.2. In this case, the in-
 824 stantaneous luminosity is written as the ratio of the rate of inelastic collisions with the inelastic cross
 825 section [37].

$$L = \frac{R_{\text{inel}}}{\sigma_{\text{inel}}} = \frac{\mu n_b f_{\text{rev}}}{\sigma_{\text{inel}}} \quad (2.2)$$

826 In this case, μ is the average number of interactions per bunch crossing in the accelerator. μ is a useful
 827 parameter for characterizing the amount of activity recorded in an experiment. As the instantaneous
 828 luminosity and thus μ increase, there are more interactions per bunch crossing and more activity in the

detector. This is often characterized with $\langle \mu \rangle$, the measured per bunch crossing μ value averaged over all bunch crossings. The interactions inside each bunch crossing that are not the main physics process of interest are often referred to as “pileup” interactions, and $\langle \mu \rangle$ is a measurement of the level of pileup in the detector.

2.1.2 EVOLUTION OF MACHINE CONDITIONS

This thesis uses datasets taken at three different center of mass energies: $\sqrt{s} = 7$ TeV data taken in the year 2011, $\sqrt{s} = 8$ TeV data taken in the year 2012, and $\sqrt{s} = 13$ TeV data taken in the year 2015. In addition to increasing center of mass energy, the instantaneous luminosity and parameters that determine it were evolving. Table 2.1 summarizes that machine conditions in each of these datasets.

	2011	2012	2015	Design
\sqrt{s} [TeV]	7	8	13	14
Number of bunches	1380	1380	1825	2808
Max. protons per bunch	1.45×10^{11}	1.7×10^{11}	1.2×10^{11}	1.15×10^{11}
Bunch spacing [ns]	50	50	25	25
Max. instantaneous luminosity [$\text{cm}^{-2}\text{s}^{-1}$]	3.7×10^{33}	7.7×10^{33}	5×10^{33}	10^{34}
β^* [m]	1.0	0.6	0.8	0.55
$\langle \mu \rangle$	11.6	20.7	13.7	-

Table 2.1: Evolution of LHC machine conditions [38, 39]

2.2 THE ATLAS DETECTOR

The ATLAS detector is a multi-purpose particle detector experiment at the LHC’s Point 1 [32]. It has nearly 4π coverage in solid angle around the interaction point. It consists of an inner detector for measuring charged particles, electromagnetic and hadronic calorimeters, and a muon spectrometer. Figure 2.2 gives an overview of the detector.

2.2.1 COORDINATE SYSTEM

Before defining the properties of the individual detectors, it is important to establish the coordinate system used. Figure 2.3 shows a schematic of the coordinate system. The azimuthal plane (perpendicular

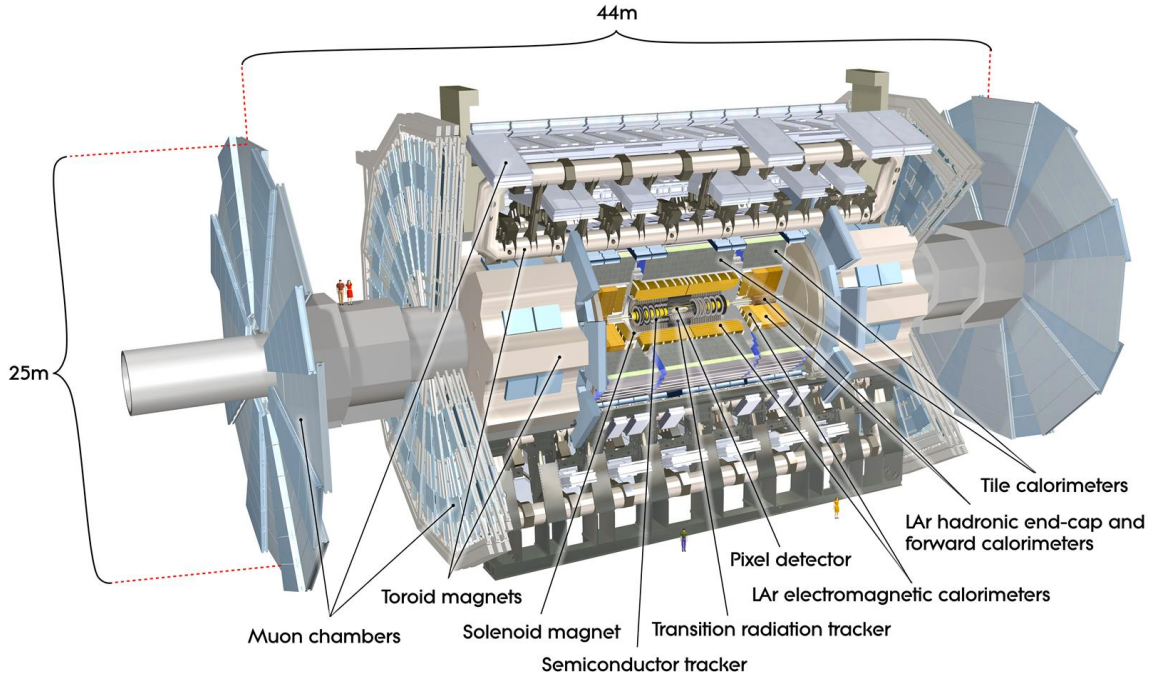


Figure 2.2: A full diagram of the ATLAS detector [32]

846 to the beam line) is defined as the x - y plane. The angle in this plane is referred to as ϕ . The angle relative
 847 to the beam axis is referred to as θ . Rather than using θ directly as a coordinate, the experiment often
 848 uses the pseudorapidity η . η is defined in equation 2.3.

$$\eta = \ln \left(\tan \left(\frac{\theta}{2} \right) \right) \quad (2.3)$$

849 Pseudorapidity is the massless approximation of rapidity, the angle used to parameterize boosts in
 850 special relativity. This is important for two reasons. First, it means that differences in η are Lorentz in-
 851 variant. Second, particle production is roughly constant in pseudorapidity. Particles with η close to zero
 852 are referred to as “central”, while those at high $|\eta|$ are called “forward”. In general, two main detector
 853 topologies can be seen in figure 2.2. There are “barrel” elements, which surround the beam line cylin-
 854 drically and are in the central region of the detector. In the forward region, there are “endcap” regions
 855 which are arranged as disks perpendicular to the beam line.

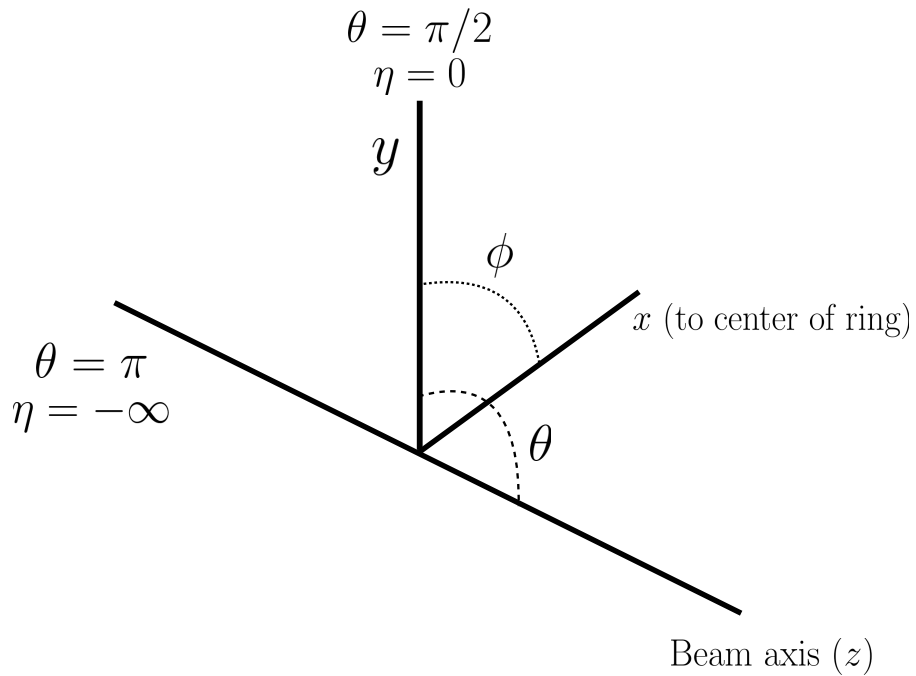


Figure 2.3: The ATLAS coordinate system

856 2.2.2 INNER DETECTOR

857 The ATLAS Inner Detector (ID) system is built for precision tracking of charged particles. It covers
 858 the range $|\eta| < 2.5$. In this range, approximately 1000 particles are generated every bunch crossing in
 859 the detector. This requires having fine granularity to achieve the resolutions required for good momen-
 860 tum measurement and vertex reconstruction.

861 The ID consists of three sub-components: the pixel detector, semiconductor tracker (SCT), and trans-
 862 ition radiation tracker (TRT). It is surrounded by a solenoid providing a 2 T axial magnetic field which
 863 bends particles in the transverse plane to allow for momentum measurement. Figure 2.4 shows the layout
 864 of each of these components.

865 PIXEL DETECTOR

866 The pixel detector is the first detector particles traverse after being generated in proton collisions and
 867 is the most granular detector. Its operation is crucial for precision tracking and vertex reconstruction as

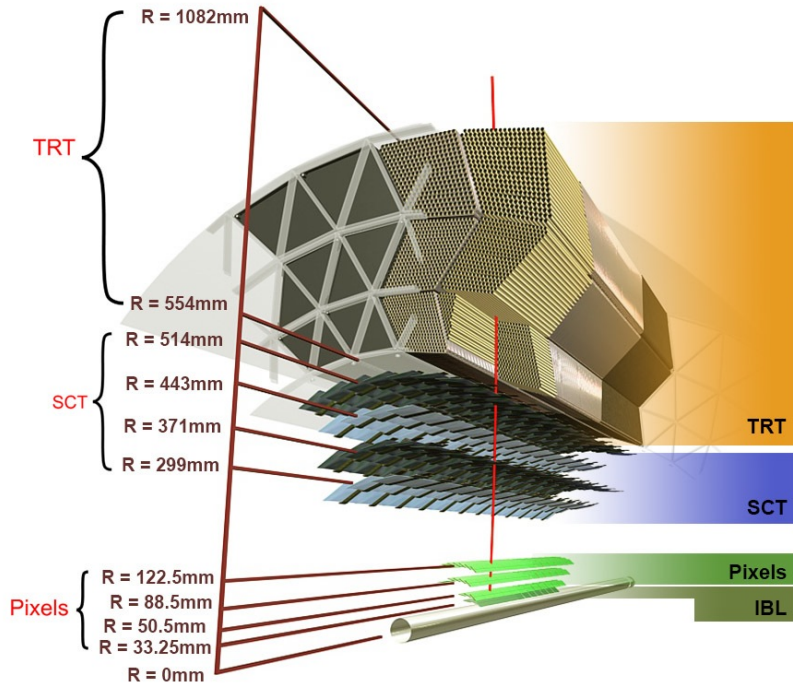


Figure 2.4: Layout of the ATLAS Inner Detector system [40]

well as higher level object reconstruction like tagging of jets from b -quarks. The basic sensing element in this subdetector is a silicon pixel detector. The operating principle for the silicon pixels is that of a $p-n$ junction. When a charged particle passes through, it creates electron-hole pairs that are then separated by the electric field. The sensors are $250\ \mu\text{m}$ thick and use oxygenated n -type wafers with readout pixels on the n^+ side of the detector [32]. Overall, the pixel detector has 1744 sensors and 80.4 million readout channels.

In the barrel region, the pixel detector has three concentric layers of sensors surrounding the beam-line. In the endcap region, it consists of disks perpendicular to the beam axis. The detector is segmented in the $R-\phi$ plane and in z . Usually, three pixel layers are crossed by a charged particle track. The intrinsic accuracies of the sensors are $10\ \mu\text{m}$ in $R-\phi$ and $115\ \mu\text{m}$ in z (or R for the endcap).

878 INSERTABLE B-LAYER

879 In Run 2, a new innermost pixel layer, known as the insertable B-layer (IBL), was added to the Inner
880 Detector [41]. This layer was added to cope with the higher luminosities planned in LHC Run 2 and

881 at the high luminosity HL-LHC. Additionally it improves tracking position resolution which in turn
882 improves the vertexing and b -tagging capabilities in ATLAS. The detector sits directly on a new beam
883 pipe, only 33.25 mm away from the collision points in the azimuthal plane.

884 **SEMICONDUCTOR TRACKER (SCT)**

885 The semiconductor tracker (SCT) consists of silicon microstrips and comprises the next four layers
886 of the ID. This sub-detector has 6.4cm long sensors that are daisy-chained into strips with a strip pitch
887 of $80\ \mu\text{m}$ [32]. Some of the strips have a small stereo angle to allow for measurement of both angular
888 coordinates. In total there are 6.3 million readout channels. The intrinsic accuracies are $17\ \mu\text{m}$ in $R\phi$
889 and $580\ \mu\text{m}$ in z (or R in the endcap).

890 **TRANSITION RADIATION TRACKER (TRT)**

891 The transition radiation tracker (TRT) serves two purposes. First, it consists of 4mm diameter straw
892 tubes filled with a 70/27/3% gas mixture of xenon, carbon dioxide, and oxygen to provide tracking of
893 charged particles. Particles typically have 36 TRT straw tube hits per track. The material in between
894 the straws is designed to induce transition radiation which can be useful for particle identification. As
895 particles pass between media with different dielectric constants, they emit transition radiation that can
896 cause additional showers in the TRT. In particular it is useful for discrimination between electrons and
897 pions or other charged hadrons, as the amount of transition radiation is proportional to the Lorentz
898 factor of the particle.

899 **2.2.3 CALORIMETERS**

900 The calorimeter system consists of two main sub-components: a fine granularity electromagnetic
901 calorimeter tailored for the measurement of photons and electrons and multiple coarser hadronic calorime-
902 ters dedicated to the measurement of hadronic showers [32]. The calorimeter system has broader cover-
903 age than the inner detector, covering the region out to $|\eta| < 4.9$. It is also designed to deliver good
904 containment of showers so as to limit leakage into the muon system. Figure 2.5 shows the layout of the
905 calorimeter system.

906 Both the electromagnetic and hadronic calorimeters are sampling calorimeters. They alternate active
 907 material for energy measurement with passive material for energy absorption. The materials used for
 908 each purpose vary based on the type of calorimeter and its location in the detector.

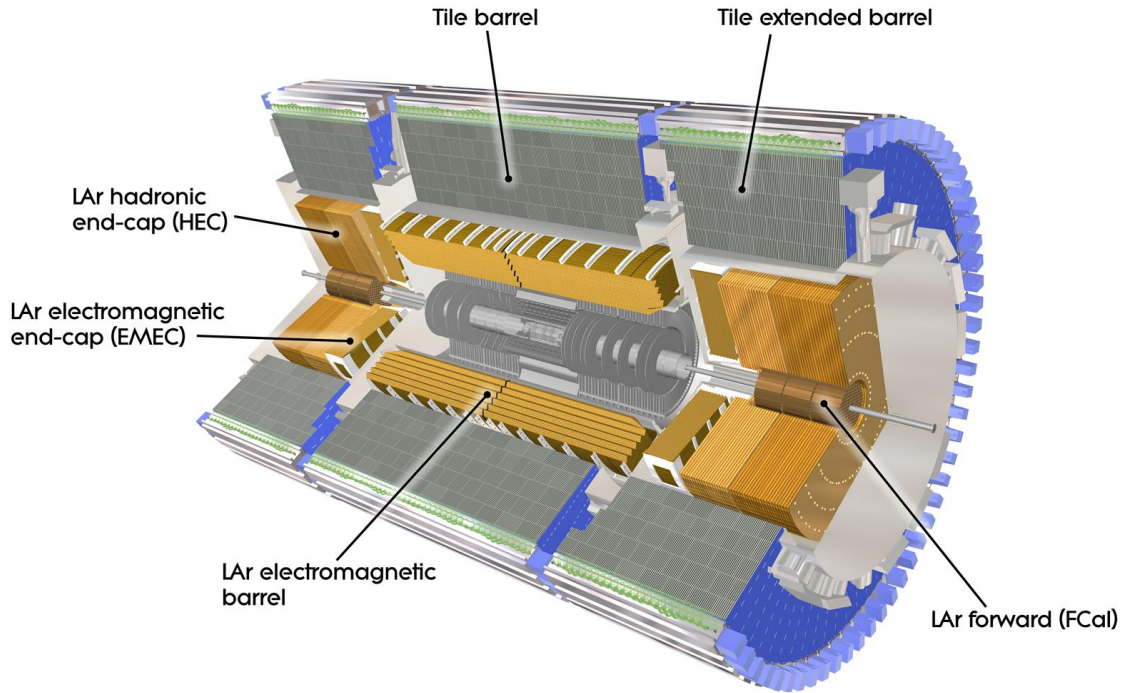


Figure 2.5: Layout of the ATLAS calorimeter system [32]

909 ELECTROMAGNETIC CALORIMETER

910 The electromagnetic calorimeter (EM calorimeter) use liquid Argon (LAr) as its active material and
 911 lead as its passive material. It is arrange in an accordion geometry to increase the absorption area while
 912 still allowing it to have no azimuthal cracks (complete symmetry in ϕ). The EM calorimeter is divided
 913 into a barrel portion that extends to $|\eta| < 1.475$ and an endcap portion going from $1.375 < |\eta| < 3.2$.
 914 The region where these two units overlap is called the “transition region”.

915 In order to provide good containment the calorimeter depth must be optimized. Typically, for elec-
 916 tromagnetic calorimeters the depth is measured in radiation lengths. In general, the intensity of a par-
 917 ticle beam attenuates exponentially in distance with a constant equal to the radiation length. That is,

918 $I(x) = I_0 e^{-x/X_0}$, where I is the intensity, x is the distance traveled, and X_0 is the radiation length.

919 The ATLAS EM calorimeter is designed to have > 22 radiation lengths in the barrel and > 24 in the
920 endcap [32].

921 **HADRONIC CALORIMETERS**

922 There are three types of hadronic calorimeters present in ATLAS: the tile calorimeter (TileCal),
923 hadronic endcap (HEC), and forward calorimeter (FCal). Each one is optimized for stopping of hadronic
924 showers and the materials chosen are specific to their placement in the detector.

925 The TileCal is a scintillating tile calorimeter placed directly outside the EM calorimeter. It uses steel as
926 the absorber and plastic scintillator tiles as the active material. It has coverage in the barrel at $|\eta| < 1.0$
927 and in the “extended barrel” region of $0.8 < |\eta| < 1.7$.

928 The HEC had two wheels perpendicular to the beam line per endcap and is located directly behind
929 the EM calorimeter endcap modules. The HEC covers the region from $1.5 < |\eta| < 3.2$, overlapping
930 slightly with both the tile calorimeter and the forward calorimeter. Like the EM calorimeter, it uses liq-
931 uid Argon as the active material, but it uses copper as the absorber.

932 The FCal covers the most forward regions of the calorimeter system, extending to the region of $3.1 <$
933 $|\eta| < 4.9$. It again uses liquid argon as its active material. For absorber, it consists of an innermost
934 module made of copper followed by a module made of tungsten.

935 The hadronic equivalent of radiation length is called the interaction length and is denoted as λ . In the
936 barrel, the hadronic calorimeter depth is approximately 9.7λ , while in the endcap is is 10λ . The outer
937 supports contribute an additional 1.3λ . This is been shown to be sufficient to limit punch-through of
938 showers to the muon system [32].

939 **2.2.4 MUON SPECTROMETER**

940 The muon spectrometer is dedicated to measuring the momentum and position of muons. It consists
941 of tracking and trigger chambers which are unique in the barrel and endcap regions. The magnetic field
942 for bending of muons is provided by a system of three large air-core toroid magnets (from which ATLAS

943 derives its name.) These magnets provide 1.5 to 5.5 Tm of bending power at $0 < |\eta| < 1.4$ and approx-
 944 imately 1 to 7.5 Tm in the endcap region of $1.6 < |\eta| < 2.7$. The entire muon system covers the range
 945 $0 < |\eta| < 2.7$. Monitored drift tubes (MDTs) are used for tracking in the barrel and the two outer
 946 layers of the endcap, while cathode strip chambers (CSCs) are used to provide tracking in the innermost
 947 endcap wheel. In the barrel, resistive plate chambers (RPCs) are used as trigger chambers while thin gap
 948 chambers (TGCs) are used in the endcap. Figure 2.6 shows the layout of the ATLAS muon system. The
 949 entire muon system is designed with the specification of providing a 10% momentum resolution for a
 950 1 TeV muon.

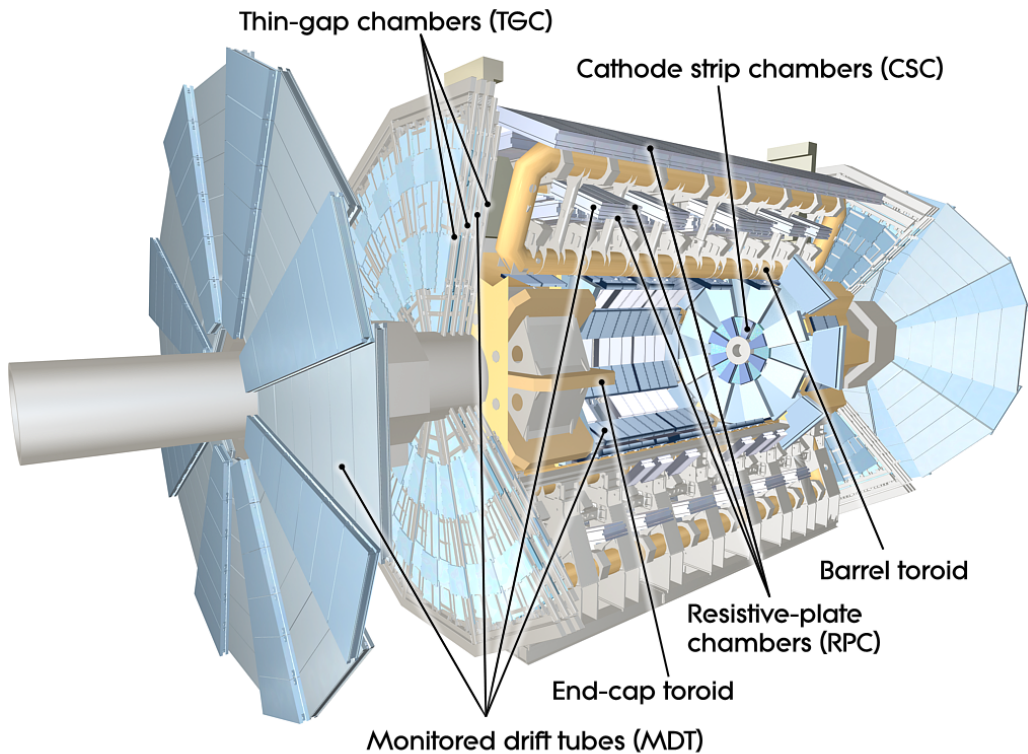


Figure 2.6: Layout of the ATLAS muon system [32]

951 MONITORED DRIFT TUBES (MDTs)

952 The monitored drift tubes (MDTs) are aluminum 3cm diameter tubes filled with a 93/7 % mixture
 953 of Argon and CO₂, with trace amounts of water. As a charged particle traverses the tube, it ionizes the

954 gas and the ions drift to a wire at the center of the tube. The radial distance of traversal of the particle in
955 the tube is determined by the drift time of the electrons, allowing for fine position resolution. The tubes
956 have an average resolution of $80 \mu\text{m}$ per tube and a maximum drift time of approximately 700ns. The
957 tubes are oriented so that they give precision measurement in η and run along ϕ . They cover $|\eta| < 2.7$,
958 except in the innermost layer of the endcap where they only go to $|\eta| < 2.0$ [32].

959 **CATHODE STRIP CHAMBERS (CSCs)**

960 The cathode strip chambers cover a narrow window of the innermost endcap region at $2.0 < |\eta| <$
961 2.7. In this region the background rates in the cavern are particularly high and the CSCs are designed
962 to handle these higher rates. The CSCs are multiwire proportional chambers with wires pointing in
963 the radial direction (away from the beam pipe). The wire serves as an anode and there are two types of
964 segmented cathode strip, one perpendicular to the wires which gives the precision measurement and one
965 parallel which provides the transverse coordinate. It has an 80/20 gas mixture of Argon and CO₂ [32].

966 **RESISTIVE PLATE CHAMBERS (RPCs)**

967 The resistive plate chambers (RPCs) are gaseous electrode-plate detectors covering the region $|\eta| <$
968 1.05. They consist of two resistive plates separated by a distance of 2 mm. The gas mixture used is a
969 94.7/5/0.3% mixture of C₂H₂F₄, Iso-C₄H₁₀, and SF₆. It has readout strips with a pitch of 23-35 mm
970 for both η and ϕ measurement and thus provides measurement of the azimuthal coordinate in the barrel
971 that the MDTs do not. The thin gas gap allows for a quick response time which makes it ideal for use in
972 the trigger. There are three layers of RPCs which are referred to as the three trigger stations. They allow
973 for both a low p_T and high p_T trigger. The coincidence of hits in the innermost chambers allows for
974 triggering of muons between 6 and 9 GeV, while the outermost layer allows the trigger to select high
975 momentum tracks in the range of 9 to 35 GeV [32].

976 **THIN GAP CHAMBERS (TGCs)**

977 The thin gap chambers (TGCs) are multiwire proportional chambers where the wire to cathode dis-
978 tance (1.4mm) is smaller than the wire-to-wire distance (1.8 mm). They contain a gas mixture of CO₂

979 and n -pentane and use a high electric field to gain good time resolution. They serve two functions in the
 980 end-cap system. First, they serve as the trigger chambers. Second, they also provide azimuthal coordi-
 981 nate measurement which the MDTs do not. They sit on the inner and middle layers of the endcap. The
 982 outermost layer's azimuthal coordinate is determined by extrapolation [32].

983 2.2.5 MAGNET SYSTEM

984 As mentioned previously, there are two independent magnet systems in ATLAS. The first is a 2 T
 985 solenoid field in the inner detector which provides bending in the azimuthal plane. The second is an
 986 approximately 0.5 T toroidal field in the muon system which provides bending in η . Figure 2.7 shows
 987 the predicted field integral as a function of $|\eta|$ [32].

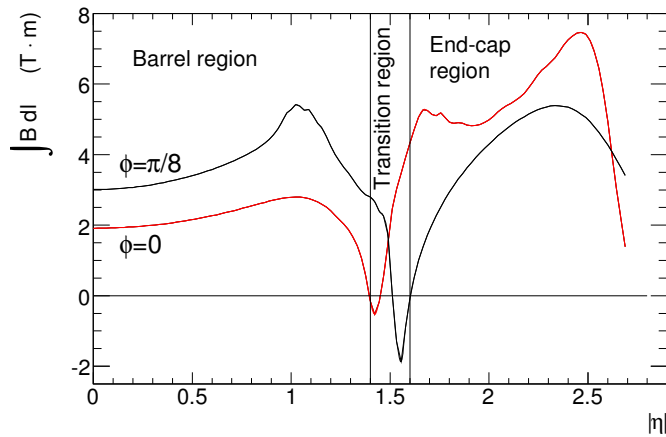


Figure 2.7: Predicted field integral as a function of $|\eta|$ for the ATLAS magnet system [32]

988 2.2.6 TRIGGER SYSTEM

989 The ATLAS trigger system searches for signatures of muons, electrons, photons, hadronically decay-
 990 ing τ leptons, and jets in order to save these events for further analysis. The trigger system in ATLAS
 991 is designed to reduce the maximum LHC event rate of 40 MHz to a more reasonable rate that can be
 992 recorded. The trigger first consists of a fast, hardware based system called the Level-1 (L1) trigger. The
 993 L1 trigger consists of independent dedicated detector sub-components that can seed regions of inter-
 994 est (RoIs) for further analysis downstream. For muons, the RPCs and TGCs are used, while in the

995 calorimeter coarsely grained sections of calorimeter cells called towers are used. Once regions of interest
 996 are seeded, a software based system called the High Level Trigger (HLT) is used to reconstruct objects
 997 and integrate information from different parts of the detector. In Run 1 of ATLAS, the HLT consisted
 998 of two separate stages: the level 2 (L2) trigger and the event filter (EF).

999 The maximum trigger rate that the L1 trigger can handle is 75 kHz. In the HLT, the rate of events
 1000 written to disk is approximately 200 Hz. Figure 2.8 shows the trigger rates for different L1 triggers in
 1001 2012 and 2015 for ATLAS [42].

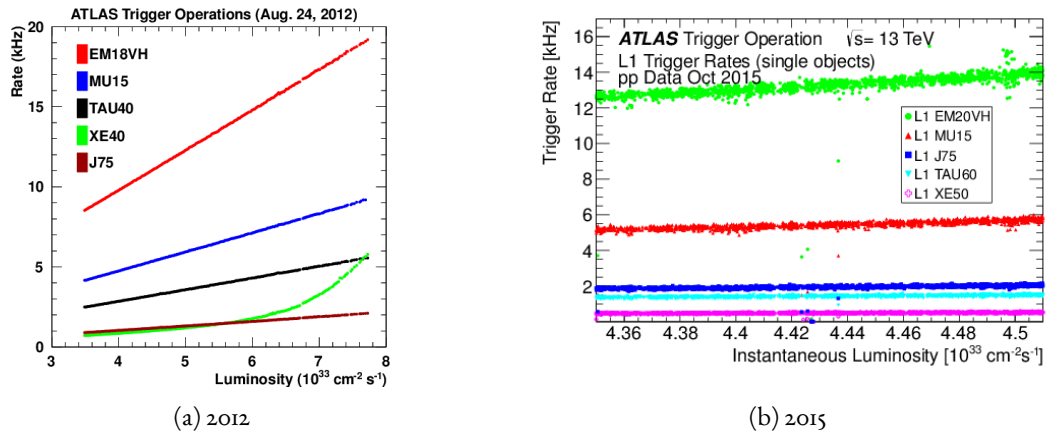


Figure 2.8: ATLAS trigger rates for Level-1 triggers as a function of instantaneous luminosity in 2012 and 2015 operation. These are single object triggers for electromagnetic clusters (EM), muons (MU), jets (J), missing energy (XE), and τ leptons (TAU). The threshold of the trigger is given in the name in GeV. [42]

1002 2.2.7 ATLAS DATASETS

1003 ATLAS has collected data at center of mass energies of 7, 8, and 13 TeV. Figure 2.9 shows the inte-
 1004 grated luminosity as a function of time for each of the three collected datasets. At $\sqrt{s} = 7$ TeV, ATLAS
 1005 recorded 5.08 fb^{-1} . Increased instantaneous luminosity in 2012 led to a larger dataset of 21.3 fb^{-1}
 1006 recorded at $\sqrt{s} = 8$ TeV. After Long Shutdown 1 (LS1) of the LHC and a restart in 2015, ATLAS
 1007 recorded 3.9 fb^{-1} of data at $\sqrt{s} = 13$ TeV. [43, 44]

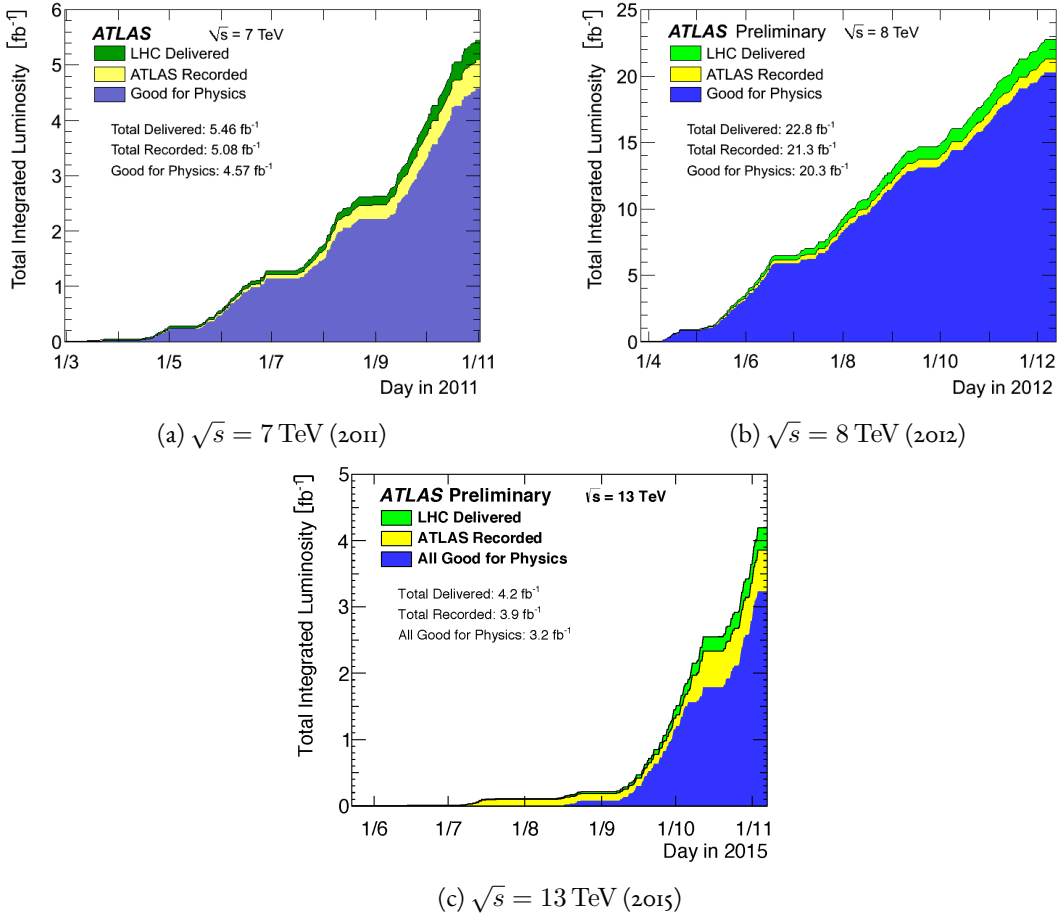


Figure 2.9: Instantaneous luminosity as a function of time for data recorded by ATLAS at different center of mass energies [43, 44]

1008 2.2.8 DETECTOR PERFORMANCE

1009 Table 2.2 summarizes the design requirements for each of the different sub-detectors. This table
 1010 shows the energy and momentum resolution of each tracking, calorimetry, and muon measurements.

1011 2.3 THE ATLAS MUON NEW SMALL WHEEL UPGRADE

1012 As the LHC continues operation, it is scheduled to be upgraded in several phases to allow it to reach
 1013 higher instantaneous luminosities and thus collect larger datasets. These conditions will open new doors
 1014 for study of rare physics processes but will also present interesting challenges that must be faced. ATLAS
 1015 will require new detector technologies to cope with the increased background rates in the cavern in these

	Required resolution
Tracking	$\sigma_{p_T}/p_T = 0.05\% p_T \oplus 1\%$
EM calorimetry	$\sigma_E/E = 10\%/\sqrt{E} \oplus 0.7\%$
Hadronic calorimetry	
Barrel and end-cap	$\sigma_E/E = 50\%/\sqrt{E} \oplus 3\%$
Forward	$\sigma_E/E = 100\%/\sqrt{E} \oplus 10\%$
Muon spectrometer	σ_{p_T}/p_T at $p_T = 1$ TeV

Table 2.2: Performance requirements for the ATLAS detector [32].

high luminosity conditions. One such upgrade, scheduled to be installed during Long Shutdown 2 (LS2) of the LHC in 2018, is the ATLAS Muon New Small Wheel (NSW) upgrade [45]. The NSW will replace the innermost end-cap wheel of the muon system with new technologies, as this is the part of the muon detector closest to the beam and thus suffers from the highest rates.

2.3.1 MOTIVATION

The motivation of the NSW is two-fold. First, the objective is to alleviate the decreased tracking efficiency that comes in a high rate environment. As figure 2.10, at the LHC design luminosity both the efficiency of recording hits and reconstructing track segments in the MDTs decreases at the LHC design luminosity.

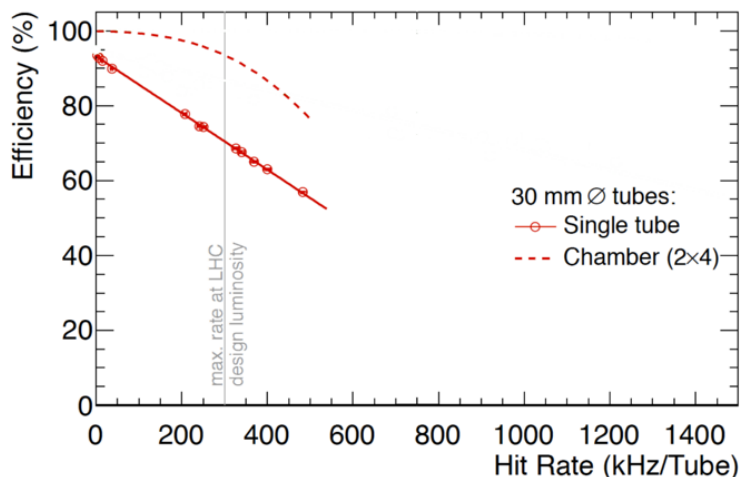


Figure 2.10: MDT tube hit (solid) and segment (dashed) efficiency as a function of hit rate per tube [45]

1025 Second, the NSW will work to alleviate the rate of fake triggers arising in the endcap. Figure 2.II
 1026 shows the extrapolated trigger rates as a function of the p_T threshold with and without the NSW up-
 1027 grade. As the figure shows, the NSW upgrade will reduce the trigger rate by an order of magnitude com-
 1028 pared to the current endcap trigger system.

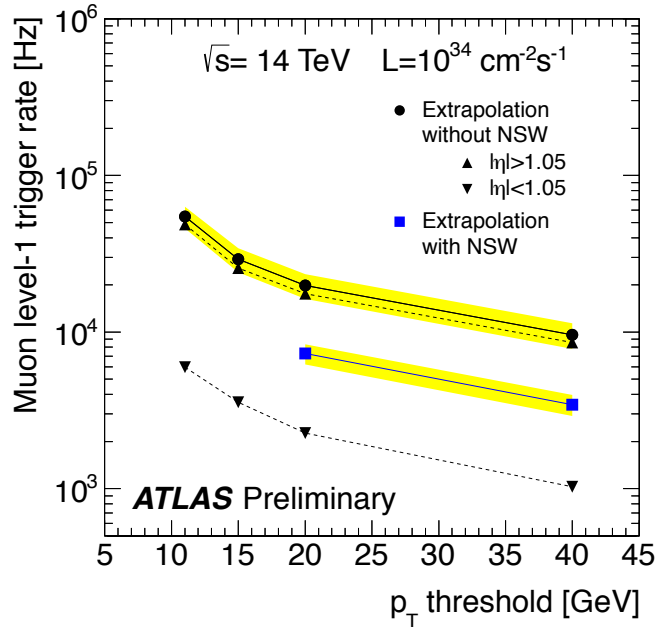


Figure 2.II: Trigger rate as a function of p_T threshold with and without the NSW upgrade [45]

1029 2.3.2 NSW DETECTOR TECHNOLOGIES

1030 The NSW will use two new detector technologies - micromesh gaseous structure detectors (mi-
 1031 cromegas) and small-strip thin gap chambers (sTGCs) [45, 46]. Unlike the previous detectors, both of
 1032 these detector technologies can be used for tracking or trigger. However, the micromegas is more suited
 1033 to tracking because of its good spatial resolution, while the sTGCs have better time resolution and are
 1034 more suited for the trigger. To maintain a fully redundant system, both technologies are used for both
 1035 purposes.

1036 **MICROMEGAS**

1037 Micromegas detectors operate using a thin metallic mesh that sits approximately $100\ \mu\text{m}$ away from
1038 the readout electrodes to create the amplification region. Above this mesh, there is a drift region on the
1039 order of a few mm in length capped by a drift electrode. As a charged particle traverses the detector, it
1040 ionizes gas and the electrons drift down towards readout strips. The timing of the drift can be used to
1041 reconstruct the angle of traversal of the particle. This is illustrated in figure 2.12. The micromegas used in
1042 ATLAS will be resistive micromegas, where the readout electrodes are topped with resistive strips [47].
1043 This alleviates the risk of sparking in the large area detectors that ATLAS will use.

1044 In ATLAS, the micromegas drift gap will be 5 mm and the amplification gap will be $128\ \mu\text{m}$. They
1045 are filled with the same gas mixture as the MDTs. They will be stacked in an octuplet in an XXUV-
1046 UVXX geometry, where X refers to straight strips and U and V refer to stereo strips at an angle of $\pm 1.5^\circ$.
1047 This arrangement allows for measurement of the azimuthal coordinate and gives a large lever arm be-
1048 tween the straight strips for triggering purposes. Figure 2.12 shows the geometry of a single micromegas
1049 detector as well as its operating principle [45].

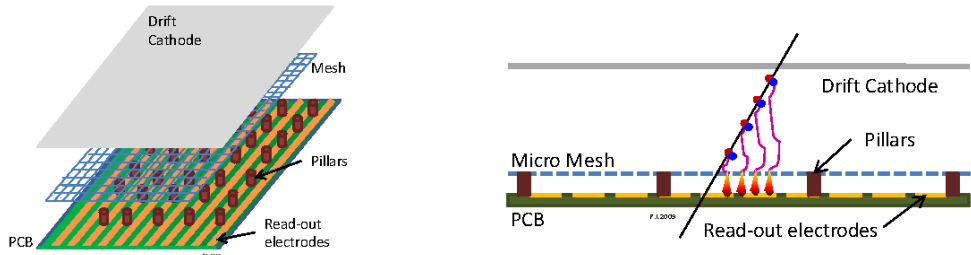


Figure 2.12: Illustrations of the geometry (left) and operating principle (right) of the micromegas detector [45]

1050 **sTGCs**

1051 The sTGCs are similar to the TGCs already described. They consist of gold-plated tungsten wires
1052 with a 1.8 mm pitch between two cathode planes 1.4 mm away from the wire plane. One cathode plane
1053 consists of strips with a 3.2 mm pitch (much smaller pitch than the TGCs), while the other consists
1054 of coarser pads that are used for defining regions of interest in the sTGC trigger algorithm. Figure 2.13
1055 shows the basic detector geometry.

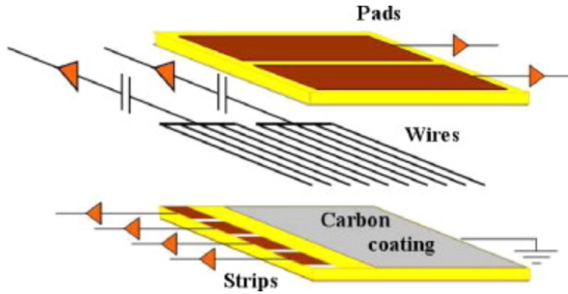


Figure 2.13: Geometry of the sTGC detector [45]

1056 2.3.3 PHYSICS IMPACT

1057 Maintaining low p_T thresholds for muons while still staying within the trigger rate budget at Level
 1058 1 (20 kHz) for the muon system is crucial for physics analyses to be successful in high luminosity con-
 1059 ditions. One realm where the lepton trigger threshold is especially important is in Higgs physics. In the
 1060 $H \rightarrow WW^*$ analysis, one of the W bosons is off shell and tends to decay to soft leptons. In associated
 1061 production of a Higgs with a W , the lepton is also important because the lepton provides the main han-
 1062 dle which allows the event to be triggered. Table 2.3 shows the impact of increasing the trigger thresholds
 1063 on these analyses. It shows that either raising the threshold or using only the barrel both have signifi-
 1064 cant impacts on the signal efficiency. With the NSW, the signal efficiency is largely maintained and the
 1065 triggers can be unprescaled.

Threshold	$H \rightarrow bb$ (%)	$H \rightarrow WW^*$ (%)
$p_T > 20$ GeV	93	94
$p_T > 40$ GeV	61	75
$p_T > 20$ GeV (barrel only)	43	72
$p_T > 20$ GeV (with NSW)	90	92

Table 2.3: Signal efficiencies for WH production with $H \rightarrow b\bar{b}$ and $H \rightarrow WW^* \rightarrow \mu\nu qq$ under different trigger configurations [45].

1066 2.4 OBJECT RECONSTRUCTION IN ATLAS

1067 ATLAS analyses first start by requiring the presence of certain reconstructed physics objects in the
 1068 event. This section will present a brief overview of the algorithms used to reconstruct electrons, muons,

1069 jets (including b -jets), and missing energy^{*}. The performance of object reconstruction and measurement
1070 will also be discussed as these are relevant to the analyses presented later. Figure 2.14 gives an overview of
1071 the different sub-detectors that each type of particle will interact with in ATLAS.

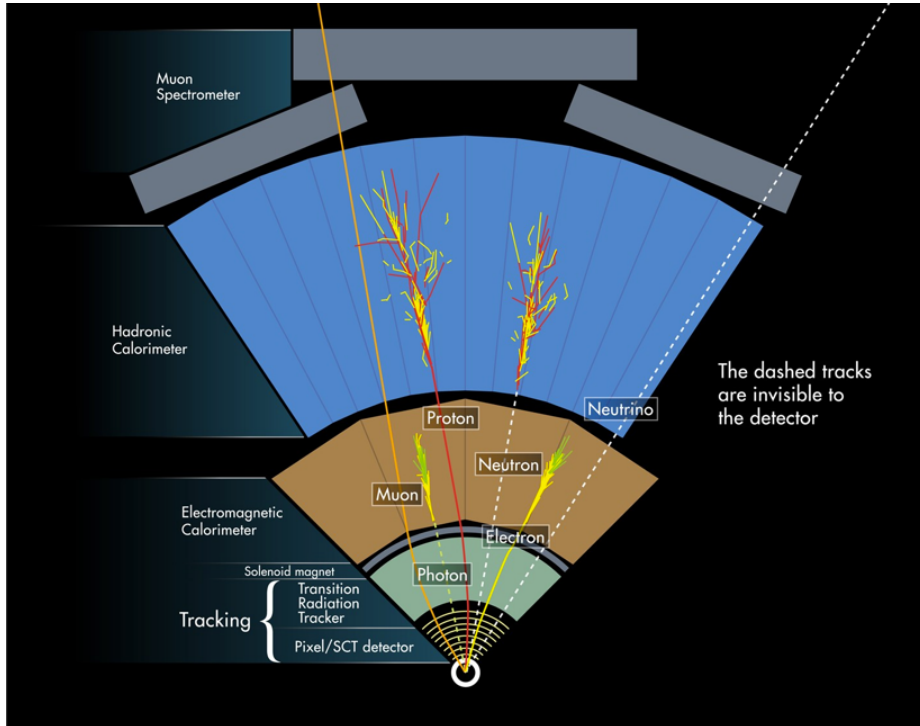


Figure 2.14: Illustration of particle interactions in ATLAS [48]

1072 2.4.I ELECTRONS

1073 Electrons in ATLAS will leave tracks in the inner detector and energy deposits in the electromagnetic
1074 calorimeter. The algorithm for recognizing the signature of electrons proceeds in two steps: reconstruc-
1075 tion and identification.

1076 In reconstruction, an electron candidate is formed by matching EM calorimeter deposits with ID
1077 tracks. The algorithm first chooses seed clusters in the EM calorimeter by using a sliding window algo-
1078 rithm that searches for towers with transverse energy larger than 2.5 GeV. In addition to seed clusters,
1079 track candidates must be identified in the ID. The algorithm selects seed tracks with $p_T > 1$ GeV that

*Reconstruction algorithms for other objects, such as photons and τ leptons, are not detailed here as these objects are not used in the presented studies.

1080 do not fit well with a pion hypothesis. Once candidate tracks are selected, they are re-fit with a Gaussian
 1081 Sum Filter (GSF) algorithm to estimate electron parameters [49]. Finally, an electron candidate is
 1082 formed if at least one track matches to a seed cluster in the calorimeter. The full details of the reconstruc-
 1083 tion algorithm can be found in reference [50].

1084 Once an electron candidate is present, identification criteria must be applied in order to reject fake
 1085 electrons from background. Many different variables are used for this identification, most of them re-
 1086 lated to the shower shape in the EM calorimeter and the amount of leakage into the hadronic calorime-
 1087 ter, as well as information from the ID and in particular the TRT. There are both cut-based and likelihood-
 1088 based criteria that range from “loose” to “very tight”. For details, see reference [50].

1089 Figure 2.15 shows the algorithm’s reconstruction efficiency of true electrons for different identification
 1090 criteria as well as the electron energy resolution in simulation [50, 51]. The reconstruction efficiency is
 1091 measured using both Z and J/ψ tag and probe techniques.

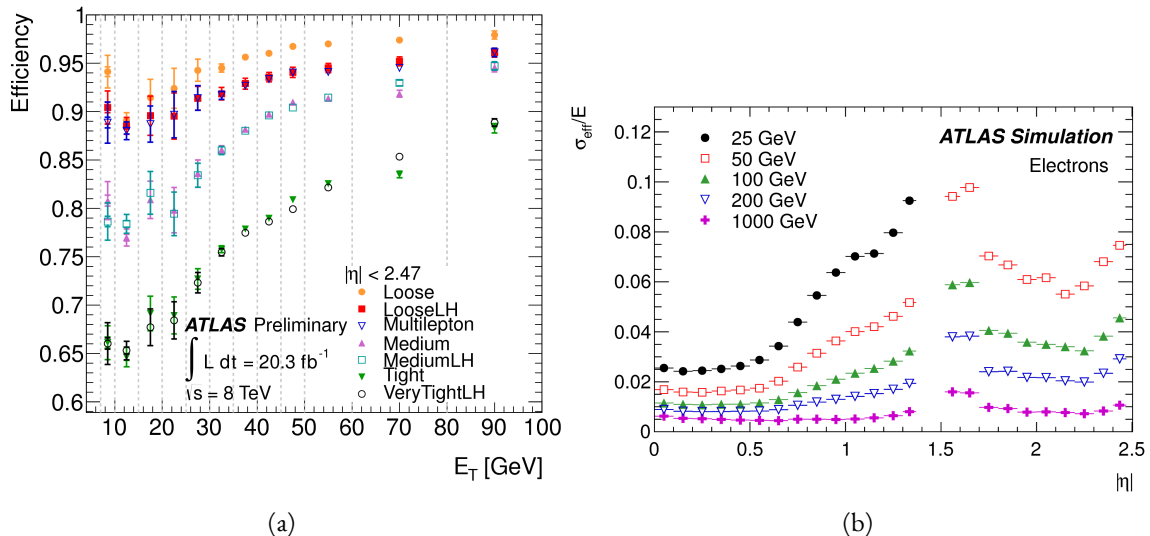


Figure 2.15: Electron performance: (a) reconstruction efficiency as a function of electron E_T [50] (b) energy resolution in simulation as a function of $|\eta|$ for different energy electrons [51]

1092 2.4.2 MUONS

1093 The ATLAS detector is designed to stop most particles before they reach the muon spectrometer.
 1094 Muons, however, are minimum ionizing particles, meaning that they will not lose a significant amount

1095 of energy through interactions with the detector and will thus pass through. Therefore, the muon recon-
1096 struction works to match tracks in the muon spectrometer with tracks in the inner detector.

1097 The first step of reconstruction is to reconstruct local straight line tracks, called segments, in each
1098 muon chamber. Segments are then fit to larger tracks that traverse the entire muon spectrometer. Such
1099 muon tracks are referred to as “standalone” tracks (SA) as they only use information from the muon
1100 spectrometer. The standalone tracks are then matched to tracks in the inner detector to form “com-
1101 bined” (CB) muons, where the combined ID and MS fit are used to determine the momentum and di-
1102 rection of the muon. To improve acceptance, segment-tagged and calorimeter-tagged muons are also
1103 reconstructed. In these cases, ID tracks are matched to segments in the MS and calorimeter deposits con-
1104 sistent with a minimum ionizing particle, respectively. The details of the reconstruction can be found in
1105 reference [52].

1106 As with electrons, once muon candidates are reconstructed they have identification criteria applied to
1107 reduce background. These criteria include the χ^2 match between the ID and MS tracks, the number of
1108 hits in the ID, overall ID and MS track fit quality, and additional variables [52]. The criteria range from
1109 “loose” to “tight” as with electrons.

1110 Figure 2.16 shows the muon reconstruction efficiency (measured with Z and J/ψ tag and probe) and
1111 invariant mass resolution [52].

1112 2.4.3 JETS

1113 When a quark or gluon is produced in collisions, it is not measured directly in ATLAS. Rather, due to
1114 QCD effects, it produces a collimated spray of hadrons in the direction of the original parton, which is
1115 known as a jet. Jets are reconstructed in ATLAS using energy deposits in the hadronic calorimeter. The
1116 first step is build “topological clusters” out of energy deposits in calorimeter cells [53, 54]. This is done
1117 using strategy where seed cells are chosen by picking cells whose energy measurements are four times the
1118 amount of noise expected for that cell. Adjacent cells with at least 2σ energy measurements are added
1119 to the cluster, then a final layer of clusters with energy above 0σ are added. Once calorimeter clusters
1120 are formed, they are clustered further into jet candidates using the anti- k_T jet clustering algorithm [55].

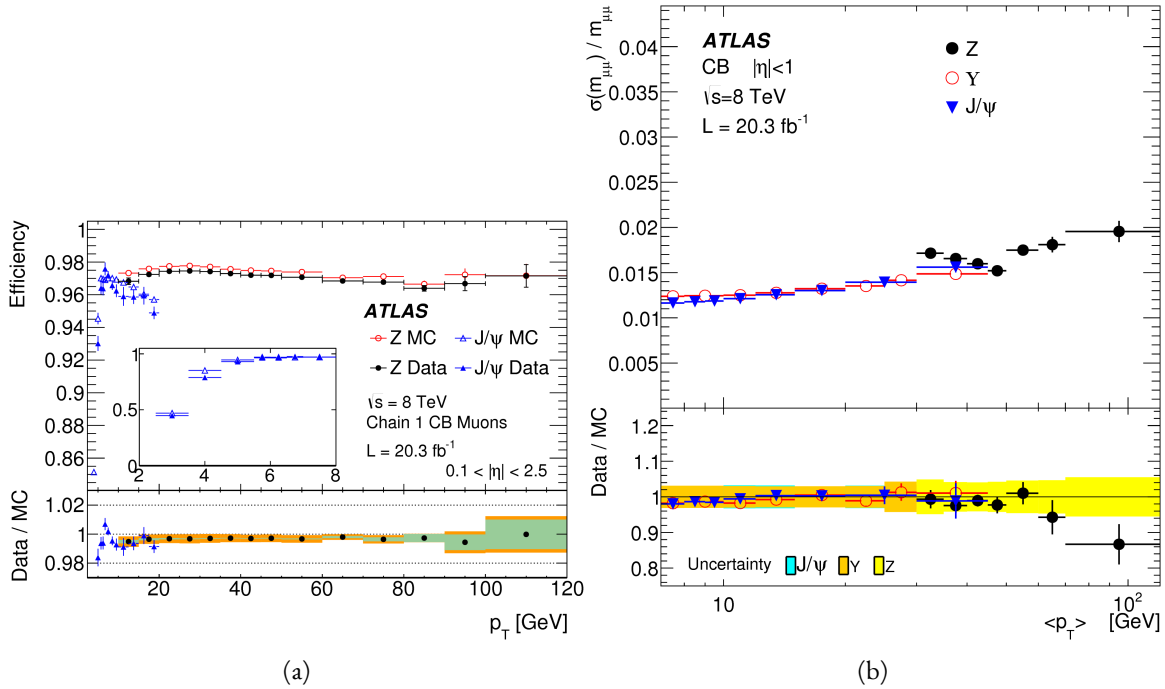


Figure 2.16: Muon performance: (a) reconstruction efficiency as a function of muon p_T (b) dimuon mass resolution as a function of average p_T [52]

1121 This algorithm uses a parameter R that appears in the denominator of the clustering distance metric and
 1122 defines the radial size of the jet in η - ϕ space.

1123 The energy response of the calorimeter must be properly characterized in order to reconstruct jet en-
 1124 ergy. Calorimeter clusters can be calibrated either with the EM calibration, where each cluster is assumed
 1125 to have come from the energy deposit of an electron or photon, or the LCW calibration, where local
 1126 cluster weights are computed to allow for local calibration of clusters as hadronic or electromagnetic.

1127 The details of the jet energy calibration are not detailed here and are discussed in reference [56].

1128 Figure 2.17 shows the jet energy response after calibration in Monte Carlo as a function of the true p_T
 1129 of the jet [56].

1130 2.4.4 b -TAGGING

1131 One important aspect of jet physics is the task of identifying the flavor of parton that produced the
 1132 measured jet. While in general this is very difficult, jets from b -quarks offer an interesting case where such
 1133 identification is possible. B mesons have a lifetime on the order of 10^{-12} seconds, which makes a $c\tau$

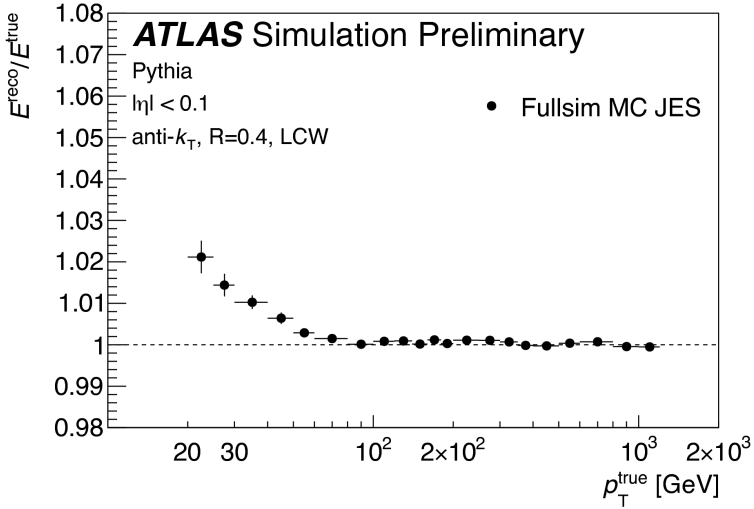


Figure 2.17: Jet energy response after calibration as a function of true p_T in simulation [56]

on the order of millimeters [6]. This type of displaced decay vertex can be identified in detectors like ATLAS and allows b -jets to be distinguished from other flavors of jets[†].

ATLAS uses a multivariate machine learning algorithm to identify jets from b -quarks. The inputs to this algorithm are determined from lower level reconstruction algorithms. There are three distinct algorithms that reconstruct variables which are used as input to the multivariate technique.

The first family is referred to as IPxD (where the x can either be 2 or 3). These algorithms use the transverse and longitudinal impact parameters d_0 and z_0 of the tracks inside a jet to determine their consistency with the primary vertex. They two or three dimensional (hence the x) templates for light flavor, charm, and bottom jets and then evaluate the likelihood of the jet coming from each of these types. The likelihood ratios are used as inputs to the multivariate algorithm.

The next two algorithms used as input are referred to as the secondary vertex (SV) and JetFitter (JF) algorithms. The SV algorithm uses tracks inside the jet to fit for vertices that are displaced from the primary vertex. The JF algorithm attempts to reconstruct the full flight path of the b by looking for multiple displaced vertices along the same line (as B decays often result in subsequent c decays).

In Run 1, the multivariate b -tagging algorithm used a neural network and was referred to as MV1.

[†]Jets from charm quarks can also be detected in this way but they do not live quite as long so the displacement of the vertex is harder to distinguish

1149 The details of this algorithm and its inputs are given in reference [57]. In Run 2, the number of in-
 1150 puts was simplified and a boosted decision tree with 24 input variables was used, referred to as MV2.
 1151 The MV2 algorithm is a boosted decision tree incorporating twenty-four input variables constructed
 1152 from three lower level input algorithms described above. Figure 2.18 summarizes the inputs to MV2.
 1153 Figure 2.19 shows the performance of each of these algorithms.

IP2D and IP3D (6 inputs)	SV1 (8 inputs)	JetFitter (8 inputs)
$\log(p_b/p_u)$	Mass	Mass
$\log(p_b/p_c)$	Energy fraction	Energy fraction
$\log(p_c/p_u)$	# tracks at vertex	# vertices
	# 2 track vertices	# tracks at vertex
	Lxy	# 1 track vertices
	L3d	# 2 track vertices
	3D significance	3D significance
	ΔR	ΔR
Kinematics (2 inputs)		
p_T		
η		

Figure 2.18: Summary of the inputs to the MV2 b -tagging algorithm

1154 2.4.5 MISSING TRANSVERSE ENERGY

1155 As noted in figure 2.14, neutrinos produced in ATLAS will pass through the detector without in-
 1156 teracting. The only way of detecting the presence of particles like neutrinos (or BSM particles that are
 1157 long-lived) is to use missing transverse momentum. The basic principle of missing transverse energy is
 1158 to use the momentum balance of the incoming protons to infer the presence of missing particles. The
 1159 net longitudinal momentum of the incoming partons that collide is not known (since each carries an un-
 1160 known fraction of the proton’s momentum). However, the protons (and thus incoming partons) have
 1161 no net momentum in the plane transverse to the beam line (the x - y) plane. Therefore, if there are no
 1162 un-measured particles in the final state, the transverse momenta of all of the final state particles should

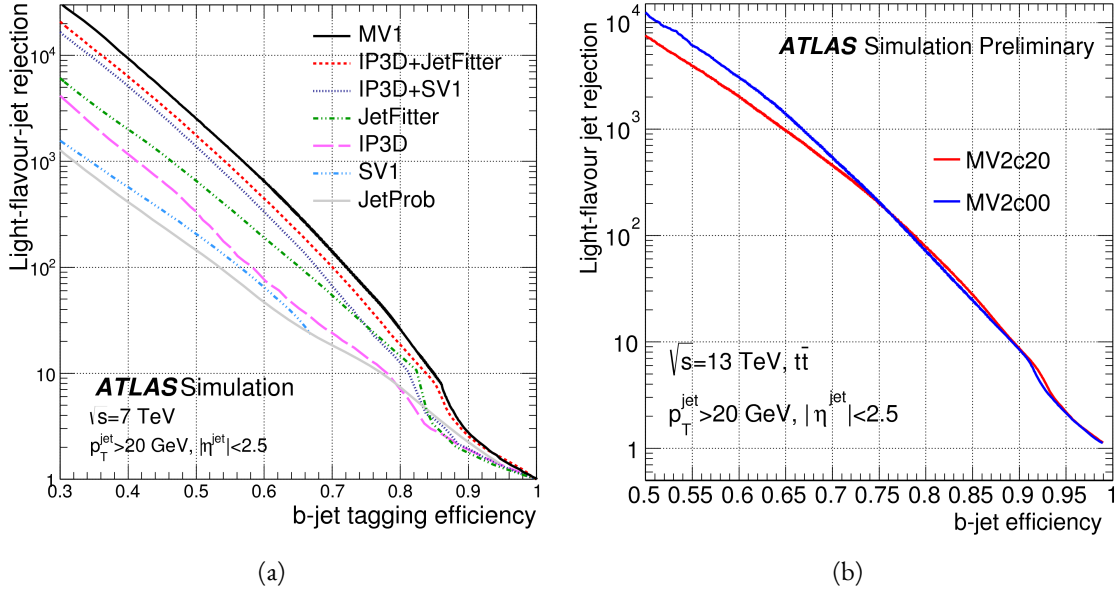


Figure 2.19: Light jet rejection (1/efficiency) vs. b -jet efficiency for MV1 and its input algorithms (a) [57] and MV2 (b) [58] in simulated $t\bar{t}$ events. The numbers in the algorithm names in (b) refer to the fraction of charm events used in the MV2 training.

balance. The magnitude of this imbalance is known as missing transverse momentum (E_T^{miss}).

The basic calculation of missing transverse momentum from calorimeter cells is given in equation 2.4 [59].

1165

$$\begin{aligned} E_x^{\text{miss}} &= - \sum_{i=1}^{N_{\text{cell}}} E_i \sin \theta_i \cos \phi_i \\ E_y^{\text{miss}} &= - \sum_{i=1}^{N_{\text{cell}}} E_i \sin \theta_i \sin \phi_i \end{aligned} \quad (2.4)$$

1166 The E_T^{miss} calculation is separated into different terms based on the objects that the calorimeter clusters

1167 are associated with. This way, each cell's contribution is calibrated appropriately according to the object.

1168 This separation of terms is shown in equation 2.5 [59].

$$\begin{aligned} E_{x(y)}^{\text{miss,calo}} &= E_{x(y)}^{\text{miss},e} + E_{x(y)}^{\text{miss},\gamma} + E_{x(y)}^{\text{miss},\tau} + E_{x(y)}^{\text{miss,jets}} \\ &\quad + E_{x(y)}^{\text{miss,softjets}} + E_{x(y)}^{\text{miss},\mu} + E_{x(y)}^{\text{miss,CellOut}} \end{aligned} \quad (2.5)$$

1169 The CellOut term of the above equation corresponds to calorimeter cells with energy deposits that are
 1170 not associated with other objects. The soft jets term comes from cells associated to jets with p_T between
 1171 7 and 20 GeV, while the jets term comes from jets with $p_T > 20$ GeV. Because muons do not deposit

¹¹⁷² significant energy in the calorimeter, the muon momentum is used for the muon term [59]. The final
¹¹⁷³ E_T^{miss} is calculated using equation 2.6.

$$E_T^{\text{miss}} = \sqrt{(E_x^{\text{miss}})^2 + (E_y^{\text{miss}})^2} \quad (2.6)$$

¹¹⁷⁴ Figure 2.20 shows the resolution of the components of the E_T^{miss} under different pileup suppression
techniques [60].

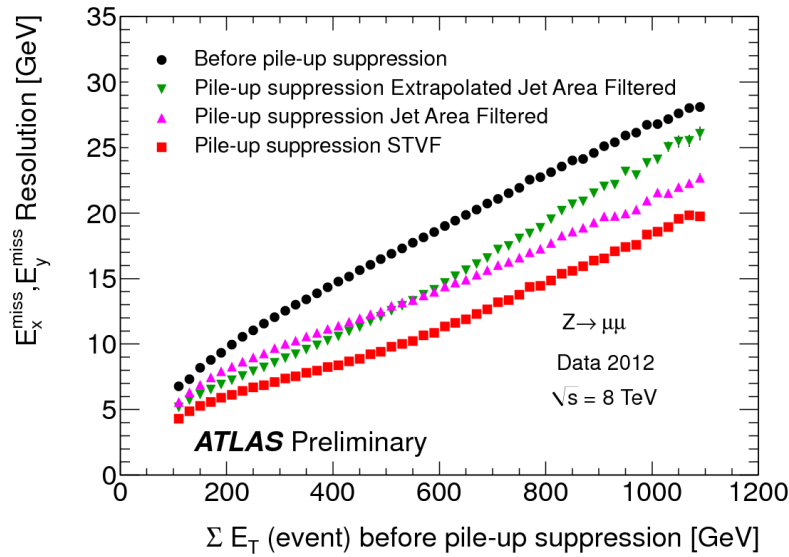


Figure 2.20: Resolution of E_T^{miss} components as a function of $\sum E_T$ before pileup suppression with different
pileup techniques [60]

¹¹⁷⁵

1176

Part II

1177

Observation and measurement of Higgs

1178

boson decays to WW^* in LHC Run I at

1179

$\sqrt{s} = 7$ and 8 TeV

*Basic research is what I am doing when I don't know
what I am doing.*

Wernher von Braun

3

1180

1181 $H \rightarrow WW^* \rightarrow \ell\nu\ell\nu$ Analysis Strategy

1182 3.1 INTRODUCTION

1183 This chapter presents an overview of the strategy for searching for a Higgs boson in the $H \rightarrow WW^* \rightarrow$
1184 $\ell\nu\ell\nu$ decay topology. Its purpose is to define in broad terms how the search and measurement are un-
1185 dertaken, before going into details on the specific sub-categories within the larger analysis. First, the
1186 properties of the Higgs signal are discussed and the associated backgrounds are presented. Next, the ob-
1187 servables used to enhance the signal to background ratio are defined. Finally, the parameters of interest
1188 in the search and measurement will be shown, along with a brief overview of the statistical treatment of
1189 the final Higgs candidates.

1190 Following this chapter, the results of three different studies within the $H \rightarrow WW^* \rightarrow \ell\nu\ell\nu$ channel
1191 are shown. Chapter 4 presents a search for Higgs boson production in gluon fusion mode and the role
1192 of the $H \rightarrow WW^*$ channel in its discovery. Chapter 5 shows the search and first observation in ATLAS
1193 of the Vector Boson Fusion (VBF) production mode of the Higgs in the $H \rightarrow WW^*$ decay channel.

1194 Finally, chapter 6 shows the combined Run 1 $H \rightarrow WW^*$ results for the measurement of the Higgs
1195 cross section and relative coupling strengths to other SM particles.

1196 3.2 THE $H \rightarrow WW^* \rightarrow \ell\nu\ell\nu$ SIGNAL IN ATLAS

1197 The signal studied in this and subsequent chapters is the Higgs boson in the WW^* final state, where
1198 each W boson subsequently decays into a charged lepton and a neutrino. In the simplest decay path,
1199 the final state consists of two neutrinos and two charged leptons, each of which can be either an electron
1200 or a muon. If a W decays to a τ lepton, only leptonic decays of the τ are considered. The τ lepton pro-
1201 duce additional neutrinos in the final state but still yield two charged leptons (where each lepton is an
1202 electron or muon). Neutrinos are not detected in ATLAS, so the final state ultimately consists of two
1203 reconstructed leptons and missing transverse momentum (denoted as E_T^{miss}). Final states where both of
1204 the charged leptons are electrons or muons are referred to as the “same flavor” ($ee/\mu\mu$) final states, while
1205 those with one electron and one muon are referred to as “different flavor” ($e\mu$ or μe).

1206 There can be additional jets produced in association with the Higgs boson. As described in detail
1207 in Chapter 1, if the Higgs is produced via vector boson fusion production, there will be two additional
1208 forward jets in the event. In gluon fusion, one or more jets can be produced through initial state radi-
1209 ation from the incoming gluons. Because of the varying background composition as a function of jet
1210 multiplicity, each bin in this variable has its own dedicated requirements applied in the search and mea-
1211 surement. The $n_j = 0$ and $n_j = 1$ bins are dedicated to gluon fusion production, while the $n_j \geq 2$ bin
1212 has separate dedicated searches for ggF and VBF production.

1213 Figure 3.1 shows the relative branching fractions for the $H \rightarrow WW^*$ process, calculated from the Par-
1214 ticle Data Group values for the W and τ branching ratios [6]. The largest branching ratio corresponds
1215 to both W bosons decaying to quark pairs at 45.44%. The second largest ratio is for one W decaying lep-
1216 tonically and the other decaying to quarks, a branching ratio of 34.18%. In all cases, ℓ denotes either an
1217 electron or muon, and the leptonic branching ratios of the τ are included. For example, the $\ell\nu qq$ final
1218 state includes one W decaying to $e\nu$, $\mu\nu$, or $\tau\nu$. In the case of the $W \rightarrow \tau\nu$ decay, the τ lepton then
1219 decays to an electron or muon via $\tau \rightarrow \nu_\tau \ell \nu_\ell$. Final states with a τ_h refer to hadronic decays of the τ .

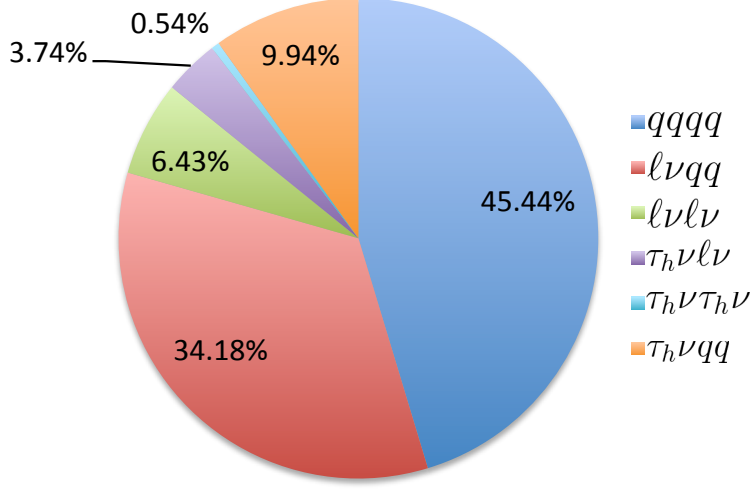


Figure 3.1: Branching ratios for a WW system. q refers to quarks. ℓ can be either an electron or muon, and the leptonic branching ratios of the τ are included. For example, the $\ell\nu qq$ final state includes one W decaying to $e\nu$, $\mu\nu$, or $\tau\nu$. τ_h refer to hadronic decays of the τ .

1220 The branching ratio of the $\ell\nu\ell\nu$ final state is 6.43%.

1221 While the $\ell\nu\ell\nu$ final state is not a large fraction of the branching ratio, there are significant advantages
 1222 to using this channel in an analysis. First, both the $qqqq$ and $\ell\nu qq$ channels suffer from a large QCD
 1223 multijet background, which is often difficult to model. Second, events in the the $\ell\nu\ell\nu$ channel in data
 1224 can be triggered more efficiently due to the presence of two leptons.

1225 3.3 BACKGROUND PROCESSES

1226 Many processes from the Standard Model can also produce a final state with two leptons and miss-
 1227 ing transverse momentum. This section describes the dominant backgrounds to Higgs production and
 1228 further explains how they can be reduced. Table 3.1 summarizes the different background processes.

1229 3.3.1 STANDARD MODEL WW PRODUCTION

1230 Non-resonant Standard Model diboson production, as shown in figure 3.2, is an irreducible back-
 1231 ground to Higgs boson production in the WW final state. It produces the same exact final state objects,

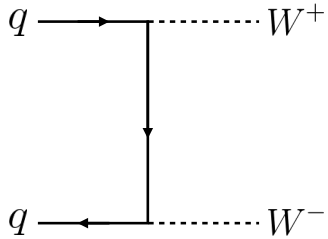


Figure 3.2: Feynman diagram for Standard Model WW production

namely leptonically decaying W bosons. There are no additional objects in the final state that allow for background reduction. Therefore the analysis solely relies on the correlations between the leptons to reduce this background.

3.3.2 TOP QUARK PRODUCTION

Top quark production can mimic the Higgs in the WW^* final state as well. Top quarks can be produced either in pairs ($t\bar{t}$ production) or singly (s -channel, t -channel, or associated production Wt). The dominant top background are $t\bar{t}$ and Wt production.

Because top quarks decay via $t \rightarrow Wb$, top pair production can produce a final state with two W bosons that then decay leptonically. In Wt production, there are two real W bosons produced, as with $t\bar{t}$. In both cases, there is at least one b -jet in the final state. By vetoing on the presence of b -jets, these top quark backgrounds can be reduced. Figure 3.3 shows the Feynman diagrams for $t\bar{t}$ and Wt production.

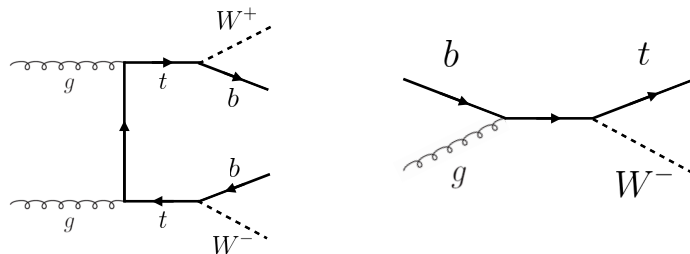


Figure 3.3: Feynman diagrams for top pair production (left) and Wt production (right)

1243 3.3.3 W +JETS BACKGROUND

1244 Single W boson production in association with jets is a unique background to Higgs production.
1245 The other backgrounds considered thus far have all included two prompt leptons, each decaying from a
1246 W boson, in the final state. In W +jets production, however, only one reconstructed lepton originates
1247 from a W . The second reconstructed lepton is either an algorithmic “fake” or the result of non-prompt
1248 decays. In the first case, the lepton is a jet misidentified as a lepton by either the electron or muon recon-
1249 struction algorithms. In the second case, the lepton may be a real lepton but coming from semi-leptonic
1250 decays of particles inside the shower of the jet. This background can be reduced by requiring that the
1251 reconstructed lepton have little activity in the surrounding region of the calorimeter (also known as an
1252 “isolation”). Figure 3.4 shows the Feynman diagram for W +jets production.

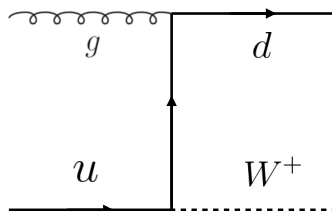


Figure 3.4: An example Feynman diagram of W +jets production

1253 3.3.4 Z/γ^* +JETS BACKGROUND

1254 Production of a Z boson or virtual photon (also known as Drell-Yan and denoted with Z/γ^*) in
1255 association with jets is also a background to Higgs production. The Z boson decays to two leptons of
1256 the same flavor. When the Z/γ^* decays directly to electrons or muons, the background enters the same
1257 flavor final state. When the Z decays to two τ leptons the background can enter the different flavor final
1258 state as well. Figure 3.5 shows the production of a Z in association with one jet. Because there are no
1259 neutrinos in this final state, variables like E_T^{miss} can be used to reduce the background*.

The E_T^{miss} cut is much more effective for the reduction of Z/γ^ production in the same flavor final state. If the background enters the different flavor final state through τ decays, there will be neutrinos present. Other requirements on the lepton invariant mass are made to reduce the $Z/\gamma^* \rightarrow \tau\tau$ background.

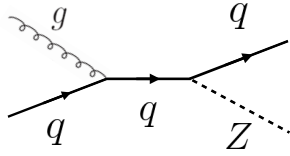


Figure 3.5: An example Feynman diagram of $Z + \text{jets}$ production

1260 3.3.5 SUBDOMINANT BACKGROUNDS

1261 There are additional processes which contribute to the background composition. These backgrounds
 1262 are subdominant and contribute less to the total background estimate than those discussed previously.
 1263 The first process is referred to as VV or “Other diboson” processes and includes multiple Standard
 1264 Model diboson processes, including WZ , ZZ , $W\gamma$, $W\gamma^*$, and $Z\gamma$ production. Additionally, there is
 1265 a background contribution from QCD multijet production. While the cross section for this process is
 1266 large, its contribution to the WW^* final state is small because two jets must be misidentified as leptons.

Category	Process	Description
SM WW	$WW \rightarrow \ell\nu\ell\nu$	Real leptons and neutrinos
Top quark production	$t\bar{t} \rightarrow WbWb \rightarrow \ell\nu b\bar{\nu} b$	Real leptons, untagged b s
	$tW \rightarrow WbW \rightarrow \ell\nu\ell\nu b$ $t\bar{b}, t\bar{q}\bar{b}$	Real leptons, untagged b Untagged b , jet misidentified as lepton
Drell-Yan	$Z/\gamma^* \rightarrow ee, \mu\mu$ $Z/\gamma^* \rightarrow \tau\tau \rightarrow \ell\nu\ell\nu\nu\nu$	“Fake” E_T^{miss} Real leptons and neutrinos
Other dibosons	$ZZ \rightarrow \ell\ell\nu\nu$	Real leptons and neutrinos
	$W\gamma^*, WZ \rightarrow \ell\nu\ell\ell, ZZ \rightarrow \ell\ell\ell\ell$ $W\gamma, Z\gamma$	Unreconstructed leptons γ reconstructed as e , unreconstructed lepton
$W + \text{jets}$	$Wj \rightarrow \ell\nu j$	Jet reconstructed as lepton
QCD multijet	jj	Jets reconstructed as leptons

Table 3.1: A summary of backgrounds to the $H \rightarrow WW^* \rightarrow \ell\nu\ell\nu$ signal

1267 3.4 SHARED SIGNAL REGION SELECTION REQUIREMENTS

1268 As presented in section 3.2, there are many different combinations of physics objects that can define
 1269 a $H \rightarrow WW^* \rightarrow \ell\nu\ell\nu$ final state. The multiplicity of jets and the flavor combinations of the leptons

1270 both lead to many potential signal regions. Additionally, signal regions can be optimized separately to
 1271 be sensitive to the distinct production modes of the Higgs. Gluon fusion, vector boson fusion, and asso-
 1272 ciated production of a Higgs all lead to unique final state topologies. Figure 3.6 delineates the different
 1273 signal regions used in the gluon fusion and vector boson fusion $H \rightarrow WW^*$ analyses. While there are
 1274 different optimizations possible in each signal region, there are also some commonly shared selections
 1275 that will be described here.

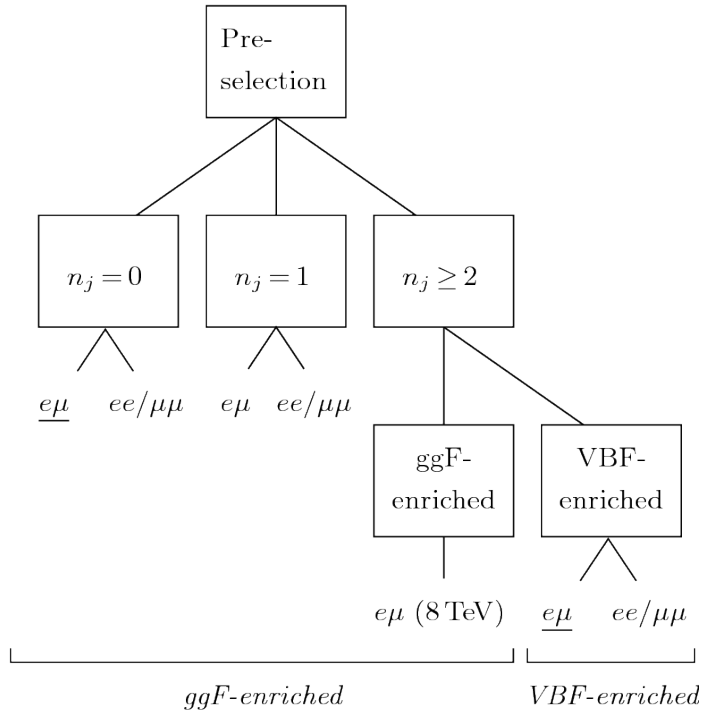


Figure 3.6: An illustration of the unique analysis signal regions [61]. The most sensitive regions for both gluon fusion and vector boson fusion production are underlined.

1276 3.4.1 EVENT PRE-SELECTION

1277 Before being sorted into the distinct signal regions, basic requirements are applied to the recon-
 1278 structed objects in the event to select Higgs-like event candidates. First, two oppositely charged leptons
 1279 are required. Once the leptons are selected, the last requirement for event pre-selection is the presence
 1280 of neutrinos. As neutrinos cannot be detected directly in ATLAS, E_T^{miss} can be used as a proxy for the
 1281 combined neutrino momentum in the transverse plane.

1282 In general, it is expected that the signal should have a harder E_T^{miss} spectrum than backgrounds, espe-
 1283 cially if these backgrounds do not contain neutrinos in the final state. When using E_T^{miss} , it is possible
 1284 mis-measurements of objects in the detector can lead to imbalances in the transverse plane. When such
 1285 a mis-measurement occurs, the E_T^{miss} vector in the transverse plane will often point in the same direc-
 1286 tion as the mis-measured object. Therefore, a new variable, $E_{T,\text{rel}}^{\text{miss}}$, is used in the pre-selection. $E_{T,\text{rel}}^{\text{miss}}$ is
 1287 defined in equation 3.1.

$$E_{T,\text{rel}}^{\text{miss}} = \begin{cases} E_T^{\text{miss}} \sin \Delta\phi_{\text{near}} & \text{if } \Delta\phi_{\text{near}} < \pi/2 \\ E_T^{\text{miss}} & \text{otherwise,} \end{cases} \quad (3.1)$$

1288 If the closest object to the E_T^{miss} vector is within $\pi/2$ radians in the transverse plane, the E_T^{miss} is pro-
 1289 jected away from this object. Otherwise, the normal E_T^{miss} vector is used. Figure 3.7 shows a graphical
 illustration of this concept.

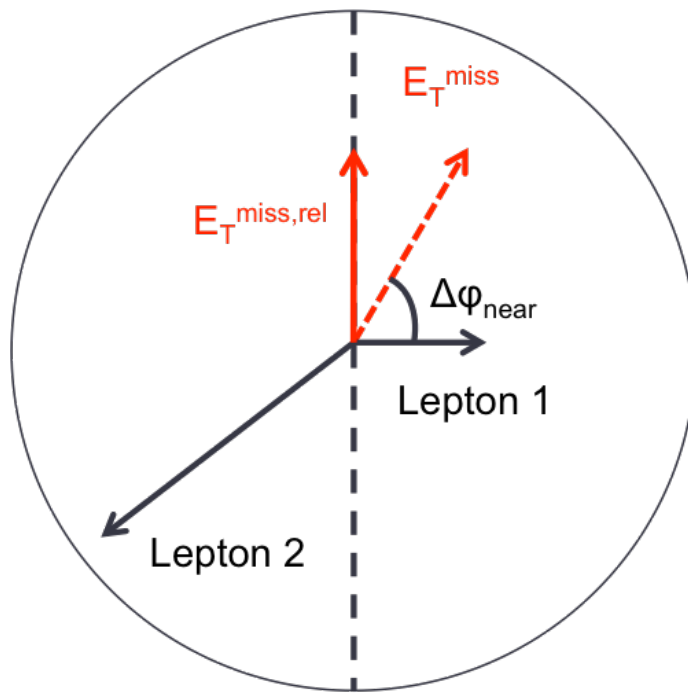


Figure 3.7: A graphical illustration of the $E_{T,\text{rel}}^{\text{miss}}$ calculation

1290
 1291 Once the lepton and E_T^{miss} pre-selections are made, the analysis is divided into different regions ac-
 1292 cording to jet multiplicity.

1293 3.4.2 JET MULTIPLICITY

1294 Jet multiplicity, denoted as n_j , is used to sub-divide the analysis into distinct signal regions. By cre-
1295 ating separate signal regions, each bin in jet multiplicity becomes sensitive to different modes of Higgs
1296 production and different backgrounds.

1297 For example, the $n_j \geq 2$ region is more sensitive to VBF production because of the two high momen-
1298 tum jets produced at matrix element level. For gluon fusion production to enter this bin, two initial state
1299 radiation jets must be emitted.

1300 Figure 3.8 shows the jet multiplicity in both the different flavor and same flavor regions after the pre-
1301 selection. It also shows the background composition in the bins of n_b . A few trends from this distribu-
1302 tion are worth noting. The first is that the Drell-Yan background dominates in the same flavor chan-
1303 nels for $n_j \leq 1$. Second, the top background becomes a clear contributor to the total background for
1304 $n_j \geq 1$. Lastly, the SM WW production dominates in the $n_j = 0$ bin, as it is an irreducible back-
1305 ground to $H \rightarrow WW^*$ production. Because of these distinct features, each jet multiplicity bin is treated
1306 separately.

1307 3.5 BACKGROUND REDUCTION IN SAME-FLAVOR FINAL STATES

1308 As described in section 3.4.2, the background composition of the same flavor final states is different
1309 from that of the different flavor states. In particular, Drell Yan processes play a much larger role because
1310 the Z/γ^* decays to same flavor leptons. Because real neutrinos are absent in the Z/γ^* decays to ee and
1311 $\mu\mu$, a requirement on E_T^{miss} should largely reduce the background. However, as this section will demon-
1312 strate, with increasing pileup conditions the resolution of the calorimeter-based E_T^{miss} degrades greatly.
1313 Therefore, two new variables for Z/γ^* background reduction are constructed and described in this sec-
1314 tion.

1315 3.5.1 PILEUP AND E_T^{miss} RESOLUTION

1316 Secondary interactions of protons in the colliding bunches of the LHC (known as pileup interac-
1317 tions, described in detail in Chapter 2) deposit energy into the ATLAS calorimeter in addition to the

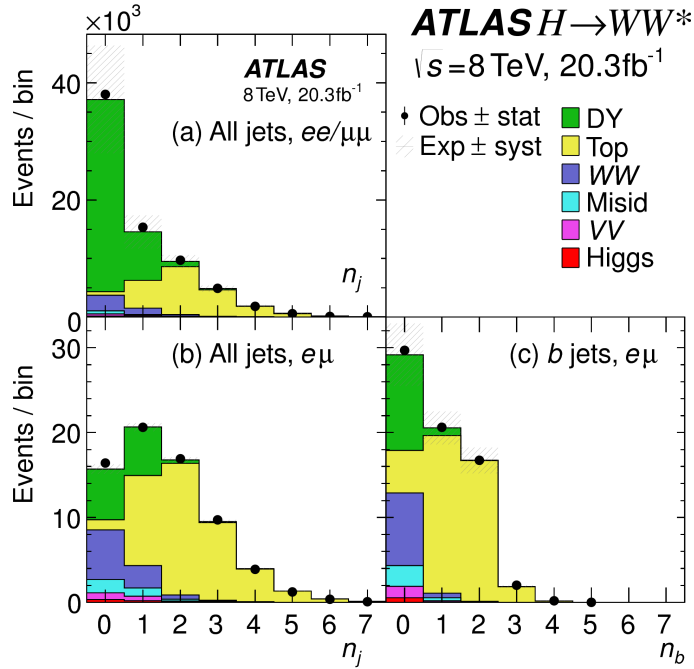


Figure 3.8: Predicted backgrounds (compared with data) as a function of n_j (a and b) and n_b (c) after pre-selection requirements

energy that comes from the hard scatter process of interest. The calculation of E_T^{miss} is fundamentally Poissonian. Summing up all of the energy deposits in individual calorimeter cells or clusters is similar to a counting experiment. The error on a mean of N in a Poisson distribution is \sqrt{N} , so the energy resolution scales as \sqrt{E} . As more energy is deposited in the calorimeter, the E_T^{miss} resolution degrades, meaning that the E_T^{miss} resolution is particularly sensitive to LHC instantaneous luminosity conditions.

Figure 3.9 shows an event display of a $Z/\gamma^* + \text{jets}$ event candidate with the twenty-five reconstructed primary vertices. This display illustrates that while the interaction of interest only has tracks coming from the hardest primary vertex, all of the secondary interactions deposit energy in the calorimeter as well.

Figure 3.10 shows the RMS of the E_T^{miss} distribution in $Z \rightarrow \mu\mu$ events (where there are no real neutrinos) as a function of the number of the average number of interactions. Under 2011 LHC conditions, this RMS was approximately 9 GeV, while under 2012 running conditions the resolution worsened to 12 GeV. The increase in pileup dilutes the E_T^{miss} variable's ability to reduce the Z/γ^* background.

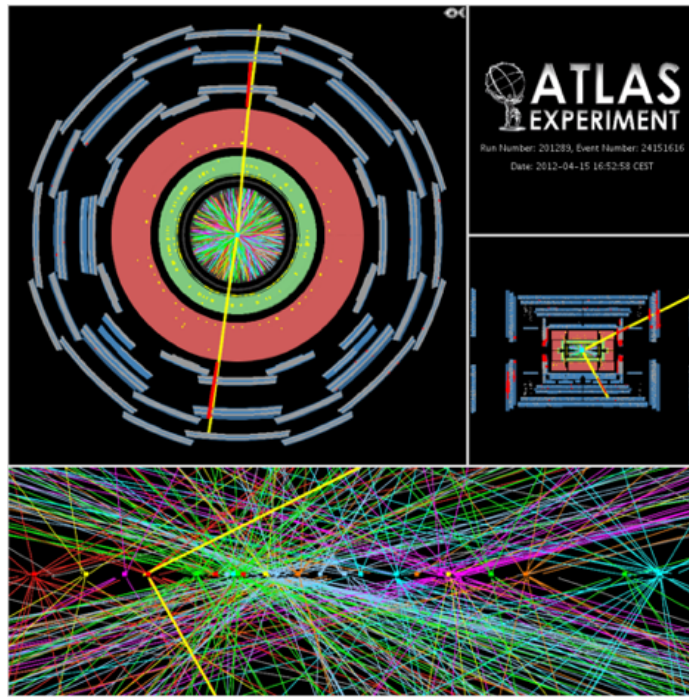


Figure 3.9: An event display of a Z/γ^* + jets event illustrating the effect of pileup interactions

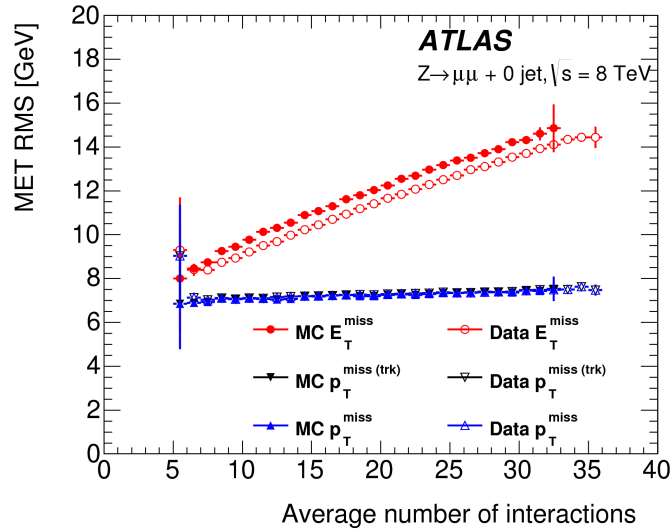


Figure 3.10: The RMS of different missing transverse momentum definitions as a function of the average number of interactions per bunch crossing

1331 3.5.2 TRACK-BASED DEFINITIONS OF MISSING TRANSVERSE MOMENTUM

1332 Because the increasing number of secondary proton-proton interactions degrades calorimeter-based
 1333 E_T^{miss} resolution, a new variable using only contributions from the primary interaction vertex is nec-

1334 essary to further reduce the Z/γ^* background. While it is not possible to associate calorimeter energy
 1335 deposits with a particular vertex, individual charged particle tracks in the Inner Detector are associated to
 1336 unique vertices. Thus, two track-based definitions of missing transverse momentum , using only tracks
 1337 coming from the primary vertex in the event, are used in the analysis. The simplest variable, $p_T^{\text{miss}(\text{trk})}$,
 1338 is the vectorial sum of the p_T of all of the tracks from the primary vertex and the selected leptons (ex-
 1339 cluding the tracks associated with the selected leptons to avoid double counting). Equation 3.2 defines
 1340 $p_T^{\text{miss}(\text{trk})}$.

$$p_T^{\text{miss}(\text{trk})} = - \left(\sum_{\text{selected leptons}} p_T + \sum_{\text{other tracks}} p_T \right), \quad (3.2)$$

1341 To further improve the resolution on the missing transverse momentum, the variable p_T^{miss} is used as
 1342 defined in equation 3.3. For selected leptons and jets, the nominal p_T measurements are used. Tracks
 1343 are used to estimate the soft component of the missing transverse momentum instead of calorimeter
 1344 measurements.

$$p_T^{\text{miss}} = - \left(\sum_{\text{selected leptons}} p_T + \sum_{\text{selected jets}} p_T + \sum_{\text{other tracks}} p_T \right), \quad (3.3)$$

1345 Figure 3.10 illustrates that these two new variables accomplish their intended purpose. The resolution as
 1346 a function of mean number of interactions for both $p_T^{\text{miss}(\text{trk})}$ and p_T^{miss} is much flatter than the depen-
 1347 dence for E_T^{miss} . Figure 3.11a shows the difference between the true and reconstructed values of missing
 1348 transverse momentum using both the track-based p_T^{miss} and calorimeter based E_T^{miss} . The RMS of the
 1349 distribution improves by 3.5 GeV when using p_T^{miss} .

1350 3.5.3 DISTINGUISHING Z/γ^* +JETS AND $H \rightarrow WW^*$ TOPOLOGIES

1351 In addition to measuring missing transverse momentum, another variable can be constructed to ex-
 1352 ploit kinematic and topological differences between the Z/γ^* background and $H \rightarrow WW^*$ signal. Be-
 1353 cause there are no real neutrinos in the final state (in the case of $Z/\gamma^* \rightarrow ee, \mu\mu$ decays), the dilepton
 1354 system will be balanced with the jets produced in the hard scatter. A new variable, f_{recoil} , is constructed
 1355 to estimate the balance between the dilepton system and recoiling jets and is defined in equation 3.4. The
 1356 transverse plane is divided into four sections, or quadrants, with one quadrant centered on the dilepton

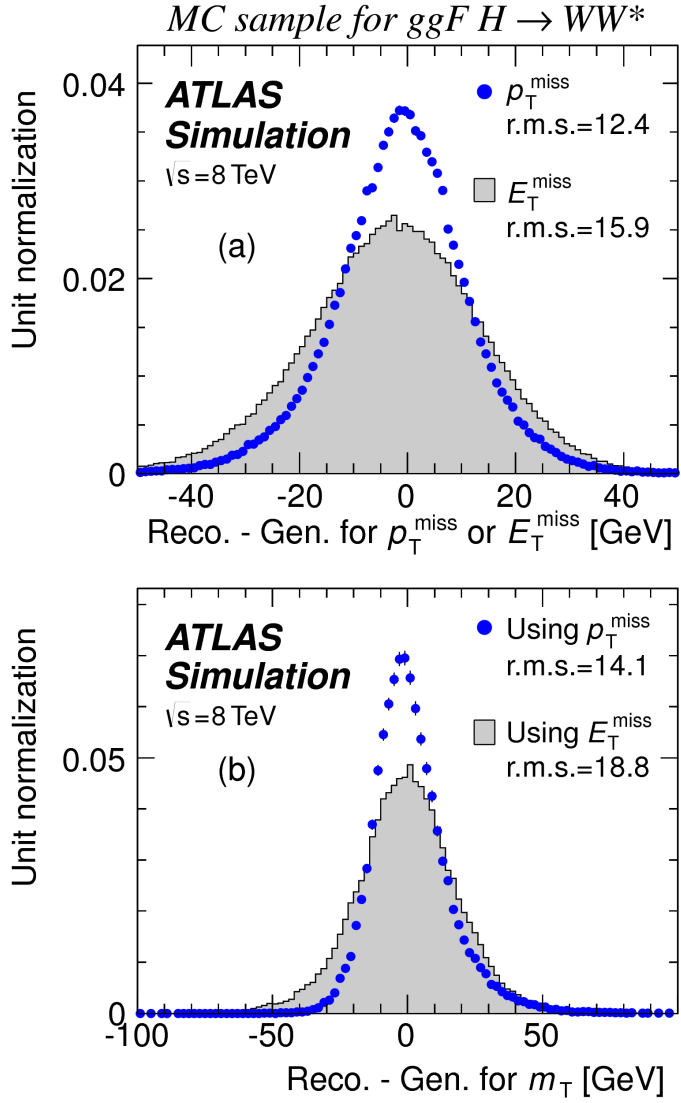


Figure 3.11: The difference between the true and reconstructed values of the missing transverse momentum (a) and m_T (b) in a gluon fusion signal sample

vector. The numerator of f_{recoil} is the magnitude of the vectorial sum of the p_T of jets in the quadrant opposite the dilepton system, weighted by each jet's Jet Vertex Fraction (JVF, described in chapter 2).
 The denominator is the magnitude of the dilepton p_T .

$$f_{\text{recoil}} = \left| \sum_{\text{jets } j \text{ in } \wedge} \text{JVF}_j \cdot \mathbf{p}_T^j \right| / p_T^{\ell\ell}. \quad (3.4)$$

1360 Figure 3.12 shows a shape comparison of the f_{recoil} distribution in a simulated $Z/\gamma^* + \text{jets}$ sample, a
 1361 $H \rightarrow WW^*$ signal sample, and other backgrounds that contain real neutrinos. The $Z/\gamma^* + \text{jets}$ events
 1362 tend to be more balanced between the dilepton system and recoiling jets, while the processes containing
 1363 real neutrinos are less balanced in the transverse plane. Thus, a requirement on f_{recoil} will reduce the
 1364 $Z/\gamma^* + \text{jets}$ background while maintaining a good signal efficiency.

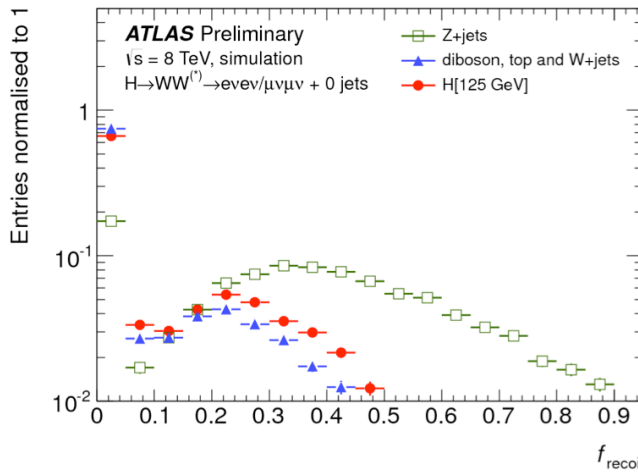


Figure 3.12: Comparison of f_{recoil} distributions for $Z/\gamma^* + \text{jets}$, $H \rightarrow WW^*$, and other backgrounds with real neutrinos.

1365 3.5.4 OPTIMIZING BACKGROUND REDUCTION SELECTION REQUIREMENTS

1366 The requirements on $p_T^{\text{miss}(\text{trk})}$ and f_{recoil} used to reduce the $Z + \text{jets}$ background must be optimized
 1367 to maximize expected signal significance in the same flavor channels. Figure 3.13 shows an optimization
 1368 of the combination of the two requirements in the gluon fusion zero jet bin. Each bin shows the ex-
 1369 pected signal significance if the $p_{T,\text{rel}}^{\text{miss}(\text{trk})}$ is required to be greater than the left edge of the bin and the
 1370 f_{recoil} is required to be less than the top edge of the bin. The figure shows that the best signal signifi-
 1371 cance comes from requiring low values of f_{recoil} (< 0.05) and $p_{T,\text{rel}}^{\text{miss}(\text{trk})}$ values greater than 45 GeV.

1372 3.6 PARAMETERS OF INTEREST AND STATISTICAL TREATMENT

1373 As with any search or measurement, there are particular parameters of the Higgs that the $H \rightarrow WW^*$
 1374 analysis is interested in measuring. In this case, the parameters of interest are the mass of the Higgs bo-

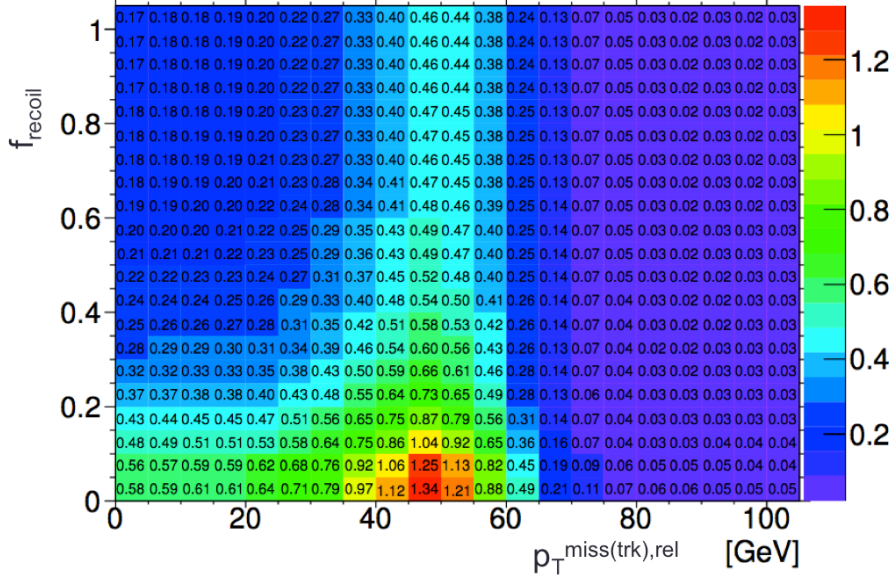


Figure 3.13: Signal significance as a function of required value for f_{recoil} and $p_{T,\text{rel}}^{\text{miss}(\text{trk})}$ in the ggF $H \rightarrow WW^*$ with $n_j = 0$

son and its production cross section. Because the $H \rightarrow WW^* \rightarrow \ell\nu\ell\nu$ process does not have a closed final state, it is not possible to measure the full invariant mass of the particle that may have produced the final state. However, a proxy for the invariant mass is defined using transverse plane information and detailed in section 3.6.1. The second parameter of interest is the ratio of the measured cross section to that expected from the Standard Model Higgs, which is denoted a μ . This is defined in equation 3.5.

$$\mu = \frac{\sigma}{\sigma_{\text{SM}}} \quad (3.5)$$

All of the likelihoods used in the statistical analysis of the final signal region events are parameterized as a function of μ . μ is a natural variable for hypothesis testing, as $\mu = 0$ corresponds to a background only hypothesis and $\mu = 1$ corresponds exactly to a Standard Model Higgs.

3.6.1 TRANSVERSE MASS

The $H \rightarrow WW^* \rightarrow \ell\nu\ell\nu$ analysis cannot reconstruct the full invariant mass of the Higgs because of the neutrinos in the final state. The transverse mass serves as a proxy for the full invariant mass by

1386 exploiting information from the transverse plane. The transverse mass is defined in equation 3.6.

$$m_T = \sqrt{(E_T^{\ell\ell} + p_T^{\text{miss}})^2 - |\vec{p}_T^{\ell\ell} + \vec{p}_T^{\text{miss}}|^2}, \quad (3.6)$$

1387 Here the $E_T^{\ell\ell}$ and $p_T^{\ell\ell}$ are the transverse energy and momentum of the dilepton system, while p_T^{miss} is a
1388 proxy for the transverse momentum of the di-neutrino system. The track-based p_T^{miss} is used in the m_T
1389 rather than the calorimeter based E_T^{miss} because it has a better resolution on the true transverse mass.
1390 Figure 3.11b shows the improvement in the RMS of the difference between the true and reconstructed
1391 transverse mass in a ggF signal sample. The RMS improves by 4.7 GeV using p_T^{miss} in the m_T calcula-
1392 tion.

1393 3.6.2 STATISTICAL TREATMENT[†]

1394 LIKELIHOOD FUNCTION

1395 The statistical analysis of final event candidates is framed as a hypothesis test, where the null hypoth-
1396 esis is background-only (no Standard Model Higgs). The first step in the analysis is to form a likelihood
1397 function for the data. In its simplest form, this likelihood is the probability of observing the number
1398 of events seen in the final signal region given knowledge of the signal strength. Because observation of
1399 events is fundamentally a Poisson counting experiment, this simple likelihood can be expressed as a Pois-
1400 son probability of observing N events given a total number of predicted signal and background events.
1401 This basic likelihood is shown in equation 3.7.

$$\mathcal{L}(\mu) = P(N|\mu S + B) \quad (3.7)$$

1402 Here, P is the Poisson probability density function, N is the total number of observed events, μ is the
1403 signal strength, S is the predicted number of signal events, and B is the predicted number of back-
1404 ground events.

1405 In particle physics, certain background estimates are commonly normalized in so-called “control” re-

[†]Many thanks to Aaron Armbruster, whose thesis [62] inspired parts of this section.

1406 gions and those predictions are scaled by the same normalization factor in the signal region. This leads
1407 to a slightly more complicated likelihood, which is a function of both the signal strength and the back-
1408 ground normalization. This is shown in equation 3.8.

$$\mathcal{L}(\mu, \theta) = P(N|\mu S + \theta B) P(N_{\text{CR}}|\theta B_{\text{CR}}) \quad (3.8)$$

1409 Here, θ serves as a “nuisance parameter”, or a parameter that is not of primary interest but still enters the
1410 likelihood. The second Poisson term enforces that the background normalization be consistent with the
1411 number of observed events in data in the control region, N_{CR} .

1412 So far, these two formulations of likelihoods have assumed a single signal region and do not take into
1413 account any shape information of potential discriminating variables. The $H \rightarrow WW^*$ analysis is di-
1414 vided into many different categories, the counting experiment described above can be performed in each
1415 individual category. As mentioned in section 3.6.1, the transverse mass is used as the primary discriminat-
1416 ing variable in many of the $H \rightarrow WW^*$ sub-analyses. The same counting experiment can be performed
1417 in each bin of the m_T distribution to incorporate some shape information. Thus, the total likelihood
1418 becomes a product over signal regions and bins of the m_T distribution. Finally, there are usually many
1419 backgrounds that are normalized in control regions. The new formulation of the likelihood takes this
1420 into account by including a product over control regions in the second Poisson term. All of these modi-
1421 fications are shown in equation 3.9.

$$\mathcal{L}(\mu, \theta) = \prod_{\substack{\text{SRs } i \\ \text{bins } b}} P\left(N_{ib} \middle| \mu S_{ib} + \sum_{\text{bkg k}} \theta_k B_{kib}\right) \prod_{\text{CRs } l} P\left(N_l \middle| \sum_{\text{bkg k}} \theta_k B_{kl}\right) \quad (3.9)$$

1422 The final step to obtain the full likelihood used in the analysis is to add nuisance parameters for the
1423 systematic uncertainties. In cases where the uncertainty does not affect the shape of m_T bin-by-bin, each
1424 systematic uncertainty ϵ is allowed to affect the expected event yields through a linear response function
1425 of the nuisance parameter, namely $\nu(\theta) = (1 + \epsilon)\theta$. If instead the uncertainty does affect the shape,
1426 the effect is instead parameterized by $\nu_b(\theta) = 1 + \epsilon_b\theta$. The value of the nuisance parameters for the
1427 systematic uncertainty are constrained with a Gaussian term that is added to the likelihood as well. This

1428 is of the form $g(\delta|\theta) = e^{-(\delta-\theta)^2/2}/\sqrt{2\pi}$, where δ is the central value and θ is a nuisance parameter.

1429 Finally, a last term is added to account for the statistical uncertainty in the Monte Carlo samples used,
1430 which adds an additional poisson term. The full likelihood used in the final statistical analysis is defined
1431 in equation 3.10.

$$\begin{aligned} \mathcal{L}(\mu, \boldsymbol{\theta}) = & \prod_{\substack{\text{SRs i} \\ \text{bins b}}} P \left(N_{ib} \left| \mu S_{ib} \cdot \prod_{\substack{\text{sig.} \\ r}} \nu_{br}(\theta_r) + \sum_{\text{bkg k}} \theta_k B_{kib} \cdot \prod_{\substack{\text{bkg.} \\ \text{syst.} \\ s}} \nu_{bs}(\theta_s) \right. \right) \\ & \cdot \prod_{\text{CRs l}} P \left(N_l \left| \sum_{\text{bkg k}} \theta_k B_{kl} \right. \right) \\ & \cdot \prod_{\substack{\text{syst} \\ t}} g(\delta_t|\theta_t) \cdot \prod_{\text{bkg k}} P(\xi_k|\zeta_k \theta_k) \end{aligned} \quad (3.10)$$

1432 The fourth term of the equation quantifies the uncertainty due to finite Monte Carlo sample size.

1433 Here, ξ represents the central value of the background prediction, θ is the associated nuisance parameter,
1434 $\zeta = (B/\delta B)^2$, where δB is the statistical uncertainty of B .

1435 The best fit value of the signal strength μ is determined by finding the values of μ and $\boldsymbol{\theta}$ that maximize
1436 the likelihood, while setting $\delta = 0$ and $\xi = \zeta$. Once the likelihood is defined, a test statistic must
1437 be built for use in hypothesis testing.

1438 TEST STATISTIC

1439 To distinguish whether the data match a background only or background and signal hypothesis, a test
1440 statistic must be used. The $H \rightarrow WW^*$ analysis uses the profile likelihood technique [63]. The first step
1441 in formulating this test statistic is to define the profile likelihood ratio, shown in equation 3.11.

$$\lambda(\mu) = \frac{\mathcal{L}(\mu, \hat{\theta}_\mu)}{\mathcal{L}(\hat{\mu}, \hat{\theta})} \quad (3.11)$$

₁₄₄₂ Here $\hat{\theta}_\mu$ is the value of θ that maximizes the likelihood for the choice of μ being tested. Additionally, $\hat{\theta}$
₁₄₄₃ and $\hat{\mu}$ represent the values of θ and μ that gives the overall maximum value of the likelihood.

₁₄₄₄ Once this is defined, a test statistic q_μ is constructed. This is shown in equation 3.12.

$$q_\mu = -2 \ln \lambda(\mu) \quad (3.12)$$

₁₄₄₅ A higher value of q_μ indicates that the data are more incompatible with the hypothesized value of μ , and
₁₄₄₆ q_0 then corresponds to the value of the test statistic for the background only hypothesis. A p_0 value is
₁₄₄₇ then defined to quantify the compatibility between the data and the null hypothesis. The p_0 value is the
₁₄₄₈ probability of obtaining a value of q_0 larger than the observed value, and this is shown in equation 3.13.

$$p_0 = \int_{q_0^{\text{obs}}}^{\infty} f(q_\mu | \mu = 0) dq_\mu \quad (3.13)$$

₁₄₄₉ Here $f(q_\mu)$ is the probability distribution function of the test statistic. Finally, the p_0 value can be con-
₁₄₅₀ verted into a signal significance, using the formula in equation 3.14, or the one-sided tail of the Gaussian
₁₄₅₁ distribution.

$$Z_0 = \sqrt{2} \operatorname{erf}^{-1}(1 - 2p_0) \quad (3.14)$$

₁₄₅₂ The threshold for discovery used in particle physics is $Z_0 \geq 5$, more commonly known as a value of 5σ .

The real voyage of discovery consists not in seeking new landscapes, but in having new eyes.

Marcel Proust

4

1453

1454

The discovery of the Higgs boson and the role of the $H \rightarrow WW^* \rightarrow \ell\nu\ell\nu$ channel

1455

1456 4.1 INTRODUCTION

1457 This chapter presents the results of the search for the Higgs boson in 4.8 fb^{-1} collected at $\sqrt{s} =$
1458 7 TeV and 5.8 fb^{-1} at $\sqrt{s} = 8 \text{ TeV}$. The results of three searches at $\sqrt{s} = 8 \text{ TeV}$ in the $H \rightarrow$
1459 $WW^* \rightarrow \ell\nu\ell\nu$, $H \rightarrow \gamma\gamma$, and $H \rightarrow ZZ \rightarrow 4\ell$ channels are combined with results of searches at
1460 $\sqrt{s} = 7 \text{ TeV}$ in the same search channels (as well as the $H \rightarrow \tau\tau$ production and associated production
1461 searches for $H \rightarrow b\bar{b}$). The results of this combination are a 5.9σ detection of a new particle consis-
1462 tent with a Higgs boson. Rather than going into detail for all of the different Higgs decay searches, this
1463 chapter will discuss the three most sensitive channels and in particular focus on $H \rightarrow WW^* \rightarrow \ell\nu\ell\nu$
1464 . While the focus is on WW^* , some of the ZZ^* and $\gamma\gamma$ results are shown for completeness. The results

¹⁴⁶⁵ not discussed here can be found in the ATLAS Higgs discovery publication [1].

¹⁴⁶⁶ **4.2 DATA AND SIMULATION SAMPLES**

¹⁴⁶⁷ The data sample used for the following results was taken in 2011 and 2012 at center of mass energies
¹⁴⁶⁸ of 7 and 8 TeV, respectively, with 4.8 fb^{-1} collected at 7 TeV and 5.8 fb^{-1} collected at 8 TeV. Higgs
¹⁴⁶⁹ production in the gluon fusion and vector boson fusion modes is modeled with **POWHEG** for the hard
¹⁴⁷⁰ scattering event and **PYTHIA** for the showing and hadronization. Associated production of a Higgs with
¹⁴⁷¹ a vector boson or top quarks is modeled via **PYTHIA**. Table 4.1 shows the Monte Carlo generators used
¹⁴⁷² for modeling the signal and background processes relevant for the three analyses to be discussed.

Process	Generator
ggF, VBF H	POWHEG + PYTHIA
$WH, ZH, t\bar{t}H$	PYTHIA
$W + \text{jets}, Z/\gamma^* + \text{jets}$	ALPGEN + HERWIG
$t\bar{t}, tW, tb$	MC@NLO + HERWIG
tqb	ACERMC + PYTHIA
$q\bar{q} \rightarrow WW$	MC@NLO + HERWIG
$gg \rightarrow WW$	GG2WW+ HERWIG
$q\bar{q} \rightarrow ZZ$	POWHEG + PYTHIA
$gg \rightarrow ZZ$	GG2ZZ+ HERWIG
WZ	MADGRAPH+ PYTHIA , HERWIG
$W\gamma + \text{jets}$	ALPGEN + HERWIG
$W\gamma^*$	MADGRAPH+ PYTHIA
$q\bar{q}/gg \rightarrow \gamma\gamma$	SHERPA

Table 4.1: Monte carlo generators used to model signal and background for the Higgs search [1].

¹⁴⁷³ **4.3 $H \rightarrow WW \rightarrow e\nu\mu\nu$ SEARCH**

¹⁴⁷⁴ The $H \rightarrow WW \rightarrow e\nu\mu\nu$ search is unique compared to the ZZ and $\gamma\gamma$ channels. The Higgs
¹⁴⁷⁵ mass cannot be fully reconstructed due to the presence of neutrinos in the final state, so the transverse
¹⁴⁷⁶ mass m_T is used as the final discriminating variable. Compared to the other channels, there are more
¹⁴⁷⁷ backgrounds here as well, as discussed in chapter 3. The same flavor final states are excluded from this
¹⁴⁷⁸ search due to high pileup in the 8 TeV dataset.

1479 4.3.I EVENT SELECTION

1480 The analysis requires to opposite charge isolated leptons, with the leading (sub-leading) lepton re-
 1481 quired to have $p_T > 25(15)$ GeV. The events are separated into different signal regions depending on
 1482 which flavor of lepton is leading ($e\mu$ for leading electron, μe for leading muon). Strict lepton quality
 1483 cuts are applied to the sample to reduce backgrounds from fake leptons.

1484 Jets are reconstructed with the anti- k_T algorithm with a radius parameter $R = 0.4$. The jets are
 1485 required to have $p_T > 25$ GeV and $|eta| < 4.5$, with jets in the tracking volume required to have a
 1486 jet vertex fraction of 0.5 and jets in the forward region required to have $p_T > 30$ GeV. The analysis is
 1487 separated into three different signal regions based on jet multiplicity: $n_j = 0, 1, \geq 2$.

1488 To indicate the presence of neutrinos in the event, a requirement of $E_{T,\text{rel}}^{\text{miss}} > 25$ GeV is made*. This
 1489 requirement significantly reduces the QCD multijet and Z/γ^* + jets backgrounds. Figure 4.1 shows the
 1490 distribution of n_j in data and simulation after applying these “pre-selection” requirements.

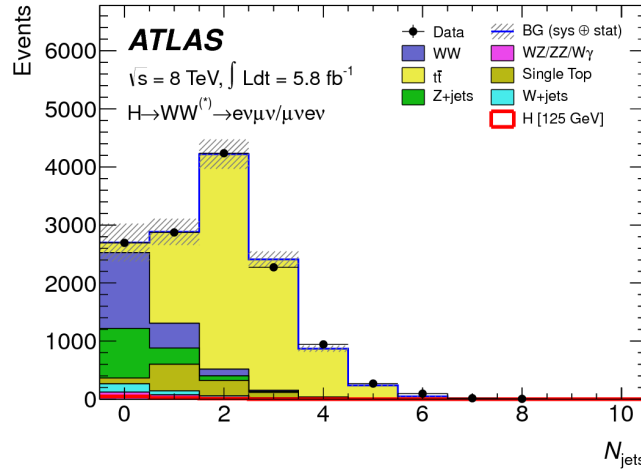


Figure 4.1: Jet multiplicity distribution in data and MC after applying lepton, jet, and $E_{T,\text{rel}}^{\text{miss}}$ selections. The WW and top backgrounds have been normalized using control samples, and the hashed band indicates the total uncertainty on the prediction. [1]

1491 Additional selections are applied to require the dilepton topology to correspond to that of a SM
 1492 Higgs. The requirements are presented here - more detailed discussion on the motivation for each re-
 1493 quirement is saved for Chapter 5. In all of the jet multiplicity channels, the dilepton system is required to

*For the definition of $E_{T,\text{rel}}^{\text{miss}}$, see chapter 3

1494 have a small gap in azimuthal angle, $\Delta\phi_{\ell\ell} < 1.8$. Similarly, the $m_{\ell\ell}$ is required to be less than 50 GeV
1495 in the lower jet multiplicity channels and less than 80 GeV in the $n_j \geq 2$ channel. In the $n_j = 0$ chan-
1496 nel, the magnitude of the dilepton p_T , $p_T^{\ell\ell}$, is required to be greater than 30 GeV.

1497 In the higher jet multiplicity channels ($n_j \geq 1$), the top background is a more important component
1498 and must be reduced. The total transverse momentum p_T^{sum} is thus required to be less than 30 GeV.
1499 Additionally, the di- τ invariant mass $m_{\tau\tau}$ (dilepton mass computed under the assumption that the neu-
1500 trinos from the τ decay are emitted collinear to the charged leptons) is used to reject $Z \rightarrow \tau\tau$ events by
1501 requiring $|m_{\tau\tau} - m_Z| > 25$ GeV. These variables are also discussed in more detail in Chapter 5.

1502 In the $n_j \geq 2$ channel, requirements are made to isolate the VBF contribution to Higgs production.
1503 The kinematics of the two leading jets are used to make these requirements. In particular, the event must
1504 have $\Delta y_{jj} > 3.8$ and $m_{jj} > 500$ GeV, along with a veto on having any additional jets with rapidity
1505 between the two leading jets.

1506 4.3.2 BACKGROUND ESTIMATION

1507 The details of the background estimation techniques used in the $H \rightarrow WW^* \rightarrow \ell\nu\ell\nu$ analysis
1508 are discussed in section 5.5. As that section refers to a later iteration of the analysis, a general discussion
1509 is given here for completeness. The dominant backgrounds are SM WW production and top (both
1510 pair and single) production, and these backgrounds have their normalizations estimated from dedicated
1511 control regions while their shapes are taken from simulation.

1512 The control sample for the Standard Model WW background is defined by making the same require-
1513 ments as the signal region with the $m_{\ell\ell}$ requirement inverted (now requiring $m_{\ell\ell} > 80$ GeV) and
1514 removing the $\Delta\phi_{\ell\ell}$ requirement. This creates a control sample that is 70% (40%) pure in the 0(1)-jet
1515 region. The correction to the pure MC-based background estimate is quantified by defining a normal-
1516 ization factor β which is the ratio of the data yield to the MC yield ($N_{\text{data}}/N_{\text{MC}}$) in this control sample.
1517 Table 4.2 shows the WW normalization factors in the $n_j = 0$ and $n_j = 1$ bins (the $n_j \geq 2$ estimate is
1518 taken directly from MC).

1519 The top background estimate is also computed separately in each jet multiplicity bin. In the $n_j = 0$

n_j	β_{WW}	β_t
= 0	1.06 ± 0.06	1.11 ± 0.06
= 1	0.99 ± 0.15	1.11 ± 0.05
≥ 2	-	1.01 ± 0.26

Table 4.2: Normalization factors (ratio of data and MC yields in a control sample) for the Standard Model WW and top backgrounds in the $H \rightarrow WW^* \rightarrow \ell\nu\ell\nu$ analysis [1]. Only statistical uncertainties are shown.

channel, the background is first normalized using data after pre-selection requirements with no selection on n_j . Then, a dedicated b -tagged control sample is used to evaluate the ratio of one-jet to two-jet events in data. The details of this technique are shown in reference [64]. In the $n_j = 1$ and the $n_j \geq 2$ regions, the top background is normalized in a control sample where the signal region selections are applied, but the b -jet veto is reversed and the Higgs topology requirements on $m_{\ell\ell}$ and $\Delta\phi_{\ell\ell}$ are removed. The resulting normalization factors for these techniques are shown in table 4.2.

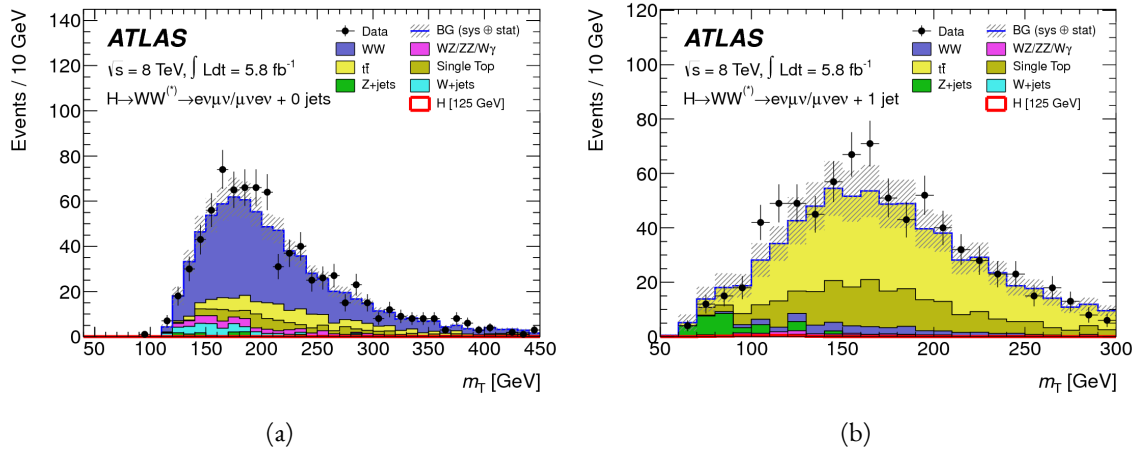


Figure 4.2: Comparison of m_T between data and simulation in the $n_j = 0$ WW (a) and $n_j = 1$ top (b) control samples [1]

The control samples which are used for background normalization can also be used to validate the modeling of the m_T distribution for each background. Figure 4.2 shows the comparison between data and MC for the m_T distribution after correcting the normalization of the backgrounds in the WW and top control regions. Good agreement between data and simulation is seen in both cases.

The $W+jets$ background estimate is taken entirely from data using a control sample with one well reconstructed lepton and one anti-identified lepton. All other backgrounds are taken purely from simu-

1532 lation.

1533 **4.3.3 SYSTEMATIC UNCERTAINTIES**

1534 The systematic uncertainties that have the largest impact on the analysis are the theoretical uncertain-
1535 ties associated with the signal cross section, and these are shared with the $Z Z^*$ and $\gamma\gamma$ channels. The
1536 uncertainties resulting from variations of the QCD scale are $+7\% / -8\%$ on the final singal yield. Those
1537 coming from variations of the parton distribution function (PDF) used in the simulation add a $\pm 8\%$
1538 uncertainty on the yield. The uncertainties on the branching ratios of the Higgs are $\pm 5\%$.

1539 The main experimental uncertainties come from variations of the jet energy scale (JES), jet energy
1540 resolution, pile-up, E_T^{miss} , b -tagging efficiency, $W + \text{jets}$ background estimate, and integrated luminosity.
1541 For more details, see reference [1].

1542 **4.3.4 RESULTS**

1543 Table 4.3 shows the signal and background yields in the final signal region after normalizing the back-
1544 grounds according to the methods described above.

	$n_j = 0$	$n_j = 1$	$n_j \geq 2$
Signal	20 ± 4	5 ± 2	0.34 ± 0.07
WW	101 ± 13	12 ± 5	0.10 ± 0.14
Other dibosons	12 ± 3	1.9 ± 1.1	0.10 ± 0.10
$t\bar{t}$	8 ± 2	6 ± 2	0.15 ± 0.10
Single top	3.4 ± 1.5	3.7 ± 1.6	-
$Z/\gamma^* + \text{jets}$	1.9 ± 1.3	0.10 ± 0.10	-
$W + \text{jets}$	15 ± 7	2 ± 1	-
Total background	142 ± 16	26 ± 6	0.35 ± 0.18
Observed in data	185	38	0

Table 4.3: Data and expected yields for signal and background in the final $H \rightarrow WW^* \rightarrow \ell\nu\ell\nu$ signal region.
Uncertainties shown are both statistical and systematic. [1]

1545 Figure 4.3 shows the m_T distribution in the $n_j \leq 1$ channels for 8 TeV data. (No events are observed
1546 in data in the $n_j \geq 2$ channels in this dataset). The excess shown here relatively flat as a function of
1547 hypothesized Higgs mass. The combined 7 and 8 TeV data gives an excess with local significance of 2.8σ
1548 with an expected significance of 2.3σ , corresponding to a μ measurement of 1.3 ± 0.5 .

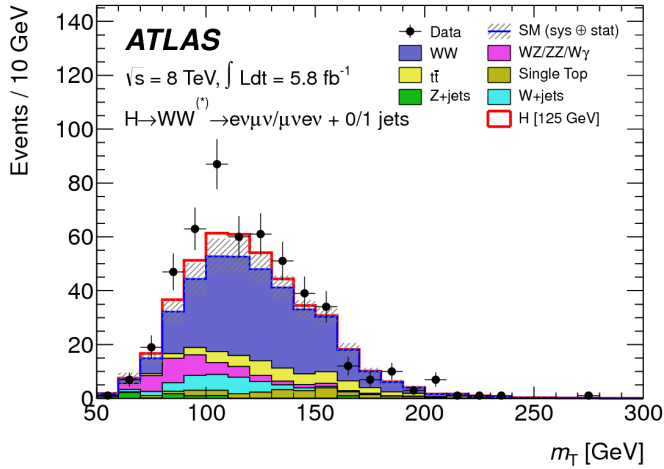


Figure 4.3: m_T distribution in the $H \rightarrow WW \rightarrow e\nu\mu\nu n_j \leq 1$ channels for 8 TeV data [1].

1549 4.4 $H \rightarrow \gamma\gamma$ SEARCH

1550 The $H \rightarrow \gamma\gamma$ search is in essence a search for a peaked excess above the falling SM diphoton mass
 1551 spectrum, with $m_{\gamma\gamma}$ as the ultimate discriminating variable. Events are selected by requiring two isolated
 1552 photons, with the leading (sub-leading) photon required to have $E_T > 40(30)$ GeV. In the 8 TeV
 1553 data, the photons are required to pass cut-based identification criteria consistent with a photon in the
 1554 electromagnetic calorimeter and little leakage in the hadronic calorimeter.

1555 The main challenges for this analysis are accurate mass reconstruction and background estimation.
 1556 In order to accurately reconstruct the invariant mass of the di-photon system, both the energy and di-
 1557 direction of the photons must be measured well. Therefore, the identification of the primary vertex of the
 1558 hard interaction is particularly important, and is done using a multivariate likelihood which combines
 1559 information about the photon direction and vertex position. The background is modeled with a falling
 1560 spectrum in $m_{\gamma\gamma}$ that is parameterized by different functions depending on the category of the event.

1561 4.4.1 RESULTS

1562 The resulting diphoton mass spectrum is shown in figure 4.4. The best fit mass value in the $\gamma\gamma$ chan-
 1563 nel alone in the combined 7 and 8 TeV data is 126.5 GeV. The local significance at this point is 4.5σ ,
 1564 with an expected significance of 2.5σ . Therefore, the measured signal strength μ is 1.8 ± 0.5 in this

1565 channel.

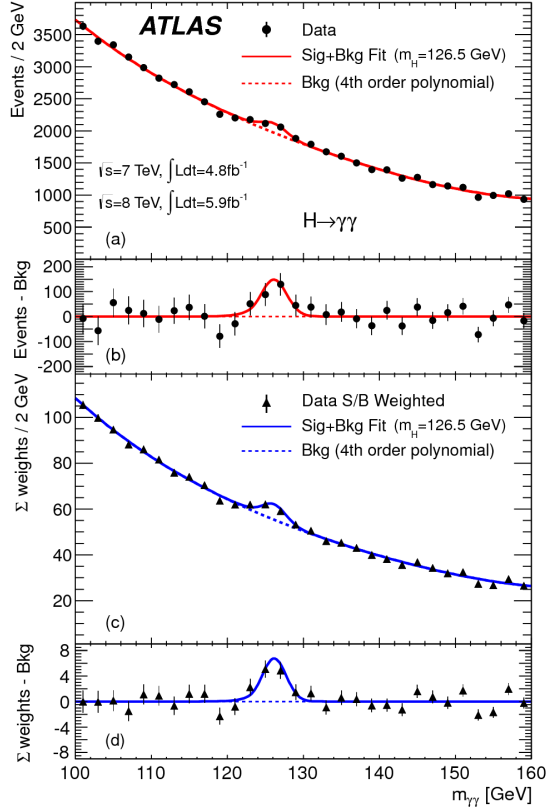


Figure 4.4: Diphoton mass spectrum in 7 and 8 TeV data. Panel a) shows the unweighted data distribution superimposed on the background fit, while panel c) shows the data where each event category is weighted by its signal to background ratio. Panels b) and d) show the respective distributions with background subtracted [1].

1566 4.5 $H \rightarrow ZZ \rightarrow 4\ell$ SEARCH

1567 The $H \rightarrow ZZ \rightarrow 4\ell$ analysis searches for a Standard Model Higgs boson decaying to two Z bosons,
 1568 each of which decays to a pair of same flavor, opposite charge isolated leptons. The ultimate discriminat-
 1569 ing variable is $m_{4\ell}$, or the invariant mass of the four selected leptons. The ℓ denotes an e or μ as with the
 1570 $H \rightarrow WW^* \rightarrow \ell\nu\ell\nu$ analysis.

1571 Four distinct signal regions are constructed depending on the flavors of the final state, additionally
 1572 separated by the flavor of the leading lepton pair. These are referred to as $4e$, $2e2\mu$, $2\mu2e$, 4μ .

1573 The main backgrounds in the $H \rightarrow ZZ \rightarrow 4\ell$ search are continuum ZZ^* production, $Z +$ jets pro-
 1574 duction, and $t\bar{t}$. The $m_{4\ell}$ distribution for background is estimated from simulation. The normalization

of the SM ZZ^* background is also taken from MC simulation, while the $Z + \text{jets}$ and $t\bar{t}$ normalizations are taken from data-driven methods.

4.5.1 RESULTS

Figure 4.5 shows the $m_{4\ell}$ spectrum measured in the 7 and 8 TeV datasets. The total number of events observed in the window between 120 and 130 GeV is 13, with 6 events in the 4μ channel, 2 events in the $4e$ channel, and 5 events in the $2e2\mu/2\mu2e$. The best fit μ value in the combined 7 and 8 TeV data occurs at 125 GeV and is measured to be 1.2 ± 0.6 . The observed significance at this mass is 3.6σ , with an expected significance of 2.7σ .

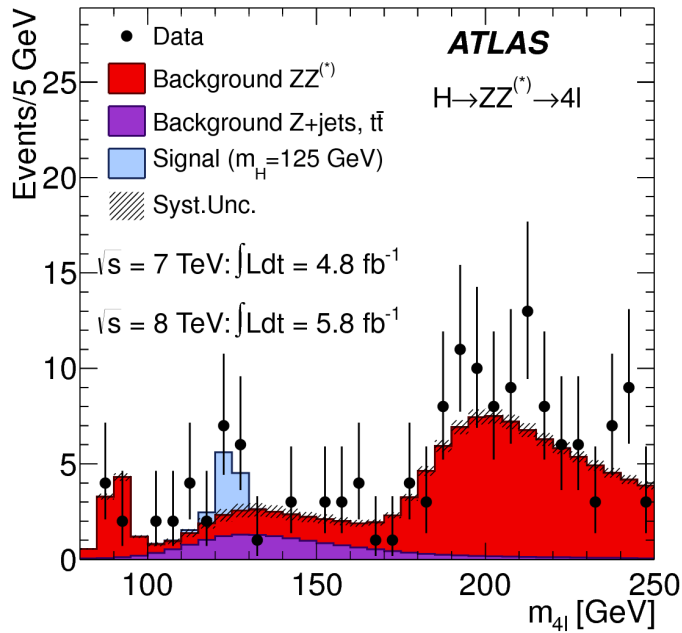


Figure 4.5: Four lepton invariant mass spectrum ($m_{4\ell}$) in 7 and 8 TeV data compared to background estimate. A 125 GeV SM Higgs signal is shown in blue [1].

4.6 COMBINED RESULTS

The statistical interpretation of the combined results is undertaken as described in section 3.6.2, with a hypothesis test based on a likelihood ratio parameterized by the Higgs signal strength μ . The null hypothesis corresponds to $\mu = 0$, while the SM Higgs corresponds to $\mu = 1$.

1587 Table 4.4 summarizes the properties of the individual channels as well as the significances of the ex-
 1588 cesses seen. The most significant observed local excess comes from the $\gamma\gamma$ channel. Figure 4.6 shows a
 1589 comparison of the observed local p_0 values as a function of hypothesized mass for the three different
 1590 search channels. Both the ZZ^* and $\gamma\gamma$ channels have very peaked excesses, while the WW^* excess can
 1591 be seen as very broad because the m_T distribution does not provide detailed information about the true
 1592 Higgs mass.

Channel	Fit var.	Observed Z_l	Expected Z_l	$\hat{\mu}$
$H \rightarrow ZZ^* \rightarrow 4\ell$	$m_{4\ell}$	3.6	2.7	1.2 ± 0.6
$H \rightarrow \gamma\gamma$	$m_{\gamma\gamma}$	4.5	2.5	1.8 ± 0.5
$H \rightarrow WW^* \rightarrow e\nu\mu\nu$	m_T	2.8	2.3	1.3 ± 0.5
Combined	-	6.0	4.9	1.4 ± 0.3

Table 4.4: Summary of the expected and observed significance and measured signal strengths in the combined 7 and 8 TeV datasets for the Higgs discovery analysis [1].

1593 Figure 4.7 shows the combined exclusion limit, p_0 , and signal strength. The highest local excess comes
 1594 at a value of 126.5 GeV and corresponds to a 6.0σ observed excess.

1595 Figure 4.8 shows a comparison of the measured signal strengths between the different Higgs search
 1596 channels. All measured μ are consistent with unity within their uncertainty, and the combined μ mea-
 1597 surement is 1.4 ± 0.3 .

1598 The likelihood can also be computed in a two-dimensional plane of m_H and μ , and this is shown in
 1599 figure 4.9. The figure shows that while the $\gamma\gamma$ and ZZ^* channels have very good mass resolution, the
 1600 excess in WW^* covers a broad mass range. The banana shape of the WW^* result is due to the fact that
 1601 the excess in this channel can either be explained by increasing the signal strength or by changing the
 1602 mass (and thus the cross section). The two parameters are correlated due to the lack of mass sensitivity in
 1603 this channel.

1604 Because multiple Higgs mass points are searched for, the local significance must be corrected for a
 1605 look-elsewhere effect to compute a true global significance. The global significance for finding a Higgs
 1606 anywhere in the mass range of 110 GeV to 600 GeV is 5.1σ . This increases slightly to 5.3σ if only mass
 1607 range from 110 to 150 GeV.

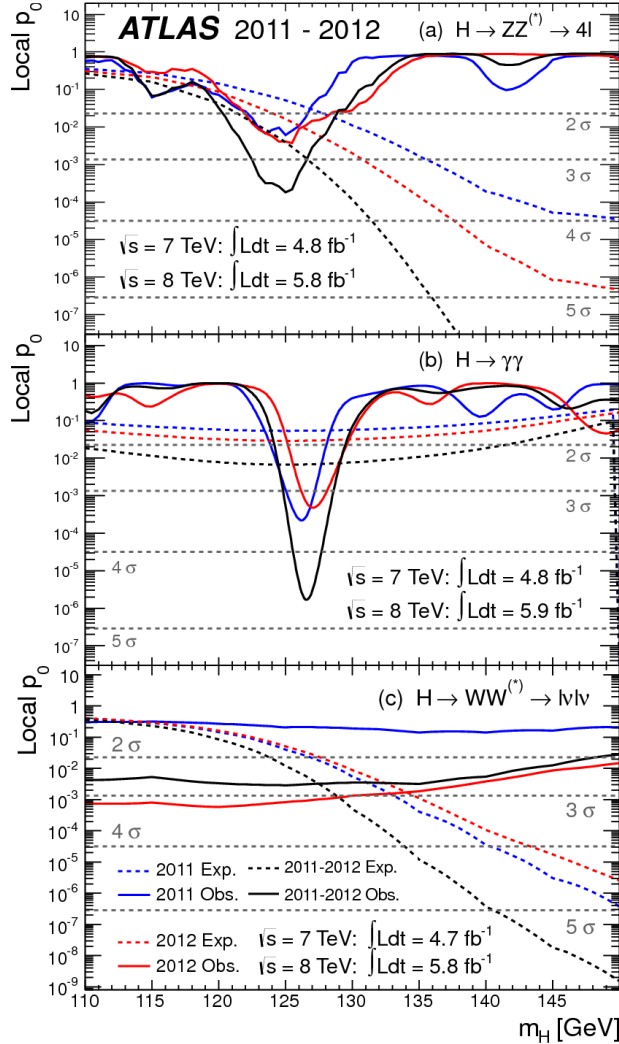


Figure 4.6: Local p_0 distribution as a function of hypothesized Higgs mass for the $H \rightarrow ZZ^* \rightarrow 4\ell$ (a), $H \rightarrow \gamma\gamma$ (b), and $H \rightarrow WW^* \rightarrow \ell\nu\ell\nu$ (c) channels. Dashed curves show expected results, while solid curves show observed. Red curves are from 7 TeV data, blue curves from 8 TeV, and black curved combined [1].

1608 4.7 CONCLUSION

1609 A search for the production of a Standard Model Higgs boson was conducted in 4.8 fb^{-1} collected
 1610 at $\sqrt{s} = 7 \text{ TeV}$ and 5.8 fb^{-1} at $\sqrt{s} = 8 \text{ TeV}$. A new particle consistent with the Higgs boson was
 1611 observed, with a mass of 126.5 GeV and a global (local) significance of $5.1(6.0)\sigma$. This is the first dis-
 1612 covery level observation of a particle consistent with the Higgs.

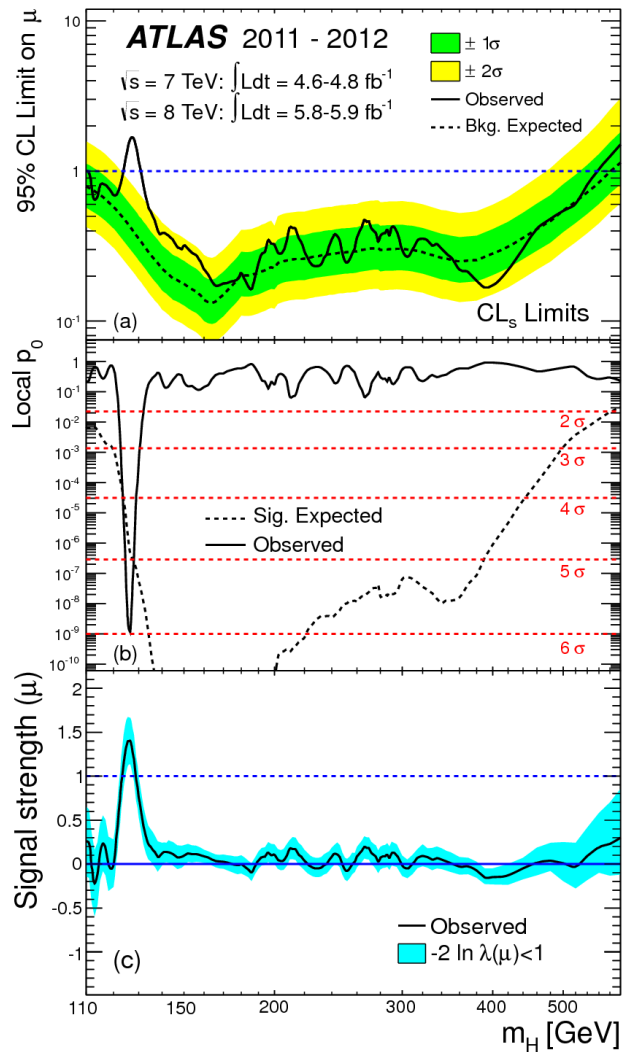


Figure 4.7: Combined 95% CL limits (a), local p_0 values (b), and signal strength measurement (c) as a function of Higgs mass [1].

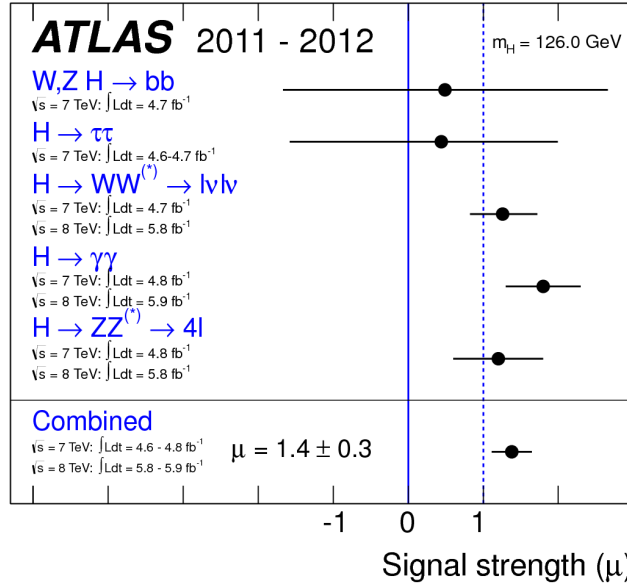


Figure 4.8: Comparison of measured signal strength μ for a 126 GeV Higgs in the 7 and 8 TeV datasets [1].

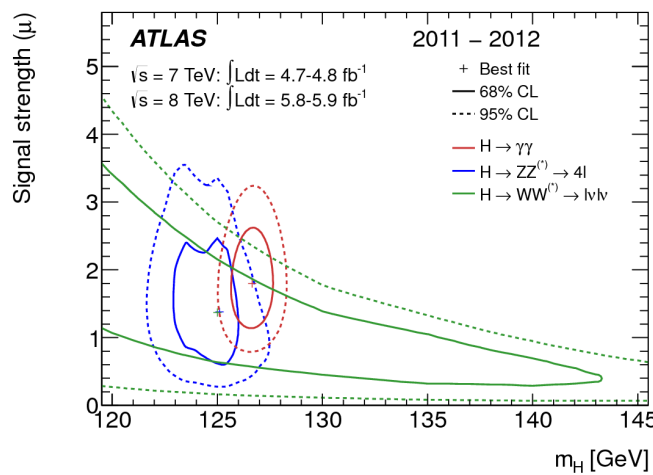


Figure 4.9: Two dimensional likelihood as a function of signal strength μ and Higgs mass m_H [1].

*The imagination of nature is far, far greater than the
imagination of man.*

Richard Feynman

5

1613

1614

Observation of Vector Boson Fusion

1615

production of $H \rightarrow WW^* \rightarrow \ell\nu\ell\nu$

1616 5.1 INTRODUCTION

1617 After the discovery of a particle consistent with the Higgs boson, the $H \rightarrow WW^*$ analysis had two
1618 main goals. The first goal was to increase the sensitivity of the analysis to fully confirm that the $H \rightarrow WW^*$
1619 process did indeed exist. The second goal was to characterize the particle as much as possible, including
1620 searching for the lower cross-section production modes, in order to confirm that it was indeed a Higgs
1621 boson. This chapter presents a dedicated search for Vector Boson Fusion (VBF) production of a Higgs
1622 boson decaying via the $H \rightarrow WW^* \rightarrow \ell\nu\ell\nu$ mode. First, basics of the topology of VBF production
1623 are presented. Then, the details of the analysis are shown, including signal region definition, background
1624 estimation techniques, and systematic uncertainties. Finally, the results of the analysis are presented. As

1625 will be shown, this analysis is the first and most sensitive observation of the VBF production mode of the
1626 Higgs on ATLAS.

1627 In the VBF channel, there are both a selection requirement based signal region analysis (known as the
1628 “cut-based”) and a multivariate analysis which uses a boosted decision tree (known as the BDT analysis).
1629 The focus of this chapter will be on the cut-based signal region, as this is an important component of the
1630 VBF analysis and in particular acts as strong validation for the final BDT result. Connections between
1631 the cut-based and BDT analyses will be discussed where appropriate.

1632 5.2 DATA AND SIMULATION SAMPLES

1633 The results presented here are with 20.3 fb^{-1} taken at $\sqrt{s} = 8 \text{ TeV}$ and 4.5 fb^{-1} taken at $\sqrt{s} =$
1634 7 TeV. The details of the LHC and detector conditions during this period are given in Chapter 2. The
1635 trigger selection defining the dataset is discussed in section 5.2.1. The simulation samples used for signal
1636 and background modeling are given in section 5.2.2.

1637 5.2.1 TRIGGERS

1638 The analysis uses a combination of single lepton and dilepton triggers to allow lowering of the p_T
1639 thresholds and increased signal acceptance. The p_T threshold on the leptons is a particularly important
1640 consideration for this signal. Because the second W produced in the decay can be off-shell, it tends to
1641 produce lower momentum leptons. Thus, being able to lower the p_T threshold while still maintaining
1642 a low background rate is critical. Figure 5.1 shows an example of the subleading lepton p_T for a VBF
1643 $H \rightarrow WW^*$ signal compared to the corresponding $t\bar{t}$ background. Note that the lepton p_T spectrum is
1644 considerably softer in the signal sample.

1645 As discussed in Chapter 2, there are multiple levels in the ATLAS trigger system, and there are differ-
1646 ent p_T thresholds imposed for the leptons at each level. Additionally, some triggers have a loose selection
1647 on the isolation of the lepton (looser than that applied offline in the analysis object selection). Table 5.1
1648 shows the thresholds used for single lepton triggers, while table 5.2 shows the thresholds coming from
1649 di-lepton triggers. The single lepton trigger efficiency for muons that pass the analysis object selection is

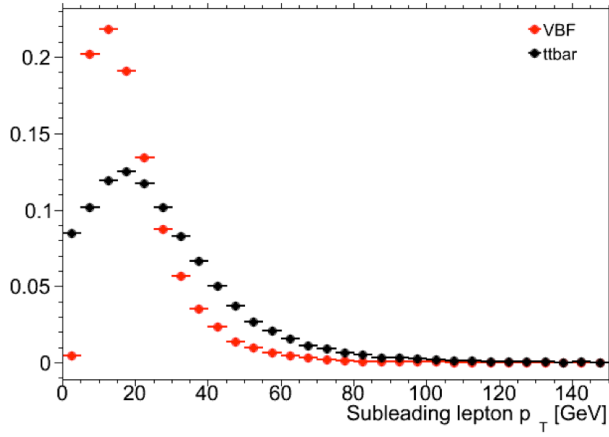


Figure 5.1: A comparison of the subleading lepton p_T spectrum between VBF $H \rightarrow WW^*$ production and $t\bar{t}$ background

1650 70% for muons in the barrel region ($|\eta| < 1.05$) and 90% in the endcap region. The electron trigger efficiency
 1651 increases with electron p_T but the average is approximately 90%. These efficiencies are measured
 1652 by combined performance and trigger signature groups [65, 66].

	Level-1 threshold	High-level threshold
Electron	18	$24i$
	30	60
Muon	15	$24i$
		36

Table 5.1: Single lepton triggers used for electrons and muons. A logical “or” of the triggers listed for each lepton type is taken. Units are in GeV, and the i denotes an isolation requirement in the trigger.

	Level-1 threshold	High-level threshold
ee	10 and 10	12 and 12
$\mu\mu$	15	18 and 8
$e\mu$	10 and 6	12 and 8

Table 5.2: Di-lepton triggers used for different flavor combinations. The two thresholds listed refer to leading and sub-leading leptons, respectively. The di-muon trigger only requires a single lepton at level-1.

1653 The combination of all triggers shown gives good efficiency for signal events. This efficiency is summarized
 1654 in table 5.3. The relative improvement in efficiency by adding the dilepton triggers is also shown

1655 in the same table. The largest gain comes in the $\mu\mu$ channel. Overall the trigger selection shows a good
 1656 efficiency for $H \rightarrow WW^*$ signal events.

Channel	Trigger efficiency	Gain from 2ℓ trigger
ee	97%	9.1%
$\mu\mu$	89%	18.5%
$e\mu$	95%	8.3%
μe	81%	8.2%

Table 5.3: Trigger efficiency for signal events and relative gain of adding a dilepton trigger on top of the single lepton trigger selection. The first lepton is the leading, while the second is the sub-leading. Efficiencies shown here are for the ggF signal in the $n_j = 0$ category but are comparable for the VBF signal.

1657 5.2.2 MONTE CARLO SAMPLES

1658 Modeling of signal and background processes in the signal region, in particular for the m_T distribu-
 1659 tion, is an important consideration for the final interpretation of the analysis. Therefore, careful consid-
 1660 eration must be paid to which Monte Carlo (MC) generators are used for specific processes. With the
 1661 exception of the $W + \text{jet}$ and multijet backgrounds, the m_T shape used as the final discriminant is taken
 1662 from simulation. (Many backgrounds are normalized from data, as described in section 5.5).

1663 Table 5.4 shows the MC generators used for the signal and background processes, as well as their cross
 1664 sections. In order to include corrections up to next-to-leading order (NLO) in the QCD coupling con-
 1665 stant α_s , the POWHEG [67] generator is often used. In some cases, only leading order generators like
 1666 ACERMC [68] and GG2VV [69] are available for the process in question. If the process requires good
 1667 modeling for very high parton multiplicities, the SHERPA [70] and ALPGEN [71] generators are used
 1668 to provide merged calculations for five or fewer additional partons. These matrix element level calcula-
 1669 tions must then be additionally matched to models of the underlying event, hadronization, and parton
 1670 shower. There are four possible generators for this: SHERPA , PYTHIA 6 [72], PYTHIA 8 [73], or HERWIG
 1671 [74] + JIMMY [75]. The simulation additionally requires an input parton distribution function (PDF).
 1672 The CT10 [76] PDFs are used for SHERPA and POWHEG simulated samples, while CTEQ6L1 [77] is used
 1673 for ALPGEN +HERWIG and ACERMC simulations. The Drell-Yan samples are reweighted to the MRST
 1674 [78] PDFs, as these are found to give the best agreement between data and simulation.

Process	MC generator	$\sigma \cdot \mathcal{B}$ (pb)
Signal		
ggF $H \rightarrow WW^*$	POWHEG +PYTHIA 8	0.435
VBF $H \rightarrow WW^*$	POWHEG +PYTHIA 8	0.0356
VH $H \rightarrow WW^*$	PYTHIA 8	0.0253
WW		
$q\bar{q} \rightarrow WW$ and $qg \rightarrow WW$	POWHEG +PYTHIA 6	5.68
$gg \rightarrow WW$	GG2VV +HERWIG	0.196
$(q\bar{q} \rightarrow W) + (q\bar{q} \rightarrow W)$	PYTHIA 8	0.480
$q\bar{q} \rightarrow WW$	SHERPA	5.68
VBS $WW + 2$ jets	SHERPA	0.0397
Top quarks		
$t\bar{t}$	POWHEG +PYTHIA 6	26.6
Wt	POWHEG +PYTHIA 6	2.35
$t\bar{q}\bar{b}$	ACERMC +PYTHIA 6	28.4
$t\bar{b}$	POWHEG +PYTHIA 6	1.82
Other dibosons (VV)		
$W\gamma$ ($p_T^\gamma > 8$ GeV)	ALPGEN +HERWIG	369
$W\gamma^*$ ($m_{\ell\ell} \leq 7$ GeV)	SHERPA	12.2
WZ ($m_{\ell\ell} > 7$ GeV)	POWHEG +PYTHIA 8	12.7
VBS $WZ + 2$ jets	SHERPA	0.0126
($m_{\ell\ell} > 7$ GeV)		
$Z\gamma$ ($p_T^\gamma > 8$ GeV)	SHERPA	163
$Z\gamma^*$ (min. $m_{\ell\ell} \leq 4$ GeV)	SHERPA	7.31
ZZ ($m_{\ell\ell} > 4$ GeV)	POWHEG +PYTHIA 8	0.733
$ZZ \rightarrow \ell\ell\nu\nu$ ($m_{\ell\ell} > 4$ GeV)	POWHEG +PYTHIA 8	0.504
Drell-Yan		
Z ($m_{\ell\ell} > 10$ GeV)	ALPGEN +HERWIG	16500
VBF $Z + 2$ jets	SHERPA	5.36
($m_{\ell\ell} > 7$ GeV)		

Table 5.4: Monte Carlo samples used to model the signal and background processes [61].

Once the basic hard scattering process is simulated, it must be passed through a detector simulation and additional pile-up events must be overlaid. The pile-up events are modeled with PYTHIA 8, and the ATLAS detector is simulated with GEANT4 [79]. Because of the unique phase space of the $H \rightarrow WW^*$

1678 analysis, events are sometimes filtered at generator level to allow for more efficient generation of relevant
1679 events. The efficiency of the trigger in MC simulation does not always match the measured efficiency in
1680 data, so trigger scale factors are applied to correct the MC efficiency to the data. These are derived by the
1681 combined performance groups [65, 66].

1682 5.3 OBJECT SELECTION

1683 In order to define the signal region, the analysis must first select the objects to be considered. The
1684 details of the object reconstruction algorithms are discussed in Chapter 2, while this section gives specific
1685 selection cuts used in the $H \rightarrow WW^*$ analysis.

1686 The first step in this process is to select a primary vertex candidates. The event's primary vertex is the
1687 vertex with the largest sum of p_T^2 for associated tracks and is required to have at least three tracks with
1688 $p_T > 450$ MeV. Many of the object selection cuts are then made relative to this chosen primary vertex.

1689 5.3.1 MUONS

1690 The analysis uses combined muon candidates, where a track in the Inner Detector has been matched
1691 to a standalone track in the Muon Spectrometer. The track parameters are combined statistically in the
1692 muon reconstruction algorithm [52]. The muons are required to be within $|\eta| < 2.5$ and have a $p_T >$
1693 10 GeV. To reduce backgrounds coming from mis-reconstructed leptons, there are requirements on
1694 the impact parameter of the muon relative to the primary vertex. The transverse impact parameter d_0
1695 is required to be small relative to its estimated uncertainty, the exact cut value being $d_0/\sigma_{d_0} < 3$. The
1696 longitudinal impact parameter z_0 must satisfy $|z_0 \sin \theta| < 1$ mm.

1697 As discussed previously, the muons must also be isolated. There are two types of lepton isolations
1698 that are calculated: track-based and calorimeter-based. For muons, the track-based isolation is defined
1699 using the scalar sum $\sum p_T$ for tracks with $p_T > 1$ GeV (excluding the muon's track) within a cone of
1700 $\Delta R = 0.3$ (0.4) for muon with $p_T > 15$ GeV ($10 < p_T < 15$ GeV). The final isolation requirement
1701 is made my requiring that this scalar sum be no more than a certain fraction of the muon's p_T . This re-
1702 quirement varies with muon p_T and the exact cuts are defined in table 5.5.

1703 The calorimeter-based muon isolation is defined using as a $\sum E_T$ calculated from calorimeter cells
 1704 using the same cone size as the track-based isolation but excluding cells with $\Delta R < 0.05$ around the
 1705 muon. This requirement is also defined as a cut on the ratio of the sum to the muon p_T and varies with
 1706 muon p_T . The cut values are also given in table 5.5.

1707 The isolation requirements loosen as a function of p_T to allow for larger signal acceptance. At low p_T ,
 1708 the isolation is tightened to reduce the $W + \text{jets}$ background which arises from a misidentified lepton.

p_T range (GeV)	Calorimeter isolation	Track isolation
10 – 15	0.06	0.06
15 – 20	0.12	0.08
20 – 25	0.18	0.12
> 25	0.30	0.12

Table 5.5: p_T dependent isolation requirements for muons. Muons are required to have the amount of calorimeter or track based cone sums be less than this fraction of their p_T .

1709 5.3.2 ELECTRONS

1710 Electrons are identified by matching reconstructed clusters in the electromagnetic calorimeter with
 1711 tracks in the inner detector. The electrons are identified using a likelihood based method [49, 50] which
 1712 takes into account the shower shapes in the calorimeter, the matching of tracks to clusters, and the
 1713 amount of transition radiation in the TRT. The electrons are required to have $|\eta| < 2.47$, and can-
 1714 didates in the transition region between the barrel and endcap ($1.37 < |\eta| < 1.52$) are excluded. As
 1715 the muons, the electrons are required to have transverse impact parameter significance < 3 , while in the
 1716 longitudinal direction they must have $|z_0 \sin \theta| < 0.4$ mm. Some electron requirements also vary with
 1717 electron E_T , and these requirements are summarized in table 5.6.

1718 The isolation for electrons are defined similarly to the muons but with unique cuts on the objects in-
 1719 cluded. The track-based isolation is defined using tracks with $p_T > 400$ MeV with cone sizes as defined
 1720 previously. The calorimeter-based isolation also uses the same cone size as the muon, but here the cells
 1721 within a 0.125×0.175 area in $\eta \times \phi$ around the electron cluster's barycenter are excluded. The other
 1722 difference with respect to muons is that the denominator of the isolation ratio is the electron's E_T rather
 1723 than p_T . The isolation cuts very with electron E_T and are defined in table 5.6.

1724 The electron is also required to not be consistent with a vertex coming from a photon conversion.

p_T range (GeV)	Quality cut	Calorimeter isolation	Track isolation
10 – 15	Very tight LH	0.20	0.06
15 – 20	Very tight LH	0.24	0.08
20 – 25	Very tight LH	0.28	0.10
> 25	Medium	0.28	0.10

Table 5.6: p_T dependent requirements for electrons. Electrons are required to have the amount of calorimeter or track based cone sums be less than this fraction of their E_T .

1725 5.3.3 JETS

1726 Jets are clustered with the anti- k_T reconstruction algorithm using a radius parameter of $R = 0.4$.

1727 They are required to have a jet vertex fraction (JVF) of at least 50%, meaning that half of the tracks asso-
1728 ciated with the jet originated from the primary vertex. Jets with no tracks associated (i.e. those outside
1729 the acceptance of the ID) do not have this requirement applied. Jets are required to have $p_T > 25$ GeV
1730 if they are within the tracking acceptance ($|\eta| < 2.4$). Jets with $2.4 < |\eta| < 4.5$ are required to have
1731 $p_T > 30$ GeV. This tighter requirement reduces jets from pileup in the region where JVF requirements
1732 cannot be applied. The two highest p_T jets in the event are referred to as the “VBF” jets and used to com-
1733 pute various analysis selections later.

1734 Identification of b -jets is done using the MV1 algorithm and is limited to the acceptance of the ID
1735 ($|\eta| < 2.5$). The operating point of MV1 that is used is the one that is 85% efficient for identifying true
1736 b -jets. This operating point has a 10.3% of mis-tagging a light quark jet as a b -jet. In order to improve
1737 the rejection of b -jets, a lower threshold than the nominal p_T threshold described above is used. For the
1738 purposes of counting the number of b -jets, jets with p_T down to 20 GeV are used.

1739 5.3.4 OVERLAP REMOVAL

1740 There are some cases where certain reconstructed objects will overlap and one will have to be chosen
1741 (for example, an electron and a jet in the calorimeter). First, the case of lepton overlap is dealt with. If
1742 an electron candidate extends into the muon spectrometer, it is removed. If a muon or electron have a
1743 $\Delta R < 0.1$, the electron is removed and the muon is kept. If two electron candidates overlap within

1744 the same radius, then the higher E_T electron is kept. Next, the overlap between leptons and jets is con-
1745 sidered. If an electron and jet are within $\Delta R < 0.3$ of one another, the electron is kept and the jet is
1746 removed. However, if a muon and jet overlap within $\Delta R < 0.3$, the jet is kept (as it is likely that the
1747 muon is the result of a semileptonic decay inside the jet).

1748 Once the overlap removal is complete, the final set of objects used in the analysis is defined.

1749 5.4 ANALYSIS SELECTION

1750 The VBF analysis uses two distinct selections. The first is a more standard selection, referred to as
1751 “cut-based”, that applies requirements on the VBF variables and uses m_T as the final discriminating
1752 variable. The second is a looser selection that uses a Boosted Decision Tree (BDT) score as the final dis-
1753 criminator in order to take advantage of the detailed correlations between the VBF variables. While the
1754 BDT analysis is ultimately more sensitive, the cut-based serves as an important component of the analy-
1755 sis. First, the cut-based allows for confirming the modeling and validity of many variables used as input
1756 to the BDT. Second, because this is the first use of such an MVA technique in the $H \rightarrow WW^*$ analysis,
1757 the cut-based selection allows confirmation of the final BDT result with a more traditional analysis. The
1758 cut-based techniques are the focus of this chapter, but connections to the BDT result will be illustrated
1759 when appropriate.

1760 One important note is that because this analysis is dedicated to the measurement of the VBF pro-
1761 duction mode of the Higgs, events coming from gluon fusion production with the Higgs decaying via
1762 $H \rightarrow WW^* \rightarrow \ell\nu\ell\nu$ are treated as background events. This will be seen throughout the various
1763 predictions shown.

1764 5.4.1 COMMON PRE-SELECTION

1765 Both the cut-based and BDT analyses have a common pre-selection that is applied before the main
1766 signal region requirements. The requirements on leptons are common to all n_j bins. The analysis re-
1767 quires two oppositely charged leptons, with the leading lepton required to have $p_T > 22$ GeV while the
1768 subleading lepton must have $p_T > 10$ GeV. Next, to remove low mass Z/γ^* events, a cut on the dilep-

1769 ton mass $m_{\ell\ell} > 10$ (12) GeV is applied in the different (same) flavor channel. In the same flavor chan-
1770 nels, there is an additional veto placed on the region around the Z peak, requiring that $|m_{\ell\ell} - m_Z| > 15$
1771 GeV.

1772 There are also requirements on the amount of missing transverse momentum in the event. These
1773 are only applied in the same flavor channels, as in the different flavor channels $t\bar{t}$ is the dominant back-
1774 ground in $n_j \geq 2$. The BDT analysis requires $p_T^{\text{miss}} > 40$ GeV and $E_T^{\text{miss}} > 45$ GeV. The cut-
1775 based analysis must select more tightly on these variables to have maximal sensitivity and thus requires
1776 $p_T^{\text{miss}} > 50$ GeV and $E_T^{\text{miss}} > 55$ GeV.

1777 Finally, because this analysis is focused on VBF, a requirement on the jet multiplicity is placed, with
1778 $n_j \geq 2$. Additionally, the analysis requires that there are no jets identified as b-quarks in the event, or
1779 $n_b = 0$.

1780 5.4.2 CUT-BASED SELECTION

1781 The cut-based selection places sequential requirements on variables reconstructed from the VBF jets
1782 in order to increase the signal to background ratio.

1783 GENERAL BACKGROUND REDUCTION

1784 Top pair production is the primary background in the $n_j \geq 2$ bin. Even though $n_b = 0$ is required,
1785 an additional variable is constructed to further suppress the top background. There is often additional
1786 QCD radiation that accompanies the $t\bar{t}$ system when it is produced. Therefore, a variable which tests for
1787 the presence of this additional radiation, p_T^{sum} , is constructed. It is defined in equation 5.1.

$$p_T^{\text{sum}} = p_T^{\ell\ell} + p_T^{\text{miss}} + \sum p_T^j \quad (5.1)$$

1788 The first cut after pre-selection in the cut-based analysis requires $p_T^{\text{sum}} < 15$ GeV to further suppress $t\bar{t}$
1789 production.

1790 In the different flavor channels, a cut is made to reduce the contamination from $Z \rightarrow \tau\tau$ decays.
1791 The di- τ invariant mass, $m_{\tau\tau}$, is constructed by assuming that the neutrinos from the τ decays were

1792 collinear with the leptons [80]. The analysis requires that this mass not be consistent with a Z by requiring $m_{\tau\tau} < m_Z - 25$ GeV.
1793

1794 VBF TOPOLOGICAL CUTS

1795 The characteristic feature of VBF production of the Higgs is the presence of two additional forward
1796 jets coming from the incoming partons which radiate the vector bosons that make the Higgs. These
1797 jets are forward because the outgoing partons still carry the longitudinal momentum of the incoming
1798 partons. Figure 5.2 shows the distribution of the η for the leading jet in a VBF event compared to a back-
1799 ground top pair production event. As can be seen, the VBF jets tend to be more forward in η , while the
1800 $t\bar{t}$ jets are more central.

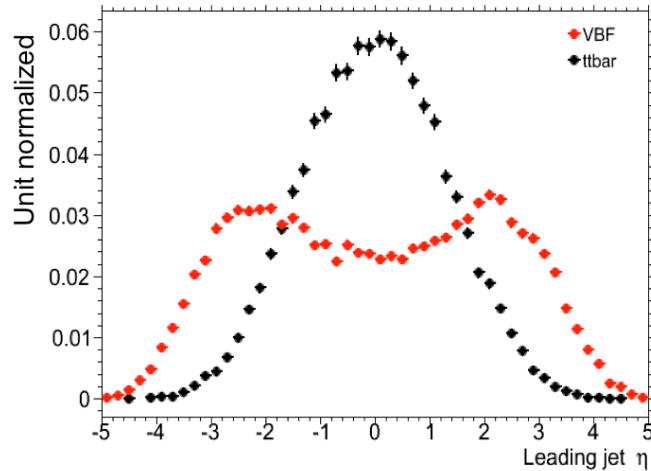


Figure 5.2: Leading jet η in VBF $H \rightarrow WW^*$ (red) and $t\bar{t}$ (black)

1801 Because the cross section for VBF production is an order of magnitude smaller than gluon fusion pro-
1802 duction, these forward jets must be used in order to better reduce background and achieve a good signal
1803 to background ratio. The dedicated VBF search selection requirements are constructed to maximally
1804 exploit the features of the unique VBF topology.

1805 Requirements on the VBF jets are collectively referred to as the “VBF topological cuts”. First, a re-
1806 quirement on the dijet invariant mass of the VBF jets, m_{jj} , is placed, requiring $m_{jj} > 600$ GeV. Next,

1807 the event is required to have a large gap in rapidity between the two VBF jets, or $\Delta y_{jj} > 3.6$. Both
 1808 of these cuts put tight requirements on the presence of two forward, high p_T jets moving in opposite
 1809 directions in the longitudinal plane.

1810 Beyond requiring the presence of the two forward VBF jets, the analysis also vetoes on the presence
 1811 of any additional jets that fall between the two VBF jets. This cut is referred to as the central jet veto, or
 1812 CJV. Any events with a third jet with $p_T > 20$ GeV whose rapidity is between the region defined by the
 1813 two VBF jets are vetoed. This can be expressed in terms of a variable called the jet centrality, defined in
 1814 equation 5.2.

$$C_{j3} = \left| \eta_{j3} - \frac{\eta_{j1} + \eta_{j2}}{2} \right| / \frac{|\eta_{j1} - \eta_{j2}|}{2}, \quad (5.2)$$

1815 Here, η_{j1} and η_{j2} are the pseudorapidities of the leading and subleading jets, respectively, while η_{j3} is
 1816 the pseudorapidity of the extra jet in the event (if one exists). Intuitively, C_{j3} is zero when η_{j3} is directly
 1817 centered between the two jets and unity when η_{j3} is aligned with either of the VBF jets. Thus, the CJV
 1818 can be expressed as a requirement that $C_{j3} > 1$.

1819 The decay products of the Higgs tend to be central as well. Thus, the analysis also requires that both
 1820 leptons in the analysis fall within the rapidity gap defined by the jets. This cut is referred to as the outside
 1821 lepton veto, or OLV. A quantitative way to define the cut is to require that the centrality of each lepton
 1822 (defined analogously to that of the third jet in equation 5.2) correspond to the lepton being within the jet
 1823 rapidity gap, or $C_\ell < 1$ for both leptons.

1824 Figure 5.3a-c shows the m_{jj} , Δy_{jj} , and $C_{\ell 1}$ variables at the stage where all previous cuts in the se-
 1825 quence have been made. The agreement between data and Monte Carlo is good, and the bottom panels
 1826 show their power in discriminating the VBF signal from the background processes.

1827 The final signal region is also split into two bins of m_{jj} , with the first bin corresponding to 600 GeV <
 1828 $m_{jj} < 1$ TeV and the second bin corresponding to $m_{jj} > 1$ TeV. The first bin has more statistics but
 1829 also a larger contribution from background, while the second bin has lower statistics but a 1:1 signal to
 1830 background ratio.

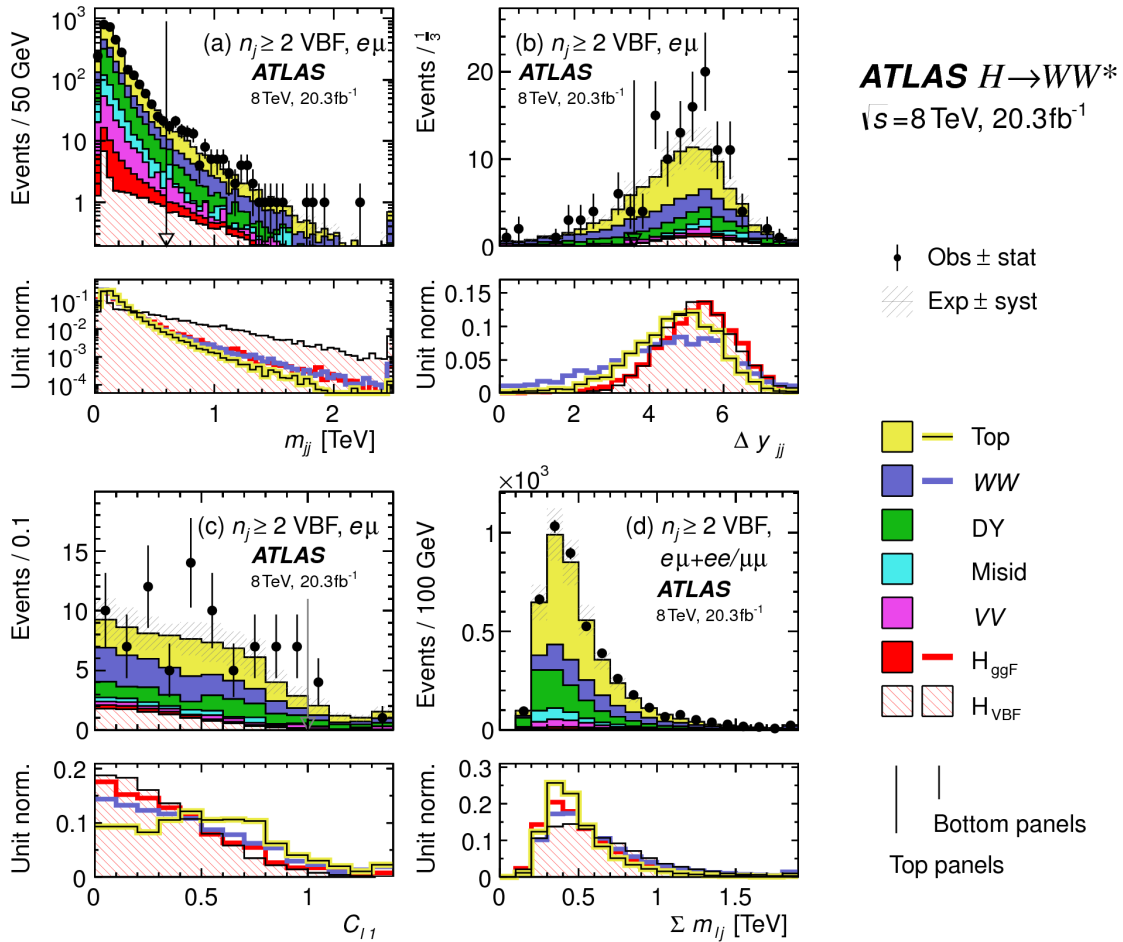


Figure 5.3: Distributions of (a) m_{jj} , (b) Δy_{jj} , (c) $C_{\ell 1}$, and (d) $\Sigma m_{\ell j}$, for the VBF analysis. The top panels compare simulation and data, while the bottom panels show normalized distributions for all background processes and signal [61].

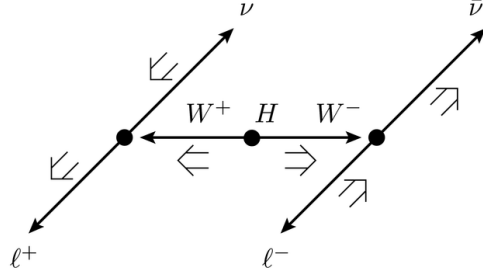


Figure 5.4: A cartoon of the WW final state. Momenta are represented with thin arrows, spins with thick arrows. [61]

1831 HIGGS TOPOLOGICAL CUTS

1832 The final state leptons will exhibit unique correlations due to the fact that they are arising from the
 1833 decay of a spin zero resonance. In particular, the spins of the final state leptons and neutrinos must all
 1834 cancel, as shown in figure 5.4. Because the neutrino has a left handed chirality and the anti-neutrino
 1835 has a right handed chirality (in the massless neutrino approximation), the spin and momentum of the
 1836 particles will be anti-aligned and aligned, respectively. In the transverse plane, the momenta of all four
 1837 final state objects must cancel as well. With the constraint of having both the momenta and the spin
 1838 alignments cancel, the final state kinematics strongly prefer having a small angle between the leptons in
 1839 the transverse plane (low $\Delta\phi_{\ell\ell}$). This angular correlation will also lead to low values of the di-lepton
 1840 invariant mass $m_{\ell\ell}$. These unique signal final state kinematic correlations will be exploited to define the
 1841 ultimate signal region.

1842 The analysis places additional requirements on the final state leptons. Two requirements on dilepton
 1843 kinematics are made that are common with lower multiplicity jet bins as well. The angle between leptons
 1844 in the transverse plane, $\Delta\phi_{\ell\ell}$, is required to be less than 1.8 radians. Additionally, the dilepton mass $m_{\ell\ell}$
 1845 is required to be less than 50 GeV.

1846 The cut-based analysis uses m_T as the final discriminating variable as in the ggF focused analysis. The
 1847 optimal number of bins in m_T was found to be three bins, with the bin boundaries at 80 and 130 GeV.

1848 Table 5.7 shows the data and estimated signal and background yields from simulation as each cut de-
 1849 scribed above is made. The table shows how each cut reduces specific backgrounds and how the overall

1850 signal to background ratio grows through the various selection requirements.

1851 Figure 5.5 shows an ATLAS event display of a candidate event in the final signal region.

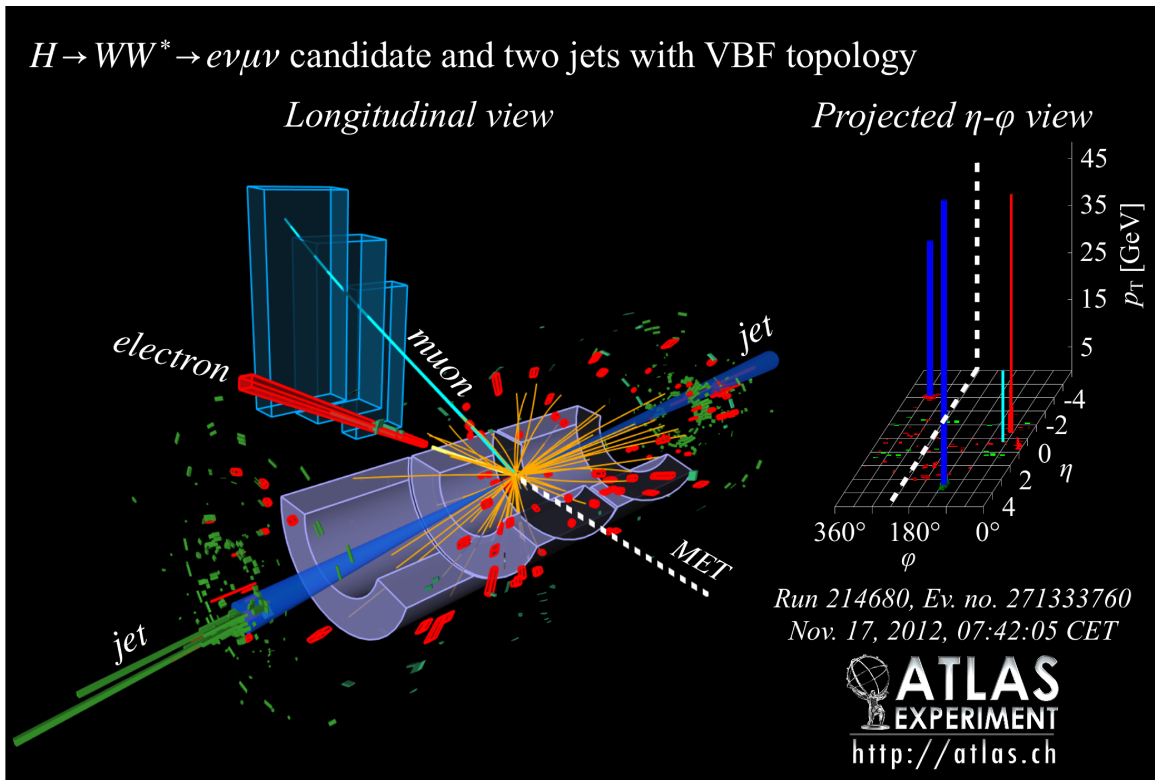


Figure 5.5: Event display of a VBF candidate event [61].

1852 5.4.3 BDT-BASED SELECTION

1853 The boosted decision tree based analysis takes a different philosophy compared to the cut-based.
1854 Rather than cutting sequentially on many variables, the BDT analysis uses many of these variables as
1855 inputs to the BDT and the output BDT score (O_{BDT}) as the final discriminant. The BDT is trained
1856 with the VBF $H \rightarrow WW^*$ simulation as the signal samples and all other processes as background, in-
1857 cluding ggF $H \rightarrow WW^*$ production. While the BDT based analysis is treated as a separate result, it has
1858 significant overlap with the cut-based selection.

Table 5.7: Event selection for the $n_j \geq 2$ VBF analysis in the 8 TeV cut-based analysis [61].

Selection	Summary						Composition of N_{bkg}									
	$N_{\text{obs}}/N_{\text{bkg}}$	N_{obs}	N_{bkg}	N_{ggF}	N_{VBF}	N_{signal}	N_{WW}	N_{WW}^{EW}	N_{top}	N_{Wj}	N_{jj}	N_{VV}	N_{misid}	$N_{\text{Drell-Yan}}$	$N_{ee/\mu\mu} N_{\tau\tau}^{\text{QCD}}$	$N_{\tau\tau}^{\text{EW}}$
$e\mu$ sample	1.00 ± 0.00	61434	61180	85	32	26	1350	68	51810	2970	847	308	380	51	3260	46
$n_b = 0$	1.02 ± 0.01	7818	7700	63	26	16	993	43	3000	367	313	193	273	35	2400	29
$p_T^{\text{sum}} < 15$	1.03 ± 0.01	5787	5630	46	23	13	781	38	1910	270	216	107	201	27	2010	23
$m_{\tau\tau} < m_Z - 25$	1.05 ± 0.02	3129	2970	40	20	9.9	484	22	1270	177	141	66	132	7.6	627	5.8
$m_{jj} > 600$	1.31 ± 0.12	131	100	2.3	8.2	—	18	8.9	40	5.3	1.8	2.4	5.1	0.1	15	1.0
$\Delta y_{jj} > 3.6$	1.33 ± 0.13	107	80	2.1	7.9	—	11.7	6.9	35	5.0	1.6	2.3	3.3	—	11.6	0.8
$C_{j3} > 1$	1.36 ± 0.18	58	43	1.3	6.6	—	6.9	5.6	14	3.0	1.3	1.3	2.0	—	6.8	0.6
$C_{l1} < 1, C_{l2} < 1$	1.42 ± 0.20	51	36	1.2	6.4	—	5.9	5.2	10.8	2.5	1.3	1.3	1.6	—	5.7	0.6
$m_{\ell\ell}, \Delta\phi_{\ell\ell}, m_{\tau\tau}$	2.53 ± 0.71	14	5.5	0.8	4.7	—	1.0	0.5	1.1	0.3	0.3	0.3	0.6	—	0.5	0.2
$ee/\mu\mu$ sample	0.99 ± 0.01	26949	27190	31	14	10.1	594	37	23440	1320	230	8.6	137	690	679	16
$n_b, p_T^{\text{sum}}, m_{\tau\tau}$	1.03 ± 0.03	1344	1310	13	8.0	4.0	229	12.0	633	86	26	0.9	45	187	76	1.5
$m_{jj}, \Delta y_{jj}, C_{j3}, C_\ell$	1.39 ± 0.28	26	19	0.4	2.9	0.0	3.1	5.5	1.0	0.2	0.0	0.7	3.8	0.7	0.1	0.1
$m_{\ell\ell}, \Delta\phi_{\ell\ell}, m_{\tau\tau}$	1.63 ± 0.69	6	3.7	0.3	2.2	0.0	0.4	0.2	0.6	0.2	0.0	0.1	1.5	0.3	0.1	0.1

1859 PRE-TRAINING SELECTION AND BDT INPUTS

1860 Before training, the common pre-selection cuts described in section 5.4.1 are applied. Additionally, the
1861 central jet veto and outside lepton veto described in section 5.4.2 are applied. The BDT has eight input
1862 variables, six of which are also variables that are used in the cut-based analysis. The six shared variables
1863 are p_T^{sum} , m_{jj} , Δy_{jj} , $m_{\ell\ell}$, $\Delta\phi_{\ell\ell}$, and m_T . The seventh variable input in the BDT is a combination of
1864 the variables used to do the OLV in the cut-based analysis. The BDT uses as input the sum of lepton
1865 centralities, or $\sum C_\ell = C_{\ell 1} + C_{\ell 2}$. The final BDT input variable, $\Sigma m_{\ell j}$, is constructed to account for
1866 the correlations between the jets and leptons in the event. It is the sum of the invariant masses of all four
1867 possible lepton-jet combinations.

1868 Figure 5.3d shows the agreement between data and simulation for the $\Sigma m_{\ell j}$ variable, as well as show-
1869 ing its discriminating power. Figure 5.6 shows the distributions of the Higgs topological variables that
1870 are shared between the cut-based and BDT analyses. Figure 5.7 shows the distributions of the VBF topo-
1871 logical variables shared between the cut-based and BDT analyses. In both cases, the VBF yield has been
1872 scaled by a factor of 50 to better show the shape difference compared to the backgrounds.

1873 Table ?? summarizes the cuts applied for the cut-based and analyses, as well as which variables are used
1874 as input to the BDT.

1875 5.5 BACKGROUND ESTIMATION

1876 This section describes the procedures used to estimate backgrounds for the VBF analysis in both the
1877 cut-based and BDT analyses.

1878 5.5.1 GENERAL STRATEGY

1879 Most of the backgrounds in the VBF analysis have shapes estimated from Monte Carlo simulation but
1880 normalizations derived from control regions in data. In essence, a normalization factor (denoted with
1881 β or abbreviated as NF) is derived by scaling the MC yield in the control region to the corresponding
1882 yield in data. Once this factor is derived, it can be used to scale the MC estimate of the background in the

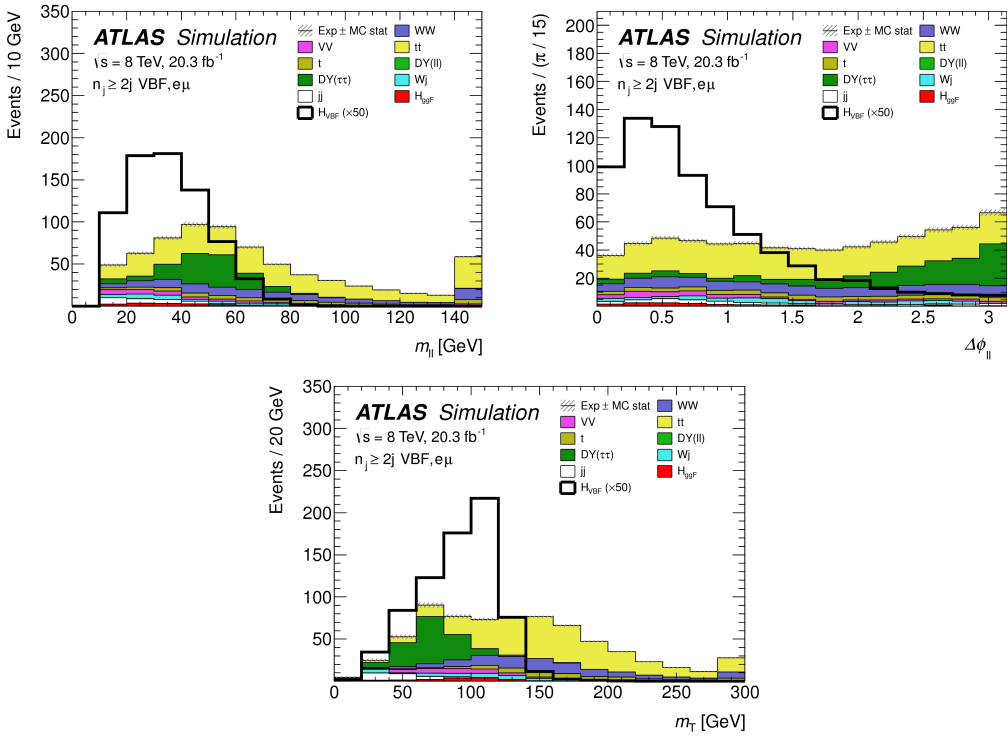


Figure 5.6: Distributions of m_{ll} (top left), $\Delta\phi_{ll}$ (top right), and m_T (bottom), Higgs topology variables used in the selection requirements of the cut-based signal region and as inputs to the BDT result. These are plotted after all of the BDT pre-training selection cuts [61].

1883 signal region. This is illustrated in equation 5.3.

$$B_{\text{SR}}^{\text{est}} = B_{\text{SR}} \times \frac{N_{\text{CR}}}{B_{\text{CR}}} \equiv B_{\text{SR}} \times \beta \quad (5.3)$$

1884 Here, B denotes the MC yield prediction in the denoted region, while N denotes the observed number
1885 of events in data in the denoted region.

1886 Another way of writing the same equation, in terms of an extrapolation factor α rather than a nor-
1887 malization factor β . The overall calculation is exactly the same. However, when phrased in this way, it
1888 shows how the uncertainty on the background estimation can be reduced. This is shown in equation 5.4.

$$B_{\text{SR}}^{\text{est}} = N_{\text{CR}} \times \frac{B_{\text{SR}}}{B_{\text{CR}}} \equiv N_{\text{CR}} \times \alpha \quad (5.4)$$

1889 Phrased this way, the equation shows that with enough statistics in the control region, a large theoretical

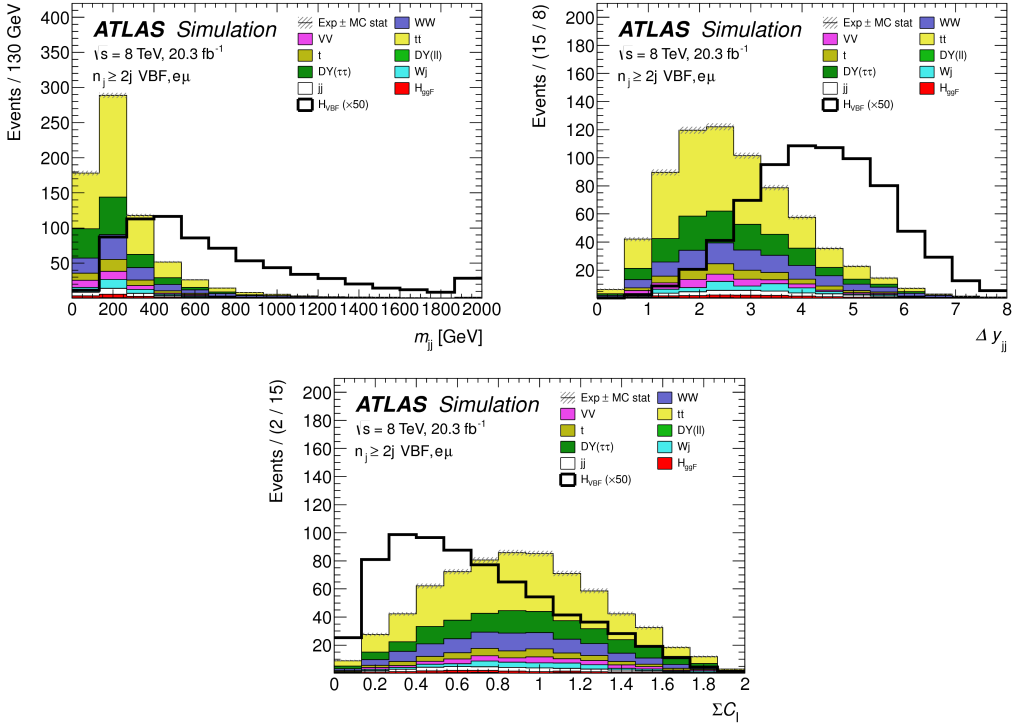


Figure 5.7: Distributions of m_{jj} (top left), Δy_{jj} (top right), $\sum C_\ell$ (bottom), VBF topology variables used in the selection requirements of the cut-based signal region and as inputs to the BDT result. These are plotted after all of the BDT pre-training selection cuts [61].

uncertainty on the overall background yield in the signal region can be replaced by a small statistical uncertainty coming from the number of data events in the CR and a smaller theoretical uncertainty on the extrapolation from the control region to the signal region.

5.5.2 TOP BACKGROUND

The normalization factor β_t for the top background in the VBF analysis is derived in a region required to have one b-tagged jet, or $n_b = 1$. In the cut-based analysis, normalization factors are computed at every stage of the cutflow by applying the appropriate cuts in the CR. These NF are then applied to the $t\bar{t}$ and single top event yields in the SR. In the BDT analysis, a single normalization factor is computed for each bin of O_{BDT} after applying the BDT pre-training cuts described previously. The computed normalization factors are derived with all flavor combinations combined in order to decrease statistical uncertainty. Additionally, in the BDT analysis, BDT bins 2 and 3 are merged for the same rea-

1902 son.

1903 Table 5.8 shows the evolution of the β_t through the cut-based selection. Table 5.9 shows the value
1904 of the β_t in each bin of O_{BDT} . In all cases, the computed factors are relatively consistent with unity,
1905 with the largest discrepancy coming in bin 1 of O_{BDT} . The normalization factors in the bins of O_{BDT}
1906 are also consistent with those derived in the cut-based signal region, increasing confidence in the BDT
1907 estimation.

Cut	β_t
$p_T^{\text{sum}} < 15 \text{ GeV}$	1.03 ± 0.01
$m_{\tau\tau} < m_Z - 25$	1.05 ± 0.01
$m_{jj} > 600 \text{ GeV}$	0.96 ± 0.06
$\Delta y_{jj} > 3.6$	1.02 ± 0.08
CJV	1.13 ± 0.16
OLV	1.01 ± 0.19
$m_{jj} < 1 \text{ TeV}$	0.94 ± 0.19
$m_{jj} > 1 \text{ TeV}$	1.48 ± 0.66

Table 5.8: Top normalization factors computed at each stage of the cut-based selection. Uncertainties are statistical only.

O_{BDT}	β_t
Bin0	1.09 ± 0.02
Bin1	1.58 ± 0.15
Bin2	0.95 ± 0.31
Bin3	0.95 ± 0.31

Table 5.9: Top normalization factors computed for each bin of O_{BDT} . Uncertainties are statistical only.

1908 Figure 5.8 shows the m_{jj} and O_{BDT} distributions in the top control region. Overall the modeling
1909 looks consistent with the data.

1910 While these normalization factors can be computed and applied to the expected background yields
1911 listed in tables like table 5.7, in the end the normalization of the top background is profiled (meaning
1912 there is a dedicated Poisson constraint) and allowed to float in the final statistical fit.

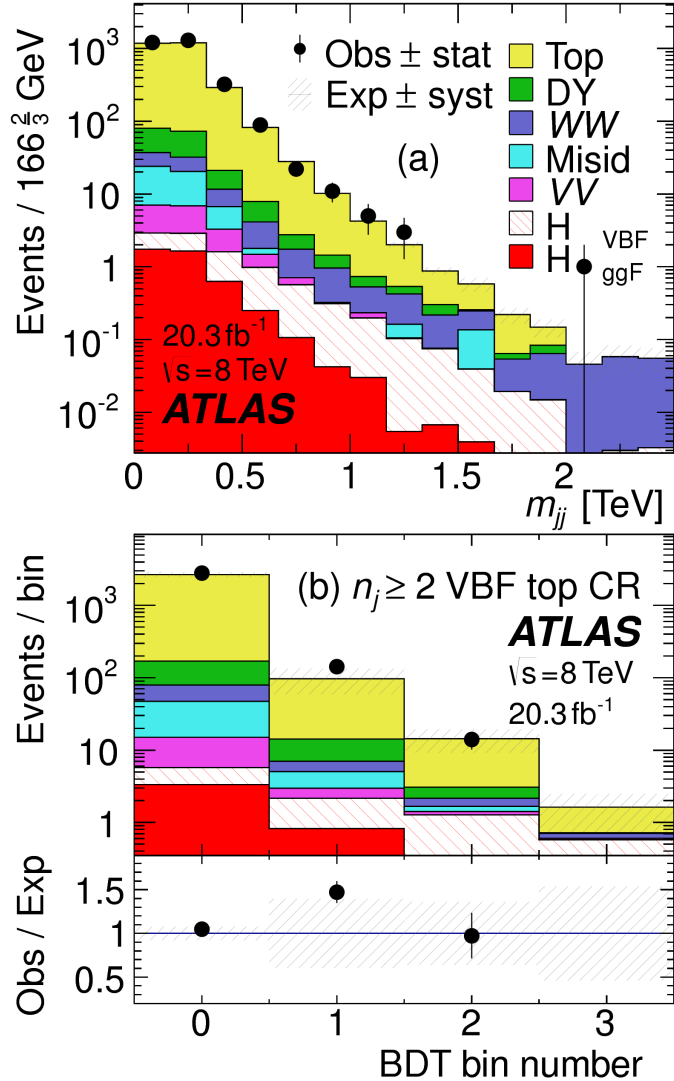


Figure 5.8: Distributions of m_{jj} (a) and O_{BDT} (b) in the VBF $n_b = 1$ top CR [61].

1913 5.5.3 $Z/\gamma^* \rightarrow \tau\tau$ BACKGROUND

1914 In the different flavor channels, the $Z/\gamma^* \rightarrow \tau\tau$ background is an important one. Di-tau production
1915 can produce an $e\mu$ final state if each τ lepton decays to a different flavor lepton.

1916 In the BDT analysis, a single normalization factor for the background is derived. A control region is
1917 defined using the pre-training selection cuts, except requiring that $|m_{\tau\tau} - m_Z| < 25$ GeV so that
1918 the region is enriched in $Z/\gamma^* \rightarrow \tau\tau$ background. Additional requirements of $m_{\ell\ell} < 80(75)$ GeV
1919 in the different (same) flavor channel, as well as $O_{\text{BDT}} > -0.48$ are applied to increase the purity of

1920 the region. The final $\beta_{Z/\gamma^* \rightarrow \tau\tau}$ is calculated to be 0.9 ± 0.3 (statistical uncertainty only). Because of
 1921 the small contribution of this background in the BDT analysis and the large statistical uncertainty, no
 1922 additional systematics are calculated. The final SR estimate is scaled by this β and not allowed to float in
 1923 the fit.

1924 The cut-based corrections are a bit more involved because they need to be applied selection by selec-
 1925 tion, as well as in the final signal region for the fit. The region is defined including all SR cuts up to the
 1926 $Z/\gamma^* \rightarrow \tau\tau$ veto, which is instead made into a Z mass peak requirement as for the BDT region. The
 1927 $m_{\ell\ell}$ cut from the BDT region is included as well. The cut-based approach aims to correct the normal-
 1928 ization of the $Z/\gamma^* \rightarrow \tau\tau$ background in two ways. First, an overall normalization factor is computed
 1929 from the control region. However, the VBF topological cuts are not included in this region, and apply-
 1930 ing them as is done in the top CR is not feasible due to limited statistics. So, instead, correction factors
 1931 (CF) to the cut efficiencies of the VBF cuts are derived in a same flavor $Z \rightarrow \ell\ell$ control region, which has
 1932 significantly more statistics. The CF is simply the ratio of the cut efficiencies in data and MC derived in
 1933 this region. In the end, the overall background estimate is given by equation 5.5.

$$N_{Z/\gamma^* \rightarrow \tau\tau}^{\text{est}} = B_{Z/\gamma^* \rightarrow \tau\tau}^{\text{SR}} \times \beta_{\tau\tau} \times \frac{\epsilon_{\text{VBF cuts}}^{\text{data}}}{\epsilon_{\text{VBF cuts}}^{\text{MC}}} \quad (5.5)$$

1934 The hypothesis is that while the normalization correction must be derived in a dedicated region, the
 1935 efficiency of the VBF cuts should not be sensitive to the type of Z/γ^* process and thus the larger control
 1936 region can be exploited to derive the CF. Figure 5.9 shows a shape comparison for the m_{jj} variable in
 1937 $Z \rightarrow \tau\tau$ events in the signal region and $Z \rightarrow \ell\ell$ events in the control region. The figure shows that the
 1938 shapes are indeed comparable and thus any CF derived in the same flavor control region can reliably be
 1939 applied in the signal region.

1940 Table 5.10 shows the overall normalization factor $\beta_{\tau\tau}$ and the efficiency correction factors for the var-
 1941 ious VBF topological cuts. In general, the statistical uncertainties on the cut efficiency corrections are
 1942 quite good, and the MC tends to underestimate the efficiency of the VBF cuts for the $Z/\gamma^* \rightarrow \tau\tau$ back-
 1943 ground. The overall normalization factor is also consistent with that calculated for the BDT analysis.

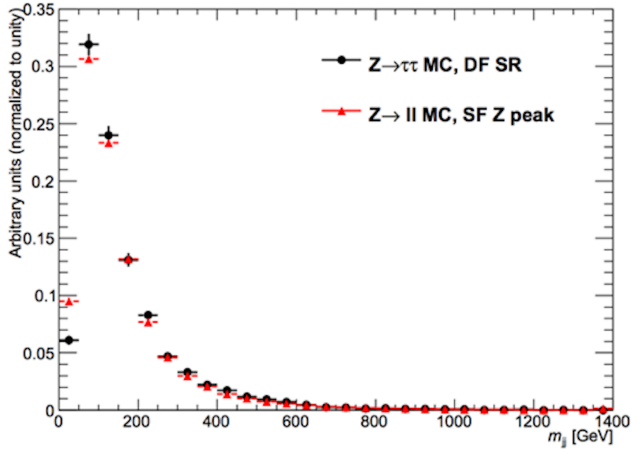


Figure 5.9: Comparison of m_{jj} shape in a same flavor $Z \rightarrow \ell\ell$ control region and the VBF cut-based signal region.

$\beta_{\tau\tau}$	0.97 ± 0.04
Cut	Correction factors
$m_{jj} > 600$ GeV	1.09 ± 0.01
$\Delta y_{jj} > 3.6$	1.14 ± 0.02
CJV	1.20 ± 0.02
OLV	1.17 ± 0.03
$m_{jj} < 1$ TeV	1.17 ± 0.06
$m_{jj} > 1$ TeV	1.18 ± 0.13

Table 5.10: $Z/\gamma^* \rightarrow \tau\tau$ correction factors for the VBF cut-based analysis. Uncertainties are statistical only.

1944 5.5.4 $Z/\gamma^* \rightarrow \ell\ell$ BACKGROUND

1945 In the same flavor channels, the $Z/\gamma^* \rightarrow \ell\ell$ background is dominant and thus must be estimated
 1946 correctly. In both the BDT and cut-based analyses, the background is estimated using the so-called
 1947 “ABCD” method. The ABCD method creates four different regions by defining cuts on two variables.
 1948 One of the regions (A) is the signal region, while the other regions are defined by inverting one of both
 1949 of the cuts. in this case, the two variables used are $m_{\ell\ell}$ and E_T^{miss} , because inverting either of the SR cuts
 1950 on these variables will give regions rich in the $Z/\gamma^* \rightarrow \ell\ell$ background. Figure 5.10 illustrates the general
 1951 strategy for each region.

1952 In both of the cut-based and BDT analyses, the Z peak region is defined with $|m_{\ell\ell} - m_Z| < 15$ GeV.
 1953 In the cut-based analysis, low $m_{\ell\ell}$ corresponds to $m_{\ell\ell} < 50$ GeV (this defines the cut-based SR) while

Region A (SR)	Region C
High E_T^{miss}	High E_T^{miss}
Low $m_{\ell\ell}$	Z peak
Region B	Region D
Low E_T^{miss}	Low E_T^{miss}
Low $m_{\ell\ell}$	Z peak

Figure 5.10: General illustration of the ABCD region definitions for $Z/\gamma^* \rightarrow \ell\ell$ background estimation.

in the BDT it is $m_{\ell\ell} < 75$ GeV. In the cut-based, high and low E_T^{miss} are defined as opposite ends of the 55 GeV cut applied for the signal region definition. The BDT low E_T^{miss} region is between 25 and 45 GeV, while the high E_T^{miss} region is $E_T^{\text{miss}} > 45$ GeV.

Once the regions are defined, the final signal region background estimate is done by taking the estimate in region B and extrapolating it to the signal region (A) by multiplying it by the ratio of regions C and D. Effectively, the Z peak region is used to estimate the efficiency of the E_T^{miss} cut in data, and then this efficiency is applied in the low $m_{\ell\ell}$ region. An additional correction is also applied for the non-closure of the method in MC. This is summarized in equations 5.6 and 5.7.

$$N_{Z/\gamma^*\rightarrow\ell\ell}^{\text{SR}} = N_{Z/\gamma^*\rightarrow\ell\ell}^{\text{B}} \times \frac{N_{Z/\gamma^*\rightarrow\ell\ell}^{\text{C}}}{N_{Z/\gamma^*\rightarrow\ell\ell}^{\text{D}}} \times f_{\text{corr}} \quad (5.6)$$

$$f_{\text{corr}} = \frac{B_{\text{MC}}^{\text{A}}/B_{\text{MC}}^{\text{B}}}{B_{\text{MC}}^{\text{C}}/B_{\text{MC}}^{\text{D}}} \quad (5.7)$$

Here, the N refer to data yields in each region with the non Z/γ^* backgrounds subtracted, while B refer to the Z/γ^* yields in MC in each region.

A normalization factor $\beta_{\ell\ell}$ is computed for each analysis as the ratio of the predicted data yield to the MC yield in the SR. The shape of the BDT distribution is taken from data region B, while the shape of the m_T distribution in the cut-based analysis is taken from Z/γ^* MC in the SR. The values of the $\beta_{\ell\ell}$ in the cut-based and BDT analyses from this method are summarized in table 5.11. They are quite

1968 consistent with one another within the statistical uncertainties. In the cut-based analysis, the same cut
 1969 efficiency correction factors shown in table 5.10 are also applied (in product with the $\beta_{\ell\ell}$) in the same
 1970 flavor channels to this background, as they were derived in the Z peak region.

	β_t
BDT Bin 1	1.01 ± 0.15
BDT Bin 2	0.89 ± 0.28
Cut-based	0.81 ± 0.21

Table 5.11: $Z/\gamma^* \rightarrow \ell\ell$ normalization factors for cut-based and BDT analyses. Uncertainties are statistical only.

1971 5.5.5 WW AND OTHER DIBOSON BACKGROUNDS

1972 The WW and other diboson backgrounds have both their shape and normalization taken from MC
 1973 simulation. They are validated in dedicated control regions and found to agree with data well.

1974 As WW is the largest of these backgrounds and is irreducible, validating the estimate is of particular
 1975 importance. The validation region is constructed by requiring the pre-selection cuts on leptons and $m_{\ell\ell}$,
 1976 $n_b = 0$, and $m_T > 100$ GeV. The m_{T2} variable [81] is an additional discriminant that will isolate
 1977 the WW background, and a requirement of $m_{T2} > 160$ GeV is placed to define the WW validation
 1978 region. This cut gives a 60% purity for the validation region. The derived normalization factor in the
 1979 region is 1.15 ± 0.19 and is thus consistent with unity. Figure 5.11 shows the m_{T2} distribution and how
 1980 it distinguishes the WW background.

1981 5.5.6 HIGGS PRODUCTION VIA GLUON-GLUON FUSION

1982 Because this analysis is dedicated to measuring the VBF contribution to Higgs production, the com-
 1983 ponent of Higgs production from gluon-gluon fusion is treated as a background. The shape is taken
 1984 directly from simulation, using the generators described in table 5.4. In the final combined fit of all dif-
 1985 ferent signal regions, the normalization is controlled by either a combined signal strength parameter μ ,
 1986 which controls the normalization of both ggF and VBF production, or a separate parameter μ_{ggF} de-
 1987 pending on the interpretation being presented in the final results.

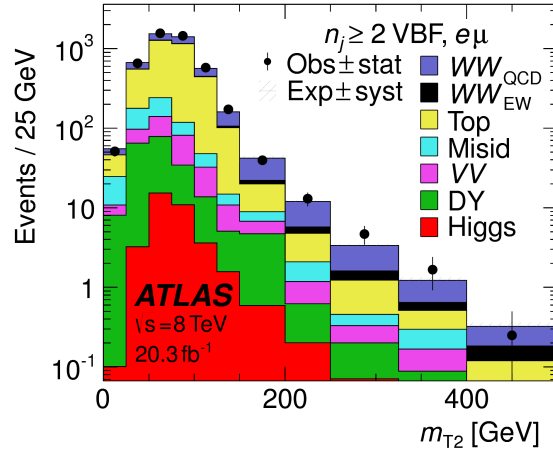


Figure 5.11: Distribution of m_{T2} in the WW validation region of the VBF analysis [61].

1988 5.5.7 BACKGROUNDS WITH MISIDENTIFIED LEPTONS

1989 As discussed previously, the $W+jets$ and QCD multijet backgrounds are derived with fully data-
 1990 driven methods. These backgrounds do not make a large contribution to the final VBF signal region but
 1991 their estimation methods are discussed briefly here.

1992 $W+jets$ BACKGROUND

1993 The $W+jets$ background enters the signal region by having one of the jets mis-reconstructed as a lep-
 1994 ton. The background is estimated by constructing a control sample with two leptons, where one lepton
 1995 passes the usual lepton quality cuts but the second lepton fails one of those cuts (also known as the “anti-
 1996 identified” lepton). This control region is rich in the $W+jets$ contribution because if a second lepton is
 1997 reconstructed in a $W+jets$ event it is likely to be poor quality. The purity of this $W+jets$ control sample
 1998 is 85% to 90% depending on the exact configuration of leptons in the final state.

1999 The signal region estimate of $W+jets$ is estimated by extrapolation from the control sample to the sig-
 2000 nal region using extrapolation factors derived in a $Z+jets$ control sample in data. The extrapolation fac-
 2001 tor is the ratio of the number of lepton candidates satisfying all quality criteria to the number of lepton
 2002 candidates anti-identified. This ratio is measured in bins of p_T and η . Thus, the final signal region esti-
 2003 mate (binned as the extrapolation factor is binned) is simply the number of events in the anti-identified

2004 lepton control sample multiplied by the extrapolation factor derived from the $Z+jets$ control sample.

2005 Figure 5.12 shows the extrapolation factors derived for electrons and muons.

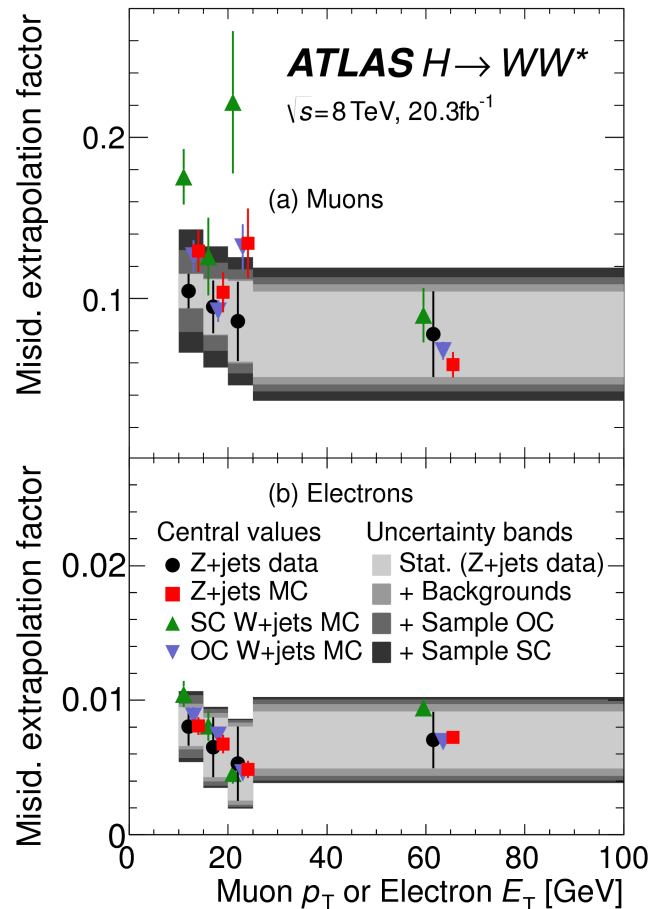


Figure 5.12: Extrapolation factors for the $W+jets$ estimate derived for muons (a) and electrons (b) as a function of lepton p_T [61].

2006 QCD MULTIJET BACKGROUND

2007 The method for estimating the multijet background is very similar to the $W+jets$ estimation method.

2008 The control sample in this case has two anti-identified leptons but otherwise satisfies all signal region requirements. The extrapolation factor is estimated from a multijet sample and applied twice to the 2009 control sample.

2011 5.5.8 BACKGROUND COMPOSITION IN FINAL SIGNAL REGION

2012 After all of these estimation procedures, the final signal region composition can be calculated. The
2013 estimated yields are all shown in table 5.7. Figure 5.13 shows the relative percentages of the different
2014 background for the different flavor and same flavor final states. In $e\mu$, the leading backgrounds are top
2015 backgrounds, ggF Higgs, and SM WW production. In $ee/\mu\mu$, the leading background is Drell-Yan,
2016 followed by top and ggF Higgs.

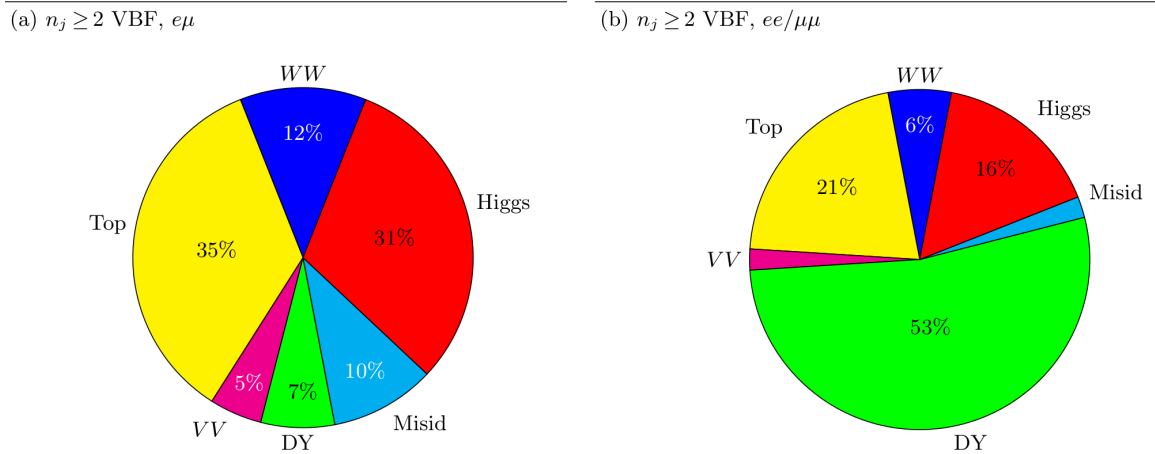


Figure 5.13: Background composition in final VBF signal region [61].

2017 5.6 SYSTEMATIC UNCERTAINTIES

2018 There are two main types of systematic uncertainties that are assessed for the analysis. First, theoreti-
2019 cal uncertainties associated with the various signal and background yield estimates are discussed. Then,
2020 experimental uncertainties due to detector effects are shown. Normalization uncertainties refer to uncer-
2021 tainties that affect the cross section of the process in question in the signal region being probed. Shape
2022 uncertainties refer to systematic uncertainties that affect the shape of the final discriminating variable
2023 (either m_T or O_{BDT}).

2024 5.6.1 THEORETICAL UNCERTAINTIES

2025 There are four main components to theoretical uncertainties assigned to signal and background pro-
2026 cesses taken from Monte Carlo. Each one is a different source of variation in the overall acceptance for
2027 that process. The first involves variation of the QCD renormalization and factorization scales used in
2028 the calculation. In this case, the two scales are varied independently and simultaneously by factors of
2029 two high or low and quantifying the resulting variation in normalization and shape for the process. This
2030 approximates the correction to the cross section that would come from including the next order of the
2031 QCD calculation (referred to as scale uncertainty). Next, there is an uncertainty associated with the PDF
2032 set used in generating the events. The uncertainty eigenvectors for the given PDF set are studied, and the
2033 envelope of maximal variation is taken as an uncertainty. Finally, there are two uncertainties associated
2034 with the choice of MC software (referred to as PDF uncertainty). An uncertainty associated with the
2035 generator chosen for the hard scattering process is evaluated by keeping the parton showering software
2036 constant but varying the matrix element generator and taking the maximal variation as an uncertainty
2037 (referred to as the generator uncertainty). The converse variation can also be done, where the matrix ele-
2038 ment generator remains constant and the generator used for the underlying event/parton shower mod-
2039 eling is varied (referred to as the UE/PS uncertainty). In cases where the background is normalized in a
2040 control region, the systematic uncertainty arises from variations of the extrapolation factor α between
2041 the CR and the SR, which can affect the normalization of the background in the SR.

2042 There are two additional uncertainties that are applied to the Higgs processes as well. First, there are
2043 uncertainties assigned to the Higgs total production cross section. Then, there are uncertainties assigned
2044 based on the fact that the analysis is done in exclusive jet bins and it is possible for signal events to mi-
2045 grate from one bin to the next depending on the presence or absence of jets. These are assigned using the
2046 Jet Veto Efficiency (JVE) procedure [18, 82] for ggF events and the Stewart-Tackmann (ST) method [83]
2047 for VBF production.

2048 Table 5.12 shows the total theory uncertainties on the backgrounds in the cut-based analysis. These are
2049 the sum in quadrature of the uncertainties from each of the variations described above.

2050 Figures 5.14 and 5.15 show the variations in the extrapolation factor from the PDF and QCD uncer-

Process	Theory syst. (%)
ggF H	48
Top	26
QCD WW	37
$Z/\gamma^* \rightarrow \tau\tau$	6.1

Table 5.12: Systematic uncertainties for various processes in the cut-based VBF analysis, given in units of % change in yield. Values are given for the low m_{jj} signal region.

tainties on the top background estimate, binned in m_T , for the cut-based analysis. In both cases, there was no significant shape uncertainty but normalization uncertainties were assigned according to the maximal variation. These uncertainties enter into the 26% total uncertainty on top quoted in table 5.12. While the estimate for the same-flavor $Z/\gamma^* \rightarrow \ell\ell$ background is data-driven, there is still a systematic uncertainty taken for the non-closure of the method in Monte Carlo. This is taken as the maximum of the deviation of the non-closure factor f_{corr} from unity and its uncertainty, or $\max(|1 - f_{\text{corr}}|, \delta f_{\text{corr}})$. For the cut-based analysis this non-closure uncertainty 23%, while for the BDT analysis it is 17%.

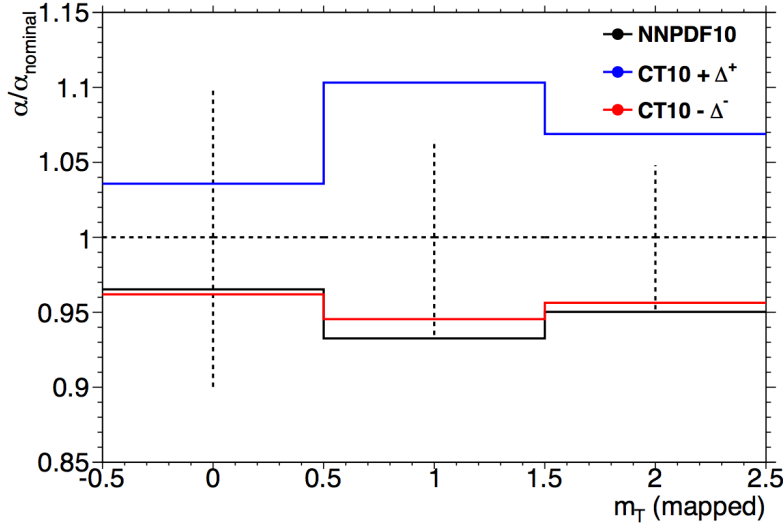


Figure 5.14: Variations in the top background extrapolation factor in the cut-based analysis due to PDF uncertainties, binned in m_T .

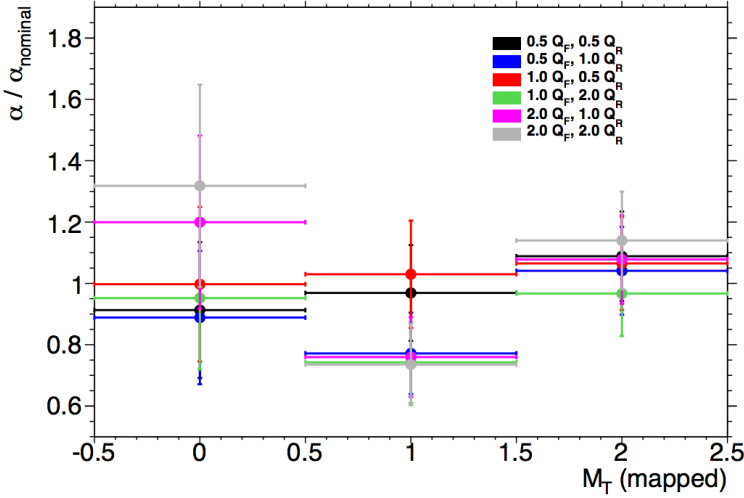


Figure 5.15: Variations in the top background extrapolation factor in the cut-based analysis due to QCD scale uncertainties, binned in m_T .

5.6.2 EXPERIMENTAL UNCERTAINTIES

In this analysis, the theoretical uncertainties end up being the most dominant, but there are some experimental uncertainties that make a contribution as well. The first is the uncertainty on the measured integrated luminosity, which affects backgrounds whose normalization is taken from MC and is measured to be 2.8% in the 8 TeV dataset [84]. The dominant sources of uncertainty overall are uncertainties on the jet energy scale and resolution and the b -tagging efficiency. Additional sources include lepton uncertainties on identification, resolution, and trigger efficiency, as well as uncertainties on the missing transverse momentum .

The jet energy scale uncertainty is split into several independent components, including jet-flavor dependent calorimeter response uncertainties, uncertainties on modeling of pile-up interactions, uncertainties on extrapolation from the central to forward detector regions, and MC non-closure [85]. The uncertainty on energy scale for jets used in this analysis ranges from 1% to 7% depending on the jet p_T and η . The jet energy resolution varies from 5% to 20%, with uncertainties ranging from 2% to 40% (the largest uncertainties occurring at the selection threshold).

The b -tagging efficiency is independently measured in data samples enriched in dileptonic decays of

Sample	Total error	Stat. error	Expt. syst. err.	Theo. syst. err.
$n_j \geq 2$ VBF-enriched				
N_{sig}	13	-	6.8	12
N_{bkg}	9.2	4.7	6.4	4.5
N_{WW}	32	-	14	28
N_{top}	15	9.6	7.6	8.5
N_{misid}	22	-	12	19
N_{VV}	20	-	12	15
$N_{\tau\tau}$ (DY)	40	25	31	2.9
$N_{ee/\mu\mu}$ (DY)	19	11	15	-

Table 5.13: Composition of the post-fit uncertainties (in %) on the total signal (N_{sig}), total background (N_{bkg}), and individual background yields in the VBF analysis [61].

2074 $t\bar{t}$ events or in events where a muon is reconstructed in the vicinity of a jet [86, 87]. The efficiencies and
 2075 their uncertainties are binned in p_T and decomposed into uncorrelated components using an eigenvector
 2076 method [88]. Uncertainties on the efficiency range from 1% to 7.8%. The uncertainty on the rate
 2077 of misidentification of c -jets as b -jets ranges from 6-14%, while the uncertainty on the rate of light jet
 2078 mis-tagging ranges from 9-19% depending on p_T and η .

2079 The total experimental uncertainties on different signal and background components are summa-
 2080 rized in table 5.13. They are compared to the level of other statistical and systematic uncertainties as well.
 2081 Overall, the experimental uncertainties are sub-dominant compared to the statistical and theoretical
 2082 uncertainties.

2083 5.7 RESULTS

2084 While the combined results of all the $H \rightarrow WW^*$ sub-analyses will be discussed in the next chapter,
 2085 this section presents the results of the VBF specific analysis and interpretations. As table 5.7 shows, the
 2086 final cut-based signal region contains 20 events in data with $m_T < 150$ GeV, 14 coming from the $e\mu$
 2087 channel and 6 coming from the $ee + \mu\mu$ channel. The BDT analysis has many more candidates due to
 2088 its looser selection, and the yields in each bin of O_{BDT} are shown in table 5.14.

2089 Figure 5.16(a) shows the final distribution of data candidates compared to the expected m_T distri-

(a) Before the BDT classification

Selection	Summary						Composition of N_{bkg}													
	$N_{\text{obs}}/N_{\text{bkg}}$	N_{bkg}	N_{obs}	N_{bkg}	N_{signal}	N_{eggF}	N_{VBF}	N_{VH}	N_{WW}^{SD}	N_{WW}^{EW}	$N_{t\bar{t}}$	N_t	N_{Wj}	N_{jj}	N_{VV}	N_{missid}	$N_{\text{Drell-Yan}}$	$N_{e/\mu}^{\text{SD}}$	$N_{e/\mu}^{\text{EW}}$	$N_{\tau\tau}^{\text{SD}}$
$e\mu$ sample	1.04 ± 0.04	718	689	13	15	2.0	90	II	327	42	29	23	31	2.2	130	2				
$ee/\mu\mu$ sample	1.18 ± 0.08	469	397	6.0	7.7	0.9	37	3	132	17	5.2	1.2	10.1	168	23	1				
(b) Bins in O_{BDT}																				
$e\mu$ sample																				
Bin 0 (not used)	1.02 ± 0.04	661	650	8.8	3.0	1.9	83	9	313	40	26	21	28	2.2	126	1				
Bin 1	0.99 ± 0.16	37	37	3.0	4.2	0.1	5.0	1.0	17	3.1	3.3	1.8	2.6	—	4.0	0.2				
Bin 2	2.26 ± 0.63	14	6.2	1.2	4.2	—	1.5	0.5	1.8	0.3	0.4	0.3	0.8	—	0.3	0.3				
Bin 3	5.41 ± 2.32	6	1.1	0.4	3.1	—	0.3	0.2	0.3	0.1	—	—	0.1	—	0.1	0.1				
$ee/\mu\mu$ sample																				
Bin 0 (not used)	1.91 ± 0.08	396	345	3.8	1.3	0.8	33	2	123	16	4.1	1.1	8.8	137	20.5	0.5				
Bin 1	0.82 ± 0.14	53	45	1.5	2.2	0.1	3.0	0.5	10.4	1.8	0.8	0.2	0.9	26	1.7	0.1				
Bin 2	1.77 ± 0.49	14	7.9	0.6	2.5	—	0.8	0.3	1.1	0.2	0.2	—	0.3	4.4	0.3	0.1				
Bin 3	6.32 ± 2.87	6	0.9	0.2	1.7	—	0.1	0.2	0.2	—	—	—	0.7	—	—	—				

Table 5.14: Event selection for the VBF BDT analysis. The event yields in (a) are shown after the pre-selection and the additional requirements applied before the BDT classification (see text). The event yields in (b) are given in bins in O_{BDT} after the classification [61].

2090 bution for signal and background. The data are very consistent with a VBF Higgs hypothesis. Fig-
 2091 ure 5.16(b) shows where the data candidates fall in the two-dimensional binning of m_T and m_{jj} used
 2092 in the fit for the cut-based analysis.

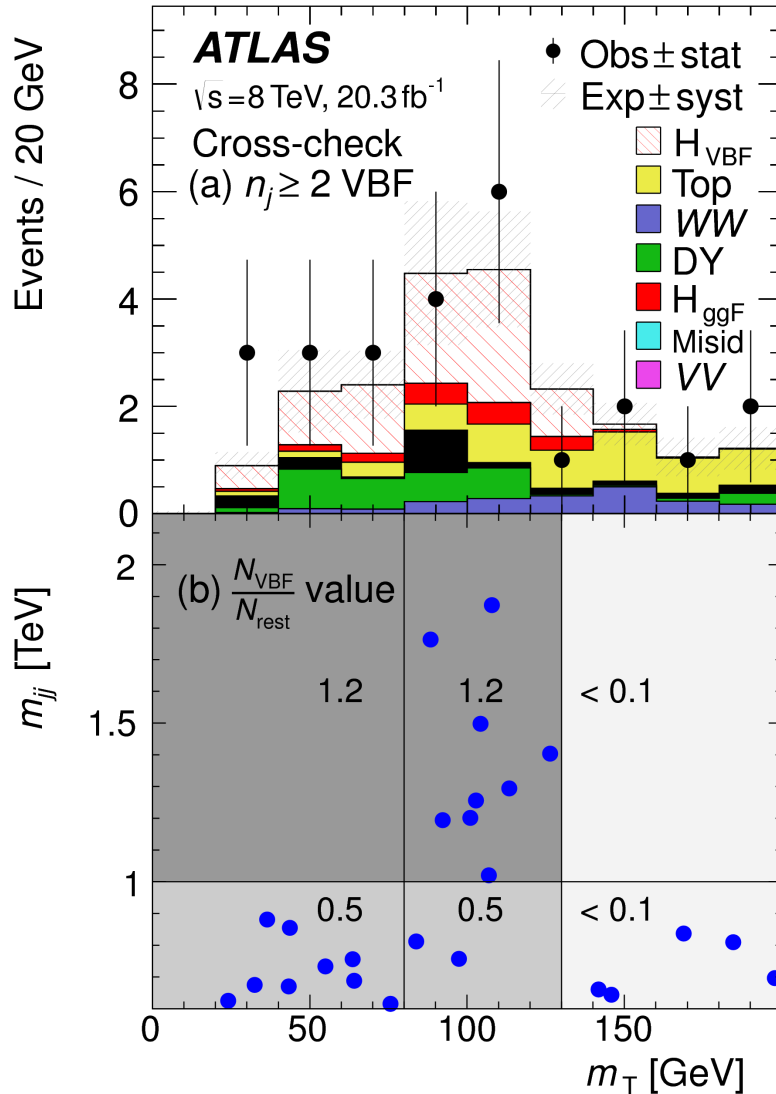


Figure 5.16: Post-fit distributions in the cut-based VBF analysis. Panel (a) shows the one-dimensional m_T distribution, while (b) shows the data candidates split into the bins of m_T and m_{jj} used in the final fit [61].

2093 Figure 5.17 shows the distributions of O_{BDT} and m_T in the VBF BDT analysis. Again the data are
 2094 quite consistent with a VBF Higgs hypothesis.

2095 Because the cut-based result is used as a validation for the BDT analysis and the two signal regions are

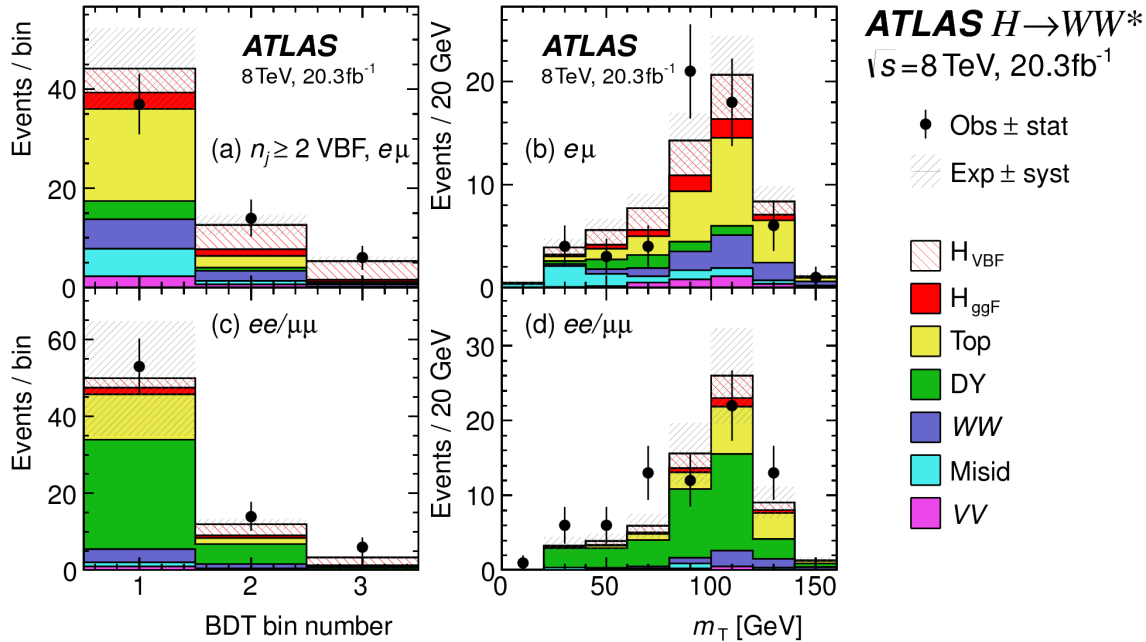


Figure 5.17: Postfit distributions in the BDT VBF analysis [61].

not fully orthogonal, it is interesting to explore which events overlap between the two analyses. Of the twenty events in the cut-based signal region, only seven were not selected by the BDT analysis, while the other thirteen also enter the BDT signal region. Figure 5.18 shows where the different analysis candidates lie in the m_{jj} - m_T plane. This shows clearly that the advantage of the BDT analysis is that it can extract signal candidates lower m_{jj} region due to its ability to recognize correlations with other variables.

While the context of these results in the broader $H \rightarrow WW^*$ statistical analysis will be presented in the next chapter, the significance of the VBF observation can be shown here. In the BDT analysis, the expected signal significance was 2.7σ , while the observed significance was 3.1σ . In the cut-based analysis, the expected significance was 2.1σ and the observed significance was 3.0σ . The compatibility between these two results can be evaluated by computing the probability of observing a larger difference in Z_0 values than the one measured. Using toy Monte Carlo with the ggF signal strength fixed to unity and considering only statistical uncertainties, this probability is computed to be 79%, indicating good agreement between the analyses. This result represents the first observation of the vector boson fusion production of a Higgs boson.

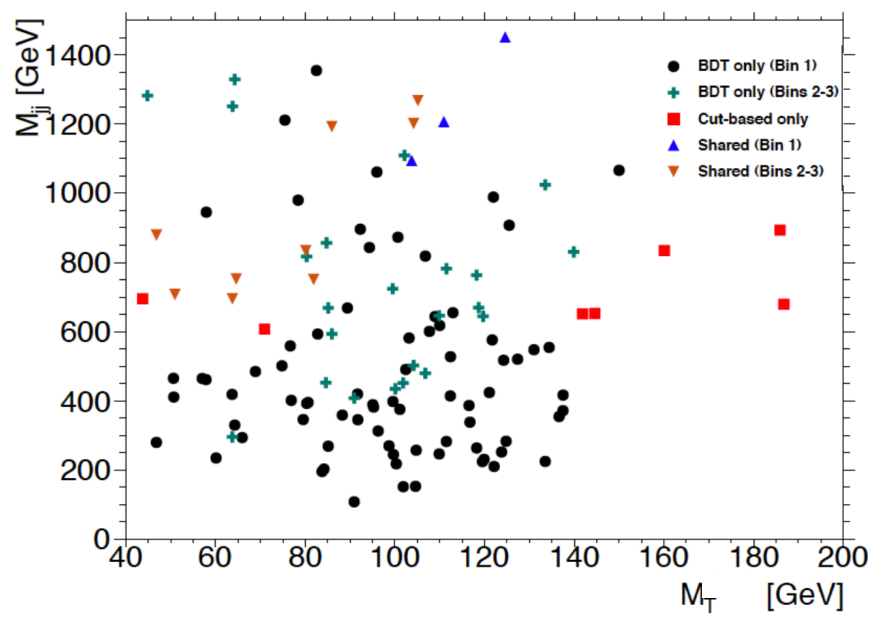


Figure 5.18: Overlap between cut-based and BDT VBF signal region candidates in the m_{jj} - m_T plane.

*The feeling is less like an ending than just another
starting point.*

Chuck Palahniuk

6

2110

2111

Combined Run I $H \rightarrow WW^* \rightarrow \ell\nu\ell\nu$

2112

results

2113

6.1 INTRODUCTION

2114

In the final statistical analysis of $H \rightarrow WW^* \rightarrow \ell\nu\ell\nu$, the dedicated gluon-gluon fusion and vector boson fusion sensitive signal regions are all combined into a single fit to determine the main parameters of interest, the Higgs signal strength μ and mass m_H . Therefore, while the specific requirements applied for the VBF sensitive analysis are discussed in chapter 5, the final measurement of these parameters can only be discussed in combination with the results of the ggF dedicated analysis. For example, because ggF Higgs production is considered a background in the VBF analysis, the ggF dedicated signal regions can actually constrain the normalization of this background in the VBF dedicated region.

2115

This chapter presents the combined interpretation of results in the $H \rightarrow WW^* \rightarrow \ell\nu\ell\nu$ analysis

SR category i				Fit var.	
n_j , flavor	$\otimes m_{\ell\ell}$	$\otimes p_T^{\ell 2}$	$\otimes \ell_2$		
$n_j = 0$	$e\mu$	$\otimes [10, 30, 55]$	$\otimes [10, 15, 20, \infty]$	$\otimes [e, \mu]$	m_T
	$ee/\mu\mu$	$\otimes [12, 55]$	$\otimes [10, \infty]$		m_T
$n_j = 1$	$e\mu$	$\otimes [10, 30, 55]$	$\otimes [10, 15, 20, \infty]$	$\otimes [e, \mu]$	m_T
	$ee/\mu\mu$	$\otimes [12, 55]$	$\otimes [10, \infty]$		m_T
$n_j \geq 2$ ggF	$e\mu$	$\otimes [10, 55]$	$\otimes [10, \infty]$		m_T
$n_j \geq 2$ VBF	$e\mu$	$\otimes [10, 50]$	$\otimes [10, \infty]$		O_{BDT}
	$ee/\mu\mu$	$\otimes [12, 50]$	$\otimes [10, \infty]$		O_{BDT}

Table 6.1: All signal regions definitions input into final statistical fit [61].

for gluon fusion and vector boson fusion Higgs production. First, the results of the dedicated gluon fusion search are presented. Then, a comparison of the individual production mode signal strengths (μ_{ggF} and μ_{VBF} and a measurement of the combined signal strength (μ) are shown. Subsequently, the measured values of the Higgs couplings to fermions and vector bosons is presented. Finally, the cross section measurement for ggF and VBF production are shown.

6.2 RESULTS OF DEDICATION GLUON FUSION $H \rightarrow WW^* \rightarrow \ell\nu\ell\nu$ SEARCH

The details of the dedicated gluon fusion $H \rightarrow WW^* \rightarrow \ell\nu\ell\nu$ search are not discussed in this thesis and instead left to more comprehensive sources [61]. However, a brief summary of the results are essential for describing the results of the full analysis and interpreting the results of the dedicated VBF search in this broader context.

Table 6.1 shows the individual signal regions that were input into the final statistical fit. The ggF dedicated bins use m_T as their discriminating variable and are separated into bins of p_T of the subleading lepton as well. The VBF dedicated bin uses the O_{BDT} distribution as its final discriminant.

Table 6.2 shows the yields in the various signal regions in both data and expected signal and back-

2136 grounds. The yields for signal and background are all scaled according to the final normalizations calcu-
2137 lated in the fit.

	N_{obs}	N_{bkg}	N_{ggF}	N_{VBF}
$n_j = 0$	3750	3430 ± 90	300 ± 50	8 ± 4
$n_j = 1$	1596	1470 ± 40	102 ± 26	17 ± 5
$n_j \geq 2, \text{ggF } e\mu$	1017	960 ± 40	37 ± 11	13 ± 1.4
$n_j \geq 2, \text{VBF}$	130	99 ± 9	7.7 ± 2.6	21 ± 3

Table 6.2: Post-fit yields in the different ggF and VBF dedicated signal regions [61].

2138 Figure 6.1 shows the final post-fit m_T distribution in the $n_j \leq 1$ regions. The data are very consistent
with the hypothesis of ggF Higgs production. These yields are used as input, along with the VBF results

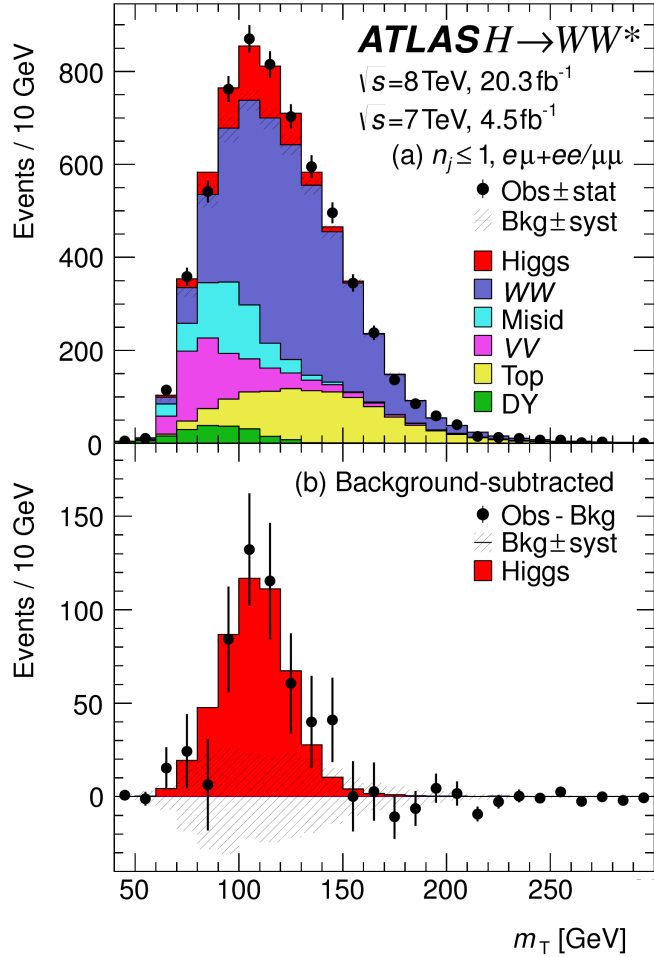


Figure 6.1: Post-fit m_T distribution in the $n_j \leq 1$ regions [61].

2139

2140 in chapter 5, for the physical interpretation of results presented in subsequent sections.

2141 **6.3 SIGNAL STRENGTH MEASUREMENTS IN GGF AND VBF PRODUCTION**

2142 When all of the signal regions are combined in the fit, there can be a combined measurement of the
 2143 signal strength as well as the individual ggF and VBF signal strengths. The combined signal strength
 2144 is the ratio of the sum of the gluon fusion and VBF cross sections to the theory prediction, or a signal
 2145 strength for the total Higgs production cross section that this analysis is sensitive to. The final measured
 2146 combined signal strength μ is measured shown in equation 6.1.

$$\begin{aligned} \mu &= 1.09 \quad {}^{+0.16}_{-0.15} \text{ (stat.)} \quad {}^{+0.08}_{-0.07} \left(\begin{array}{l} \text{expt} \\ \text{syst} \end{array} \right) \quad {}^{+0.15}_{-0.12} \left(\begin{array}{l} \text{theo} \\ \text{syst} \end{array} \right) \quad \pm 0.03 \left(\begin{array}{l} \text{lumi} \\ \text{syst} \end{array} \right) \\ &= 1.09 \quad {}^{+0.16}_{-0.15} \text{ (stat)} \quad {}^{+0.17}_{-0.14} \text{ (syst)} \\ &= 1.09 \quad {}^{+0.23}_{-0.21}. \end{aligned} \tag{6.1}$$

2147 Figure 6.2 gives the best fit signal strength $\hat{\mu}$ as a function of the hypothesized Higgs mass. The value
 2148 at 125.36 GeV corresponds to the μ quoted in equation 6.1. This value of the Higgs mass is used because
 2149 it is the most precise mass measurement from ATLAS, a result of the combined $\gamma\gamma$ and ZZ mass mea-
 2150 surements [89].

2151 As explained in chapter 3, a probability p_0 can be computed using the test statistic q_0 to quantify the
 2152 probability that the background could fluctuate to produce an excess at least as large as the one observed
 2153 in the data. The local p_0 value is shown in figure 6.3 as a function of m_H . The minimum p_0 value is
 2154 at $m_H = 130$ GeV and corresponds to a significance of 6.1σ . The curve is relatively flat and the sig-
 2155 nificance is the same at 125.36 GeV within the quoted precision. The expected significance for a signal
 2156 with strength $\mu = 1.0$ is 5.8σ . This represents the first discovery level significance measurement in the
 2157 $H \rightarrow WW^* \rightarrow \ell\nu\ell\nu$ analysis.

2158 All the results presented so far in this section have been for the combined gluon fusion and VBF pro-
 2159 duction modes. However, each signal strength can be calculated separately in the likelihood as well.
 2160 There are two ways to do this. First, the likelihood can be parameterized in terms of a single parameter,

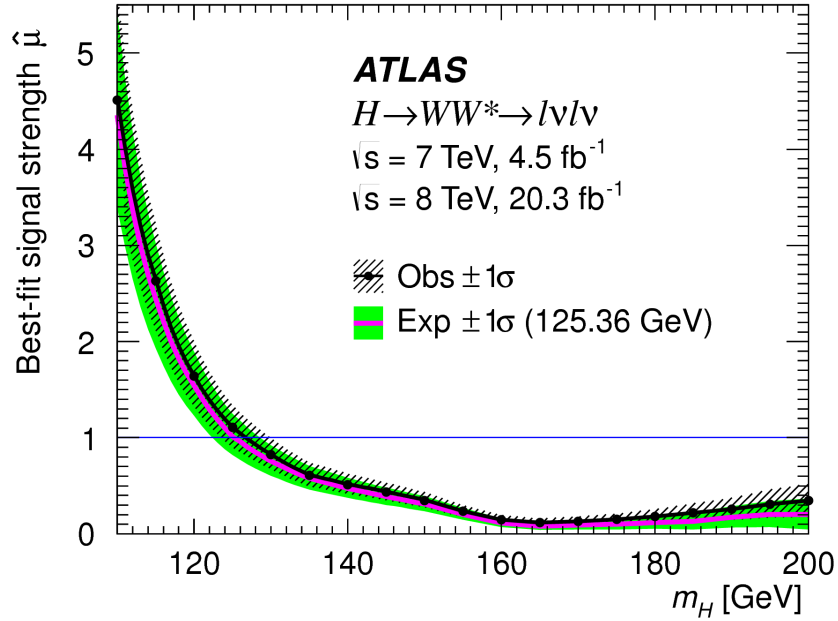


Figure 6.2: Best fit signal strength $\hat{\mu}$ as a function of hypothesized m_H [61].

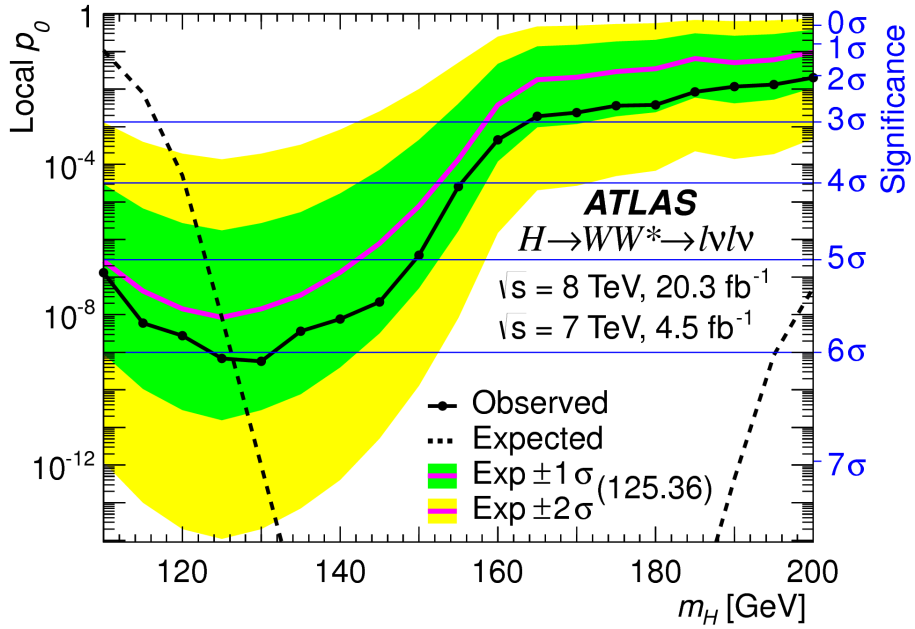


Figure 6.3: Local p_0 as a function of m_H [61].

²¹⁶¹ the ratio of the VBF and gluon fusion signal strengths. With this method, the significance of the VBF
²¹⁶² observation can be evaluated. Figure 6.4 shows the likelihood as a function of the ratio $\mu_{\text{VBF}}/\mu_{\text{ggF}}$.

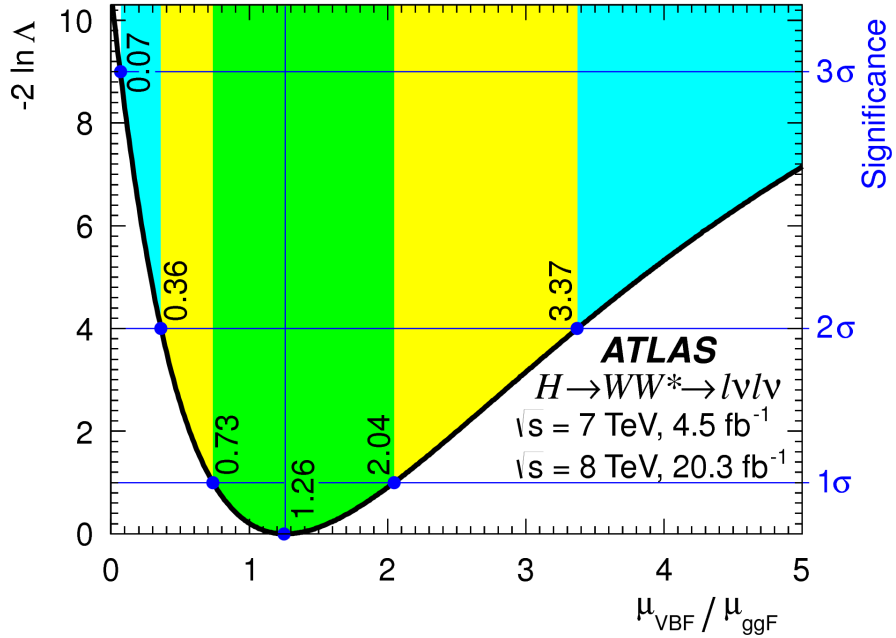


Figure 6.4: Likelihood as a function of $\mu_{\text{VBF}} / \mu_{\text{ggF}}$ [61].

2163 The best fit value of the ratio of signal strengths is shown in equation 6.2. Within the quoted uncer-
 2164 tainties, it is consistent with a ratio of unity.

$$\frac{\mu_{\text{VBF}}}{\mu_{\text{ggF}}} = 1.26^{+0.61} (\text{stat.})^{+0.50} (\text{syst.}) = 1.26^{+0.79}_{-0.53} \quad (6.2)$$

2165 The null hypothesis for VBF production corresponds to a ratio of $\mu_{\text{VBF}} / \mu_{\text{ggF}} = 0$. The likelihood in
 2166 figure 6.4 gives a significance of 3.2σ at $\mu_{\text{VBF}} / \mu_{\text{ggF}} = 0$, as quoted in chapter 5.

2167 In addition to the ratio of signal strengths, each signal strength can be varied independently in the
 2168 likelihood as well. Figure 6.5 shows the two dimensional likelihood scan in the $\mu_{\text{ggF}}-\mu_{\text{VBF}}$ plane. The
 2169 best fit values of the two signal strengths are shown in equation 6.3. Both are consistent with unity
 2170 within their uncertainties.

$$\begin{aligned} \mu_{\text{ggF}} &= 1.02 \pm 0.19^{+0.22}_{-0.18} = 1.02 \pm 0.29 \\ \mu_{\text{VBF}} &= 1.27 \pm 0.40^{+0.44}_{-0.21} = 1.27 \pm 0.53. \end{aligned} \quad (6.3)$$

(stat.) (syst.)

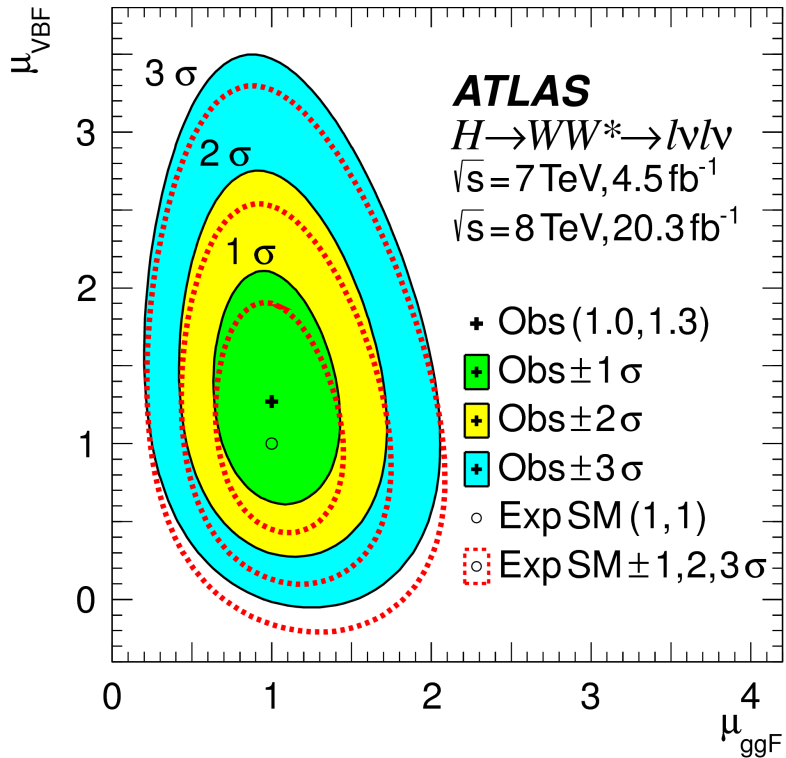


Figure 6.5: Likelihood scan as a function of μ_{VBF} and μ_{ggF} [61].

2171 6.4 MEASUREMENT OF HIGGS COUPLINGS TO VECTOR BOSONS AND FERMIONS

2172 Similar to the parameterization of signal strength, the couplings of the Higgs to fermions and bosons
 2173 can also be parameterized. The parameter of interest in this case is κ , or the ratio of the measured cou-
 2174 pling to the standard model expectation. Both the fermion and boson couplings have these so-called
 2175 scale factors, κ_F for fermions and κ_V for bosons. Gluon fusion production is sensitive to the fermion
 2176 couplings through the top quark loops in its production, while VBF production is sensitive to the vec-
 2177 tor boson couplings in its production. Both modes are sensitive to the vector boson couplings in their
 2178 decays. The signal strengths will have dependence on the coupling scale factors as described in equa-
 2179 tion 6.4 [18].

$$\begin{aligned} \mu_{\text{ggF}} &\propto \frac{\kappa_F^2 \cdot \kappa_V^2}{(\mathcal{B}_{H \rightarrow f\bar{f}} + \mathcal{B}_{H \rightarrow gg}) \kappa_F^2 + (\mathcal{B}_{H \rightarrow VV}) \kappa_V^2} \\ \mu_{\text{VBF}} &\propto \frac{\kappa_V^4}{(\mathcal{B}_{H \rightarrow f\bar{f}} + \mathcal{B}_{H \rightarrow gg}) \kappa_F^2 + (\mathcal{B}_{H \rightarrow VV}) \kappa_V^2}. \end{aligned} \quad (6.4)$$

2180 Figure 6.6 shows the two-dimensional likelihood scan of κ_F and κ_V . The best-fit values are given in
 2181 equation 6.5. The best-fit values are consistent with unity within their uncertainties.

$$\begin{aligned} \kappa_F &= 0.93 & +0.24 & +0.21 & = 0.93 & +0.32 \\ \kappa_V &= 1.04 & +0.07 & +0.07 & = 1.04 & \pm 0.11. \end{aligned} \quad (6.5)$$

(stat.) (syst.)

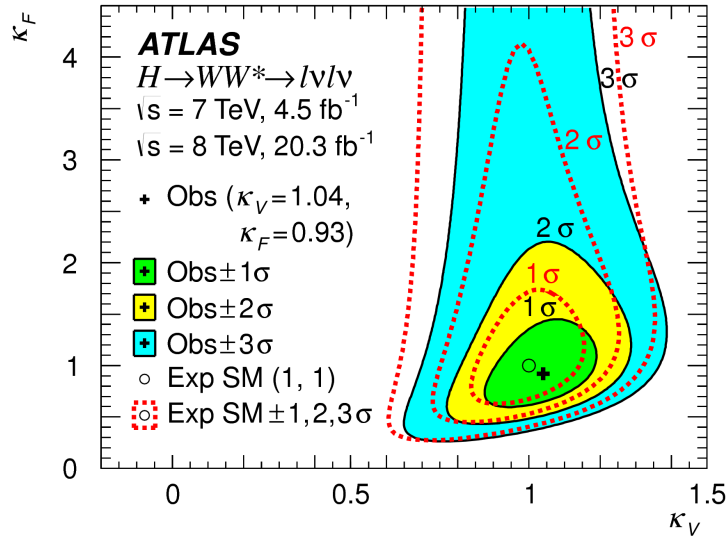


Figure 6.6: Likelihood scan as a function of κ_F and κ_V [61].

2182

2183 6.5 HIGGS PRODUCTION CROSS SECTION MEASUREMENT

2184 Another measurement that comes naturally from the signal strength numbers quoted earlier is the
 2185 production cross section and 7 and 8 TeV for both gluon fusion and VBF production. The general
 2186 equation for calculating the cross section is given in equation 6.6.

$$\begin{aligned} (\sigma \cdot \mathcal{B}_{H \rightarrow WW^*})_{\text{obs}} &= \frac{(N_{\text{sig}})_{\text{obs}}}{\mathcal{A} \cdot \mathcal{C} \cdot \mathcal{B}_{WW \rightarrow \ell\nu\ell\nu}} \cdot \frac{1}{\int L dt} \\ &= \hat{\mu} \cdot (\sigma \cdot \mathcal{B}_{H \rightarrow WW^*})_{\text{exp}} \end{aligned} \quad (6.6)$$

2187 $(N_{\text{sig}})_{\text{obs}}$ is the number of events observed in data. \mathcal{A} is the geometric and kinematic acceptance of the
 2188 detector, while \mathcal{C} is the efficiency of the signal region selection for events that are reconstructed in the
 2189 detector. The branching ratio of a WW system to leptons must also be divided out. The production
 2190 cross section depends on the center of mass energy and the production mode desired (gluon fusion or
 2191 VBF), and so three separate cross section measurements are quoted in equation 6.7.

$$\begin{aligned}
 \sigma_{\text{ggf}}^{\text{7TeV}} \cdot \mathcal{B}_{H \rightarrow WW^*} &= 2.0 \pm 1.7^{+1.2}_{-1.1} = 2.0^{+2.1}_{-2.0} \text{ pb} \\
 \sigma_{\text{ggf}}^{\text{8TeV}} \cdot \mathcal{B}_{H \rightarrow WW^*} &= 4.6 \pm 0.9^{+0.8}_{-0.7} = 4.6^{+1.2}_{-1.1} \text{ pb} \\
 \sigma_{\text{vbf}}^{\text{8TeV}} \cdot \mathcal{B}_{H \rightarrow WW^*} &= 0.51^{+0.17}_{-0.15} {}^{+0.13}_{-0.08} = 0.51^{+0.22}_{-0.17} \text{ pb.}
 \end{aligned} \tag{6.7}$$

(stat.) (syst.)

2192 The predicted cross section values for gluon fusion are 3.3 ± 0.4 pb at 7 TeV and 4.2 ± 0.5 pb at 8 TeV,
 2193 consistent with the measured values within their uncertainties. For vector boson fusion, the predicted
 2194 cross section is 0.35 ± 0.02 pb, again consistent with the measured value.

2195 6.6 CONCLUSION

2196 The combined analysis of the gluon fusion and vector boson fusion processes in $H \rightarrow WW^* \rightarrow$
 2197 $\ell\nu\ell\nu$ in the 7 and 8 TeV datasets has yielded the first discovery level significance for Higgs production in
 2198 this decay channel. Additionally, precise measurements of the couplings to vector bosons and fermions
 2199 are given. Finally, signal strengths and cross sections for each production mode are measured. Figure 6.7
 2200 shows the $H \rightarrow WW^* \rightarrow \ell\nu\ell\nu$ measurements in comparison with other Higgs decay channels in
 2201 ATLAS. The measurement of signal strength from this channel remains the most sensitive in both the
 2202 gluon fusion and VBF production modes for the Run 1 dataset.

ATLAS

Individual analysis

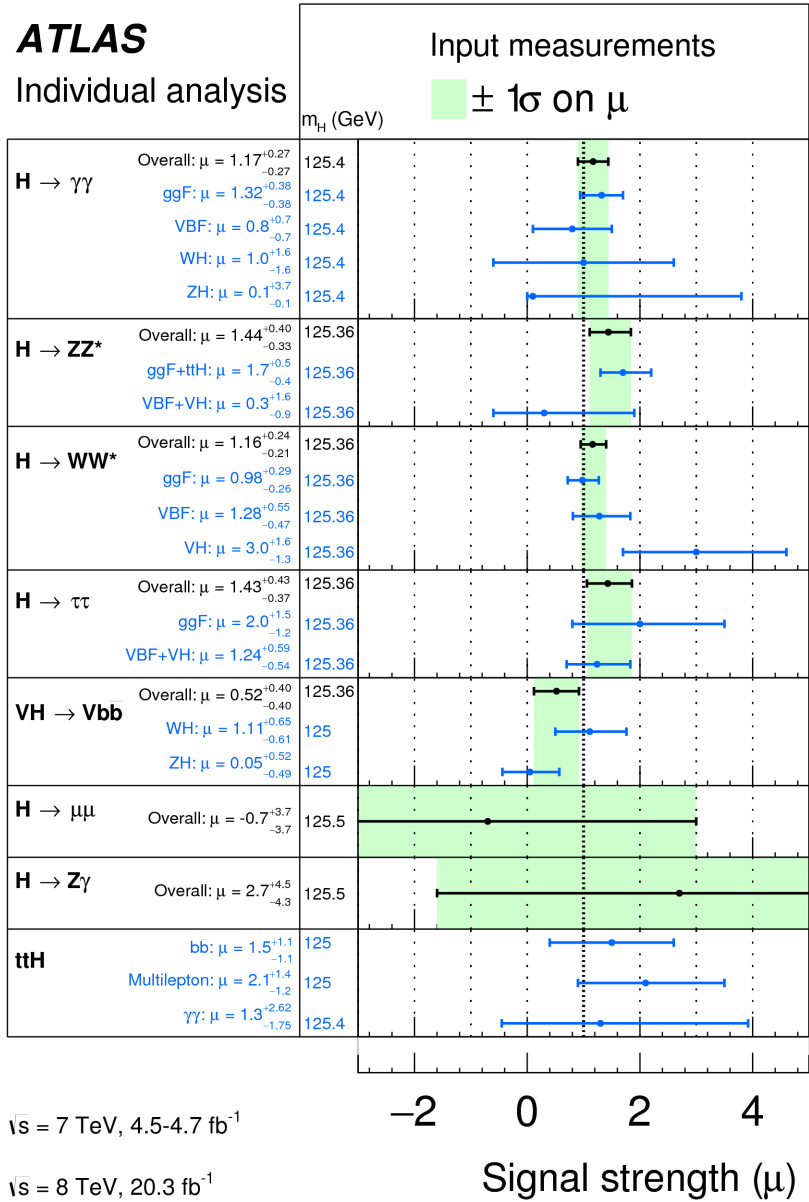


Figure 6.7: Comparison of signal strength measurements in different Higgs decay channels on ATLAS [90].

2203

Part III

2204

Search for Higgs pair production in the

2205

$HH \rightarrow b\bar{b}b\bar{b}$ channel in LHC Run 2 at $\sqrt{s} =$

2206

13 TeV

Passion is in all great searches and is necessary to all creative endeavors.

W. Eugene Smith

7

2207

2208 Search for Higgs pair production in boosted 2209 $b\bar{b}b\bar{b}$ final states

2210 7.1 INTRODUCTION

2211 After the discovery of the Higgs boson in the ATLAS Run 1 dataset and the subsequent measure-
2212 ments of its properties, the Higgs transformed into a potential tool in searches for physics beyond the
2213 Standard Model. The pair production cross section of the Higgs can be enhanced through BSM physics.
2214 Studying di-Higgs production also probes the Higgs self-coupling, shedding light on the structure
2215 of the Higgs potential. This chapter presents a search for resonant production of a Higgs pair in the
2216 $X \rightarrow HH \rightarrow b\bar{b}b\bar{b}$ final state in 3.2 fb^{-1} of data collected at $\sqrt{s} = 13 \text{ TeV}$. In particular, this
2217 chapter focuses on a search for this final state in the regime where m_X is large ($\gtrsim 1 \text{ TeV}$) and the Higgs
2218 bosons in the decay are significantly boosted. A tailored selection for this boosted selection, using novel

2219 techniques in jet substructure and b -tagging, is discussed. Then, the data-driven background estimate is
 2220 presented. Finally, the results of the search are shown. The signal models used as benchmarks are a spin-
 2221 2 Randall Sundrum graviton (RSG) and a narrow width spin-0 resonance. These models are described
 2222 in more detail in Chapter 1. Limits on signal models are reserved for the next chapter where the results of
 2223 this chapter are combined with the results of a separate selection dedicated to the lower m_X regime.

2224 **7.2 MOTIVATION**

2225 With the center of mass energy increase from $\sqrt{s} = 8$ TeV to $\sqrt{s} = 13$ TeV, the LHC and ATLAS
 2226 are able to probe new resonances at higher mass scales than previously accessible in Run 1. This is a
 2227 powerful motivator for searching for a new resonance in the early 13 TeV data. Figure 7.1 shows the
 2228 ratios of parton luminosities between 8 and 13 TeV for different resonance masses. For a resonance of
 2229 $M_X = 2$ TeV, the cross section at $\sqrt{s} = 13$ TeV is roughly a factor of 10 larger than at $\sqrt{s} = 8$ TeV.

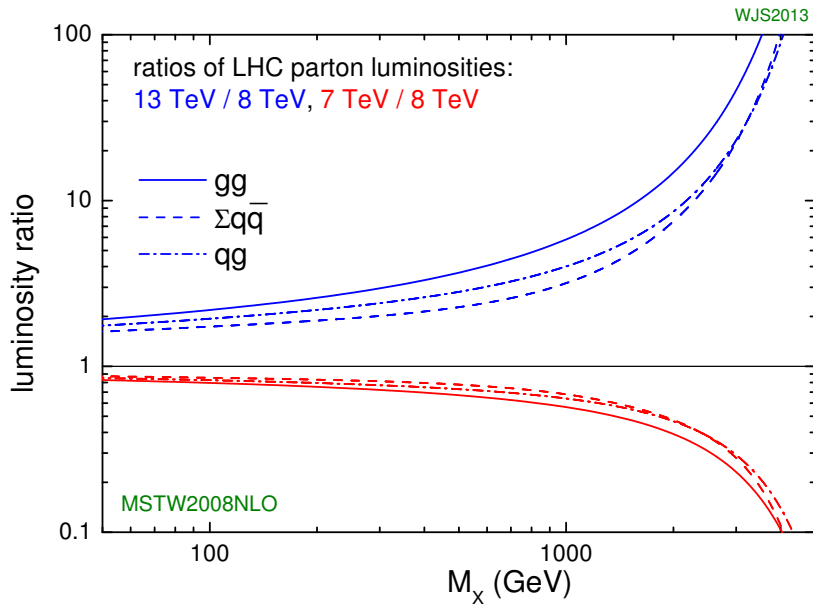


Figure 7.1: Parton luminosity ratios as a function of resonance mass M_X for 13/8 TeV and 7/8 TeV [91].

2230 Higgs pair production offers a vast array of unprobed regions of phase space where searches for BSM
 2231 physics can be made. Chapter 1 discusses some possibilities for both resonant and non-resonant enhance-

ment of the di-Higgs production cross section. Given the increased mass reach of the LHC in Run 2, it is particularly important to focus on resonant searches at high m_X . One consideration when conducting a search in the HH final state is which decay modes of the Higgs to consider. Figure 7.2 shows the branching ratio of the HH final state for different combinations of decays of each individual Higgs. As the largest branching ratio for the 125 GeV Higgs is $H \rightarrow b\bar{b}$, the $HH \rightarrow b\bar{b}b\bar{b}$ branching ratio is also the largest at 33%.

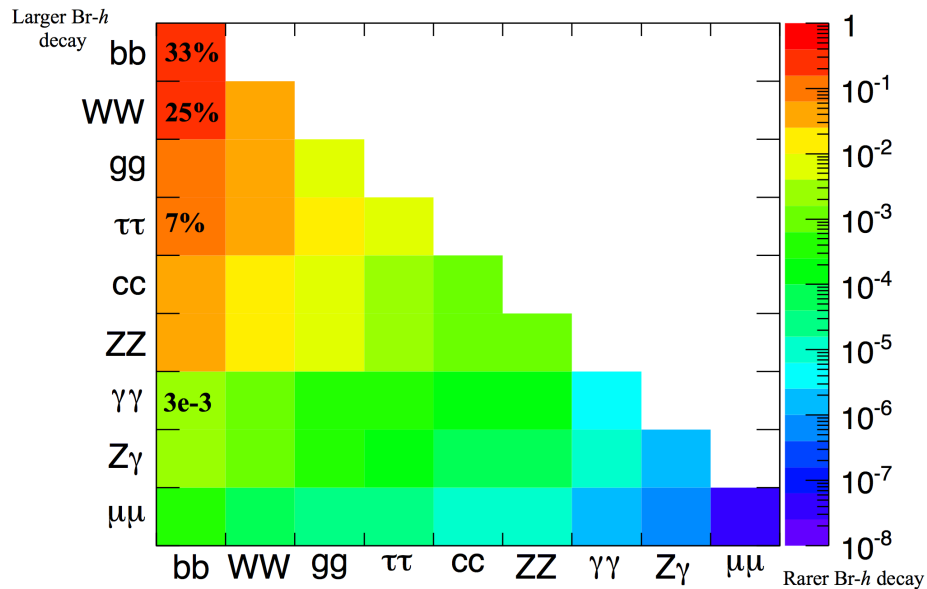


Figure 7.2: Summary of HH branching ratios [92].

At high m_X , the Higgs bosons resulting from the decay of a heavy resonance will have large p_T^* . The ΔR between the decay products of the Higgs is inversely proportional to the Higgs p_T , as shown in equation 7.1.

$$\Delta R \approx \frac{2m}{p_T} \quad (7.1)$$

Figure 7.3 shows the minimum ΔR between truth level B decay vertices in simulation samples for Randall-Sundrum gravitons of different masses. The figure shows that as the mass of the graviton increases, the ΔR distribution between the b quarks in the Higgs decay tends to shift to lower values. Because of this effect, it is necessary to tailor a selection to target these merged b -jets.

*In the limit that $m_H \ell \ell m_X$, the Higgs p_T is roughly $m_X/2$.

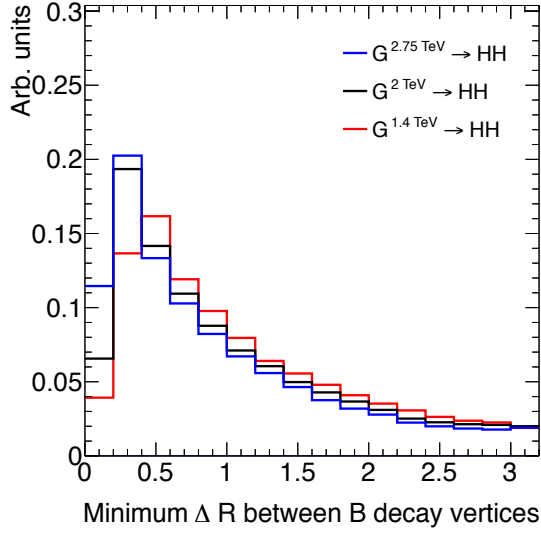


Figure 7.3: Minimum ΔR between B decay vertices for different RSG masses in a $G_{KK}^* \rightarrow HH \rightarrow 4b$ sample with $c = 1$

2245 7.3 DATA AND SIMULATION SAMPLES

2246 7.3.1 SIGNAL MODELS

2247 While the resonance search is by its nature generic (as it is a simple search for a peak in the $4b$ invariant
 2248 mass spectrum), there are two signal models that the selection requirements have been optimized for.
 2249 The first is Randall-Sundrum (RSG) model, where a tower of massive spin-2 Kaluza-Klein gravitons
 2250 is predicted. The second is a heavy narrow spin-0 resonance, the so-called “heavy Higgs”. This type of
 2251 resonance arises, for example, in the two Higgs doublet model (2HDM). More details about the physics
 2252 of these models and their motivation is given in chapter 1.

2253 Signal graviton (G_{KK}^*) events are generated at leading order (LO) with **MADGRAPH5 v2.2.2** [93].
 2254 The PDF set used is the **NNPDF2.3 LO** set [94]. For modeling parton shower and hadronization in jets,
 2255 **PYTHIA 8.186** is used with the A14 tune [73, 95]. The free parameters in the RSG model are the graviton
 2256 mass and the coupling constant $c \equiv k/\bar{M}_{\text{Pl}}$ [†]. Both the production cross section and width of the
 2257 graviton are proportional to c^2 . Samples are generated at both $c = 1$ and $c = 2$ for a variety of mass

[†] k is the curvature constant for the warped extra dimension and \bar{M}_{Pl} is the Planck mass divided by 8π

2258 points between 300 GeV and 3 TeV.

2259 The second signal sample is a heavy spin-0 resonance H with a fixed width of $\Gamma_H = 1$ GeV. This
2260 is generated with `MADGRAPH5` and uses the `CT10` PDF set [76]. The parton shower and hadronization
2261 are handled by `HERWIG ++` with the `CTEQ6L1` PDF set and the `UEEE5` event tune [77, 96, 97]. Because
2262 the width and branching ratios depend on 2HDM parameters, each mass point generated with this fixed
2263 width corresponds to a different point in the 2HDM parameter phase space. Mass points are generated
2264 between 300 GeV and 1 TeV as with the RSG signal samples.

2265 7.3.2 BACKGROUND SAMPLES

2266 While the dominant QCD multijet background is estimated with a fully data-driven method, the
2267 sub-dominant backgrounds $t\bar{t}$ and $Z + \text{jets}$ are modeled with some input from simulation.

2268 $t\bar{t}$ events are simulated at next-to-leading order (NLO) with the `POWHEG-BOX` version 1 generator us-
2269 ing the `CT10` PDF set [98]. The parton shower, hadronization, and underlying event are simulated with
2270 `PYTHIA 6.428` with the `CTEQ6L1` PDF set [72]. The Perugia 2012 tune is used [99]. NNLO QCD cor-
2271 rections to the cross sections are computed in `Top++ 2.0` [100]. The top quark mass is set to 172.5 GeV.
2272 The shapes of distributions in $t\bar{t}$ are taken from MC while the normalization is taken from data.

2273 Finally, the $Z + \text{jets}$ background is simulated with `PYTHIA 8.186` and the `NNPDF2.3` LO PDF set. This
2274 background is negligible compared to the others and is taken fully from MC.

2275 7.3.3 DATA SAMPLE AND TRIGGER

2276 This analysis is done on 3.2 fb^{-1} of data taken in 2015 at $\sqrt{s} = 13$ TeV. The details of the ma-
2277 chine conditions during this time can be found in Chapter 2. Only data which was taken during stable
2278 beam conditions with all detectors functioning is used. Events must pass a trigger which requires a single
2279 360 GeV large radius ($R = 1.0$) jet to be reconstructed in the HLT. Figure 7.4 shows the trigger effi-
2280 ciency for various trigger options as a function of graviton mass. Above $m_G > 1$ TeV, the single large
2281 radius jet trigger is 99% efficient for events passing the signal selection.

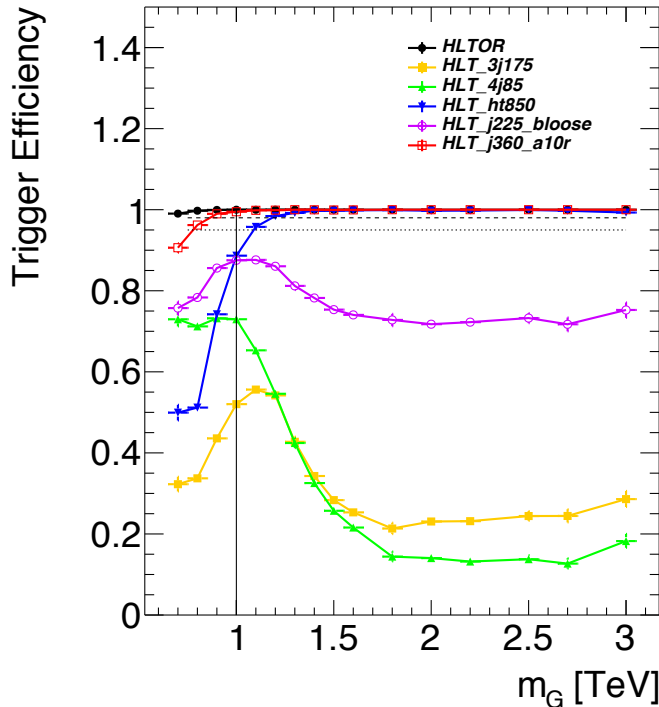


Figure 7.4: Trigger efficiency for events passing all signal region selections as a function of mass in $G_{KK}^* \rightarrow HH \rightarrow 4b$ samples with $c = 1$ [101]. In the trigger names, “j” refers to a jet or jets. “ht” refers to H_T , the scalar sum of transverse momenta in the event. “bloose” refers to a loose b -tagging requirement applied to the jet. “a10r” refers to anti- k_T jets with $R = 1.0$. The numbers at the end are the thresholds on the given quantity in GeV.

2282 7.4 EVENT RECONSTRUCTION AND OBJECT SELECTION

2283 The boosted selection first begins by defining a unique set of objects that can be exploited to increase
 2284 signal efficiency in the kinematic regime where the final state b -jets are very merged.

2285 7.4.1 LARGE RADIUS ($R = 1.0$) JETS

2286 The first step towards reconstructing the final state is to define objects that can be used to measure
 2287 the kinematics of the Higgs bosons. In the boosted selection anti- k_T jets with a radius parameter of 1.0
 2288 are used. These jets are much larger in angular size than the typical $R = 0.4$ jets and are intended to
 2289 encompass both jets resulting from the Higgs decay[‡]. The jets are built from clusters in the calorimeter

[‡]This is in contrast to the resolved selection, which uses two $R = 0.4$ anti- k_T jets for each Higgs

2290 calibrated with local calibration weighting [56].

2291 Because of the large extent of these jets, great care must be taken to remove potential contributions of
2292 calorimeter clusters from pile-up. This is done using a technique called jet trimming [102]. With trim-
2293 ming, the constituents of the large radius jet are re-clustered with a smaller radius with the k_T algorithm.
2294 Then, these so-called subjets are removed from the larger jet if $p_T^{\text{subjet}}/p_T^{\text{jet}} < f_{\text{cut}}$. In this analysis, the
2295 subjet radius is $R = 0.2$ and $f_{\text{cut}} = 0.05$. Trimming has been shown to improve the mass resolution
2296 of large radius jets. Figure 7.5 shows the effect of trimming on the large radius jet mass (M_J). Because
2297 the large radius jet fully contains the higgs decay products, its invariant mass should correspond to the
2298 125 GeV mass of the Higgs. The trimming algorithm brings the jet mass much closer to the expected
2299 Higgs mass and improves the mass resolution.

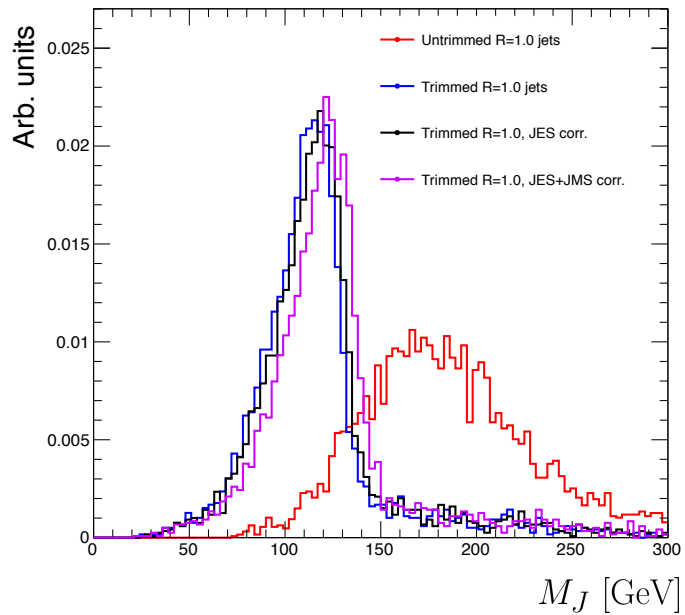


Figure 7.5: Comparison of untrimmed and trimmed jet masses for large radius jets in a RSG sample with $m_{G_{KK}^*} = 1 \text{ TeV}$. JES (JMS) refers to the standard jet energy (mass) scale calibration for ATLAS [56].

2300 The large radius jets are required to satisfy $250 < p_T < 1500 \text{ GeV}$. They must also be within
2301 $|\eta| < 2.0$ in order to ensure that the full jet is within the inner detector tracking volume. Finally, they
2302 are required to have $M_J > 50 \text{ GeV}$. The upper p_T cut and lower threshold on mass are applied to
2303 correspond to the kinematic range where uncertainties are available in ATLAS calibrations [103, 104].

2304 7.4.2 TRACK JETS AND b -TAGGING

2305 Because the b -jets from boosted Higgs decays are so close together (as illustrated in figure 7.3), narrow
2306 radius jets are required to fully resolve both b -jets. The minimum radius feasible for jets based on
2307 calorimeter deposits is determined by the calorimeter granularity. However, because b -tagging relies on
2308 information from the inner detector, it is possible to define another type of jet that can have a smaller
2309 radius and better b -tagging resolution. These jets are called “track jets” [104, 105].

2310 Track jets are formed by applying the usual anti- k_T clustering algorithm to tracks that are required
2311 to be consistent with the primary vertex. After the jet axis has been determined using these tracks, a sec-
2312 ond step of track association is also performed to add tracks that can be useful for b -tagging [105]. In this
2313 analysis, the tracks are clustered with a radius parameter of $R = 0.2$. This radius has been shown to
2314 give good performance in boosted Higgs tagging [104, 105]. Figure 7.6 shows a comparison among dif-
2315 ferent track jet radii of the efficiency for reconstructing two b -jets from each Higgs in a RSG sample as a
function of mass. Track jets with radius of 0.2 give the best performance, especially at high mass. In this

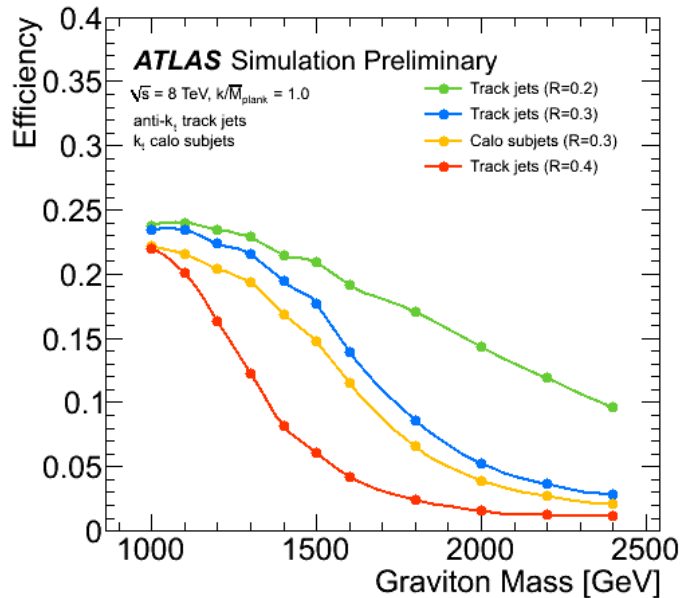


Figure 7.6: Efficiency of finding two b -jets from each Higgs in an RSG event using calorimeter jets with $R = 0.3$ or different track jet radii [105]

2316

2317 analysis, track jets are required to have $p_T > 10 \text{ GeV}$ and $|\eta| < 2.5$. They must also have at least two
2318 tracks.

2319 **7.4.3 MUONS**

2320 Muons are used in this study to correct the four-momenta of calorimeter jets by accounting for semi-
2321 leptonic b decays. The muons used are combined ID and MS muons which must satisfy tight identifica-
2322 tion requirements [52]. The muons must have $p_T > 4 \text{ GeV}$ and $|\eta| < 2.5$. Table 7.1 summarizes the
2323 object requirements described in this section.

	R	p_T	$ \eta $	M
Calorimeter jets	1.0	$250 < p_T < 1500 \text{ GeV}$	< 2.0	$> 50 \text{ GeV}$
Track jets	0.2	$> 10 \text{ GeV}$	< 2.5	-
Muons	-	4 GeV	< 2.5	-

Table 7.1: Summary of requirements on objects used in the $X \rightarrow HH \rightarrow b\bar{b}b\bar{b}$ search

2324 **7.5 EVENT SELECTION**

2325 The first requirement in the boosted selection is for ≥ 2 large radius jets satisfying the selections out-
2326 lined above. The two highest momentum large-R jets in the event are referred to as “Higgs candidates”.
2327 The leading jet is required to have $p_T > 350 \text{ GeV}$.

2328 Track jets satisfying the object selections are matched to Higgs candidate jets via ghost association [106].
2329 Each Higgs candidate must have at least 2 track jets associated with it. These basic requirements are illus-
2330 trated in figure 7.7.

2331 The QCD multijet background produces less central jets than high mass resonances, so there is an ad-
2332 ditional requirement that the two Higgs candidates be close together in η . The large-R jets are required
2333 to satisfy $|\Delta\eta(JJ)| < 1.7$.

2334 **7.5.1 MASS REQUIREMENTS**

2335 The final set of requirements ensures that the Higgs candidates are consistent with expected proper-
2336 ties of the 125.0 GeV Higgs. First, a variable (X_{hh}) is defined to measure the consistency of both of the

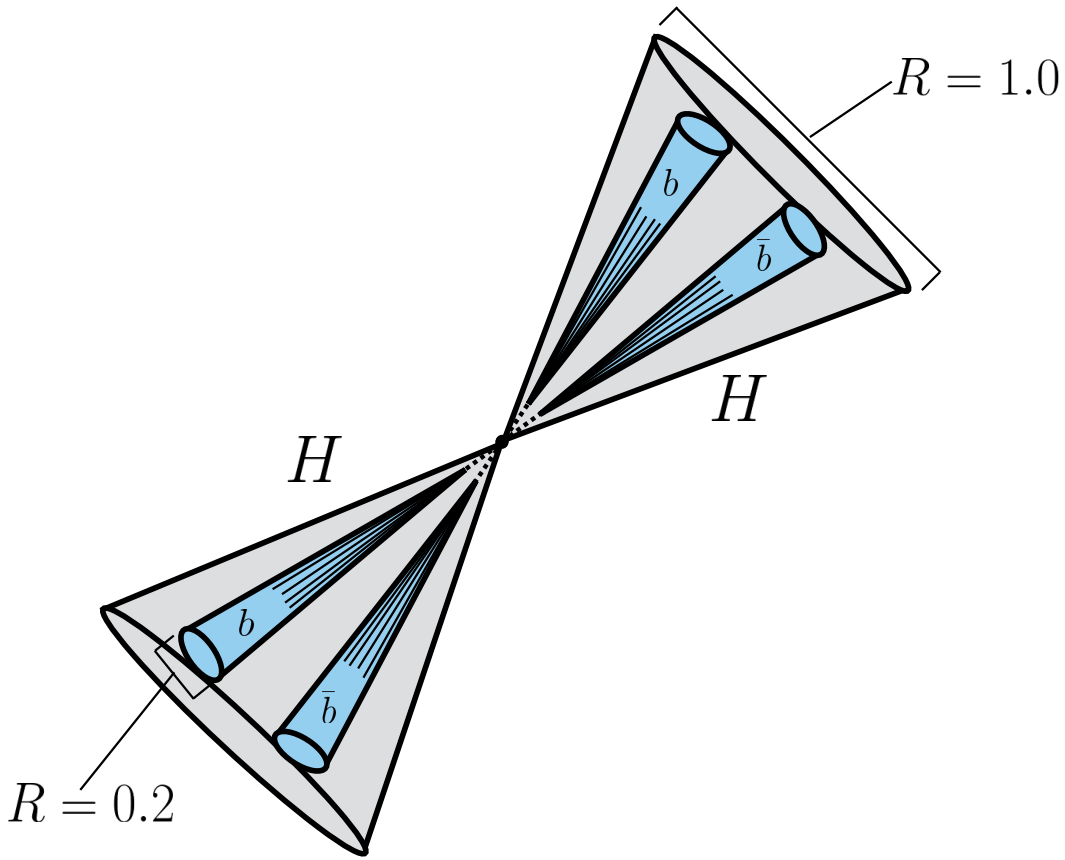


Figure 7.7: Illustration of the boosted selection requirements on Higgs candidates. Each large-radius calorimeter jet (Higgs candidate) must contain two track jets

²³³⁷ Higgs candidate jets with the SM Higgs mass. This is shown in equation 7.2.

$$X_{hh} = \sqrt{\left(\frac{M_J^{\text{lead}} - 124 \text{ GeV}}{0.1 M_J^{\text{lead}}}\right)^2 + \left(\frac{M_J^{\text{sublead}} - 115 \text{ GeV}}{0.1 M_J^{\text{sublead}}}\right)^2} \quad (7.2)$$

²³³⁸ The mass values in the X_{hh} formula are optimized to maximize signal efficiency. The sub-leading jet
²³³⁹ typically has a lower mass due to semi-leptonic b decays and final state radiation. X_{hh} effectively acts as
²³⁴⁰ a χ^2 measurement of the consistency of the two Higgs candidate masses with the signal hypothesis. The
²³⁴¹ denominators of each term ($0.1 M$) give the uncertainty on the mass measurement for the large radius
²³⁴² jets. Events are required to satisfy $X_{hh} < 1.6$.

²³⁴³ Before making the requirement on X_{hh} , the masses of the Higgs candidates are corrected for semi-

leptonic b decays using muons with the criteria outlined in the previous section. Any muons within a $\Delta R < 0.2$ of a b -tagged track jet (as described in the next section) have their four-momenta added to the four-momentum of the Higgs candidate. This correction does not affect the pre-selection requirements but does affect the X_{hh} requirement and the final invariant mass distribution used.

7.5.2 b -TAGGING REQUIREMENTS

The last requirement applied is on the number of b -tagged track jets. There are two signal regions defined. The first requires exactly four b -tagged track jets, two in each Higgs candidate (known as the $4b$ signal region). At high resonance masses, this requirement is inefficient, so an additional signal region requiring only three b -tagged track jets is also defined (known as the $3b$ signal region). While this has a larger background it is also more efficient for high resonance masses. For both signal regions, the MV_{2c2o} algorithm, where the training sample for the algorithm has 20% charm events is used. More details for this algorithm can be found in Chapter 2.

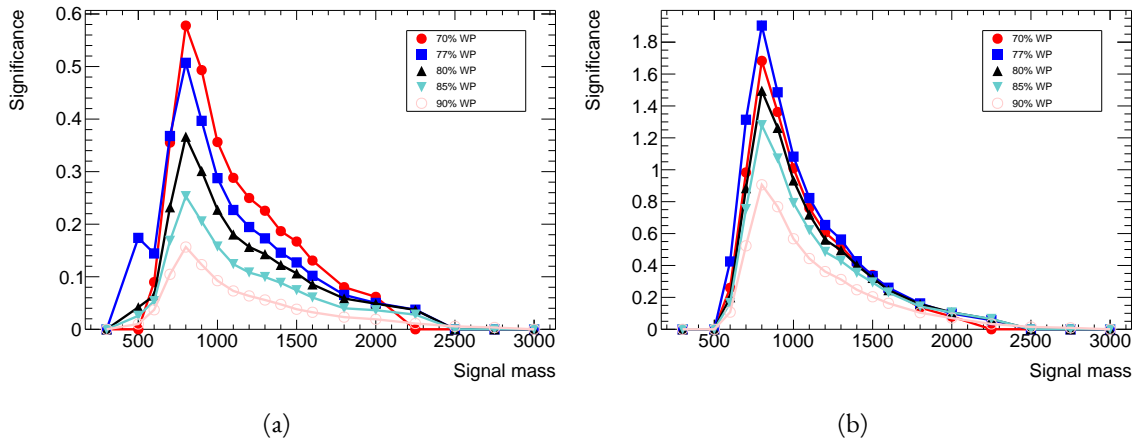


Figure 7.8: Estimated significance as a function of signal mass for RSG $c = 1$ models in the $3b$ (a) and $4b$ (b) regions for different b -tagging efficiency working points

Once the algorithm is selected, an efficiency working point must also be chosen. This working point defines the efficiency with which true b -jets are tagged and also fixes the overall background rejection of the algorithm. Higher efficiency working points accept more true b -jets but also allow for more background. Five different working points (70%, 77%, 80%, 85%, 90%) are tested. With each working

2360 point, the full data driven background estimation method is run to quantify the amount of background
 2361 that will be present in the final signal region. The significance is quantified using the median discovery
 2362 significance for signal and background with Poisson errors, given in equation 7.3 [107].

$$Z = \sqrt{2 \left((s + b) \ln \left(1 + \frac{s}{b} \right) - s \right)} \quad (7.3)$$

2363 Here, s is the expected number of signal events and b is the expected number of background events. This
 2364 formula is derived using Poisson statistics with errors on both the signal and background. It is used be-
 2365 cause it is valid in the regime where s and b are of the same order. Note that in the limit where s is much
 2366 smaller than b , this equation reduces to the more well known s/\sqrt{b} . Figure 7.8 shows the estimated sig-
 2367 nificance as a function of signal mass in RSG $c = 1$ models for the $3b$ and $4b$ signal regions. The 77%
 2368 working point gives the best performance over a wide range of masses in the $4b$ signal region. As this is
 2369 the region which contributes the most to the total discovery significance, the 77% efficiency working
 2370 point is chosen for the analysis.

2371 7.5.3 SELECTION EFFICIENCY

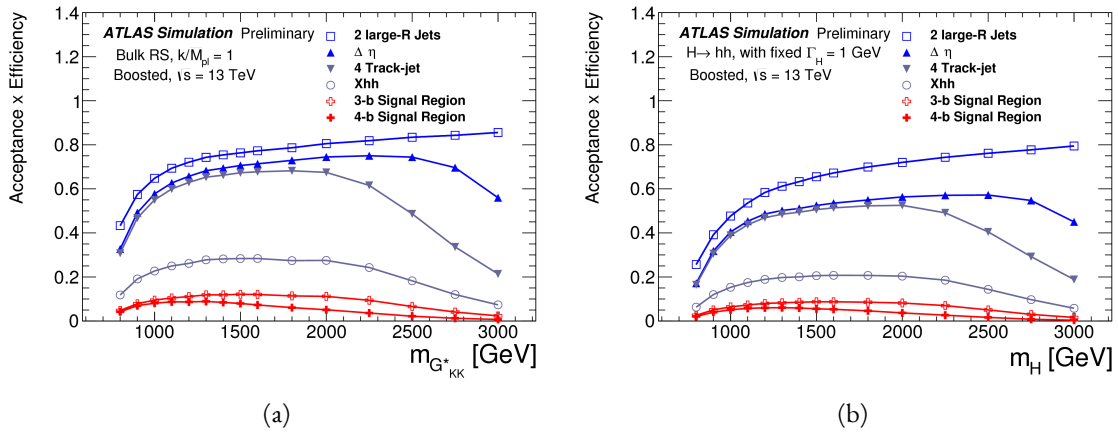
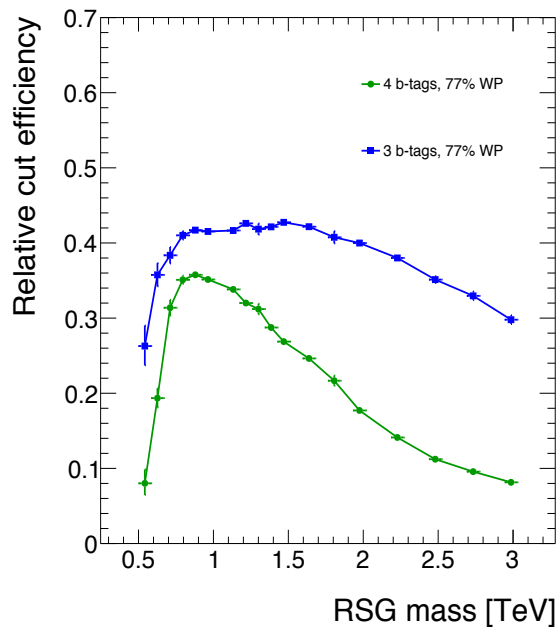


Figure 7.9: Acceptance \times efficiency as a function of mass for (a) RSG and (b) narrow heavy scalar signal models [108].

2372 Figure 7.9 shows the product of acceptance and efficiency as a function of mass for both the RSG and
 2373 narrow heavy scalar resonance signal models. After $m_X > 1$ TeV, the efficiency of the $4b$ requirement

2374 begins to decline. After $m_X > 2$ TeV, the efficiency of requiring two track jets in each Higgs candidate
 2375 begins to decline as well. Both of these behaviors illustrate the difficulty of resolving the merged decay
 2376 products at high mass. More details on the degradation of the b -tagging efficiency at high masses are
 2377 shown in appendix A.

2378 Figure 7.10 shows a more detailed comparison of the signal efficiency in the $3b$ vs $4b$ signal regions for
 2379 the RSG model. The efficiencies shown here are relative to all prior selection requirements.



2380 Figure 7.10: Efficiency of requiring 3 or 4 b -tagged track jets vs. RSG mass. The efficiency quoted is relative to the
 2381 previous selection requirements (rather than an absolute efficiency).

2382 The final discriminating variable used in the boosted analysis is M_{2J} , the invariant mass of the two
 2383 Higgs candidates. In order to improve the mass resolution, the four-momenta of each Higgs candidate
 2384 are scaled by m_h/M_J . The effect of this correction is small in the boosted analysis but is done for consistency
 with the resolved selection. Table 7.2 shows the effect of the selection requirements on signal and
 background simulations as well as data.

Selection	Data	$m_{G_{KK}^*} = 1\text{TeV}$	$m_{G_{KK}^*} = 2\text{TeV}$	$t\bar{t}$	$Z+\text{jets}$
$N(\text{fiducial large-R jets}) \geq 2$	2202396	23.3	0.48	32345.2	4255.7
leading large-R jet $p_T > 350\text{ GeV}$	1873741	22.9	0.48	26511.7	3649.9
Both large-R jet $m > 50\text{ GeV}$	1854625	21.2	0.47	24369.8	3575.8
Both large-R jet $p_T < 1500\text{ GeV}$	1853601	21.2	0.46	24346.5	3572.9
$ \Delta\eta(JJ) < 1.7$	1435273	20.8	0.44	20751.0	3265.8
≥ 2 track-jets per large-R jet	1224727	19.8	0.40	18234.5	2692.6
$3 b\text{-tags}, X_{hh} < 1.6$	316	3.4	0.067	46.7	2.0
$4 b\text{-tags}, X_{hh} < 1.6$	20	2.9	0.030	1.4	0.0

Table 7.2: Effect of boosted selection on data, RSG signal models, $t\bar{t}$, and $Z+\text{jets}$. The numbers from simulation are normalized with the MC generator cross section and do not take into account the data driven estimates described in section 7.6 [109].

2385 7.6 DATA-DRIVEN BACKGROUND ESTIMATION

2386 The largest background to this final state is QCD multijet production, constituting 80-90% of the to-
 2387 tal background. Because of the difficulties in modeling higher order QCD processes, this background is
 2388 estimated with a fully data-driven method. The only other non-negligible background is $t\bar{t}$, constituting
 2389 the other 10-20%. Due to the presence of $t\bar{t}$ in the sideband region where the QCD background will be
 2390 estimated, the normalization of the QCD and $t\bar{t}$ backgrounds are simultaneously estimated.

2391 7.6.1 MASS REGION DEFINITIONS

2392 The first step in the data-driven background estimate is to define a sideband mass region where the
 2393 background normalization can be derived. Additionally, a control region is defined where the back-
 2394 ground estimate can be validated. The control (CR) and sideband (SB) regions are defined using a radial
 2395 distance in the two-dimensional large-R jet mass plane, R_{hh} , which is defined in equation 7.4.

$$R_{hh} = \sqrt{(M_J^{\text{lead}} - 124\text{ GeV})^2 + (M_J^{\text{sublead}} - 115\text{ GeV})^2} \quad (7.4)$$

2396 Events in the sideband region are required to fail the signal region $X_{hh} < 1.6$ requirement and have
 2397 $R_{hh} > 35.8\text{ GeV}$. The control region consists of those events which are not in the signal or sideband

[§]The $Z+\text{jets}$ background is a sub-percent level contribution

regions. Figure 7.11 shows the definition of the signal, control, and sideband mass regions. Table 7.3 sum-

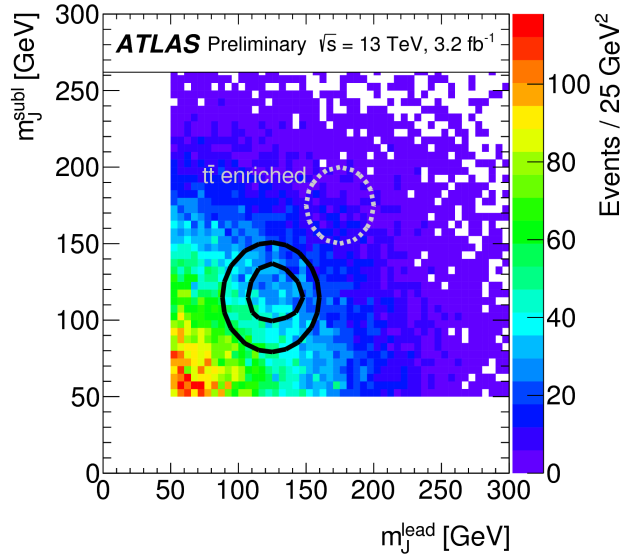


Figure 7.11: M_J^{sublead} vs. M_J^{lead} in a 2 b -tag data sample. The signal region is defined by the inner black contour ($X_{hh} < 1.6$) and the sideband region is defined by the outer contour ($R_{hh} > 35.8 \text{ GeV}$). The region between the black contours is the control region. The mass region which is enriched in $t\bar{t}$ background is also shown for illustration. [108]

2398

2399 marizes the mass region selections for the three different regions used in the analysis.

Region	Requirement	Notes
Signal Region (SR)	$X_{hh} < 1.6$	-
Control Region (CR)	$R_{hh} < 35.8 \text{ GeV}$ and $X_{hh} > 1.6$	Used for validation of background estimates
Sideband Region (SB)	$R_{hh} > 35.8 \text{ GeV}$	Used to derive background normalization

Table 7.3: Mass region definitions used for background estimation

2400 7.6.2 BACKGROUND ESTIMATION

2401 The method for estimating the background in this analysis is similar to the ABCD method presented
 2402 in Chapter 5. In this case, the two handles used to define different regions for the estimate are the num-
 2403 ber of b -tagged track jets and the mass regions. A region requiring exactly two b -tagged track jets in one

2404 large-R jet (referred to as the 2-tag or 2*b* region) is defined for use in the background estimate. The num-
2405 ber of expected background events in the 3*b* and 4*b* signal regions is then given by equation 7.5.

$$N_{\text{bkg}}^{\text{3(4)-tag,SR}} = \mu_{\text{Multijet}} N_{\text{Multijet}}^{\text{2-tag,SR}} + \beta_{t\bar{t}} N_{t\bar{t}}^{\text{3(4)-tag,SR}} + N_{Z+\text{jets}}^{\text{3(4)-tag,SR}} \quad (7.5)$$

2406 In this equation, $N_{\text{bkg}}^{\text{3(4)-tag}}$ is the expected number of background events in the 3*b* or 4*b* signal regions.
2407 $N_{\text{Multijet}}^{\text{2-tag}}$ is the number of multijet events in the 2-tag region. $N_{t\bar{t}}^{\text{3(4)-tag}}$ is the number of $t\bar{t}$ events
2408 predicted in the MC for the 3*b* or 4*b* signal region, and the variable is similarly defined for the $Z+\text{jets}$
2409 background. The $\beta_{t\bar{t}}$ parameter is a scale factor used to correct the normalization of the $t\bar{t}$ estimate in
2410 the signal region. μ_{Multijet} is an extrapolation factor that is derived in the sideband region and used to
2411 estimate the ratio of 2-tag events to 3(4)-tag events in the signal region. It is defined in equation 7.6.

$$\mu_{\text{Multijet}} = \frac{N_{\text{Multijet}}^{\text{3(4)-tag,SB}}}{N_{\text{Multijet}}^{\text{2-tag,SB}}} = \frac{N_{\text{data}}^{\text{3(4)-tag,SB}} - \beta_{t\bar{t}} N_{t\bar{t}}^{\text{3(4)-tag,SB}} - N_{Z+\text{jets}}^{\text{3(4)-tag,SB}}}{N_{\text{data}}^{\text{2-tag,SB}} - \beta_{t\bar{t}} N_{t\bar{t}}^{\text{2-tag,SB}} - N_{Z+\text{jets}}^{\text{2-tag,SB}}} \quad (7.6)$$

2412 The $t\bar{t}$ scale factor ($\beta_{t\bar{t}}$) and the QCD multijet extrapolation factor (μ_{Multijet}) are estimated together in
2413 a simultaneous fit in the sideband region. Then, the number of events in the 2-tag signal region is used,
2414 along with the $t\bar{t}$ estimate in the 3*b* and 4*b* signal regions and μ_{Multijet} , to estimate the total number of
2415 background events in the two final signal regions. The shape of the final discriminant $M_{2,J}$ is also taken
2416 from the 2-tag signal region where there are more statistics. This method is illustrated graphically in
2417 figure 7.12.

2418 In the 3*b* region, the fit yields values of $\mu_{\text{Multijet}} = 0.160 \pm 0.03$ and $\beta_{t\bar{t}} = 1.02 \pm 0.09$. In the 4*b*
2419 region, the fit gives $\mu_{\text{Multijet}} = 0.0091 \pm 0.0007$ and $\beta_{t\bar{t}} = 0.82 \pm 0.39$. The uncertainties quoted
2420 are statistical only. The larger uncertainties in the 4*b* values indicate the lower statistics available in that
2421 region.

2422 Figure 7.13 shows the distributions of data and background estimates in the 3*b* and 4*b* sideband re-
2423 gions after the background fit has been done. The normalizations are constrained from the fit to match
2424 that of the data, but good modeling of the shape of the mass of the leading large-R jet is seen as well. The
2425 shapes of the kinematic distributions in the 4*b* region are taken from the 3*b* region due to the better MC

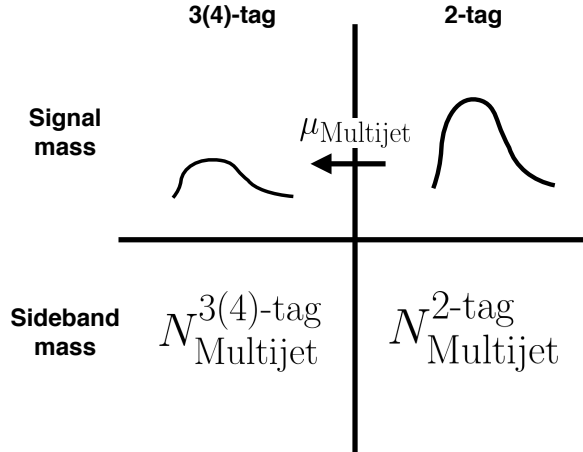


Figure 7.12: An illustration of the data-driven background estimation technique for the boosted analysis

²⁴²⁶ statistics in that region.

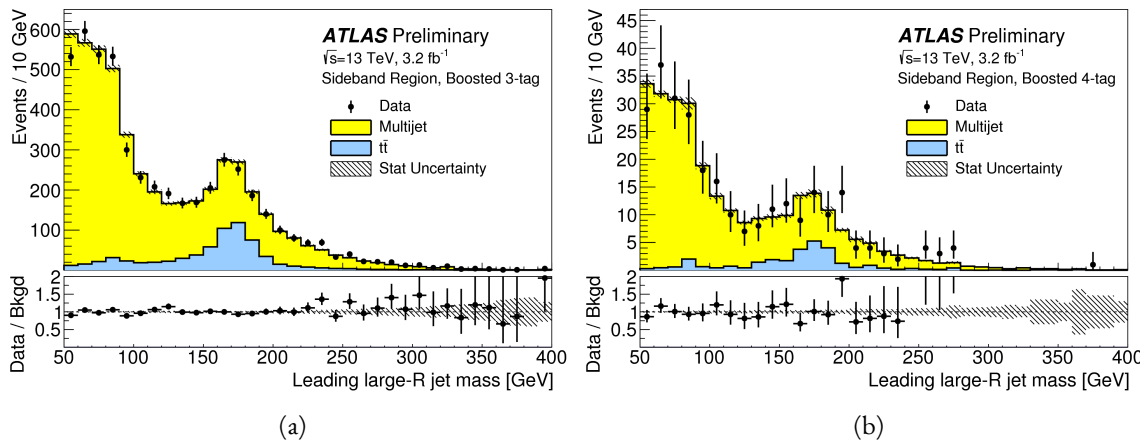


Figure 7.13: Leading large-R jet mass in the 3b (a) and 4b (b) sideband regions. The multijet and $t\bar{t}$ backgrounds are estimated using the data-driven methods described above. Because their normalizations are derived in the sideband region, the total background normalization is constrained by default to match the normalization of the data [108].

²⁴²⁷ 7.6.3 BACKGROUND SHAPE FIT

²⁴²⁸ As mentioned in the previous section, the background shape in the 3-tag and 4-tag signal regions is
²⁴²⁹ taken from the 2-tag signal mass region. Due to the limited statistics available, the background shapes are

2430 additionally smoothed after being extrapolated to the 3-tag and 4-tag signal regions. Only the data in the
 2431 range $900 < M_{2J} < 2000$ GeV is included in the fit due to the limited statistics available above 2 TeV.
 2432 Both the $t\bar{t}$ and QCD multijet background are independently fit with an exponential shape, $y = e^{ax+b}$.
 2433 Other shapes are considered and used for the systematic uncertainties. Table 7.4 shows the fit values for
 2434 the parameters. Because both the 3b and 4b QCD shapes come from the 2-tag region, the slopes derived
 2435 are very similar.

	a	b
QCD (4b)	0.00545 ± 0.00021	5.44 ± 0.24
$t\bar{t}$ (4b)	0.00746 ± 0.00021	4.88 ± 0.36
QCD (3b)	0.00545 ± 0.00021	8.30 ± 0.24
$t\bar{t}$ (3b)	0.00746 ± 0.00021	8.58 ± 0.36

Table 7.4: Parameters derived for exponential fit to background M_{2J} shape in the 3b and 4b signal regions [109]

2436 7.6.4 VALIDATION OF BACKGROUND ESTIMATE

2437 The background estimate can be validated by using the method to estimate the number of events in
 2438 the control mass region rather than the signal mass region. Figure 7.14 shows the M_{2J} distribution in
 2439 the 3b and 4b control regions, comparing data and background estimates. In both cases, both the back-
 2440 ground shape and normalization are consistent with the data, indicating good agreement. The ratio of
 2441 data to the background estimates is also fit to a line in the figure to test for any shape difference. The
 2442 slope of the line is within 1σ (from the fit uncertainties) of flat, further indicating that the data is consis-
 2443 tent with the background estimate in the control region.

2444 Table 7.5 shows the yields in data and background estimates in the 3-tag and 4-tag sideband and con-
 2445 trol regions. Again, here, it can be seen that the total number of predicted background events from the
 2446 data driven method is consistent with the number of data events in the region.

2447 7.7 SYSTEMATIC UNCERTAINTIES

2448 The systematic uncertainties in this analysis can be divided into two broad categories. The first type
 2449 is uncertainties associated with the modeling of the signal processes. The second type of uncertainty is

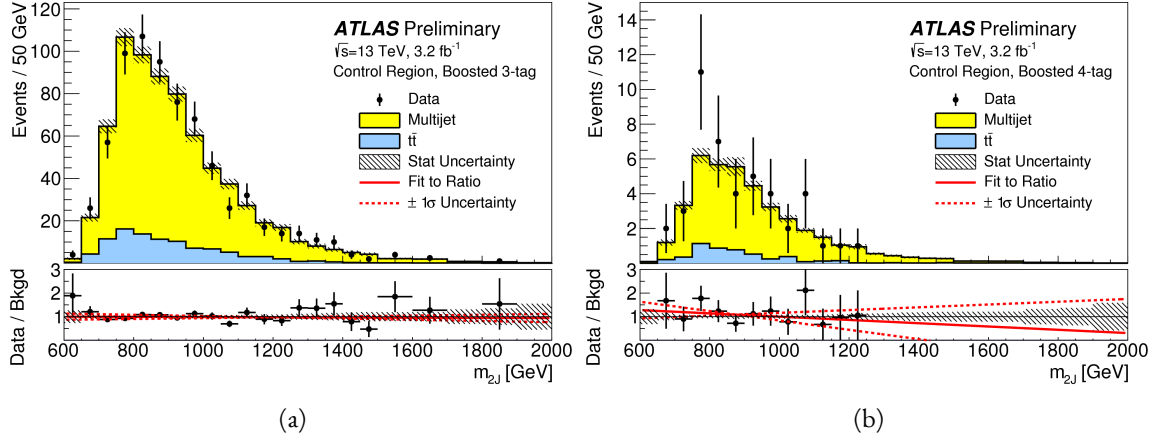


Figure 7.14: Di-jet invariant mass (M_{2J}) in the 3b (a) and 4b (b) control regions. The multijet and $t\bar{t}$ backgrounds are estimated using the data-driven methods described above [108].

Sample (3-tag)	Sideband Region	Control Region
Multijet	4328 ± 27	607 ± 10
$t\bar{t}$	683.5 ± 8.1	99.6 ± 3.1
$Z+jets$	31.8 ± 3.7	7.7 ± 1.8
Total	5043 ± 28	715 ± 11
Data	5043	724
Sample (4-tag)	Sideband Region	Control Region
Multijet	247.4 ± 1.5	34.7 ± 0.6
$t\bar{t}$	28.4 ± 1.5	5.1 ± 0.7
$Z+jets$	3.4 ± 1.2	0.6 ± 0.5
Total	279.2 ± 2.5	40.3 ± 1.0
Data	279	45

Table 7.5: The number of events in data and predicted background events in the boosted 3-tag and 4-tag sideband and control regions. The uncertainties shown are statistical only. [108]

2450 associated with both the shape and normalization of the background prediction.

2451 7.7.1 SIGNAL MODELING UNCERTAINTIES

2452 The signal modeling uncertainty has three main components: theoretical uncertainty on the accep-
2453 tance, experimental uncertainties on the large-R jets, and experimental uncertainties on the track jets

2454 related to b -tagging. In this analysis the experimental uncertainties are the most significant.

2455 The first uncertainty on signal modeling is the theoretical uncertainty on the acceptance. As explained
2456 in section 5.6.1, there are four components to this uncertainty. The first is related to missing higher order
2457 terms from the matrix element calculations which is estimated by varying the QCD renormalization and
2458 factorization scales. The second is uncertainty due to the PDF set used. The third is a generator uncer-
2459 tainty which is estimated by modifying the generator used to model the underlying event and hadroniza-
2460 tion. Finally, there is an uncertainty associated with the modeling of the initial state and final state radia-
2461 tion (ISR/FSR). The total theoretical uncertainty on the signal yield is 3%, and this is dominated by the
2462 ISR/FSR modeling.

2463 There are uncertainties on the large-R jets in both the jet energy scale (JES) and jet energy resolution
2464 (JER) as well as the jet mass scale (JMS) and jet mass resolution (JMR). These are evaluated using $\sqrt{s} =$
2465 8 TeV data from Run 1 of ATLAS and extrapolated to the Run 2 beam and detector conditions using
2466 MC[¶]. The details of these uncertainties can be found in reference [110].

2467 Uncertainties on the track jets are related to the b -tagging efficiency. The total uncertainty on the sig-
2468 nal yield due to b -tagging is evaluated by propagating variations of the b -tagging efficiency through the
2469 boosted selection requirements. The uncertainties are calculated jet-by-jet and parameterized as a func-
2470 tion of b -jet p_T and η [88]. For high p_T b -jets (with $p_T > 300$ GeV), the uncertainties are extrapolated
2471 using MC simulation from the lower p_T b -jets [111].

2472 Table 7.6 shows the systematic uncertainties on the signal normalization for models with $m_{G_{KK}^*} =$
2473 1.5 TeV and both $c = 1$ and $c = 2$ as well as a narrow width heavy scalar. The dominant uncertainty
2474 comes from b -tagging and this uncertainty is larger in the 4-tag region than the 3-tag region.

2475 7.7.2 BACKGROUND UNCERTAINTIES

2476 Uncertainties on the QCD multijet background normalization and shape are estimated using the con-
2477 trol mass region. As shown previously, the background predictions in the control region match with the
2478 data yields within the statistical uncertainty in both the 3-tag and 4-tag control regions. As an additional

[¶]The uncertainties are correspondingly larger due to the uncertainty of this extrapolation.

Source	Background		G_{KK}^*	H
	$c = 1$	$c = 2$		
Luminosity	-	5.0	5.0	5.0
3-tag				
JER	< 1	< 1	< 1	< 1
JES	2	< 1	< 1	< 1
JMR	1	12	12	11
JMS	5	14	13	17
b -tagging	1	23	22	23
Theoretical	-	3	3	3
Multijet Normalization	3	-	-	-
Statistical	2	1	1	1
Total	7	31	30	33
4-tag				
JER	< 1	< 1	< 1	< 1
JES	< 1	< 1	< 1	< 1
JMR	4	12	13	13
JMS	5	13	13	14
b -tagging	2	36	36	36
Theoretical	-	3	3	3
Multijet Normalization	14	-	-	-
Statistical	3	1	1	1
Total	15	42	42	43

Table 7.6: Summary of systematic uncertainties in the total background and signal event yields (expressed in %) in the boosted 3-tag and 4-tag signal regions. Systematic uncertainties on the signal normalization are shown for models with $m_{G_{\text{KK}}^*} = 1.5$ TeV and both $c = 1$ and $c = 2$ as well as a narrow width heavy scalar.

2479 protection, the statistical uncertainty on the background prediction in the control region is assigned as a
 2480 systematic uncertainty on the normalization of the QCD background.

2481 Additional robustness tests are done by varying the definition of the control mass region and the b -
 2482 tagging requirements used to define the 2-tag sample. In all cases, the effect of the variations is found to
 2483 be within the statistical uncertainties on the background normalization in the control region.

2484 Shape uncertainties on the background are evaluated using two techniques. First, as shown in fig-
 2485 ure 7.14, the ratio between the data and background prediction is fit with a linear function. The uncer-

2486 tainties on the slope of this fit are assigned as shape uncertainties. An additional uncertainty is assigned
 2487 by using alternate power law fit functions for the smoothing of the background shape. Table 7.7 shows
 2488 the alternate shapes used. The largest difference between the nominal fit function and the alternates,
 2489 taking into account the 1σ uncertainty band on each fit as well, is taken as a shape uncertainty.

Functional Form
$f_1(x) = p_0(1 - x)^{p_1}x^{p_2}$
$f_2(x) = p_0(1 - x)^{p_1}e^{p_2 x^2}$
$f_3(x) = p_0(1 - x)^{p_1}x^{p_2}x$
$f_4(x) = p_0(1 - x)^{p_1}x^{p_2} \ln x$
$f_5(x) = p_0(1 - x)^{p_1}(1 + x)^{p_2}x$
$f_6(x) = p_0(1 - x)^{p_1}(1 + x)^{p_2} \ln x$
$f_7(x) = \frac{p_0}{x}(1 - x)^{p_1-p_2} \ln x$
$f_8(x) = \frac{p_0}{x^2}(1 - x)^{p_1-p_2} \ln x$

Table 7.7: Alternate fit functions used to model the M_{2J} distribution in the QCD multijet background. In the equations, $x = M_{2J}/\sqrt{s}$.

2490 The uncertainties on the $t\bar{t}$ background are obtained by propagating the various experimental varia-
 2491 tions (JES, JER, JMS, JMR, b -tagging) through the analysis selection requirements. Table 7.6 summarizes
 2492 the background uncertainties in the 3-tag and 4-tag regions.

2493 7.8 RESULTS

2494 Table 7.8 shows the observed yields in the 3-tag and 4-tag signal regions for the boosted analysis com-
 2495 pared to the predicted number of background events. In the 3-tag region, 316 events are observed with
 2496 a predicted background of 285 ± 19 . In the 4-tag region, 20 events are observed with a predicted back-
 2497 ground of 14.6 ± 2.4 . Figure 7.15 shows the M_{2J} distribution in the 3-tag and 4-tag regions. There are
 2498 some small excesses in the data, in particular in the 3-tag region around $M_{2J} \approx 900$ GeV and in the
 2499 region of $1.6 < M_{2J} < 2.0$ TeV. The significance of these excesses will be evaluated in the next chapter
 2500 in the statistical combination with the resolved results.

Sample	Signal Region (3-tag)	Signal Region (4-tag)
Multijet	235 ± 14	13.5 ± 2.4
$t\bar{t}$	48 ± 22	1.2 ± 1.0
$Z+jets$	2.0 ± 2.2	-
Total	285 ± 19	14.6 ± 2.4
Data	316	20
G_{KK}^* (1000 GeV), $c = 1$	3.4 ± 0.9	2.9 ± 1.1

Table 7.8: Observed yields in the 3-tag and 4-tag signal regions for the boosted analysis compared to the predicted number of background events Errors correspond to the total uncertainties in the predicted event yields. The yields for a graviton with $m_{G_{KK}^*} = 1$ TeV and $c = 1$ are also shown. [108]

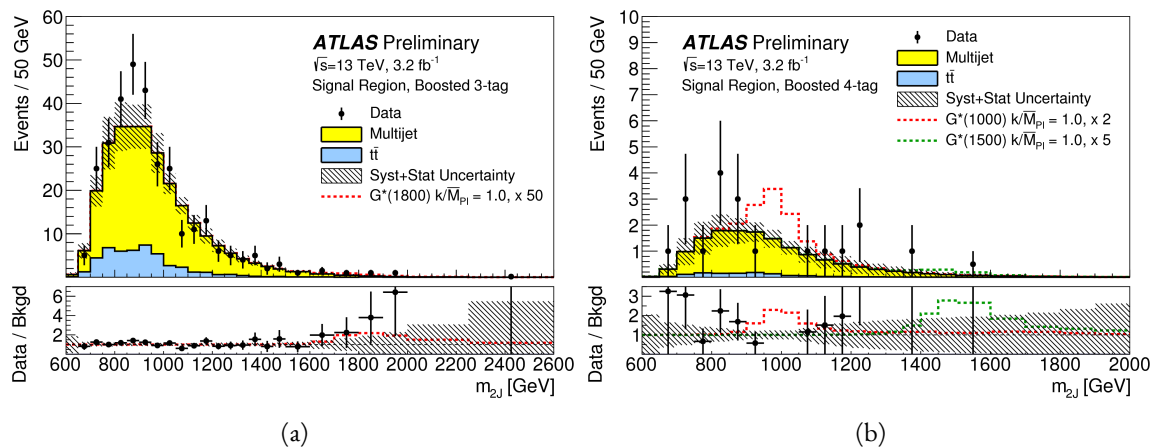


Figure 7.15: Di-jet invariant mass (M_{2J}) in the 3b (a) and 4b (b) signal regions. The multijet and $t\bar{t}$ backgrounds are estimated using the data-driven methods described above. In the 3b region, a graviton signal with $m_{G_{KK}^*} = 1.8$ TeV and $c = 1$ is overlaid, with the cross section multiplied by a factor of 50 so that the signal is visible. In the 4b region, signals with $m_{G_{KK}^*} = 1.0$ TeV and $m_{G_{KK}^*} = 1.5$ TeV are overlaid, both with $c = 1$ and the yields multiplied by factors of 2 and 5 respectively [108].

*There is no real ending. It's just the place where you stop
the story.*

Frank Herbert

8

2501

2502

Combined limits from boosted and resolved 2503 searches

2504

8.1 INTRODUCTION

2505

In order to cover the full mass range of possible resonances decaying to di-Higgs final states, two distinct tailored selections were produced. The resolved selection is more sensitive in the mass range of $400 < m_X < 1100$ GeV while the boosted selection is more sensitive to masses in the range $1100 < m_X < 3000$ GeV. Chapter 7 presents the details of the boosted selection and results. In setting limits on spin-2 Randall-Sundrum graviton (RSG) and narrow width heavy scalar (H) models, the results of the boosted selection are combined with the results of the resolved selection to cover the full mass range.

2512

This chapter presents limits on signal models resulting from the $X \rightarrow HH \rightarrow b\bar{b}b\bar{b}$ search in both

2513 the resolved and boosted selections. It first presents a brief overview of the resolved results that go into
 2514 the limit setting. Then, an overview of the statistical methods used for the search and limit setting is
 2515 given. Finally, limits on the RSG and heavy scalar models are presented.

2516 **8.2 RESOLVED RESULTS**

2517 The details of the resolved selection will not be presented here and can be found in reference [108]. In
 2518 basic terms, the selection searches for four $R = 0.4$ b-tagged calorimeter jets (where each pair of jets is
 2519 one Higgs candidate). This is distinct from the boosted methodology which searches for merged decay
 2520 products. The backgrounds to the resolved selection are the same as those presented in Chapter 7 for the
 2521 boosted analysis.

2522 Table 8.1 shows the results for data yields and expected background in the resolved signal region. Fig-
 2523 ure 8.1 shows the M_{2J} distribution in the resolved signal region. The total number of events is consis-
 2524 tent with the prediction and no significant excess is seen. One event in the boosted 4-tag signal is shared
 2525 with the resolved signal region and has a mass of 852 GeV.

Sample	Signal Region Yield
Multijet	43.3 ± 2.3
$t\bar{t}$	4.3 ± 3.0
$Z+jets$	-
Total	47.6 ± 3.8
Data	46
SM hh	0.25 ± 0.07
$G_{KK}^*(800 \text{ GeV}), c = 1$	5.7 ± 1.5

Table 8.1: Observed yields in the resolve selection 4-tag signal region compared to the predicted number of background events Errors correspond to the total uncertainties in the predicted event yields. The yields for a graviton with $m_{G_{KK}^*} = 800$ GeV and $c = 1$ are also shown. [108]

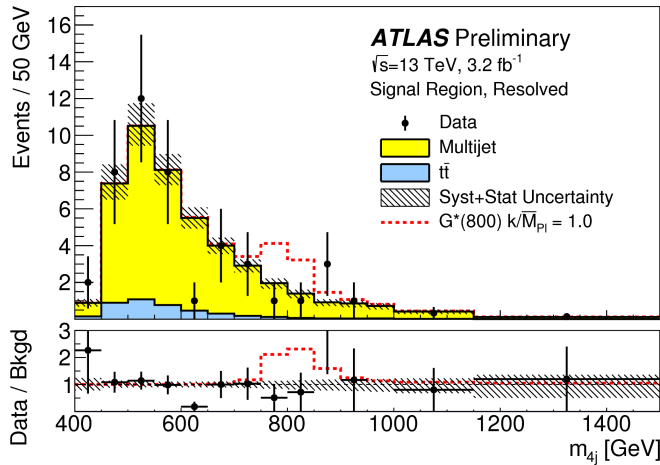


Figure 8.1: Di-jet invariant mass (M_{2J}) in the resolved signal region. A graviton signal with $m_{G_{KK}^*} = 800 \text{ GeV}$ and $c = 1$ is overlaid. [108].

2526 8.3 SEARCH TECHNIQUE AND RESULTS

2527 The statistical technique used for the search in this analysis is the same as that used in the $H \rightarrow WW^*$
 2528 analysis presented in section 3.6.2. The test statistic q_0 is used to define the p -values which measure the
 2529 compatibility of the data with the background-only hypothesis corresponding to a signal strength $\mu =$
 2530 0.

2531 Local p_0 values are computed to quantify the probability that the background could produce a fluc-
 2532 tuation greater than or equal to the one observed in the data. In the resolved analysis, no significant ex-
 2533 cesses are observed. The largest discrepancy with respect to the background only hypothesis occurs near
 2534 a resonance mass of 900 GeV and is found to be less than 2σ in significance.

2535 In the boosted selection, the largest local excess is a broad excess in the $3b$ signal region that begins
 2536 near $M_{2J} \approx 1.7 \text{ GeV}$. Assuming a G_{KK}^* with this mass and $c = 1.0$, the local significance of this excess
 2537 is 2.0σ .

2538 8.4 LIMIT SETTING

2539 In the absence of any significant excess observed in the data, limits on different signal models can be
 2540 set. This section describes the limit setting procedure and presents combined results of the resolved and

2541 boosted analyses.

2542 8.4.1 LIMIT SETTING PROCEDURE

2543 The procedure used for setting exclusion limits in this analysis is the CL_s method [112]. The first step
2544 in setting the limits is to define a test statistic which will be used. For limit setting, the test statistic is
2545 shown in equation 8.1.

$$\widetilde{q}_\mu = \begin{cases} -2 \ln \frac{L(\mu, \hat{\theta}(\mu))}{L(0, \hat{\theta}(0))} & \hat{\mu} < 0 \\ -2 \ln \frac{L(\mu, \hat{\theta}(\mu))}{L(\hat{\mu}, \hat{\theta})} & 0 \leq \hat{\mu} < \mu \\ 0 & \hat{\mu} > \mu \end{cases} \quad (8.1)$$

2546 In the above equation, μ is the value of the signal strength under test, $\hat{\mu}$ is the best fit μ , $\hat{\theta}$ is the
2547 best fit value of the nuisance parameters, $\hat{\theta}$ is the best fit value of the nuisance parameters under the fixed
2548 μ value, and L is the Poisson likelihood of the data (as described in section 3.6.2).

2549 The test statistic \widetilde{q}_μ is constructed to protect against two interesting corner cases when setting the
2550 upper limit on the cross section. First, it protects against negative signal strengths μ which are unphys-
2551 ical. Second, it does not count excesses in the data larger than those expected by a signal strength μ as
2552 evidence against the μ hypothesis.

2553 The CL_s statistic is constructed by taking a ratio of two probabilities. CL_{s+b} is the probability that
2554 the signal+background hypothesis would produce a value of the test statistic that is less than or equal
2555 to the observed value*. CL_b is the probability that the background only hypothesis will pro-
2556 duce a value of the test statistics less than or equal to the observed. The CL_s statistic is then the ratio
2557 $\text{CL}_{s+b}/\text{CL}_b$. A 95% upper limit on the cross section is set at the value of μ that makes the CL_s statistic
2558 less than 5%.

2559 In practice, the limits are computed numerically within an asymptotic approximation for the distri-
2560 bution of the test statistic \widetilde{q}_μ . The details of this approximation can be found in reference [63].

2561 The resolved and boosted analyses are combined using a very simple procedure rather than a full sta-
2562 tistical combination. For each mass point tested, the limit which gives the most stringent constraint is

*Lower values of \widetilde{q}_μ mean better compatibility

2563 used. This means that for mass points below 1.1 TeV the resolved signal region is used, while at and
2564 above this point the combination of the orthogonal 3b and 4b boosted signal regions is used.

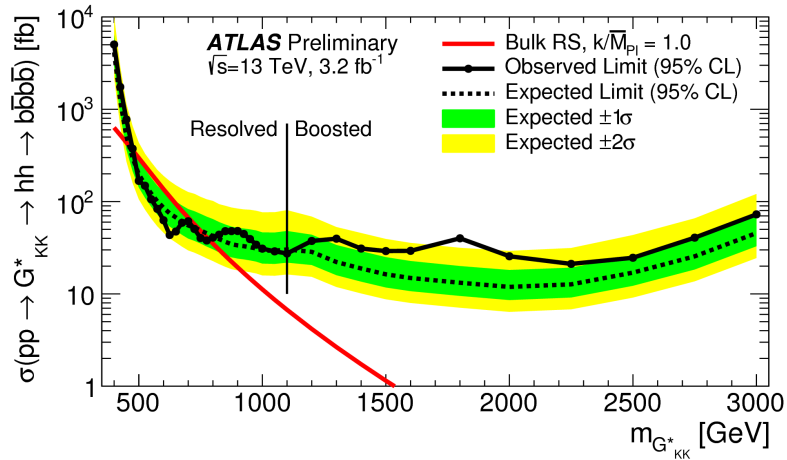
2565 **8.4.2 LIMIT SETTING RESULTS**

2566 Figure 8.2 shows the combined 95% upper bounds as a function of mass for three different models:

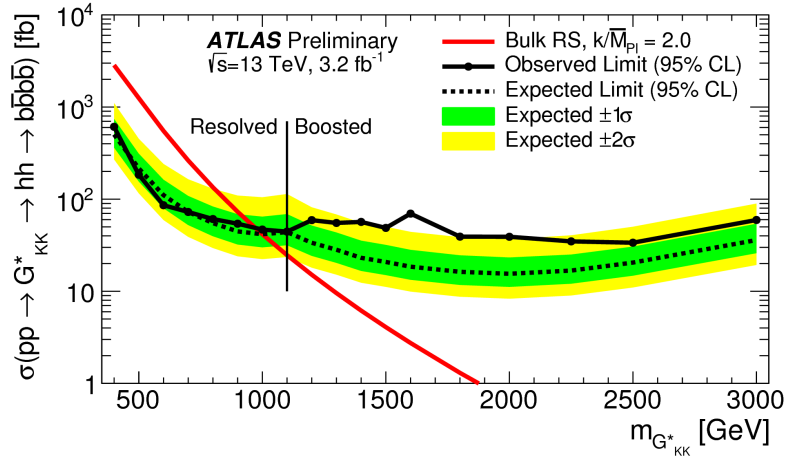
2567 G_{KK}^* with $c = 1$, G_{KK}^* with $c = 2$, and a narrow heavy scalar H .

2568 The cross section of $\sigma(pp \rightarrow G_{\text{KK}}^* \rightarrow hh \rightarrow b\bar{b}b\bar{b})$ with $c = 1$ is constrained to be less than 70 fb
2569 for masses in the range $600 < m_{G_{\text{KK}}^*} < 3000$ GeV. For the RSG model with $c = 2$, cross sections
2570 limits between 40 fb and 200 fb are set for the mass range of $500 < m_{G_{\text{KK}}^*} < 3000$ GeV. Masses in
2571 the range of $475 < m_{G_{\text{KK}}^*} < 785$ GeV are excluded with $c = 1$ (with an exclusion of the range 465
2572 to 745 GeV expected). Masses less than 980 GeV are excluded with $c = 2$ (with an exclusion for masses
2573 less than 1 TeV expected).

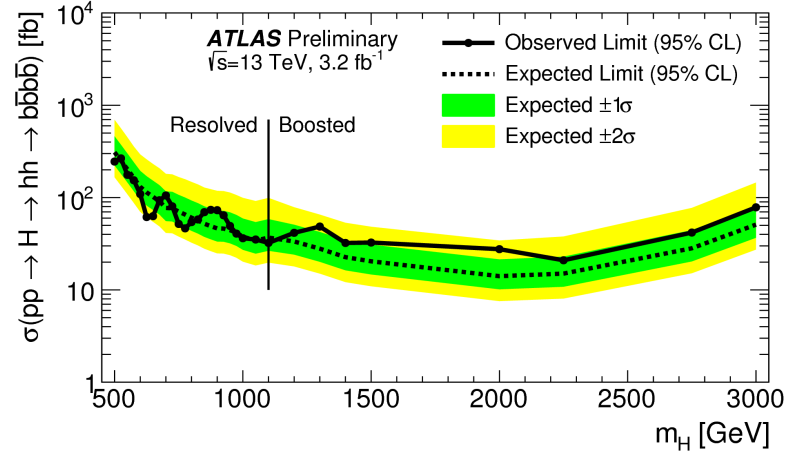
2574 In the heavy Higgs model, the cross section upper limits for $\sigma(pp \rightarrow H \rightarrow hh \rightarrow b\bar{b}b\bar{b})$ ranges from
2575 30 to 300 fb in the mass range of $500 < m_H < 3000$ GeV. The resolved analysis can also set an upper
2576 limit on the Standard Model di-Higgs production cross section discussed in chapter 3. The upper limit
2577 on $\sigma(pp \rightarrow hh \rightarrow b\bar{b}b\bar{b})$ in the Standard Model is constrained to be less than 1.22 pb.



(a) Bulk RS, $c = 1$



(b) Bulk RS, $c = 2$



(c) Spin-0 narrow-width H boson

Figure 8.2: Expected and observed upper limit as a function of mass for G^*_{KK} in the RSG model with (a) $c = 1$ and (b) $c = 2$, as well as (c) H with fixed $\Gamma_H = 1$ GeV, at the 95% confidence level in the CL_s method. [108]

2578

Part IV

2579

Looking ahead

9

2580

Conclusion

2581

2582 After being sought for many years at different collider experiments, the Higgs boson was discov-
2583 ered by the ATLAS and CMS experiments in 2012, confirming the leading theory for the source of elec-
2584 troweak symmetry breaking and filling in the last missing piece of the Standard Model. After its discov-
2585 ery, measurements of the particle's detailed properties and searches for new particles decaying to Higgs
2586 final states were both extremely important in constraining physics beyond the Standard Model. This dis-
2587 sertation presented this evolution through two results: the observation and measurement of the Higgs
2588 boson in the $H \rightarrow WW^* \rightarrow \ell\nu\ell\nu$ channel at $\sqrt{s} = 7$ TeV and $\sqrt{s} = 8$ TeV and a search for Higgs
2589 pair production in the $HH \rightarrow b\bar{b}b\bar{b}$ channel at $\sqrt{s} = 13$ TeV with the ATLAS detector in pp collisions
2590 at the Large Hadron Collider.

2591 In the $H \rightarrow WW^* \rightarrow \ell\nu\ell\nu$, results from both the discovery of the Higgs boson and the full
2592 ATLAS Run 1 dataset were presented. The Higgs boson was discovered with a 6.1σ significance in a
2593 combination of the $H \rightarrow \gamma\gamma$, $H \rightarrow ZZ4\ell$, $H \rightarrow WW^* \rightarrow \ell\nu\ell\nu$ with 4.2 fb^{-1} at $\sqrt{s} = 7$ TeV

and 5.2 fb^{-1} at $\sqrt{s} = 8 \text{ TeV}$. With the full 20.3 fb^{-1} at $\sqrt{s} = 8 \text{ TeV}$ and 4.2 fb^{-1} at $\sqrt{s} = 7 \text{ TeV}$, ATLAS achieved discovery level significance in the $H \rightarrow WW^*$ channel alone and obtained the first observation of vector boson fusion production in that channel. The combined signal strength is measured to be $\mu = 1.09^{+0.23}_{-0.21}$. The total observed significance of the $H \rightarrow WW^*$ process is observed to be 6.1σ (with 5.8σ expected). Advanced methods for background reduction and estimation, particularly in same-flavor lepton final states, are shown. The VBF signal strength is measured to be $\mu_{\text{VBF}} = 1.27^{+0.53}_{-0.45}$ with an observed significance of 3.2σ (with 2.7σ expected).

These results required many novel innovations. The increase of pileup interactions in the higher instantaneous luminosity LHC conditions of 2012 led to a degradation of missing transverse momentum resolution. As a result, the prominent $Z/\gamma^* + \text{jets}$ background of the same flavor $H \rightarrow WW^* \rightarrow \ell\nu\ell\nu$ final states increased greatly. New variables, including a track-based missing transverse momentum and a measurement of the balance between the dilepton system and recoiling jets, allowed for significant reduction of this background. In the VBF channel, selections were optimized to exploit the unique VBF final state topology. Incorporating these variables into a boosted decision tree technique allowed the analysis to exceed the 3σ observation threshold.

After the end of Run 1, the results of Higgs measurements from ATLAS were combined with those from CMS to produce the most precise measurements of the Higgs boson so far [113]. Figure 9.1 shows the combination of ATLAS and CMS data for the Higgs signal strength in and coupling measurements. In the signal strength measurements of gluon fusion and vector boson fusion, the $H \rightarrow WW^*$ channel provides the tightest constraints. Additionally, the Higgs coupling to W bosons is the most precisely measured with a relative uncertainty of 10%.

With the discovery of the Higgs firmly established and its properties measured, a natural next step was to search for new physics with Higgs final states. At $\sqrt{s} = 13 \text{ TeV}$, a search for Higgs pair production in the $b\bar{b}b\bar{b}$ final state with 3.2 fb^{-1} was conducted. A signal region optimized for the boosted final states arising from high mass resonances was constructed. This signal region utilized large-radius calorimeter jets and b -tagging with small radius track jets to maximize the signal acceptance. No significant excesses were observed, and upper limits on cross sections are placed for spin-2 Randall Sun-

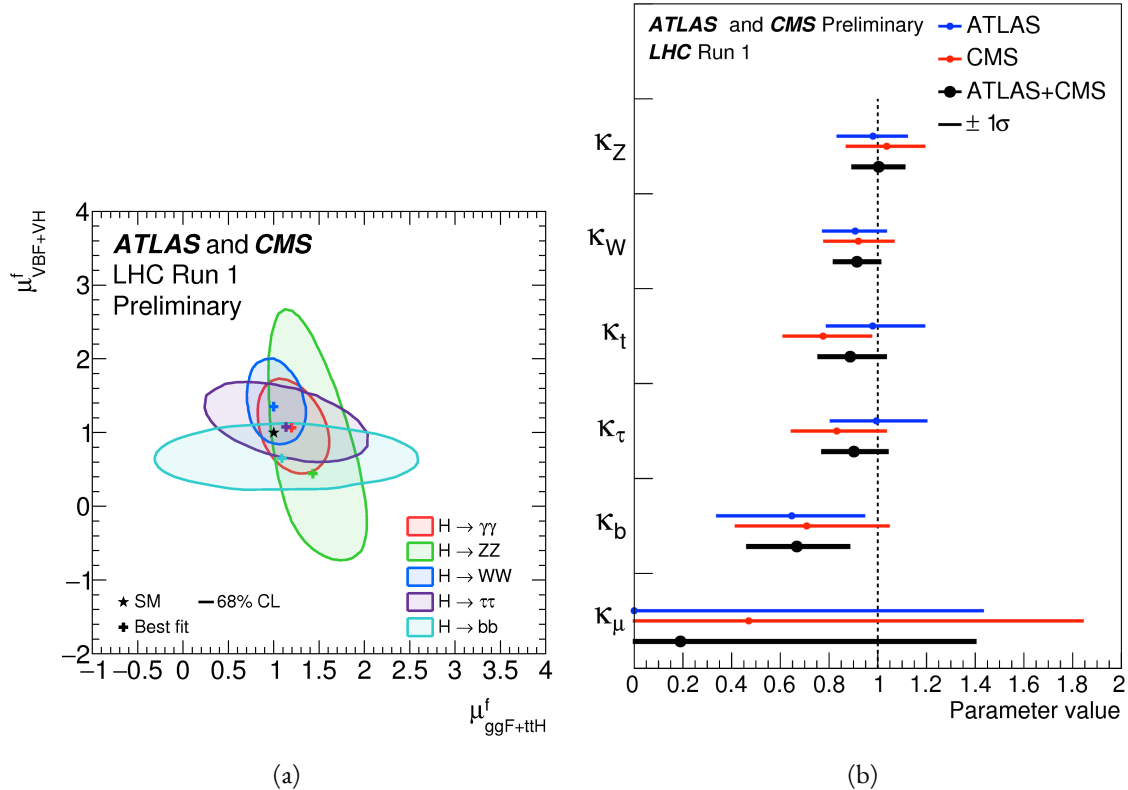


Figure 9.1: Combined ATLAS and CMS measurements in Run 1 for (a) Higgs signal strength in gluon fusion and VBF and (b) Higgs couplings normalized to their SM predictions

drum gravitons (RSG) and narrow spin-0 resonances. The increase in center of mass energy in Run 2 allowed this analysis to extend upper limits up to 3 TeV, while previous results from ATLAS in Run 1 only quotes limits up to 2 TeV. The cross section of $\sigma(pp \rightarrow G_{KK}^* \rightarrow hh \rightarrow b\bar{b}b\bar{b})$ with $k/\bar{M}_{\text{Pl}} = 1$ is constrained to be less than 70 fb for masses in the range $600 < m_{G_{KK}^*} < 3000$ GeV. For the RSG model with $k/\bar{M}_{\text{Pl}} = 2$, cross sections limits between 40 fb and 200 fb are set for the mass range of $500 < m_{G_{KK}^*} < 3000$ GeV. The cross section upper limits for $\sigma(pp \rightarrow H \rightarrow hh \rightarrow b\bar{b}b\bar{b})$ ranges from 30 to 300 fb in the mass range of $500 < m_H < 3000$ GeV.

While there has been a rigorous program of measurements and searches involving the Higgs, there is still much room for improvement at the High Luminosity LHC (HL-LHC) and beyond. The measured signal strength for VBF production in $H \rightarrow WW^*$ still has a relative error at the level of 40%, largely dominated by statistical uncertainty. Projections for the HL-LHC show that the uncertainty on the VBF signal strength can be reduced to approximately 15% with 3000 fb^{-1} [14, 15]. This uncertainty

2633 also assumes that theoretical uncertainties on the signal, which would be the largest contribution in this
 2634 dataset, remain as they are now. Improvements in the theoretical understanding of the Higgs signal
 2635 would also reduce the signal strength uncertainty dramatically. Such precision measurements allow for
 2636 measurements of the Higgs coupling to vector bosons precise to the few percent level, therefore giving
 2637 much power to constrain or discover new physics.

2638 The prospects for detection of resonant di-Higgs production at the HL-LHC are also quite promising.
 2639 Figure 9.2 shows projections for the discovery significance of RSG signals at the HL-LHC in the
 2640 $X \rightarrow HH \rightarrow b\bar{b}b\bar{b}$ search [115]. In all detector budget scenarios, a 1.5 TeV resonance is above or near
 2641 5σ significance, while a 2 TeV resonance is between 4-5 σ except for the lowest budget.

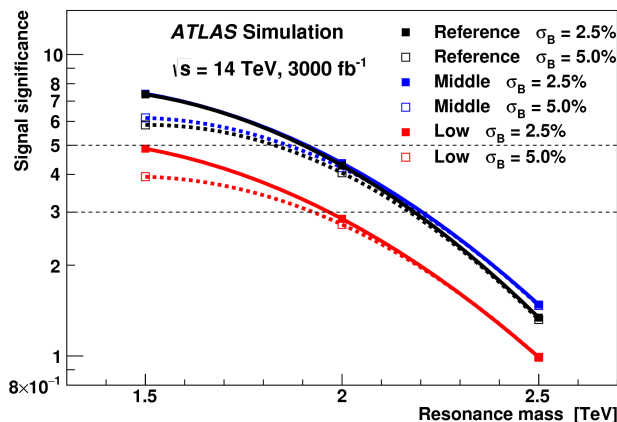


Figure 9.2: Discovery significance for RSG models at the HL-LHC in three different budget scenarios [115]. Systematic uncertainties on the background prediction (σ_B) of 2.5% and 5.0% are both tested.

2642 The Higgs will continue to be an incredibly powerful tool in the understanding of nature at the HL-
 2643 LHC and beyond. Through both precision measurements and searches, the nature of electroweak sym-
 2644 metry breaking will be better understood and the potential for the discovery of physics beyond the Stan-
 2645 dard Model has never been greater.

A

2646

2647

b-tagging performance at high p_T

2648 One of the limiting factors of the signal acceptance in the $X \rightarrow HH \rightarrow b\bar{b}b\bar{b}$ search at high res-
2649 onance masses is the degradation of the *b*-tagging efficiency for high p_T jets. This appendix presents a
2650 study of the underlying causes of this degradation.

2651 A.I CHANGES IN MV2 SCORE AT HIGH p_T

2652 The degradation of *b*-tagging at high p_T was studied in particular in the context of RSG models at
2653 high mass. Figure A.1 shows the p_T of the leading track jet inside of the leading calorimeter jet in RSG
2654 events. At high $m_{C_{KK}^*}$, the p_T spectrum of track jets is much harder than at lower masses due to the
2655 increased Higgs p_T .

2656 Figure A.2 shows the MV2c2o algorithm score for the leading and subleading track jets inside of the
2657 leading calorimeter jet. In both cases, it can be seen that at higher RSG masses the MV2 score shifts to-
2658 wards more background like (negative) values. Additionally, this effect is more pronounced in the lead-

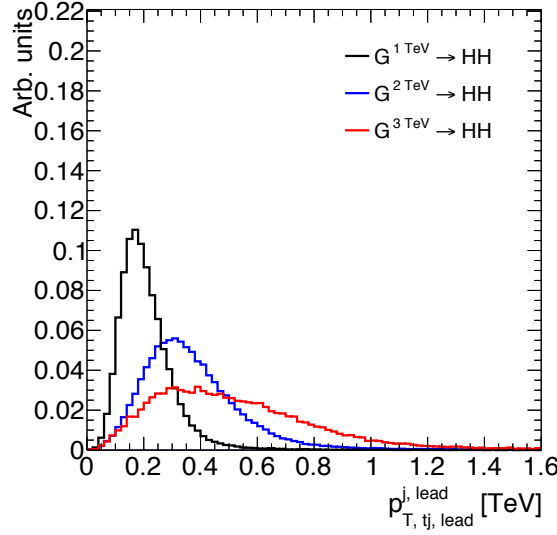


Figure A.1: p_T of the leading track jet in the leading calorimeter jet for different signal masses in RSG $c = 1$ models

2659 ing track jet than the subleading.

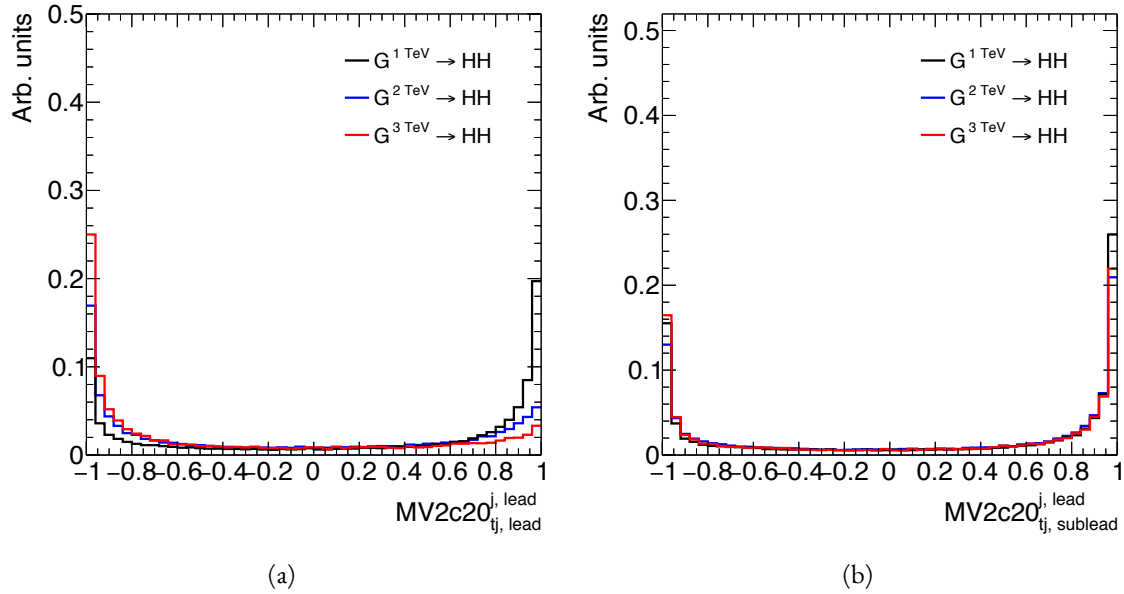


Figure A.2: MV2c20 score for the leading track jet (a) and subleading track jet (b) of the leading calorimeter jet for different signal masses in RSG $c = 1$ models

2660 To understand what is causing this change in the MV2c20 score, the same comparisons can be made
 2661 for the input variables of MV2c20. The focus in these comparisons will be on the leading track jet as
 2662 this is the one seen to have the largest difference in MV2 score. Figure A.3 shows the log likelihood ratio

2663 $\log(p_b/p_u)$ from the IP₃D (three dimensional impact parameter) algorithm. At higher masses, the IP₃D
 2664 likelihood ratio distribution does become more background-like.

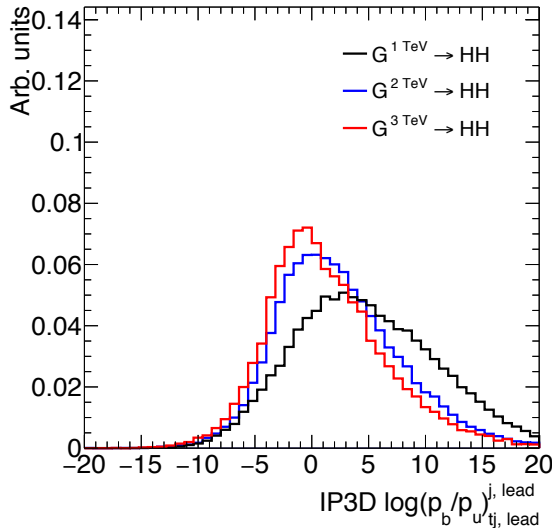


Figure A.3: IP₃D log-likelihood ratio ($\log(p_b/p_u)$) of the leading track jet in the leading calorimeter jet for different signal masses in RSG $c = 1$ models

2665 Figure A.4 shows the mass and number of tracks at the secondary vertex computed by the SV1 algo-
 2666 rithm. When there is no secondary vertex found, the algorithm assigns a default negative value for these
 2667 quantities. Both of these distributions show that there is a significantly larger fraction of jets where no
 2668 secondary vertex is found in the high mass samples compared to the $m_{G_{\text{KK}}^*} = 1 \text{ TeV}$ sample. The SV1
 2669 algorithm's inability to find a secondary vertex could be an important factor in the overall MV₂ score
 2670 shift, as this eliminates eight of the input variables that would normally contribute information to the
 2671 algorithm.

2672 Figure A.5 shows the same quantities for the JetFitter algorithm. In this case, there is also a change in
 2673 the fraction of jets which have their secondary vertices successfully reconstructed, but this change is not
 2674 as drastic as that seen in SV1. There is also an increase in the number of jets which have high values of
 2675 mass.

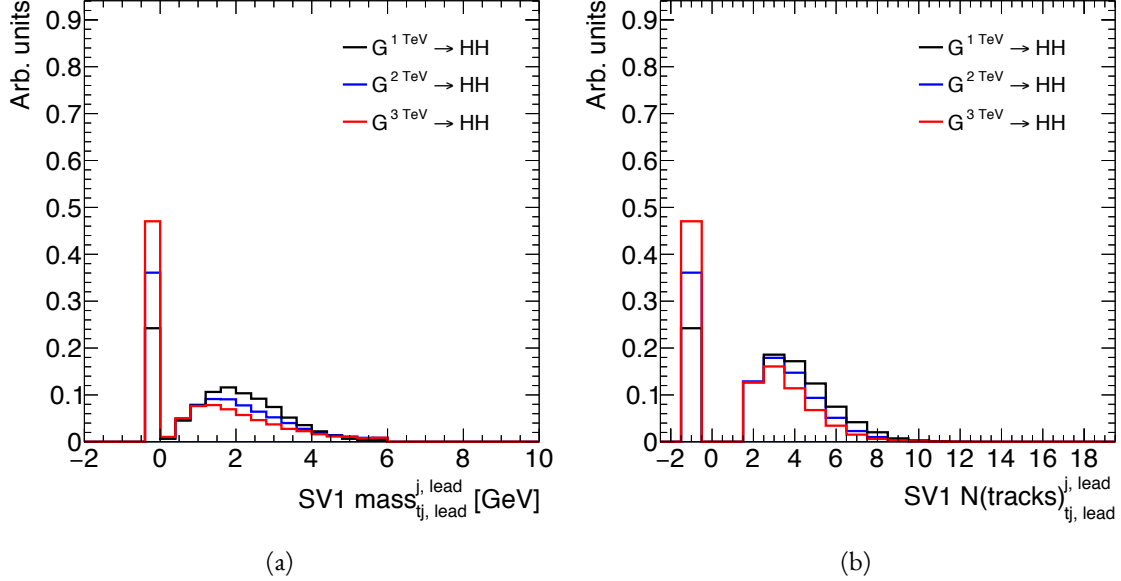


Figure A.4: Mass (a) and number of tracks (b) for the secondary vertices computed with the SV1 algorithm. When no secondary vertex is found, the quantities are assigned to default negative values.

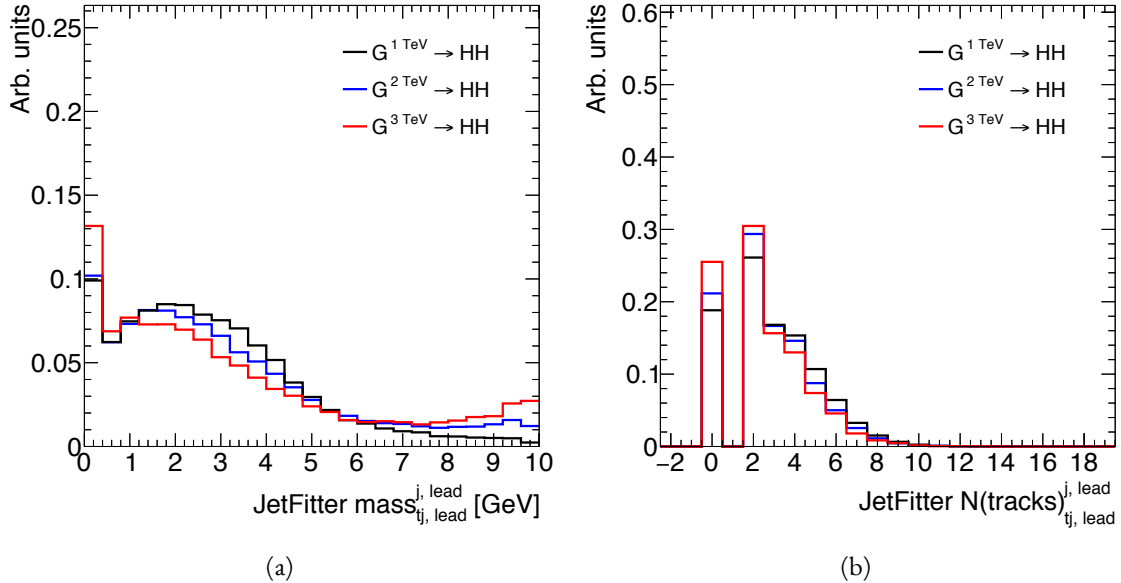


Figure A.5: Mass (a) and number of tracks (b) for vertices computed with the JetFitter algorithm. When no vertices are found, the quantities are assigned to default negative values.

2676 A.2 TAGGING EFFICIENCY BY INDIVIDUAL JET

2677 In the last section, the largest changes in MV₂ score were seen for the leading track jet inside the lead-
 2678 ing calorimeter jet. To confirm that the overall 4*b* tagging efficiency is indeed degrading because of degra-

2679 dation of the leading track jet efficiency, the tagging efficiency for each individual jet as a function of
 2680 mass can be compared. This is shown in figure A.6. The figure shows that the leading jet tagging effi-
 2681 ciency in both calorimeter jets degrades heavily, while the sub-lead jet tagging efficiency remains rela-
 2682 tively constant.

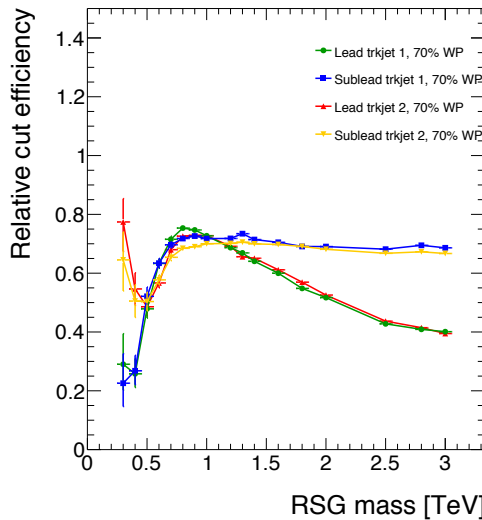


Figure A.6: MV2c20 b -tagging efficiency for each of the four track jets in the boosted $4b$ selection as a function of RSG mass for $c = 1$ models.

2683 A.3 EFFECT OF MULTIPLE b -QUARKS INSIDE ONE JET

2684 One hypothesis for why the efficiency of b -tagging the leading track jet degrades is that at high masses,
 2685 the b quarks get close enough together that both of them are inside of the leading track jet. Because MV2
 2686 is not tuned for tagging multiple b quarks inside one jet, the tagging efficiency could degrade. Figure A.7
 2687 shows MV2 scores and SV1 mass for cases where there are two b quarks at truth level within the radius
 2688 of the leading track jet compared to cases where there is only one true b^* . This figure suggests that the
 2689 presence of two b -quarks inside the leading jet is not the cause of the degradation in efficiency. There is a
 2690 change in the shape of the MV2 score distribution, but it is not nearly as pronounced as that seen in A.2

*When two truth b quarks are required in the leading jet, the subleading jet is required to have zero. When one is required for the leading, one is also required for the subleading.

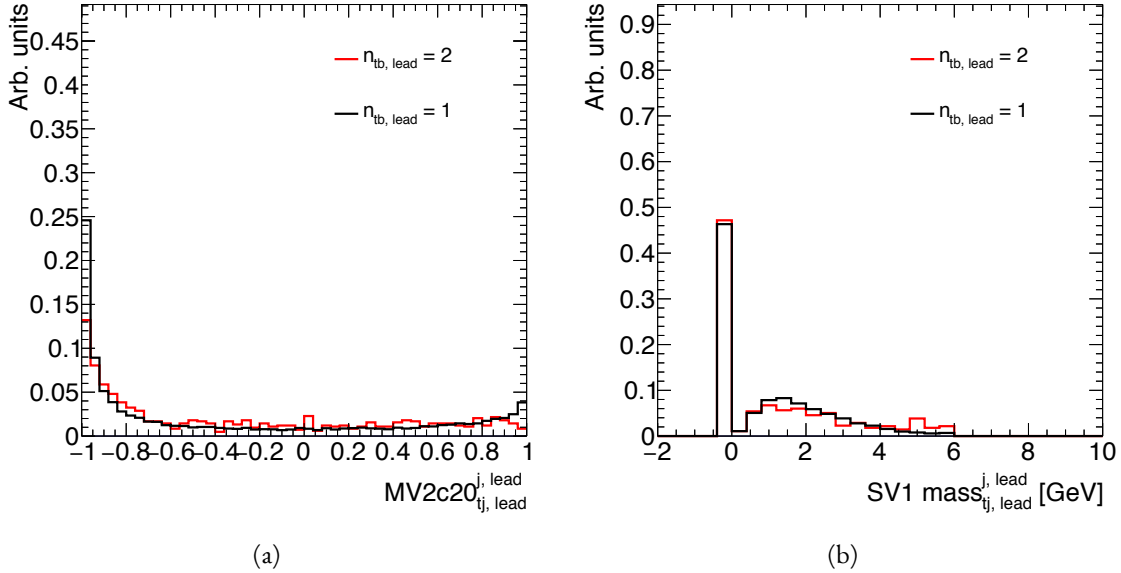


Figure A.7: MV2c20 score (a) and SV1 mass (b) for leading track jets with two truth b quarks ($n_{tb,\text{lead}} = 2$) compared to those with only one truth b ($n_{tb,\text{lead}} = 1$).

at higher masses. Additionally, the fraction of jets with no secondary vertex found is nearly identical in the track jets with two truth b -quarks.

2693 A.4 CHANGES IN TRACK QUALITY AT HIGH p_T

Another hypothesis for the degradation of the b -tagging efficiency is a decrease in track quality for high p_T b jets. One way to check the overall quality of the tracking inside the jet is to investigate quantities related to the leading track inside of the track jet. Figure A.8 shows the fit χ^2/n_{DOF} and number of hits in the pixel detector for the leading track of the leading track jet. In both cases, the figure shows that in higher mass samples, the quality of the leading track inside of the track jet degrades substantially. The fit quality is lessened and the tracks have less hits in the pixel detector. This is likely due to the fact that at higher p_T , the B -hadron will sometimes live long enough to miss the IBL and first pixel layer, thus decreasing the number of hits on the track.

To check whether this is the cause for the shift in the MV2 score and the higher difficulty in reconstructing secondary vertices, jets whose leading track have at least four pixel hits are compared with those whose tracks have less than four pixel hits. The results for the MV2 score and SV1 mass are shown in

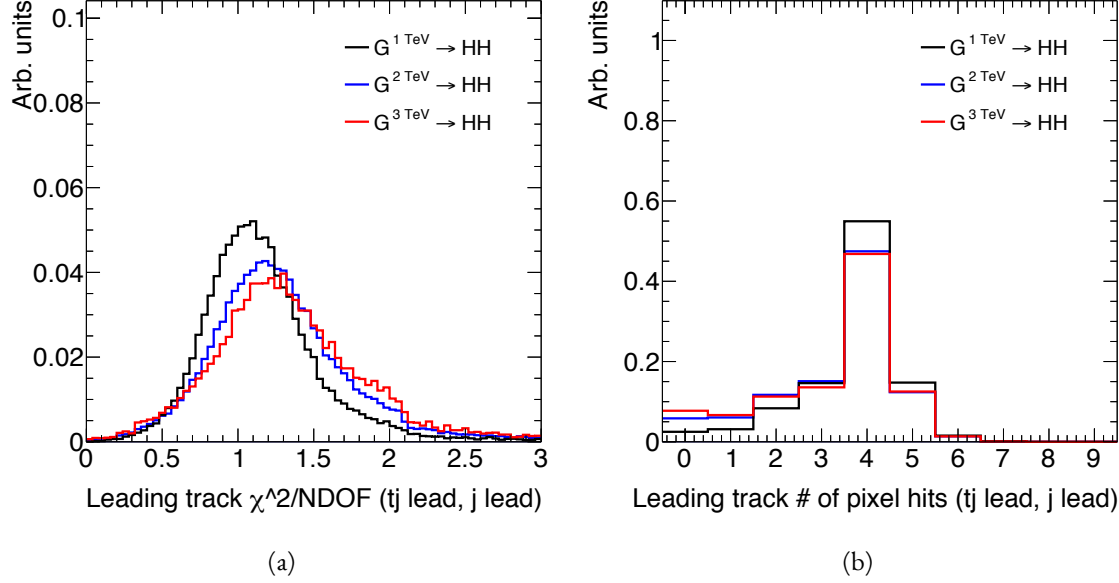


Figure A.8: Track fit χ^2/n_{DOF} (a) and number of pixel detector hits (b) for the leading track of the leading track jet in different mass RSG $c = 1$ samples

figure A.9. Track jets where the leading track does not have at least four pixel hits are more likely to not

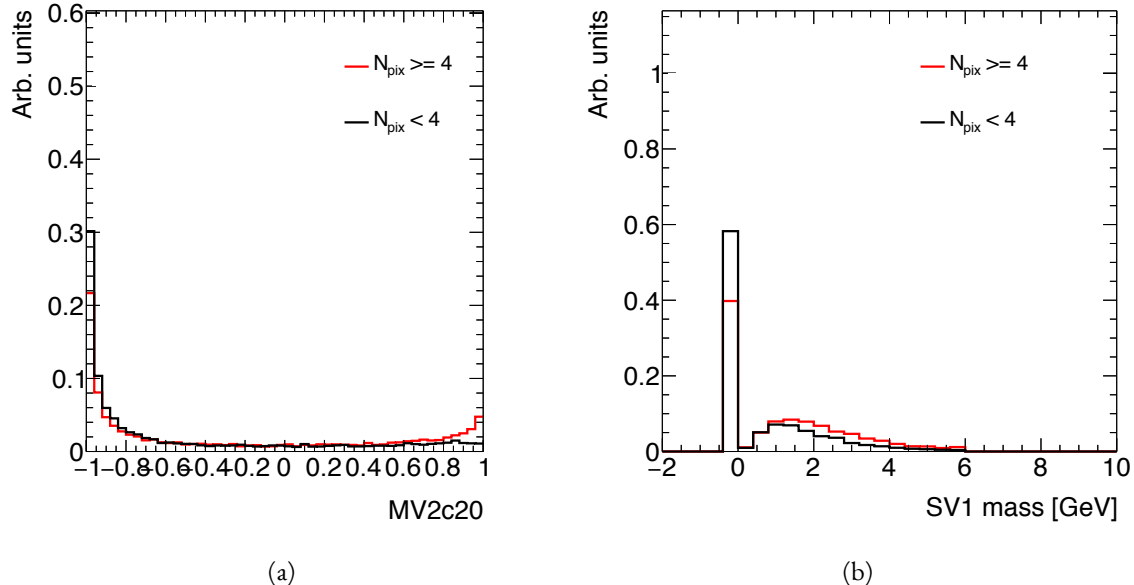


Figure A.9: MV2c20 score (a) and SV1 mass (b) for leading track jets whose leading track jet has at least four pixel hits ($N_{\text{pix}} \geq 4$) compared to those which do not ($N_{\text{pix}} < 4$).

2705

2706 have a secondary vertex reconstructed. Additionally, their MV2c20 score is shifted more significantly to

₂₇₀₇ background-like values. This seems to confirm the hypothesis that degrading track quality is responsible
₂₇₀₈ for the lowered b -tagging efficiency at high p_{T} .

References

2709

- 2710 [1] Georges Aad et al. Observation of a new particle in the search for the Standard Model Higgs
2711 boson with the ATLAS detector at the LHC. *Phys. Lett.*, B716:1–29, 2012. doi: 10.1016/j.physletb.
2712 2012.08.020.
- 2713 [2] Serguei Chatrchyan et al. Observation of a new boson at a mass of 125 GeV with the CMS experi-
2714 ment at the LHC. *Phys. Lett.*, B716:30–61, 2012. doi: 10.1016/j.physletb.2012.08.021.
- 2715 [3] David Griffiths. *Introduction to elementary particles*. 2008.
- 2716 [4] F. Halzen and Alan D. Martin. *QUARKS AND LEPTONS: AN INTRODUCTORY*
2717 *COURSE IN MODERN PARTICLE PHYSICS*. 1984. ISBN 0471887412, 9780471887416.
- 2718 [5] Christopher G. Tully. *Elementary particle physics in a nutshell*. 2011.
- 2719 [6] K. A. Olive et al. Review of Particle Physics. *Chin. Phys.*, C38:090001, 2014. doi: 10.1088/
2720 1674-1137/38/9/090001.
- 2721 [7] Matthew D. Schwartz. *Quantum Field Theory and the Standard Model*. Cambridge University
2722 Press, 2014. ISBN 1107034736, 9781107034730. URL <http://www.cambridge.org/us/academic/subjects/physics/theoretical-physics-and-mathematical-physics/quantum-field-theory-and-standard-model>.
- 2725 [8] S. Dawson. Introduction to electroweak symmetry breaking. In *High energy physics and cos-
2726 mology. Proceedings, Summer School, Trieste, Italy, June 29-July 17, 1998*, pages 1–83, 1998. URL
2727 <http://alice.cern.ch/format/showfull?sysnb=0301862>.
- 2728 [9] S. L. Glashow. Partial Symmetries of Weak Interactions. *Nucl. Phys.*, 22:579–588, 1961. doi:
2729 10.1016/0029-5582(61)90469-2.
- 2730 [10] Steven Weinberg. A Model of Leptons. *Phys. Rev. Lett.*, 19:1264–1266, 1967. doi: 10.1103/
2731 PhysRevLett.19.1264.
- 2732 [11] A. Salam. *Elementary Particle Theory*. Almqvist and Wiksell, Stockholm, 1968.
- 2733 [12] J. Iliopoulos S.L. Glashow and L. Maiani. *D2:1285*, 1970.
- 2734 [13] R. Keith Ellis, W. James Stirling, and B. R. Webber. QCD and collider physics. *Camb. Monogr.
2735 Part. Phys. Nucl. Phys. Cosmol.*, 8:1–435, 1996.

- 2736 [14] P. W. Higgs. Broken symmetries and the masses of gauge bosons. *13*:508, 1964.
- 2737 [15] P. W. Higgs. Spontaneous symmetry breakdown without massless bosons. *145*:1156, 1966.
- 2738 [16] F. Englert and R. Brout. Broken symmetry and the mass of gauge vector mesons. *13*:321, 1964.
- 2739 [17] G. S. Guralnik, C. R. Hagen, and T. W. .B. Kibble. Global conservation laws and massless parti-
2740 cles. *Phys. Rev. Lett.*, *13*:585, 1964. doi: [10.1103/PhysRevLett.13.585](https://doi.org/10.1103/PhysRevLett.13.585).
- 2741 [18] LHC Higgs Cross Section Working Group, S. Heinemeyer, C. Mariotti, G. Passarino, and
2742 R. Tanaka (Eds.). Handbook of LHC Higgs Cross Sections: 3, Higgs Properties. 2013.
- 2743 [19] J. Baglio, A. Djouadi, R. Gröber, M. M. Mühlleitner, J. Quevillon, and M. Spira. The mea-
2744 surement of the Higgs self-coupling at the LHC: theoretical status. *JHEP*, *04*:151, 2013. doi:
2745 [10.1007/JHEP04\(2013\)151](https://doi.org/10.1007/JHEP04(2013)151).
- 2746 [20] Matthew J. Dolan, Christoph Englert, and Michael Spannowsky. New Physics in LHC Higgs
2747 boson pair production. *Phys. Rev.*, *D87*(5):055002, 2013. doi: [10.1103/PhysRevD.87.055002](https://doi.org/10.1103/PhysRevD.87.055002).
- 2748 [21] Roberto Contino, Margherita Ghezzi, Mauro Moretti, Giuliano Panico, Fulvio Piccinini, and
2749 Andrea Wulzer. Anomalous Couplings in Double Higgs Production. *JHEP*, *08*:154, 2012. doi:
2750 [10.1007/JHEP08\(2012\)154](https://doi.org/10.1007/JHEP08(2012)154).
- 2751 [22] R. Grober and M. Mühlleitner. Composite Higgs Boson Pair Production at the LHC. *JHEP*, *06*:
2752 020, 2011. doi: [10.1007/JHEP06\(2011\)020](https://doi.org/10.1007/JHEP06(2011)020).
- 2753 [23] Lisa Randall and Raman Sundrum. A Large mass hierarchy from a small extra dimension. *Phys.*
2754 *Rev. Lett.*, *83*:3370–3373, 1999. doi: [10.1103/PhysRevLett.83.3370](https://doi.org/10.1103/PhysRevLett.83.3370).
- 2755 [24] Kaustubh Agashe, Hooman Davoudiasl, Gilad Perez, and Amarjit Soni. Warped Gravitons at the
2756 LHC and Beyond. *Phys. Rev.*, *D76*:036006, 2007. doi: [10.1103/PhysRevD.76.036006](https://doi.org/10.1103/PhysRevD.76.036006).
- 2757 [25] A. Liam Fitzpatrick, Jared Kaplan, Lisa Randall, and Lian-Tao Wang. Searching for the Kaluza-
2758 Klein Graviton in Bulk RS Models. *JHEP*, *09*:013, 2007. doi: [10.1088/1126-6708/2007/09/013](https://doi.org/10.1088/1126-6708/2007/09/013).
- 2759 [26] Julien Baglio, Otto Eberhardt, Ulrich Nierste, and Martin Wiebusch. Benchmarks for Higgs Pair
2760 Production and Heavy Higgs boson Searches in the Two-Higgs-Doublet Model of Type II. *Phys.*
2761 *Rev.*, *D90*(1):015008, 2014. doi: [10.1103/PhysRevD.90.015008](https://doi.org/10.1103/PhysRevD.90.015008).
- 2762 [27] G. C. Branco, P. M. Ferreira, L. Lavoura, M. N. Rebelo, Marc Sher, and Joao P. Silva. Theory
2763 and phenomenology of two-Higgs-doublet models. *Phys. Rept.*, *516*:1–102, 2012. doi: [10.1016/j.physrep.2012.02.002](https://doi.org/10.1016/j.physrep.2012.02.002).
- 2765 [28] Howard E. Haber and Oscar Stål. New LHC benchmarks for the \mathcal{CP} -conserving two-Higgs-
2766 doublet model. *Eur. Phys. J.*, *C75*(10):491, 2015. doi: [10.1140/epjc/s10052-015-3697-x](https://doi.org/10.1140/epjc/s10052-015-3697-x).

- 2767 [29] Jose M. No and Michael Ramsey-Musolf. Probing the Higgs Portal at the LHC Through Reso-
 2768 nant di-Higgs Production. *Phys. Rev.*, D89(9):095031, 2014. doi: 10.1103/PhysRevD.89.095031.
- 2769 [30] Johan Alwall, Michel Herquet, Fabio Maltoni, Olivier Mattelaer, and Tim Stelzer. MadGraph
 2770 5:Going Beyond. *JHEP*, 1106:128, 2011. doi: 10.1007/JHEP06(2011)128.
- 2771 [31] Lyndon R Evans and Philip Bryant. LHC Machine. *J. Instrum.*, 3:S08001. 164 p, 2008. URL
 2772 <https://cds.cern.ch/record/1129806>. This report is an abridged version of the LHC
 2773 Design Report (CERN-2004-003).
- 2774 [32] ATLAS Collaboration. The ATLAS experiment at the CERN Large Hadron Collider. *JINST*, 3:
 2775 S08003, 2008. doi: 10.1088/1748-0221/3/08/S08003.
- 2776 [33] CMS Collaboration. The cms experiment at the cern lhc. *Journal of Instrumentation*, 3(08):
 2777 S08004, 2008. URL <http://stacks.iop.org/1748-0221/3/i=08/a=S08004>.
- 2778 [34] LHCb Collaoration. The LHCb Detector at the LHC. *JINST*, 3:S08005, 2008. doi: 10.1088/
 2779 1748-0221/3/08/S08005.
- 2780 [35] ALICE Collaboration. The alice experiment at the cern lhc. *Journal of Instrumentation*, 3(08):
 2781 S08002, 2008. URL <http://stacks.iop.org/1748-0221/3/i=08/a=S08002>.
- 2782 [36] Lyndon Evans. The Large Hadron Collider. In Holstein, BR and Haxton, WC and Jawahery,
 2783 A, editor, *ANNUAL REVIEW OF NUCLEAR AND PARTICLE SCIENCE, VOL 61*,
 2784 volume 61 of *Annual Review of Nuclear and Particle Science*, pages 435–466. 2011. doi: {10.1146/annurev-nucl-102010-130438}.
- 2785 [37] ATLAS Collaboration. Luminosity Determination in pp Collisions at $\sqrt{s} = 7$ TeV Using the
 2786 ATLAS Detector at the LHC. *Eur. Phys. J.*, C 71:1630, 2011. doi: 10.1140/epjc/s10052-011-1630-5.
- 2787 [38] Mike Lamont for the LHC team. The First Years of LHC Operation for Luminosity Production.
 2788 International Particle Accelerator Conference, 2013. URL https://accelconf.web.cern.ch/accelconf/IPAC2013/talks/moyab101_talk.pdf.
- 2789 [39] Paul Collier for the LHC team. LHC Machine Status. CERN Resource Review Board, 2015.
 2790 URL <https://cds.cern.ch/record/2063924/files/CERN-RRB-2015-119.PDF>.
- 2791 [40] Track Reconstruction Performance of the ATLAS Inner Detector at $\sqrt{s} = 13$ TeV. Technical
 2792 Report ATL-PHYS-PUB-2015-018, CERN, Geneva, Jul 2015. URL <http://cds.cern.ch/record/2037683>.

- 2796 [41] M Capeans, G Darbo, K Einsweiller, M Elsing, T Flick, M Garcia-Sciveres, C Gemme, H Perneg-
2797 ger, O Rohne, and R Vuillermet. ATLAS Insertable B-Layer Technical Design Report. Tech-
2798 nical Report CERN-LHCC-2010-013, ATLAS-TDR-19, CERN, Geneva, Sep 2010. URL
2799 <https://cds.cern.ch/record/1291633>.
- 2800 [42] ATLAS Collaboration. ATLAS Trigger Operations Public Results. 2015. URL <https://twiki.cern.ch/twiki/bin/view/AtlasPublic/TriggerOperationPublicResults>.
- 2801 [43] ATLAS Collaboration. ATLAS Luminosity Public Results, Run 1. 2012. URL <https://twiki.cern.ch/twiki/bin/view/AtlasPublic/LuminosityPublicResults>.
- 2802 [44] ATLAS Collaboration. ATLAS Luminosity Public Results, Run 2. 2015. URL <https://twiki.cern.ch/twiki/bin/view/AtlasPublic/LuminosityPublicResultsRun2>.
- 2803 [45] T Kawamoto, S Vlachos, L Pontecorvo, J Dubbert, G Mikenberg, P Iengo, C Dallapiccola,
2804 C Amelung, L Levinson, R Richter, and D Lellouch. New Small Wheel Technical Design Re-
2805 port. Technical Report CERN-LHCC-2013-006, ATLAS-TDR-020, CERN, Geneva, Jun 2013.
2806 URL <https://cds.cern.ch/record/1552862>. ATLAS New Small Wheel Technical Design
2807 Report.
- 2808 [46] Y. Giomataris, Ph. Rebours, J.P. Robert, and G. Charpak. Micromegas: a high-granularity
2809 position-sensitive gaseous detector for high particle-flux environments. *Nuclear Instruments
2810 and Methods in Physics Research Section A: Accelerators, Spectrometers, Detectors and As-
2811 sociated Equipment*, 376(1):29 – 35, 1996. ISSN 0168-9002. doi: [http://dx.doi.org/10.1016/0168-9002\(96\)00175-1](http://dx.doi.org/10.1016/0168-9002(96)00175-1). URL <http://www.sciencedirect.com/science/article/pii/0168900296001751>.
- 2812 [47] T. Alexopoulos, J. Burnens, R. de Oliveira, G. Glonti, O. Pizzirusso, V. Polychronakos,
2813 G. Sekhniaidze, G. Tsipolitis, and J. Wotschack. A spark-resistant bulk-micromegas chamber for
2814 high-rate applications. *Nuclear Instruments and Methods in Physics Research Section A: Acceler-
2815 ators, Spectrometers, Detectors and Associated Equipment*, 640(1):110 – 118, 2011. ISSN 0168-9002.
2816 doi: <http://dx.doi.org/10.1016/j.nima.2011.03.025>. URL <http://www.sciencedirect.com/science/article/pii/S0168900211005869>.
- 2818 [48] Joao Pequenao and Paul Schaffner. An computer generated image representing how ATLAS
2819 detects particles. Jan 2013. URL <https://cds.cern.ch/record/1505342>.
- 2820 [49] Improved electron reconstruction in ATLAS using the Gaussian Sum Filter-based model for
2821 bremsstrahlung. Technical Report ATLAS-CONF-2012-047, CERN, Geneva, May 2012. URL
2822 <https://cds.cern.ch/record/1449796>.

- 2828 [50] Electron efficiency measurements with the ATLAS detector using the 2012 LHC proton-proton
2829 collision data. Technical Report ATLAS-CONF-2014-032, CERN, Geneva, Jun 2014. URL
2830 <https://cds.cern.ch/record/1706245>.
- 2831 [51] Georges Aad et al. Electron and photon energy calibration with the ATLAS detector using LHC
2832 Run 1 data. *Eur. Phys. J.*, C74(10):3071, 2014. doi: 10.1140/epjc/s10052-014-3071-4.
- 2833 [52] Georges Aad et al. Measurement of the muon reconstruction performance of the ATLAS detec-
2834 tor using 2011 and 2012 LHC proton–proton collision data. *Eur. Phys. J.*, C74(11):3130, 2014. doi:
2835 10.1140/epjc/s10052-014-3130-x.
- 2836 [53] W Lampl, S Laplace, D Lelas, P Loch, H Ma, S Menke, S Rajagopalan, D Rousseau, S Snyder,
2837 and G Unal. Calorimeter Clustering Algorithms: Description and Performance. Technical
2838 Report ATL-LARG-PUB-2008-002. ATL-COM-LARG-2008-003, CERN, Geneva, Apr 2008.
2839 URL <https://cds.cern.ch/record/1099735>.
- 2840 [54] Georges Aad et al. Topological cell clustering in the ATLAS calorimeters and its performance in
2841 LHC Run 1. 2016.
- 2842 [55] Matteo Cacciari, Gavin P. Salam, and Gregory Soyez. The Anti-k(t) jet clustering algorithm.
2843 *JHEP*, 04:063, 2008. doi: 10.1088/1126-6708/2008/04/063.
- 2844 [56] Monte Carlo Calibration and Combination of In-situ Measurements of Jet Energy Scale, Jet En-
2845 ergy Resolution and Jet Mass in ATLAS. Technical Report ATLAS-CONF-2015-037, CERN,
2846 Geneva, Aug 2015. URL <http://cds.cern.ch/record/2044941>.
- 2847 [57] Georges Aad et al. Performance of *b*-Jet Identification in the ATLAS Experiment. 2015.
- 2848 [58] Expected performance of the ATLAS *b*-tagging algorithms in Run-2. Technical Report ATL-
2849 PHYS-PUB-2015-022, CERN, Geneva, Jul 2015. URL <http://cds.cern.ch/record/2037697>.
- 2850 [59] Georges Aad et al. Performance of Missing Transverse Momentum Reconstruction in Proton-
2851 Proton Collisions at 7 TeV with ATLAS. *Eur. Phys. J.*, C72:1844, 2012. doi: 10.1140/epjc/
2852 s10052-011-1844-6.
- 2853 [60] Performance of Missing Transverse Momentum Reconstruction in ATLAS studied in Proton-
2854 Proton Collisions recorded in 2012 at 8 TeV. Technical Report ATLAS-CONF-2013-082, CERN,
2855 Geneva, Aug 2013. URL <http://cds.cern.ch/record/1570993>.
- 2856 [61] ATLAS Collaboration. Observation and measurement of Higgs boson decays to WW* with the
2857 ATLAS detector. *Phys. Rev. D*, 92(012006), 2015.

- 2859 [62] Aaron James Armbruster. Discovery of a Higgs Boson with the ATLAS detector. 2013. CERN-
 2860 THESIS-2013-047.
- 2861 [63] G. Cowan, K. Cranmer, E. Gross, and O. Vitells. Asymptotic formulae for likelihood-based tests
 2862 of new physics. *Eur. Phys. J., C* 71:1554, 2011. doi: 10.1140/epjc/s10052-011-1554-0.
- 2863 [64] ATLAS Collaboration. Limits on the production of the Standard Model Higgs Boson in pp
 2864 collisions at $\sqrt{s} = 7$ TeV with the ATLAS detector. *Eur. Phys. J., C* 71:1728, 2011. doi: 10.1140/
 2865 epjc/s10052-011-1728-9.
- 2866 [65] ATLAS Collaboration. Performance of the ATLAS muon trigger in pp collisions at $\sqrt{s} = 8$
 2867 TeV. *Eur. Phys. J. C*, (arXiv:1408.3179. CERN-PH-EP-2014-154):75. 19 p, Aug 2014. URL <https://cds.cern.ch/record/1749694>.
- 2869 [66] ATLAS collaboration. Electron trigger performance in 2012 ATLAS data, 2015. ATLAS-COM-
 2870 DAQ-2015-091.
- 2871 [67] Paolo Nason. A new method for combining NLO QCD with shower Monte Carlo algorithms.
 2872 *JHEP*, 11:040, 2004.
- 2873 [68] B. P. Kersevan and E. Richter-Was. The Monte Carlo event generator AcerMC version 2.0 with
 2874 interfaces to PYTHIA 6.2 and HERWIG 6.5. 2004.
- 2875 [69] Nikolas Kauer and Giampiero Passarino. Inadequacy of zero-width approximation for a light
 2876 Higgs boson signal. 2012.
- 2877 [70] T. Gleisberg, Stefan Hoeche, F. Krauss, M. Schonherr, S. Schumann, et al. Event generation with
 2878 SHERPA 1.1. *JHEP*, 0902:007, 2009. doi: 10.1088/1126-6708/2009/02/007.
- 2879 [71] Michelangelo L. Mangano et al. ALPGEN, a generator for hard multiparton processes in
 2880 hadronic collisions. *JHEP*, 0307:001, 2003. doi: 10.1088/1126-6708/2003/07/001.
- 2881 [72] Torbjorn Sjostrand, Stephen Mrenna, and Peter Z. Skands. PYTHIA 6.4 Physics and Manual.
 2882 *JHEP*, 0605:026, 2006. doi: 10.1088/1126-6708/2006/05/026.
- 2883 [73] Torbjorn Sjostrand, Stephen Mrenna, and Peter Z. Skands. A Brief Introduction to PYTHIA 8.1.
 2884 *Comput.Phys.Commun.*, 178:852–867, 2008. doi: 10.1016/j.cpc.2008.01.036.
- 2885 [74] G. Corcella et al. HERWIG 6: An event generator for hadron emission reactions with interfering
 2886 gluons (including super-symmetric processes). *JHEP*, 01:010, 2001. doi: 10.1088/1126-6708/2001/
 2887 01/010.
- 2888 [75] J. M. Butterworth, Jeffrey R. Forshaw, and M. H. Seymour. Multiparton interactions in photo-
 2889 production at HERA. *Z. Phys., C* 72:637, 1996. doi: 10.1007/s002880050286.

- 2890 [76] Jun Gao, Marco Guzzi, Joey Huston, Hung-Liang Lai, Zhao Li, et al. The CT10 NNLO Global
 2891 Analysis of QCD. *Phys. Rev.*, D89:033009, 2014. doi: 10.1103/PhysRevD.89.033009.
- 2892 [77] P. M. Nadolsky. Implications of CTEQ global analysis for collider observables. *Phys. Rev.*, D 78:
 2893 013004, 2008. doi: 10.1103/PhysRevD.78.013004.
- 2894 [78] A. Sherstnev and R. S. Thorne. Parton distributions for the LHC. *Eur. Phys. J.*, C 55:553, 2009.
 2895 doi: 10.1140/epjc/s10052-008-0610-x.
- 2896 [79] S. Agostinelli et al. GEANT4, a simulation toolkit. *Nucl. Instrum. Meth.*, A 506:250, 2003. doi:
 2897 10.1016/S0168-9002(03)01368-8.
- 2898 [80] R.K. Ellis, I. Hinchliffe, M. Soldate, and J.J. Van Der Bij. Higgs decay to $\tau+\tau$ -a possible signature
 2899 of intermediate mass higgs bosons at high energy hadron colliders. *Nuclear Physics B*, 297(2):
 2900 221 – 243, 1988. ISSN 0550-3213. doi: [http://dx.doi.org/10.1016/0550-3213\(88\)90019-3](http://dx.doi.org/10.1016/0550-3213(88)90019-3). URL
 2901 <http://www.sciencedirect.com/science/article/pii/0550321388900193>.
- 2902 [81] Eilam Gross and Ofer Vitells. Transverse mass observables for charged Higgs boson searches at
 2903 hadron colliders. *Phys. Rev.*, D81:055010, 2010. doi: 10.1103/PhysRevD.81.055010.
- 2904 [82] J. R. Andersen et al. Les Houches 2013: Physics at TeV Colliders: Standard Model Working
 2905 Group Report. 2014.
- 2906 [83] I. Stewart and F. Tackmann. Theory uncertainties for Higgs mass and other searches using jet
 2907 bins. *Phys. Rev.*, D 85:034011, 2012. doi: 10.1103/PhysRevD.85.034011.
- 2908 [84] ATLAS Collaboration. Luminosity Determination in pp Collisions at $\sqrt{s} = 7$ TeV Using the
 2909 ATLAS Detector at the LHC. *Eur. Phys. J.*, C 71:1630, 2011. doi: 10.1140/epjc/s10052-011-1630-5.
- 2910 [85] Jet energy scale and its systematic uncertainty in proton-proton collisions at $\sqrt{s} = 7$ tev with
 2911 atlas 2011 data. *ATLAS-CONF-2013-004*, 2013.
- 2912 [86] Calibrating the b -tag efficiency and mistag rate in 35 pb^{-1} of data with the atlas detector.
 2913 *ATLAS-CONF-2011-089*, 2011.
- 2914 [87] ATLAS Collaboration. Measurement of the b -tag Efficiency in a Sample of Jets Containing
 2915 Muons with 5 fb^{-1} of Data from the ATLAS Detector. *ATLAS-CONF-2012-043*, 2012. URL
 2916 <http://cdsweb.cern.ch/record/1435197>.
- 2917 [88] ATLAS Collaboration. Calibration of b -tagging using dileptonic top pair events in a combinatorial
 2918 likelihood approach with the ATLAS experiment. (ATLAS-CONF-2014-004), 2014. URL
 2919 <http://cds.cern.ch/record/1664335>.

- 2920 [89] Georges Aad et al. Measurement of the Higgs boson mass from the $H \rightarrow \gamma\gamma$ and $H \rightarrow ZZ^* \rightarrow$
 2921 4ℓ channels with the ATLAS detector using 25 fb^{-1} of pp collision data. *Phys. Rev.*, D90(5):
 2922 052004, 2014. doi: 10.1103/PhysRevD.90.052004.
- 2923 [90] Georges Aad et al. Measurements of the Higgs boson production and decay rates and coupling
 2924 strengths using pp collision data at $\sqrt{s} = 7$ and 8 TeV in the ATLAS experiment. *Eur. Phys. J.*,
 2925 C76(1):6, 2016. doi: 10.1140/epjc/s10052-015-3769-y.
- 2926 [91] W.J. Stirling. $7/8$ and $13/8\text{ TeV}$ LHC luminosity ratios. 2013. URL http://www.hep.physics.ac.uk/~wstirlin/plots/lhclumi7813_2013_v0.pdf.
- 2927 [92] J Alison. Experimental Studies of hh. Oct 2014. URL <http://cds.cern.ch/record/1952581>.
- 2928 [93] J. Alwall et al. The automated computation of tree-level and next-to-leading order differential
 2929 cross sections, and their matching to parton shower simulations. *JHEP*, 07:079, 2014.
- 2930 [94] Richard D. Ball et al. Parton distributions with LHC data. *Nucl. Phys. B*, 867:244, 2013.
- 2931 [95] ATLAS Collaboration. ATLAS Run 1 Pythia8 tunes. (ATL-PHYS-PUB-2014-021), Nov 2014.
 2932 URL <https://cds.cern.ch/record/1966419>.
- 2933 [96] M. Bahr et al. Herwig++ Physics and Manual. *Eur. Phys. J. C*, 58:639–707, 2008. doi: 10.1140/
 2934 epjc/s10052-008-0798-9.
- 2935 [97] Stefan Gieseke, Christian Rohr, and Andrzej Siodmok. Colour reconnections in Herwig++. *Eur.*
 2936 *Phys. J. C*, 72:2225, 2012. doi: 10.1140/epjc/s10052-012-2225-5.
- 2937 [98] Simone Alioli, Paolo Nason, Carlo Oleari, and Emanuele Re. A general framework for imple-
 2938 menting NLO calculations in shower Monte Carlo programs: the POWHEG BOX. *JHEP*, 06:
 2939 043, 2010.
- 2940 [99] Peter Zeiler Skands. Tuning Monte Carlo Generators: The Perugia Tunes. *Phys. Rev. D*, 82:
 2941 074018, 2010. doi: 10.1103/PhysRevD.82.074018.
- 2942 [100] Michal Czakon and Alexander Mitov. Top++: A Program for the Calculation of the Top-Pair
 2943 Cross-Section at Hadron Colliders. 2011.
- 2944 [101] Baojia (Tony) Tong. Private communication.
- 2945 [102] D. Krohn, J. Thaler, and L.-T. Wang. Jet Trimming. *JHEP*, 02:084, 2010. doi: 10.1007/
 2946 JHEP02(2010)084.
- 2947 [103] ATLAS Collaboration. Identification of Boosted, Hadronically Decaying W Bosons and Com-
 2948 parisons with ATLAS Data Taken at $\sqrt{s} = 8\text{ TeV}$. 2015.

- 2951 [104] Expected Performance of Boosted Higgs ($\rightarrow b\bar{b}$) Boson Identification with the ATLAS Detector
 2952 at $\sqrt{s} = 13$ TeV. Technical Report ATL-PHYS-PUB-2015-035, CERN, Geneva, Aug 2015. URL
 2953 <https://cds.cern.ch/record/2042155>.
- 2954 [105] Flavor Tagging with Track Jets in Boosted Topologies with the ATLAS Detector. Technical
 2955 Report ATL-PHYS-PUB-2014-013, CERN, Geneva, Aug 2014. URL [https://cds.cern.ch/](https://cds.cern.ch/record/1750681)
 2956 [record/1750681](https://cds.cern.ch/record/1750681).
- 2957 [106] Matteo Cacciari and Gavin P. Salam. Pileup subtraction using jet areas. *Phys. Lett. B*, 659:119,
 2958 2008. doi: [10.1016/j.physletb.2007.09.077](https://doi.org/10.1016/j.physletb.2007.09.077).
- 2959 [107] Glen Cowan, Eilam Gross. Discovery significance with statistical uncertainty in the background
 2960 estimate. 2008. URL <http://www.pp.rhul.ac.uk/~cowan/stat/notes/SigCalcNote.pdf>.
- 2961 [108] Search for pair production of Higgs bosons in the $b\bar{b}b\bar{b}$ final state using proton-proton collisions
 2962 at $\sqrt{s} = 13$ TeV with the ATLAS detector. Technical Report ATLAS-CONF-2016-017, CERN,
 2963 Geneva, Mar 2016. URL <https://cds.cern.ch/record/2141006>.
- 2964 [109] Qi Zeng. Private communication.
- 2965 [110] ATLAS Collaboration. Identification of boosted, hadronically-decaying W and Z bosons in
 2966 $\sqrt{s} = 13$ TeV Monte Carlo Simulations for ATLAS. (ATL-PHYS-PUB-2015-033), Aug 2015.
 2967 URL <https://cds.cern.ch/record/2041461>.
- 2968 [111] ATLAS Collaboration. Performance of b -Jet Identification in the ATLAS Experiment. 2015.
- 2969 [112] Alexander L. Read. Presentation of search results: The CL(s) technique. *J. Phys. G*, 28:2693,
 2970 2002. doi: [10.1088/0954-3899/28/10/313](https://doi.org/10.1088/0954-3899/28/10/313).
- 2971 [113] Measurements of the Higgs boson production and decay rates and constraints on its couplings
 2972 from a combined ATLAS and CMS analysis of the LHC pp collision data at $\sqrt{s} = 7$ and 8 TeV.
 2973 Technical Report ATLAS-CONF-2015-044, CERN, Geneva, Sep 2015. URL <http://cds.cern.ch/record/2052552>.
- 2974 [114] Projections for measurements of Higgs boson signal strengths and coupling parameters with the
 2975 ATLAS detector at a HL-LHC. Technical Report ATL-PHYS-PUB-2014-016, CERN, Geneva,
 2976 Oct 2014. URL <http://cds.cern.ch/record/1956710>.
- 2977 [115] ATLAS Phase-II Upgrade Scoping Document. Technical Report CERN-LHCC-2015-020.
 2978 LHCC-G-166, CERN, Geneva, Sep 2015. URL <http://cds.cern.ch/record/2055248>.



THIS THESIS WAS TYPESET using L^AT_EX, originally developed by Leslie Lamport and based on Donald Knuth's T_EX.

The body text is set in 11 point Egenolff-Berner Garamond, a revival of Claude Garamont's humanist typeface. The above illustration, *Science Experiment 02*, was created by Ben Schlitter and released under CC BY-NC-ND 3.0. A template that can be used to format a PhD dissertation with this look & feel has been released under the permissive AGPL license, and can be found online at github.com/asm-products/Dissertate or from its lead author, Jordan Suchow, at suchow@post.harvard.edu.